Universidade Vigo

Departamento de Química Física

Tesis Doctoral

RATIONAL SYNTHESIS AND SELF-ASSEMBLY OF ANISOTROPIC PLASMONIC NANOPARTICLES

Director:
Prof. Dr. Luis M. Liz Marzán

Candidato:
Leonardo Scarabelli

Vigo, Diciembre de 2015

BiO NanoPlasmOnics

CIC biomaGUNE

D. Luis Manuel Liz Marzán, Catedrático del Departamento de Química Física de la Universidad de Vigo informa que:

Leonardo Scarabelli, licenciado en Química, ha realizado en el Centro de Investigaciones Cooperativas en Biomateriales (CICbiomaGUNE) de San Sebastián bajo su dirección el trabajo descrito en la presente memoria, que lleva por título "Rational Synthesis and Self-Assembly of Anisotropic Plasmonic Nanoparticles", y que presenta para optar al grado de Doctor por la Universidad de Vigo con Mención Internacional.

Vigo, 14 de Diciembre de 2015

Fdo. Luis Manuel Liz Marzán

CONTENTS

ABBREVIATIONS

5-BrSA	5-Bromo Salicylic Acid
AA	Ascorbic Acid
AFM	Atomic Force Microscopy
AgEn	Degree of Silver Elongation
AR	Aspect Ratio
Au@Ag	Silver coated Gold
BDAC	BenzylDimethylAmmonium Chloride
BEM	Boundary Element Method
CL	Cathodoluminescence
CLPR	Controlled Living Polymerization Reaction
CTAB	CetylTrimethylAmmonium Bromide
CTAC	CetylTrimethylAmmonium Chloride
CV	Crystal Violet
DFM	Dark Field Microscopy
DFT	Density Functional Theory
DLS	Dynamic Light Scattering
DMF	DiMethylFormamide
EDX o EDS	Energy-Dispersive X-ray Spectroscopy
EELS	Electron Energy Loss Spectroscopy
EF	Enhancement Factor
FFT	Fast Fourier Transform
FIB	Focused Ion Beam
FWHM	Full Width at Half Maximum
GMRES	Generalized Minimal Residual Method
HAADF	High Angle Annular Dark Field
HOMO	Highest Occupied Molecular Orbital
HR-SEM	High Resolution Scanning Electron Microscopy
HR-TEM	High Resolution Scanning Electron Microscopy
ICP-MS	Inductively Coupled Plasma Mass Spectrometry
IR	InfraRed
IUPAC	International Union of Pure and Applied Chemistry
LDOS	Local Density Of States
LSPR	Localized Surface Plasmon Resonance
LUMO	Lowest Unoccupied Molecular Orbital
MLFMA	Multilevel Fast Multipole Algorithm

MoM	Method of Moments
MUDOL	(1-mercaptoundec-11-yl)hexa(ethyleneglycol)
NA	Numerical Aperture
NIR	Near InfraRed
PDMS	Poly(DimethylSiloxane)
PVP	Polyvinylpyrrolidone
Q-factor	Quality factor
SANS	Small Angle Neutron Scattering
SAXS	Small Angle X-ray Scattering
SEM	Scanning Electron Microscopy
SERRS	Surface Enhanced Resonant Raman Scattering
SERS	Surface Enhanced Raman Scattering
SIRT	Simultaneous Iterative Reconstruction Technique
STEM	Scanning Transmission Electron Microscopy
TEM	Transmission Electron Microscopy
TVM	Total Variation Minimization
UPD	UnderPotential Deposition
XPS	X-ray Photoelectron Spectroscopy
ZLP	Zero-Loss Peak

SCOPE OF THE THESIS

This thesis work has been carried out in the framework of the ERC Advanced Grant *Plasmaquo* (nº 267867), which focused on the development of novel nanostructured plasmonic materials based on crystalline assemblies of anisotropic nanoparticles, to be used as optical enhancers for the surface enhanced Raman scattering detection of bacterial Quorum Sensing signaling molecules. More specifically, the thesis was oriented toward the design of such nanostructures, and on the characterization of their optical properties by means of various experimental techniques. In particular, the ability to assemble nanoparticles into ordered nanostructures relies on the narrow size dispersion of the building blocks; therefore the first part of the experimental work was dedicated to the optimization of various synthetic procedures. Since the final goal was the application of these nanostructures for surface enhanced Raman spectroscopy, our synthetic efforts focused on gold and silver nanoparticles: in fact, while silver is plasmonically more active and is therefore giving rise to higher enhancement factors (lowering the limit of detection of the device), gold is chemically more inert and robust towards oxidation, and offers a wider range of synthetic possibilities. The self-assembly of the synthesized building blocks was optimized to control the formation of ordered nanostructured with different sizes and shapes over large areas (centimeters squared), exploiting simple procedures and giving importance to low cost and reproducibility of the fabricated devices. The experimental part was carried out mainly in the Bionanoplasmonics Laboratory at CIC biomaGUNE (San Sebastián), complemented by two research stay periods at the University of Hamburg and at Rice University in Houston. Importantly, part of the results included in the thesis stem from collaborations with external groups, mainly regarding the theoretical interpretation of the results, and advanced electron tomography, as well as plasmon mapping by electron microscopy techniques. Exploiting the complementary expertise of our laboratory and our collaborators, we were able to develop improved synthetic protocols for the wet-chemistry synthesis of different plasmonic nanoparticles, and to implement their rational directed self-assembly into plasmonic nanostructures designed for biosensing. In what follows we present a brief outline of each chapter.

In Chapter II, we start presenting a broad overview of the state of the art for the synthesis of anisotropic noble metal nanoparticles; followed by presentation of optimized synthetic protocols. We investigated the effect of the addition of 5-Bromo salicylic acid on the synthesis of single crystal gold nanorods, exploiting its reducing properties as a new handle for tuning the nanorod aspect ratio (section II.2.7). We additionally proposed a new approach for the controlled overgrowth of gold nanoparticles, based on their redispersion in a pre-reduced solution of gold precursor. In section II.3 we describe the optimization of the synthesis of gold nanotriangles (also termed nanoprisms) through the control of the degree of twinning in gold seeds. Finally, in section II.4 we display the work on the selective deposition of silver onto the tips of penta-twinned gold nanorod cores, introducing the concept of *controlled linear nanowire growth*. By establishing a constant silver deposition rate, the length of the wires was found to increase linearly with time, allowing us to suppress side reactions and produce nanowire lengths up to several microns in a highly controlled manner and without loss of quality.

In Chapter III we proceed with the analysis of nanoparticle self-assembly. Single crystal gold nanorods were packed into supercrystals with variable height (up to several microns). We exploited the surface properties of the nanorods upon coating with a neutral thiol, as well as the confined drying into a PDMS mould. Under suitable experimental conditions, the nanorod building-blocks organized into extended smectic phases, with most of the gold nanorods standing with their long axes perpendicular to the substrate (section II.1). These supercrystals present a high concentration of hot spots, which render these substrates as interesting candidates for surface enhanced Raman scattering spectroscopy.

Finally, in Chapter IV we focus our attention on the characterization of plasmonic nanostructures. In particular, correlated single particle analysis was performed on nanoprisms (section IV.2.1) and silver-gold-silver bimetallic nanowires (section IV.2.2). We experimentally compared electron energy loss spectroscopy and cathodoluminescence on the very same particles, followed by correlation with the far-field classical concepts of extinction

and scattering cross-sections. In the case of silver-gold-silver bimetallic nanowires, electron energy loss spectroscopy allowed us to investigate the influence of the gold cores on the optical properties of the plasmonic nanoantennas. In section IV.2.3, we analyze the near-field properties of gold nanorod supercrystals, and in particular we focus our attention on the relationship between the number of layers and the distribution of hot spots. Interestingly, we demonstrate that increasing the number of nanorod layers does not guarantee an increase in the electric field enhancement at the top layer of the supercrystals.

As a whole, this thesis presents significant advancement in both synthesis and self-assembly of different anisotropic plasmonic nanoparticles. The presented results could have important applications in several fields, such as nanomedicine, biosensing or catalysis.

Uomini, uomini del mio presente
non mi consola l'abitudine a questa mia forzata solitudine.
Io non pretendo il mondo intero, vorrei soltanto un luogo, un posto più sincero
dove magari un giorno molto presto io finalmente possa dire questo è il mio posto
dove rinasca, non so come e quando, il senso di uno sforzo collettivo per ritrovare il mondo.

L'appartenenza è assai di più della salvezza personale
è la speranza di ogni uomo che sta male e non gli basta esser civile.
E' quel vigore che si sente se fai parte di qualcosa
che in sé travolge ogni egoismo personale
con quell'aria più vitale che è davvero contagiosa.

Benvenuto il luogo dove tanta gente non fa massa.

Giorgio Gaber (1939 – 2003)

CHAPTER

INTRODUCTION

I.1. NANOTECHNOLOGY AND NANOSCALE

Nowadays, many people believe that nanotechnology will be the next technological revolution, and that after the digital era, human society will enter into the "nano-era". As a matter of fact, nanotechnology can represent the biggest technological leap in human history, being expected to provide groundbreaking solutions to many challenges that threaten our future: it promises faster computers, improved security, longer healthier lives and a cleaner Earth. Indeed, the outputs of the 2011 investigation of the Engineering and Physical Sciences Research Council about the grand challenges of material science for the next century, two out of four points are strongly related with nanotechnology, namely "Assembling and control at the nanoscale" and "Smart design of Functional Materials".[1]

The starting point of the nanotechnology history is often referred to the lecture by Richard Feynman in 1959, entitled "There's plenty of room at the bottom".[2] In his vision, small machines will be able to assemble smaller components which can be used to build even smaller machines. This concept can be extrapolated to its very limit, where atomic size machinery can assemble components atom by atom, in this way being able to construct literally everything (having at disposal enough time and energy). Other researchers contribute to this idea; for example, Marvin Minsky was the first to recognize the intrinsic limit of a top-down approach for the miniaturization of electronic components,[3] while Eric Drexler introduced the concept of assembler, i.e. a nanoscale machine able to create nanostructured materials and most importantly to replicate itself and create other nanoscale machines.[4] This vision brings us to the ultimate aim of nanotechnology, i.e. the bottom-to-bottom assembly at the atomic scale. More realistically, the huge distance that separates the nanoscale from the classical world forces us to find alternative intermediate solutions to achieve this goal; this solution has been found in the production of nanometric building-blocks, ideally identical to one another (within a given type), properly designed to be assembled into structures suitable to human use. This concept is the fundamental basis of self-assembly (see chapter III).

But why nano? What is so especially interesting in the nanoscale? We can infer the answers to these questions starting from looking at some definitions of nanotechnology: "nanotechnology is concerned with systems whose structures and components exhibit novel

and significantly improved physical, chemical, and biological properties, phenomena, and processes due to their nanoscale size" (US National Nanotechnology Initiative),[5] "nanotechnology is a group of emerging technologies in which the structure of matter is controlled at the nanometer scale to produce novel materials and devices that have useful and unique properties" (US Foresight Institute), or "nanotechnology pertains to the processing of materials in which structure of a dimension of less than 100 nm is essential to obtain the required functional performance".[6]

From all these definitions, we can observe that the emergence of new properties as the size is reduced is particular emphasized, together with the focus on a practical use of the produced devices.[7] The first feature leads to two important conclusions: i) such properties have to be somehow related to the dimensions of the object under study, i.e. they must be size-dependent, and ii) there must be a point of discontinuity marking the appearance of a state where the properties of matter differ from those at both atomic and bulk scales. In this sense we can state that nanotechnology asserts that "less is different", meaning that when decreasing particle size a whole family of new phenomena arises, with the need for a new level of description.[8] This digs a deep groove between chemistry and nanotechnology: in fact a molecule is defined as the smallest unit maintaining all the properties of bulk matter, exactly the opposite to a nanoobject. This "crossover length" at which a particular size-dependent "nano-property" arises can be used to define the term nanoscale; clearly, the borders of this definition will change depending on which phenomena we are considering.

In what follows we present an overview of the most important size-dependent properties arising at the nanoscale. Plasmonic properties will be treated in a separated section (section I.2), since they represent the main subject of this thesis work.

I.1.1 Structural Properties

A first fundamental consequence of the size-dependent nature of nanotechnology, which alone explains many of the new phenomena that we study, is the relevance of surfaces. In fact, a reduction of the volume of an object implies inevitably an increment in the surface to volume ratio. When reaching the nanoscale, the fraction of atoms that belong to the surface, and their properties, cannot be neglected as happens at the bulk scale:[9] for a 10 nm

nanoobject, about 30% of the atoms are located at the surface, and this percentage reaches 60% if the size is reduced down to 2 nm (**Figure I.1A**).[10] In particular, being in a completely altered steric and coordinative environment compared to the inner (or bulk) atoms, surface atoms are characterized by a different chemistry and generally a higher reactivity.

A direct phenomenological effect is the *melting point depression*:[11–13] for a wide range of materials (from metals to semiconductors to insulators), an inverse proportionality has been found between the melting point and the dimensions of the object.[14] This effect can be described through Gibbs-Thomson equation, describing the liquid-solid interface dependence of the melting point (T_{melt}); for a sphere of radius R:

$$\frac{T_{melt}(R)}{T_{melt}(bulk)} = 1 - \frac{2\sigma_{sl}}{H_f \rho_S R} \quad \textbf{[I.1]}$$

where σ_{sl} is the solid-liquid interface energy, H_f is the bulk heat of fusion and ρ_s is the solid state density. This inverse proportionality has been evidenced in several experiments;[15–22] for example, in the specific case of gold, the melting temperature of a 2 nm nanoparticle is around 700 °C, with a *melting point depression* around 45% (**Figure I.1B**).

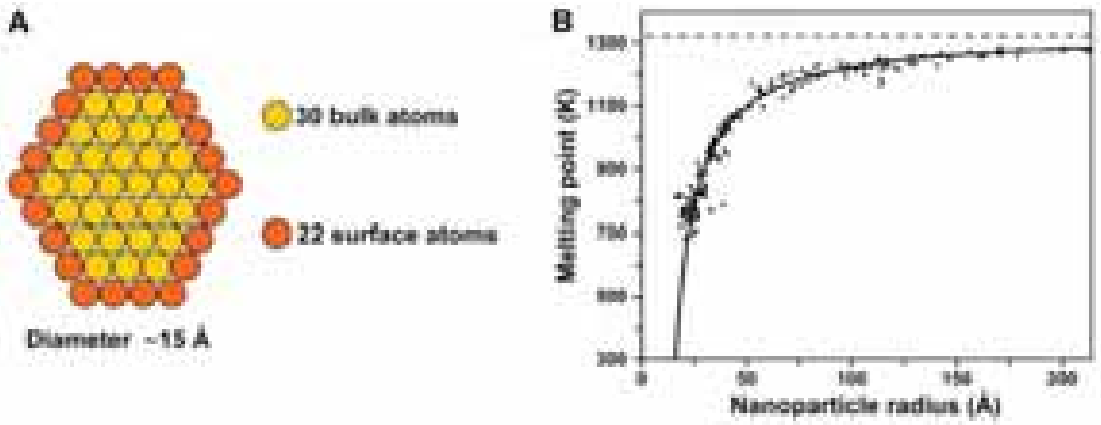

Figure I.1: A: Schematic 2D cross-section of a spherical nanoparticle made of 52 atoms. **B:** Experimental melting point for gold as a function of particle size. The solid black line is a least-squares fit; the dotted line indicates the bulk melting point of gold (1337 K). Adapted from **B:** Ref.16.

The lower cohesion energy of the surface atoms plays a fundamental role in nanosynthesis. The possibility of controlling the crystallographic facets of the product relies on the addition of specific surface active agents during crystal growth. On the other hand, the ability to select between a thermodynamic or kinetic product depends on the ratio between the kinetic constants of reduction and migration of the atoms along the surface of the growing particles.[23,24] Also, important effects like Ostwald ripening (small crystals particles dissolve and redeposit onto larger crystals)[25–27] or the predisposition of nanoobjects to agglomerate are all direct consequences of the tendency of the system towards a reduction of surface energy. All these aspects will be treated in detail in the introduction to chapter II.

Another related effect that is worth mentioning is the size-dependent nature of the lattice parameters.[28–30] The incomplete coordinative environment of the surface atoms generates an inward resulting force that creates a surface energy similar to the surface tension of liquids, leading to a decrease of interatomic spacing. Keeping the example of a 2 nm gold nanoparticle, the interatomic separation is reduced from 2.88 to 2.45 Å. This must be kept in mind when trying to identify the crystallographic habit of small nanoparticles.

All this considerations are extremely important for the application of nanoparticles in catalysis.

I.1.2. Electronic Properties

In a crystal, electrons are delocalized on all *n* atoms; following the molecular orbital theory, they lead to the formation of *n* bonding and *n* anti-bonding orbitals. At the bulk scale the number of atoms is enough to create a continuum of electronic states, generating the conductive and valence electronic bands; when entering into the nanoscale, *n* decreases and the discrete nature of electronic levels reappears (**Figure I.2A**).[31]

Between the two bands there is a forbidden zone called band gap, that can be related to *n* with the following equation:[32]

$$\delta = \frac{4E_F}{3n} \quad \textbf{[I.2]}$$

Where δ is the band gap and E_F is the Fermi energy.

Reducing the dimensions of the object, the energy gap increases (also called HOMO-LUMO gap if the electronic bands turn into discrete levels, Highest Occupied Molecular Orbital and Lowest Unoccupied Molecular Orbital respectively). This has important consequences on the ionization energy, which can increase by few eV, significantly affecting the standard reduction potentials; for example, in the case of gold the ΔE_{rid}^{0} ($Au^{3+}|Au$) is 1.5 V for the bulk metal, and shifts to -1.5 V for a nanometric sample.[33] Moreover, since the value of the band gap in comparison to the thermal energy K_BT is responsible to the electronic nature of a material (conductor, semiconductor or insulator) a reduction in size can lead to a metal-to-insulator transition.

Moreover, when an electron is excited, due to Coulomb interaction with the corresponding hole it is possible to define an associated exciton diameter (D_{ex}); at the nanoscale, the size of the nanoparticle becomes comparable or even smaller than D_{ex}, leading to quantum confinement effects.[34–38] For semiconductor materials, typical size values where this effect starts to occur are in the range of few to few hundred nanometers.[39,40] When this happens the energy gap between electrons and holes increases proportionally to the degree of confinement, leading to a blueshift of both optical absorption and luminescent emission.[34,41] Nanoparticles showing this kind of effect are generally referred to as quantum dots.[42,43] They present a strong band gap luminescence that is finely tunable by changing the size of the particles (**Figure I.2B - C**) and are of particular interest for a wide range of optical applications, like fluorescent labels, optical amplifiers or thin film electroluminescent devices.[44]

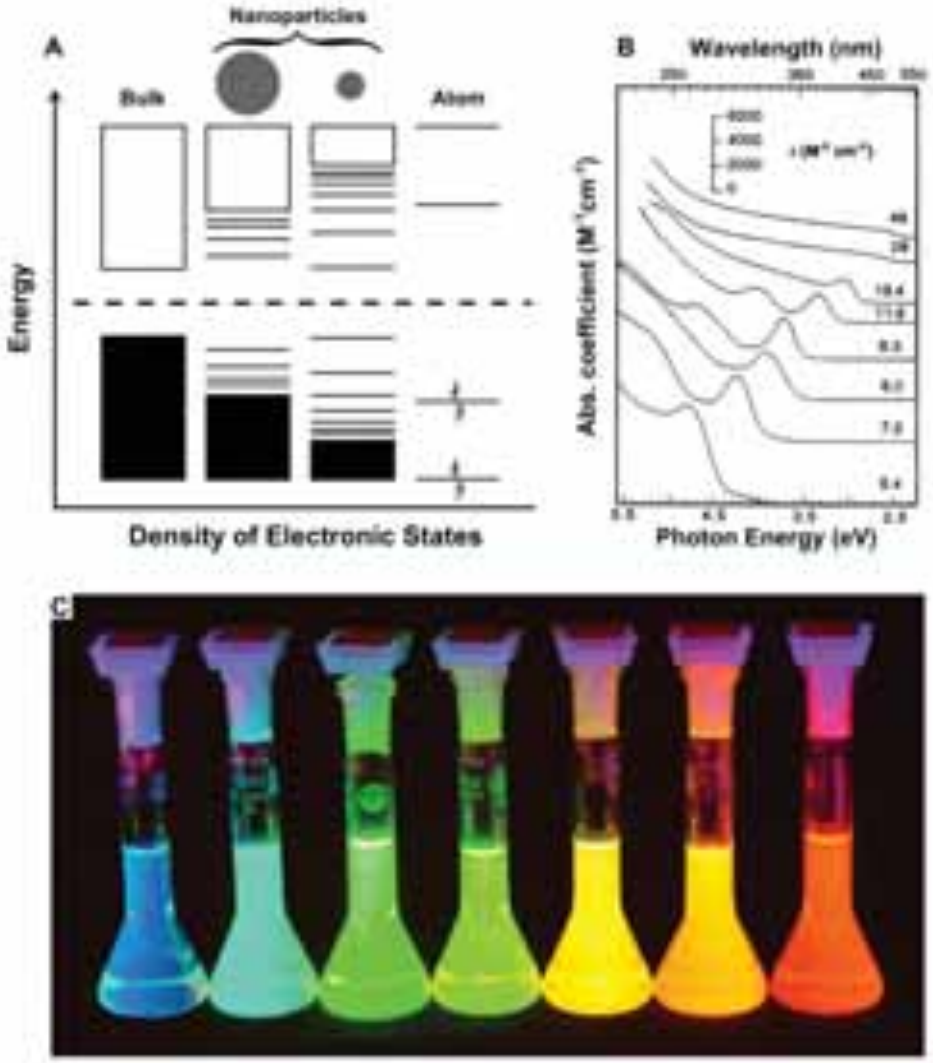

Figure I.2. A: Scheme of the density of states in semiconductor clusters as a function of their size. The dotted line represents the Fermi Energy. **B:** Quantum confinement effects on the absorption spectra of CdS nanocrystal quantum dots. The numbers reported for each line are the radii of the clusters in nanometers. **C:** Optical image of colloidal solution of quantum dots with increasing size (from left to right). Adapted from **B:** Ref.45

I.1.3. Magnetic Properties

Bulk crystalline magnetic materials are internally divided into magnetic domains, each characterized by a parallel alignment of the magnetic moments of the constituent atoms. Nanoparticles below a certain dimension however, present only one single domain. This transition to single domain implies a zero net magnetization in the absence of external fields,

since the nanoparticles are free to re-orient in the medium.[46] Therefore the ferromagnetic behavior is lost, and magnetic colloids behave like paramagnetic materials; nonetheless, since their magnetic susceptibility is orders of magnitude higher (typically 10^3 - 10^4 μ_B), this phenomenon is called superparamagnetism. Similarly to what happens for semiconductor nanoparticles, the critical diameter for this transition depends on the specific material, being approximately 150 nm for Fe_3O_4, 70 nm for Co and 14 nm for Fe.[46]

Magnetic colloids have potential applications as recording media, magnetic sensors and biocompatible tools for diagnosis and therapy.[47–50] In particular their ability to self-assemble or self-organize in the presence of external magnetic fields makes them optimal candidates for new generation hybrid materials.[51]

I.2. PLASMONIC PROPERTIES

The emergence of plasmons at the nanoscale is probably one of the most dramatic effects studied in nanotechnology. The number of scientific publications has risen dramatically during the last twenty years. Nowadays, Plasmonics has become one of the most active branches of nanotechnology, with the promise of bringing significant contributions in many different fields, like energy, medicine, biosensing, electronics and so on.[52–63] Plasmonic properties have however been used long before their scientific comprehension. The first uses are related to the origins of red-colored glass, originally obtained using copper (already in Egypt and Mesopotamia). With the discovery of *aqua regia*, copper was replaced by gold; the oldest glass artifact that has been recovered is the famous Lycurgus cup, dated around the IV century (**Figure I.3A**). Elemental analysis of the glass in the cup revealed the presence of minute amounts of gold and silver in a approximate ratio of 70:30.[64–68] Even though many elusive references can be found in older scripts, we have to wait till the seventeenth century to find a proper description for the preparation of a gold pigment, the so-called Purple of Cassius (**FigureI.3B**).[69] The chemistry behind this method was elucidated only in the nineteenth century,[70] thanks to the work of Richard Adolf Zsigmondy;[70,71] it involves two stages: formation of a gold sol and its stabilization. The former consists of a redox reaction between auric chloride and stannous chloride, while the stabilization was achieved through

co-precipitation of the formed nanoparticles with tin hydroxide (product of the hydrolysis of stannic chloride):[71]

$$Sn^{2+} + 2Au^{+} \longrightarrow Sn^{4+} + 2Au^{0} \quad \textbf{[I.3]}$$

$$SnCl_4 + 4H_2O \longrightarrow Sn(OH)_4 + 4HC \quad \textbf{[I.4]}$$

Paracelsus was the first to describe the preparation of gold nanoparticle colloids, in the fifteenth century; he gave them the name of *drinkable gold*, exalting their beneficial effect for the treatment of venereal diseases. The first scientific approach however came much later with the work of Michael Faraday, who in 1857 published an extensive paper on the optical properties of thin films and colloidal suspensions of gold particles (**Figure I.3C**).[72] Interestingly, this work was actually an attempt of Faraday to explain the properties of the Purple of Cassius. He came to the conclusion that the different coloration was directly linked to the dimensions of the gold particles and the thickness of the thin films.[73] Moreover, he made the first observation on the intrinsic thermodynamic instability of the gold colloids: the color changes with time (a clear sign of a change in the particle dimension) and the process resulted to be irreversible. Finally, he discovered the first synthetic and stabilization process of gold nanoparticles in water.[74]

Figure I.3. A: The Lycurgus cup, late Roman (IV century CE), preserved at the British Museum in London. **B:** Particular of one stained glass at Canterbury Cathedral. **C:** Faraday's gold colloidal solutions preserved at the Royal Society in London.

I.2.1. Plasmons in Metallic Nanoobjects

Metals are characterized by a high number of quasi-free electrons that are not bound to a single atom, but are instead free to move throughout the entire structure of the crystal. These electrons can be excited by an incoming electromagnetic wave: the electron cloud oscillates in response to the oscillating electric field of the incident wave. These two oscillations meet resonant conditions at a specific wavelength, generating a plasmon wave. Surface plasmons can thus be defined as collective coherent oscillations of the conduction band electrons of a metal at the metal-dieletric interface. The interaction between electrons and electric field is described by the dielectric function of the material $\varepsilon(\omega)$. There are multiple possible physical descriptions for the dielectric functions, depending on the characteristics of the system under investigation; in the case of metals, a very simple and useful description is given by the Drude-Lorentz-Sommerfeld model (generally called simply Drude model).[64,75,76] This model was proposed at the beginning of the twentieth century, and is based on the application of the kinetic theory to the conduction band electrons of a metal: basically, the electrons are treated like a cloud of charged particles, and the positively charged particles, i.e. the metal atoms, are considered to be fixed. The Drude dielectric function can be written as:

$$\varepsilon(\omega) = 1 - \frac{\omega_p^2}{\omega^2 - i\ \omega} \quad \textbf{[I.5]}$$

where ω_p is the plasma frequency and Γ is a damping constant. Observing equation **[I.5]** we can deduce that surface plasmons occur always at energies that are lower than the bulk plasmon energy, i.e. only for few metals surface plasmons arise in the visible range, which include silver (ω_p= 3.8 eV) and gold (ω_p= 2.6 eV).[75] This equation is generally rearranged as:

$$\varepsilon(\omega) = \varepsilon_1(\omega) + i\varepsilon_2(\omega) \quad \textbf{[I.6]}$$

Where $\varepsilon_1(\omega)$ and $\varepsilon_2(\omega)$ are the real and imaginary parts of the dielectric function, respectively. At the nanoscale the wavelength of the incident electromagnetic fields is much larger than the nanoparticle dimensions. Therefore, the electron cloud of the particle is entirely affected by the electric fields. This implies the generation of a net charge separation

that in turn creates a restoring force due to Coulomb attraction; this implies an accumulation of charges alternately on opposite side of the particles, which induces an electric field with a $\pi/2$ phase lag compared to the excitation field (**Figure I.4**).[51] Due to these conditions the phenomenon takes the name of Localized Surface Plasmon Resonance (LSPR).[64,76]

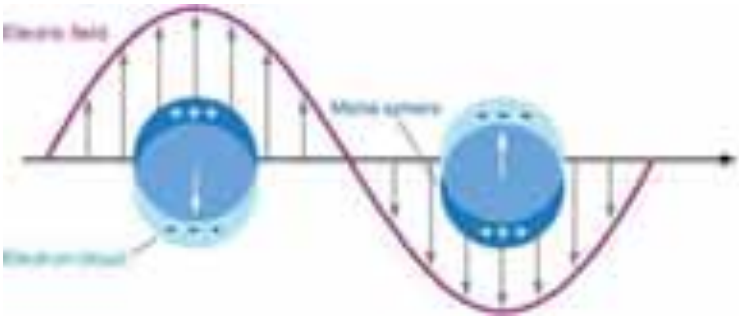

Figure 1.4: Schematic representation of the effect of an incoming electromagnetic wave on the electron cloud of spherical nanoparticles.

Another important consequence of the reduced size of the probed particle is that the spatial dependence of the electromagnetic field can be ignored; in other words we are in the *quasi-static approximation* regime.[75,77,78] This allows us to greatly simplify the physical description, and will have other important consequences pointed out below.

The internal electric field generated by the particle (E_0) and its polarizability (α) can be written as:

$$E_p = E_0 \frac{3\varepsilon_m}{\varepsilon+2\varepsilon_m} \quad \textbf{[I.7]}$$

and

$$\alpha = 4\pi\varepsilon_0 R^3 \frac{\varepsilon-\varepsilon_m}{\varepsilon+2\varepsilon_m} \quad \textbf{[I.8]}$$

Where E_0 is the external electric field, ε_m is the dielectric constant of an embedding medium, and R is the radius of the particle.

Searching for the maximum of one of the two equations corresponds to identifying the resonance conditions for the generation of an LSPR. The maximum is found when:

$$| \varepsilon + 2\varepsilon_m | = Minimum \quad \textbf{[I.9]}$$

And substituting equation **[I.6]** we find:

$$[\varepsilon_1(\omega) + 2\varepsilon_m]^2 + \varepsilon_2(\omega)^2 = Minimum \textbf{ [I.10]}$$

This means that a negative ε_1 and a small ε_2 are necessary; both these conditions are typical of the dielectric functions of metals.

In 1908 Gustav Mie proposed a simplified approach based on the resolution of Maxwell's equations for the case of a nanometric sphere immersed in an electromagnetic field.[79] Using this formalism it is possible to write the extinction cross-section as:[51,76]

$$\sigma_{ext}(\omega) = \frac{24\pi^2 R^3 \cdot \varepsilon_m^{3/2}}{\lambda} \frac{\varepsilon_2(\omega)}{[\varepsilon_1(\omega)+2\varepsilon_m]^2+\varepsilon_2(\omega)^2} \textbf{ [I.11]}$$

Importantly, the conditions to maximize the cross-section are identical to that indicated above (equation **[I.10]**). A similar expression can be written for the scattering cross-section; moreover, both scattering and extinction cross-sections depend on particle size, and their ratio varies as $1/R^3$. Therefore, the contribution of scattering increases for bigger particles, as illustrated in **Figure I.5** using boundary element method (BEM) calculations.[80]

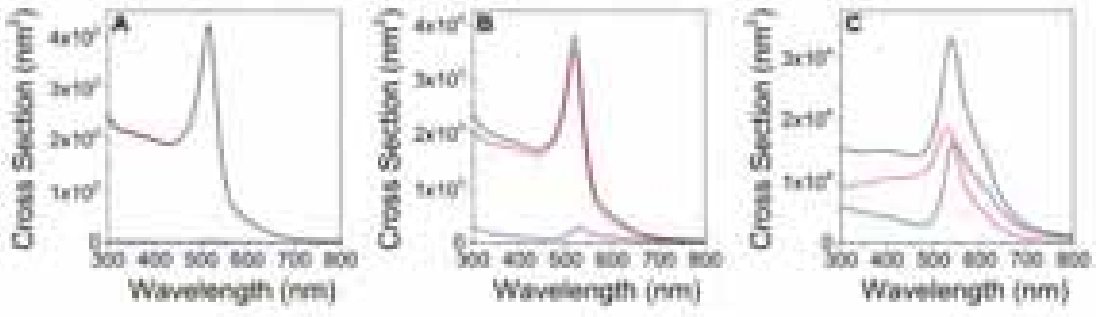

Figure I.5. Extinction (black line), absorption (red line) and scattering (blue line) cross-section for gold nanoparticle of different diameter: **A:** 20 nm, **B:** 40 nm and **C:** 80 nm.

Another important consequence of the quasi-static approximation is that, since the exciting electric field is static over the entire nanoparticle, it can only couple to a dipolar charge distribution. This condition is fulfilled only for small particles; for bigger clusters, the damping constant in equation **[I.5]** becomes bigger, and retardation effects make it impossible to neglect the spatial variation of the exciting electromagnetic field, and other

multipoles, like quadrupolar modes, can be excited, even though with a lower efficiency (i.e. they are generally less intense).

It is worth mentioning here that the principal relaxation mechanism is electron-phonon scattering, which results in the generation of heat. This local increase of temperature has been proposed as a possible localized treatment for cancer, better known as photothermal therapy.

I.2.2. Tuning Plasmon Resonances

Equation **[1.10]** does not offer any handle to shift the plasmon resonance condition. In particular the size-dependent nature of the plasmon generation does not show, since the radius *R* influences only the intensity and not the position of the LSPR. This is true only within the quasi-static approximation; in fact, the experimentally observed redshift of the dipolar plasmon as a function of particle size is a well-known retardation effect.

Another possibility for tuning the plasmon wavelength is the presence of ε_m in the expression of the resonance conditions; this is translated in practice into a spectral shift of the plasmon bands when varying the dielectric constant of the medium, which can be directly linked to its refractive index:

$$R.I. = \sqrt{\varepsilon_m \mu_m} \quad \textbf{[I.12]}$$

Where R.I. is the refractive index and μ_m is the magnetic permeability of the medium. This concept is the basis of plasmonic sensing.

Changing particle shape is another possibility to tune the position (and the number) of LSPRs. This can be mathematically demonstrated using an ellipsoid as a model system.

The object is characterized by three axes $a = b \neq c$, and an eccentricity and distortion parameter equal to $e = \frac{\sqrt{a^2-b^2}}{a}$ and $\delta = \frac{a-b}{a+b}$ respectively.

Still in the quasi-static approximation, we can write the polarizability along one of the *i* axes, with *i=a,b,c*, as:

$$\alpha_i = \varepsilon_0 \frac{\varepsilon(\omega)-\varepsilon_m}{\varepsilon_m+[\varepsilon(\omega)-\varepsilon_m]L_i} \cdot V_{cluster} \quad \textbf{[I.13]}$$

where $V_{cluster}$ is the volume of the ellipsoid, equal to $4\pi/3 \cdot abc$, and L_i is the depolarization factor, a purely geometric factor. In analogy to the case of the sphere, we can find the resonant conditions by maximizing the polarizability. For an ellipsoid, $L_a = L_b \neq L_c$, i.e. two of three possible directions are degenerate cases, leaving two different resonance conditions.[64,76] These results have been experimentally verified for nanorods, which display two plasmon bands, a transversal one (the degenerate case) and a longitudinal one. Interestingly the two bands result to be orthogonal, i.e. it is possible to selectively excite one of them by changing the orientation of the ellipsoid compared to the polarization of the incident field.

A final property that can be exploited to tune the optical response of plasmonic nanostructures is the possibility of coupling plasmons in different particles: when the distance between two plasmonic nanoobjects is of the order of few nanometers, their electron clouds start to interact with each other.[81,82] The rigorous mathematical treatment of this kind of nanostructures is rather complicated, but an electromagnetic analog of molecular orbital theory has been proposed by Nordlander and co-workers which greatly simplified the calculation and interpretation of the results:[83,84] the resulting plasmon resonances can be views as hybridized elementary plasmons in the same way as molecular orbitals are formed from atomic orbitals. Interestingly, the analogy allows interpreting the hybridized plasmons in terms of bonding and antibonding combinations (**Figure I.6A - B**).[85–87] Moreover, also the spatial distribution of these plasmonic modes resembles that of molecular orbitals, with the bonding ones localized at the gaps between the interacting particles (as the bonding orbitals are localized between the interacting atoms, **Figure I.6C**);[86] this creates areas characterized by an extremely high electric field (see section 1.2.3).[88,89]

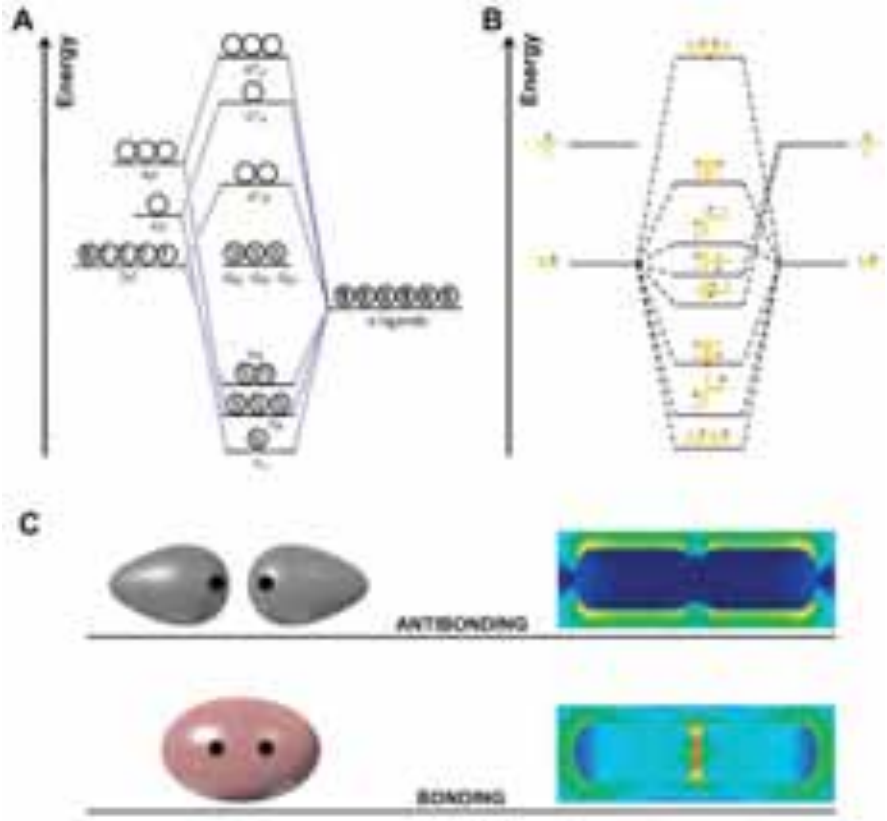

Figure I.6. A: Ligand-Field theory scheme summarizing the hybridization of σ-bonds in an octahedral ML6. **B:** Plasmon hybridization schemes for nanorod dimers in different geometric arrangements. **C:** Bonding and antiboding hybridized orbitals (**left**) and plasmons (**right**). Adapted from **B:** Ref.55, **C:** Ref.86.

I.2.3. Surface Enhanced Raman Scattering

Surface Enhanced Raman Scattering (SERS) is based on measuring the Raman scattering signal of molecules. An important characteristic of Raman spectroscopy is that, being based on a scattering phenomenon, signal intensities are extremely low, i.e. the Raman scattering cross-sections of molecules are typically in the order of 10^{-29} - 10^{-30} cm^2, several orders of magnitude lower than absorption or extinction cross-sections (typically in the range of 10^{-16} cm^2).[90] The mechanism of Raman scattering can be easily visualized using Jablonski diagrams, as depicted in **Figure I.7**. Raman signals derive from an inelastic scattering phenomenon; therefore the scattered photons can have lower or higher energies compared to

the incident ones, giving rise to Stokes (**Figure I.7A**) and anti-Stokes (**Figure I.7B**) Raman signals, respectively.[91]

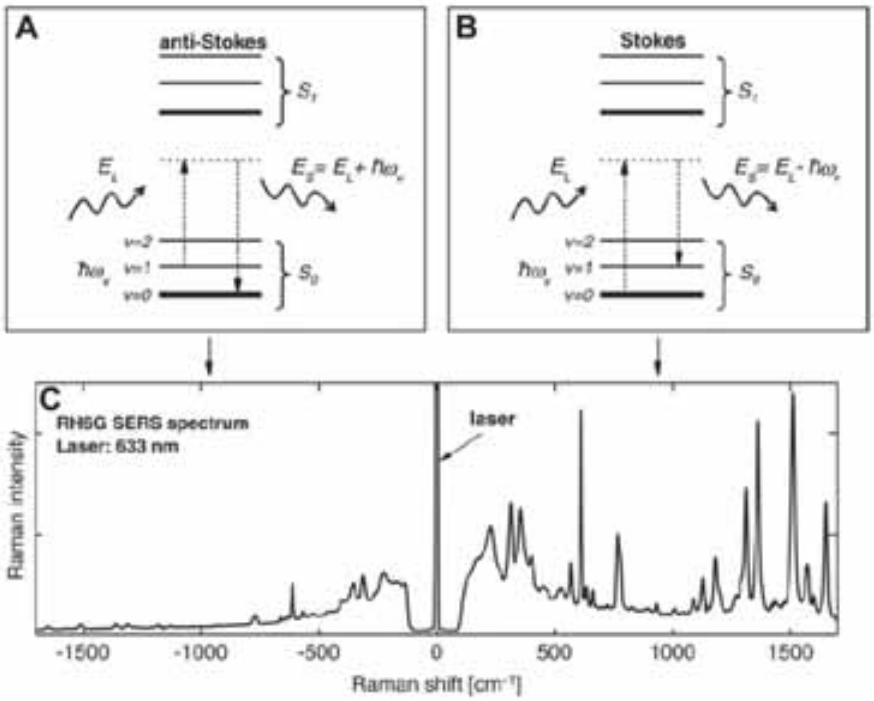

Figure I.7. Simplified Jablonski diagrams of anti-Stokes (**A**) and Stokes **(B**) Raman processes. The Stokes process starts with the molecule in v= 0 vibrational ground state of S_0 and ends in v =1, thus producing a scattered photon with a lower energy than the incoming one; on the other hand anti-Stokes scattering starts with the molecule already in the v = 1 vibrational excited state of S_0 and ends in v = 0, thus producing a scattered photon with an energy larger than the incoming one. **C:** A typical Raman (in fact SERS here) spectrum for rhodamine 6G with several Raman scattering peaks on the Stokes side and their (weaker) anti-Stokes counterparts. Adapted from Ref.91

Jablonski diagrams also explain how Raman photons are related to the vibrational energy levels, rendering Raman a vibrational spectroscopy. It is however important to make a distinction with standard infrared (IR) spectroscopy: in fact, IR spectroscopy is based on absorption and not on scattering, i.e. the selection rules of the two techniques are different, meaning that an IR-allowed vibration is not necessarily Raman-allowed.[92]

The low intensity of the signals explains why Raman spectroscopy remained in the shadow for roughly fifty years after its discovery in 1921 by the Nobel laureate Chandrasekhara Venkata Raman,[93] and why its scientific success is closely linked to the discovery of SERS, in 1974.[94,95] The signal enhancement is mainly provided by plasmon resonances in the metal

substrate. As explained above the interaction with an electromagnetic field induces a resonant electric field inside the nanoparticle (section I.2.1). Looking at equation **[I.7]** we can clearly understand how, by imposing the resonance conditions (i.e. searching for the minimum of the denominator, equation **[I.10]**) the induced electric field will be much larger than the exciting one.[96] Practically translated, a molecule that is located in the proximity of a metal particle whose plasmon is being excited experiences a much higher electric field, which is translated into a higher Raman scattering signal. In particular, SERS intensity can be written as

$$I_{SERS} = \alpha_{mol}^2 \cdot \left|E_p(\omega_{inc})\right|^2 \cdot \left|E_p(\omega_{inc} - \omega_{vib})\right|^2 \textbf{ [I.14]}$$

where α_{mol} is the molecule polarizability, $E_p(\omega_{inc})$ is the induced plasmonic electric field at the wavelength of the incident light, and $E_p(\omega_{inc} - \omega_{vib})$ is the outgoing electric field generated after the interaction with the probed molecule. Equation **[I.14]** is generally approximated as:

$$I_{SERS} = \alpha_{mol}^2 \cdot \left|E_p(\omega_{inc})\right|^4 \textbf{ [I.15]}$$

Since the wavelength of the incoming and Raman photons are close to each other (this approximation starts to fail when the exciting light is chosen in the red/IR part of the spectrum). This means that a plasmon electric field enhancement of 100-fold will translate into a Raman intensity enhancement of 10^8! This is generally quantified trough the SERS Enhancement Factor (EF), which represents the main figure of merit for SERS devices, and can be expressed as:

$$EF = \frac{I_{SERS}/N_{SERS}}{I_{Raman}/N_{Raman}} \textbf{ [I.16]}$$

Where I_{SERS} and I_{Raman} are the intensity of the SERS and Raman signals, respectively, and N_{SERS} and N_{Raman} are the numbers of molecules contributing to the SERS and Raman signal, respectively. Is important to keep in mind, that in order to appropriately measure an EF the conditions for SERS and Raman measurement should be the same, but, due to the very nature of SERS, this is generally not possible. Moreover it is very complicated to experimentally measure the number of probed molecules with high precision.

The possibility of boosting the signals comes however along with a significant restriction: since the electric field strength scales with the distance as d^{-3}, the SERS intensity will scale accordingly as d^{-12}.; this underlies how SERS, as stated in its acronym, is a surface spectroscopic technique.

What we have described so far is the so-called electromagnetic enhancement. This effect can be further boosted through plasmon coupling; as explained in the last part of section 1.2.2, when two particles are sufficiently close to each other, their plasmon modes can be hybridized creating new plasmon modes. Interestingly the plasmon spatial distribution of these hybridized plamsons shows a concentration of the electric field enhancement in the gap between the interacting particles (**Figure I.6C**). These highly enhancing environments are called hot spots, and are able to provide enough intensity enhancement for the detection of single molecules, as has been demonstrated in several publications.[88,97–100] These high enhancements however will also be highly localized: only the few molecules positioned at the right places will take advantage of the hot-spot environment.[101] To give an example, it has been demonstrated that 63 out of 1 million molecules located in the hot-spots contribute to 24% of the overall SERS signal, while 61% of the 1 million molecules that are located in low electric field positions contribute just 4%.[102] Another example can be found in **Figure I.8** where a single molecule SERS spectrum is compared to the Raman spectrum of roughly a million molecules; the comparison is even more striking if we take into account the integration time for the two acquisitions: 0.05 and 400 s for SERS and Raman, respectively![103] Overall, metal plasmonic substrates can provide SERS EFs in the range of 10^3 - 10^8 and up to 10^{10} – 10^{11} for hot spots.[91]

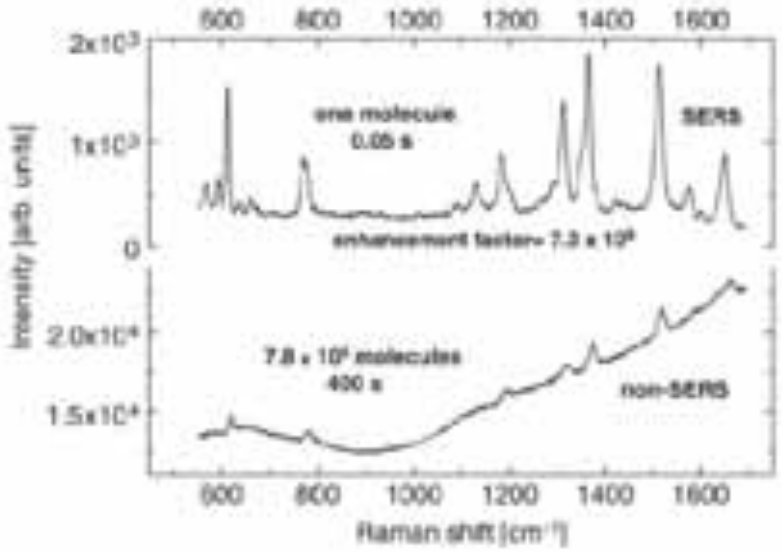

Figure I.8. Raman (**bottom**) and SERS (**top**) spectra at 633nm laser excitation (3mW) for rhodamine 6G. The (vertical) intensity axis is in arbitrary units but the same for both spectra. **Bottom spectrum:** signal of ca. 1 million molecules with 400 s integration time. **Top spectrum:** signal from a single rhodamine molecule under the same experimental conditions but with 0.05 s integration time. In order to go from the spectrum at the bottom to the one at the top, an amplification of the Raman signal by an EF of ~ $7.3 \cdot 10^9$ is required. Adapted from Ref.91

Apart from the electromagnetic enhancement, there is another contribution that can be exploited to increase SERS signals: the so-called chemical enhancement, which is related to the electronic properties of the probed molecules and in particular with their polarizability (see equation **[I.15]**). This effect arises from two contributions: intrinsic properties of the molecule, and/or the interaction of the molecule with the substrate. In the first case the probed analyte shows by itself a higher Raman cross-section; these are the so-called Raman dyes, typically molecules characterized by extended conjugation of π electrons. The second contribution is present when the polarizability of the analyte changes due to charge transfer with the metal surface; this effect is the scattering equivalent of charge transfer bands typical of metal coordination complexes. When the chemical enhancement contributes significantly to the final SERS intensity (typically with an extra EF of 10^1 - 10^3), we speak about SERRS or SE(R)RS, meaning Surface Enhanced Resonant Raman Scattering.

Finally, it is important to remember that even though Raman and SERS are closely related, a SERS spectrum does not necessarily overlap to its Raman analogue. In fact, the presence of

the surface introduces new selection rules that can influence the relative intensity of the different vibrations;[104,105] moreover, the orientation of the probed molecules is another factor that can influence the spectral profile.[106,107]

I.3. REFERENCES

(1) Physics grand challenges - EPSRC website https://www.epsrc.ac.uk/research/ourportfolio/themes/physicalsciences/introduction/grandchallenges/
(2) Feynman, R. P. *Eng. Sci.* **1960**, *23* (5), 22–36.
(3) Minsky, M. L. *IJ Good Ed Heimann Lond.* **1962**, 139.
(4) Drexler, K. E. *Proc. Natl. Acad. Sci.* **1981**, *78* (9), 5275–5278.
(5) Washington, D.C.: National Science and Technology Council, Committee on Technology, Subcommittee on Nanoscale Science, Engineering and Technology 2000.
(6) Corbett, J.; McKeown, P. A.; Peggs, G. N.; Whatmore, R. *CIRP Ann.-Manuf. Technol.* **2000**, *49* (2), 523–545.
(7) Ramsden, J. *Nanotechnology: an introduction*; William Andrew, 2011.
(8) Anderson, P. *Science* **1972**, *177* (4047), 393–396.
(9) Schmid, G. *Chem. Rev.* **1992**, *92* (8), 1709–1727.
(10) Sander, D. *Curr. Opin. Solid State Mater. Sci.* **2003**, *7* (1), 51–57.
(11) Kofman, R.; Cheyssac, P.; Aouaj, A.; Lereah, Y.; Deutscher, G.; Bendavid, T.; Penisson, J.; Bourret, A. *Surf. Sci.* **1994**, *303* (1-2), 231–246.
(12) Couchman, P.; Jesser, W. *Nature* **1977**, *269* (5628), 481–483.
(13) Yacaman, M. J.; Ascencio, J. A.; Canizal, G. *Surf. Sci.* **2001**, *486* (1-2), L449–L453.
(14) Burda, C.; Chen, X. B.; Narayanan, R.; El-Sayed, M. A. *Chem. Rev.* **2005**, *105* (4), 1025–1102.
(15) Sambles, J. *Proc. R. Soc. Lond. Ser. -Math. Phys. Sci.* **1971**, *324* (1558), 339 – &.
(16) Buffat, P.; Borel, J. *Phys. Rev. A* **1976**, *13* (6), 2287–2298.
(17) Castro, T.; Reifenberger, R.; Choi, E.; Andres, R. *Phys. Rev. B* **1990**, *42* (13), 8548–8556.
(18) Dick, K.; Dhanasekaran, T.; Zhang, Z. Y.; Meisel, D. *J. Am. Chem. Soc.* **2002**, *124* (10), 2312–2317.
(19) Lewis, L. J.; Jensen, P.; Barrat, J. L. *Phys. Rev. B* **1997**, *56* (4), 2248–2257.
(20) Liu, H. B.; Ascencio, J. A.; Perez-Alvarez, M.; Yacaman, M. J. *Surf. Sci.* **2001**, *491* (1-2), 88–98.
(21) Nayebi, P.; Zaminpayma, E. *J. Clust. Sci.* **2009**, *20* (4), 661–670.
(22) Shim, J. H.; Lee, B. J.; Cho, Y. W. *Surf. Sci.* **2002**, *512* (3), 262–268.
(23) Lohse, S. E.; Burrows, N. D.; Scarabelli, L.; Liz-Marzán, L. M.; Murphy, C. J. *Chem. Mater.* **2013**, 34–43.
(24) Xia, Y.; Xia, X.; Peng, H.-C. *J. Am. Chem. Soc.* **2015**, 7947–7966.
(25) Ostwald, W. *Lehrbuch der allgemeinen chemie*, **1885**.
(26) Ostwald, W.; Bodenstein, M.; Clusius, K.; Bonhoeffer, K. F.; Falkenhagen, H. *Zeitschrift für physikalische Chemie*; Akademische Verlagsgesellschaft Geest & Portig, 1897.
(27) ast s, N. G.; Comenge, J.; Puntes, V. *Langmuir* **2011**, *27* (17), 11098–11105.
(28) Berry, C. *Phys. Rev.* **1952**, *88* (3), 596–599.
(29) Wasserman, H. J.; Vermaak, J. S. *Surf. Sci.* **1970**, *22* (1), 164 – &.
(30) Goldstein, A.; Echer, C.; Alivisatos, A. *Science* **1992**, *256* (5062), 1425–1427.
(31) Volokitin, Y.; Sinzig, J.; deJongh, L. J.; Schmid, G.; Vargaftik, M. N.; Moiseev, I. I. *Nature* **1996**, *384* (6610), 621–623.
(32) Rao, C. N. R.; Kulkarni, G. U.; Thomas, P. J.; Edwards, P. P. *Chem. Soc. Rev.* **2000**, *29* (1), 27–35.
(33) Pradeep, T.; Anshup. *Thin Solid Films* **2009**, *517* (24), 6441–6478.
(34) Efros, A. L.; Efros, A. L. *SPIE Milest. Ser.* **2005**, *180*, 71–74.
(35) Brus, L. E. *J. Chem. Phys.* **1984**, *80* (9), 4403–4409.
(36) Banyai, L.; Koch, S. W. *Phys. Rev. Lett.* **1986**, *57* (21), 2722.
(37) Berry, C. R. *Phys. Rev.* **1967**, *153* (3), 989.
(38) Berry, C. R. *Phys. Rev.* **1967**, *161* (3), 848.
(39) Yoffe, A. D. *Adv. Phys.* **1993**, *42* (2), 173–262.
(40) Sze, S. M.; Ng, K. K. *Physics of semiconductor devices*; John Wiley & Sons, 2006.
(41) Mattoussi, H.; Radzilowski, L. H.; Dabbousi, B. O.; Thomas, E. L.; Bawendi, M. G.; Rubner, M. F. *J. Appl. Phys.* **1998**, *83* (12), 7965–7974.

(42) Mekis, I.; Talapin, D. V.; Kornowski, A.; Haase, M.; Weller, H. *J. Phys. Chem. B* **2003**, *107* (30), 7454–7462.
(43) Alivisatos, A. P. *Science* **1996**, *271* (5251), 933–937.
(44) Schlamp, M. C.; Peng, X. G.; Alivisatos, A. P. *J. Appl. Phys.* **1997**, *82* (11), 5837–5842.
(45) Vossmeyer, T.; Katsikas, L.; Giersig, M.; Popovic, I.; Diesner, K.; Chemseddine, A.; Eychmuller, A.; Weller, H. *J. Phys. Chem.* **1994**, *98* (31), 7665–7673.
(46) LesliePelecky, D. L.; Rieke, R. D. *Chem. Mater.* **1996**, *8* (8), 1770–1783.
(47) Hergt, R.; Dutz, S.; Mueller, R.; Zeisberger, M. *J. Phys.-Condens. Matter* **2006**, *18* (38), S2919–S2934.
(48) Gloeckl, G.; Hergt, R.; Zeisberger, M.; Dutz, S.; Nagel, S.; Weitschies, W. *J. Phys.-Condens. Matter* **2006**, *18* (38), S2935–S2949.
(49) Gupta, A. K.; Gupta, M. *Biomaterials* **2005**, *26* (18), 3995–4021.
(50) Qin, J.; Laurent, S.; Jo, Y. S.; Roch, A.; Mikhaylova, M.; Bhujwalla, Z. M.; Muller, R. N.; Muhammed, M. *Adv. Mater.* **2007**, *19* (18), 2411–2411.
(51) Dhont, J. K. G.; Meier, G.; Richter, D.; Zorn, R.; Vliegenthart, G.; Gompper, G. *46th IFF Spring School 2015 - Functional Soft Matter - Lecture Notes*; FZJ-2015-01910; Theorie der Weichen Materie und Biophysik , Neutronenstreuung , Weiche Materie, 2015.
(52) de Aberasturi, D. J.; Serrano-Montes, A. B.; Liz-Marzán, L. M. *Adv. Opt. Mater.* **2015**, *3* (5), 602–617.
(53) Hamon, C.; Liz-Marzán, L. M. *Chem. - Eur. J.* **2015**, *21* (28), 9956–9963.
(54) Chen, H.; Shao, L.; Li, Q.; Wang, J. *Chem. Soc. Rev.* **2013**, *42* (7), 2679–2724.
(55) Pérez-Juste, J.; Pastoriza-Santos, I.; Liz-Marzán, L. M.; Mulvaney, P. *Coord. Chem. Rev.* **2005**, *249* (17–18), 1870–1901.
(56) Vigderman, L.; Khanal, B. P.; Zubarev, E. R. *Adv. Mater.* **2012**, *24* (36), 4811–4841.
(57) Langer, J.; Novikov, S. M.; Liz-Marzán, L. M. *Nanotechnology* **2015**, *26* (32), 322001.
(58) Huang, X.; Neretina, S.; El-Sayed, M. A. *Adv. Mater.* **2009**, *21* (48), 4880–4910.
(59) Guerrero-Martínez, A.; Barbosa, S.; Pastoriza-Santos, I.; Liz-Marzán, L. M. *Curr. Opin. Colloid Interface Sci.* **2011**, *16* (2), 118–127.
(60) Huang, X.; El-Sayed, I. H.; El-Sayed, M. A. *Methods Mol. Biol. Clifton NJ* **2010**, *624*, 343–357.
(61) Li, N.; Zhao, P.; Astruc, D. *Angew. Chem. Int. Ed.* **2014**, *53* (7), 1756–1789.
(62) Lohse, S. E.; Murphy, C. J. *J. Am. Chem. Soc.* **2012**, *134* (38), 15607–15620.
(63) Thorkelsson, K.; Bai, P.; Xu, T. *Nano Today* **2015**, *10* (1), 48–66.
(64) Louis, C.; Pluchery, O. *Gold nanoparticles for physics, chemistry and biology*; World Scientific, 2012.
(65) Brill, R. H. *Proc 7th Intern. Cong Glass Brux. Sect. B Pap. 223* 1965.
(66) Barber, D.; Freestone, I. *Archaeometry* **1990**, *32*, 33–45.
(67) Hornyak, G. L.; Patrissi, C. J.; Oberhauser, E. B.; Martin, C. R.; Valmalette, J. C.; Lemaire, L.; Dutta, J.; Hofmann, H. *Nanostructured Mater.* **1997**, *9* (1-8), 571–574.
(68) Freestone, I.; Meeks, N.; Sax, M.; Higgitt, C. *Gold Bull.* **2007**, *40* (4), 270–277.
(69) Hunt, L. B. *Gold Bull.* **1976**, *9* (4), 134–139.
(70) Carbert, J. *Gold Bull.* **1980**, *13* (4), 144–150.
(71) Weyl, W. A. *Soc. Glass Technol.* **1951**.
(72) Thompson, D. *Gold Bull.* **2007**, *40* (4), 267–269.
(73) Tweney, R. D. *Perspect. Sci.* **2006**, *14* (1), 97–121.
(74) Faraday, M. *Philos. Trans. R. Soc. Lond.* **1857**, *147* (0), 145–181.
(75) Kociak, M.; Stéphan, O. *Chem. Soc. Rev.* **2014**, *43* (11), 3865–3883.
(76) Kreibig, U.; Vollmer, M. **1995**.
(77) Novotny, L.; Hecht, B. *Principles of nano-optics*; Cambridge university press, 2012.
(78) Bohren, C. F.; Huffman, D. R. *Absorption and scattering of light by small particles*; John Wiley & Sons, 2008.
(79) Mie, G. *Ann. Phys.* **1908**, *330* (3), 377–445.
(80) García de Abajo, F. J. *Phys. Rev. Lett.* **1998**, *80* (23), 5180–5183.

(81) Landau, L. D.; Bell, J. S.; Kearsley, M. J.; Pitaevskii, L. P.; Lifshitz, E. M.; Sykes, J. B. *Electrodynamics of continuous media*; elsevier, 1984; Vol. 8.
(82) Lassiter, J. B.; Aizpurua, J.; Hernandez, L. I.; Brandl, D. W.; Romero, I.; Lal, S.; Hafner, J. H.; Nordlander, P.; Halas, N. J. *Nano Lett.* **2008**, *8* (4), 1212–1218.
(83) Prodan, E. *Science* **2003**, *302* (5644), 419–422.
(84) Prodan, E.; Nordlander, P. *J. Chem. Phys.* **2004**, *120* (11), 5444.
(85) Nordlander, P.; Oubre, C.; Prodan, E.; Li, K.; Stockman, M. I. *Nano Lett.* **2004**, *4* (5), 899–903.
(86) Shao, L.; Woo, K. C.; Chen, H.; Jin, Z.; Wang, J.; Lin, H.-Q. *ACS Nano* **2010**, *4* (6), 3053–3062.
(87) Funston, A. M.; Novo, C.; Davis, T. J.; Mulvaney, P. *Nano Lett.* **2009**, *9* (4), 1651–1658.
(88) Nie, S. M.; Emery, S. R. *Science* **1997**, *275* (5303), 1102–1106.
(89) Wang, Z. J.; Pan, S. L.; Krauss, T. D.; Du, H.; Rothberg, L. J. *Proc. Natl. Acad. Sci. U. S. A.* **2003**, *100* (15), 8638–8643.
(90) Schlücker, S. *Angew. Chem. Int. Ed.* **2014**, *53* (19), 4756–4795.
(91) Le Ru, E.; Etchegoin, P. *Principles of Surface-Enhanced Raman Spectroscopy: and related plasmonic effects*; Elsevier, 2008.
(92) Fateley, W. G.; Dollish, F. R.; McDevitt, N. T.; Bentley, F. F.; others. *Correl. Method* **1972**.
(93) Raman, C. V.; Krishnan, K. S. *Nature* **1928**, *121* (3048), 501–502.
(94) Jeanmaire, D.; Vanduyne, R. *J. Electroanal. Chem.* **1977**, *84* (1), 1–20.
(95) Fleischmann, M.; Hendra, P.; Mcquilla.aj. *Chem. Phys. Lett.* **1974**, *26* (2), 163–166.
(96) Pluchery, O.; Humbert, C.; Valamanesh, M.; Lacaze, E.; Busson, B. *Phys. Chem. Chem. Phys.* **2009**, *11* (35), 7729–7737.
(97) Le Ru, E. C.; Grand, J.; Sow, I.; Somerville, W. R. C.; Etchegoin, P. G.; Treguer-Delapierre, M.; Charron, G.; Félidj, N.; Lévi, G.; Aubard, J. *Nano Lett.* **2011**, *11* (11), 5013–5019.
(98) Michaels, A. M.; Nirmal, M.; Brus, L. E. *J. Am. Chem. Soc.* **1999**, *121* (43), 9932–9939.
(99) Xu, H. X.; Bjerneld, E. J.; Kall, M.; Borjesson, L. *Phys. Rev. Lett.* **1999**, *83* (21), 4357–4360.
(100) Kneipp, K.; Wang, Y.; Kneipp, H.; Perelman, L. T.; Itzkan, I.; Dasari, R.; Feld, M. S. *Phys. Rev. Lett.* **1997**, *78* (9), 1667–1670.
(101) Zuloaga, J.; Prodan, E.; Nordlander, P. *Nano Lett.* **2009**, *9* (2), 887–891.
(102) Fang, Y.; Seong, N.-H.; Dlott, D. D. *Science* **2008**, *321* (5887), 388–392.
(103) Le Ru, E. C.; Blackie, E.; Meyer, M.; Etchegoin, P. G. *J. Phys. Chem. C* **2007**, *111* (37), 13794–13803.
(104) Moskovits, M. *J. Chem. Phys.* **1982**, *77* (9), 4408–4416.
(105) Moskovits, M.; Suh, J. S. *J. Phys. Chem.* **1984**, *88* (23), 5526–5530.
(106) Creighton, J. A. *Surf. Sci.* **1983**, *124* (1), 209–219.
(107) Yu, Q.; Golden, G. *Langmuir* **2007**, *23* (17), 8659–8662.

CHAPTER

II

SYTHESIS OF ANISOTROPIC NOBLE METAL NANOPARTICLES

II.1. ANISOTROPIC NOBLE METAL NANOCRYSTALS: THE ROLE OF HALIDES

Terms such as nanorods, nanowires, nanoprisms, nanostars, etc. have become common within the scientific literature for a wide variety of materials, among which metals occupy a central place.[1–9] The reason behind this is the large influence that nanocrystal morphology has on several physical and chemical properties, including optical[2,4,8] and electronic response[5,7,10] or catalytic activity.[11] Anisotropy not only offers a versatile tool to tune the optical response of gold and silver nanoparticles, through variations in their LSPRs, but also important changes in the electronic conductivity through confinement effects, and on the catalytic activity through the availability of high index facets that can facilitate adsorption and surface reactions that are not possible on other surfaces.[1–5,7–12] However, despite the huge volume of literature related to synthesis, characterization and applications of colloidal anisotropic metal nanoparticles,[1–4,7–12] the mechanisms behind their formation are still under lively debate.[3,8,11–13] Even if the seeded growth method (described in detail in section II.1.2) is accepted as the most efficient one for the synthesis of uniform gold nanoparticles of many different morphologies, it is unclear why growth proceeds along specific preferential directions.[3,8] The growth of preformed isotropic seeds into anisotropic nanoparticles requires a symmetry-breaking event, which has not yet been undisputedly disclosed.[3] Since the seeded growth process takes place in a rather complex mixture of salts and surfactants, a variety of mechanisms have been proposed to explain symmetry breaking and anisotropic growth.[8] From a template effect from micellar arrangements of surfactant molecules[8,14] through the selective adsorption of surfactants on certain crystallographic facets,[3] even to the effects of exciting LSPR modes during growth,[15] researchers have invoked a variety of parameters as the main reason behind anisotropic growth. Materials scientists favor crystallographic strain as a mechanism to promote anisotropic growth, although how strain arises in colloidal nanoparticles at the atomic level may involve adsorbates, soft structures, etc. It is possible that all of these parameters are somehow involved in the process. is It also clear that the different shapes are characterized by different crystallographic facets, suggesting that these solvent-exposed faces have the lowest surface energy and thereby provide the energetically most favorable morphology.[3,12] However, surface energies are not

only affected by the atomic arrangement within the corresponding crystalline lattice (face centered cubic for these metals), but also by the adsorption of other chemical moieties.[12] In most metal nanoparticle synthesis methods performed in water or polar solvents, other ions (apart from surfactants and/or polymers) are present. Typically, these ions include halides (mainly chloride, bromide or iodide).[1–4,6–11] Halide ions have a strong tendency to adsorb on metallic surfaces and thus they are likely to affect the corresponding surface energies.[3,8,12,15] A number of reports have been recently published, regarding the specific use of halides to direct the formation of a certain nanocrystal shape.[12,16–23] For example, bromide is often claimed to be indispensable to obtain well-defined gold nanorods, while iodide has been reported to poison nanorod formation and induce the formation of nanoplates, as well as various platonic shapes.[12,16–20]

II.1.1. Types of Anisotropic Nanoparticle Shapes

Noble metal nanoparticles come in a wide variety of shapes, ranging from the Platonic to branched and irregular nanostructures. Many excellent articles have reviewed the wide variety of shapes (and their nuanced variations) that metal nanoparticles can have.[3,7,12,24–29] **Figure II.1** reviews the major classes of anisotropic nanoparticle shapes and their distinguishing features.

II.1.1.1. Rods and Wires

The first major class of anisotropic nanoparticle shapes comprises one-dimensional structures, namely rods and wires, where the main difference is the longitudinal length. Rods (and wires) can be a single rectangular or octagonal crystal, a singly twinned crystal, or a five-fold pentagonal twinned crystal.[13,18,30–33] The most common 1D structures are the single crystal octagonal rod/wire (**Figure II.1A**) and the five-fold twinned pentagonal rod/wire (**Figure II.1B**). Although they are both 1D structures, the direction and exposed crystal faces are different between these two rod/wire structures. Single crystal structures are elongated in the <001> direction,[18,34] whereas pentagonally twinned structures are elongated in the <110> direction.[18,33] The pentatwinned rods/wires have five lateral facets; however, they are not well defined as either {100}, {110}, or both.[18,33] The eight lateral facets of single crystal

rods/wires were originally thought to be dominated by {100} and {110};[35] however, recent work has demonstrated that the lateral facets are actually higher-index facts (i.e., {250}) that are beveled at their intersections by {110} facets.[34] On their ends, the five-fold twinned rods/wires are bound by {111} whereas the single crystal rods/wires are mainly bound by {100} with {110} and {111} facets to round out the ends.[18,30,31,33]

II.1.1.2. Platonic Shapes

The next class of anisotropic nanoparticles has aspect ratios near one and mainly differs in the number of crystal facets. They are variants of the five platonic shapes (i.e., polyhedrons with the same regular polygon for facets with the same number of polygons meeting at each corner): tetrahedron (4 triangle facets), hexahedron (i.e., cube) (6 square facets), octahedron (8 triangle facets), dodecahedron (12 pentagon facets), and icosahedron (20 triangle facets) (**Figure II.1C – G**).[3,12,13,24–27,36,37] Geometrically, these polyhedrons always have identical polygon facets of their respective number; however, nanoparticles are not nearly so perfect. Their facets are not always the same size or regular polygons and their corners can be truncated resulting in variations such as: {221}-faceted trisoctahedrons, {110}-faceted rhombic dodecahedrons, and even {730}-faceted tetrahexahedrons or {720}-faceted concave hexahedrons (**Figure II.1H – K**).[12,13,24] Generally speaking, tetrahedrons, octahedrons, and icosahedrons are dominated by {111}, whereas hexahedrons are bound by {100} and dodecahedrons by {110}.[25,38]

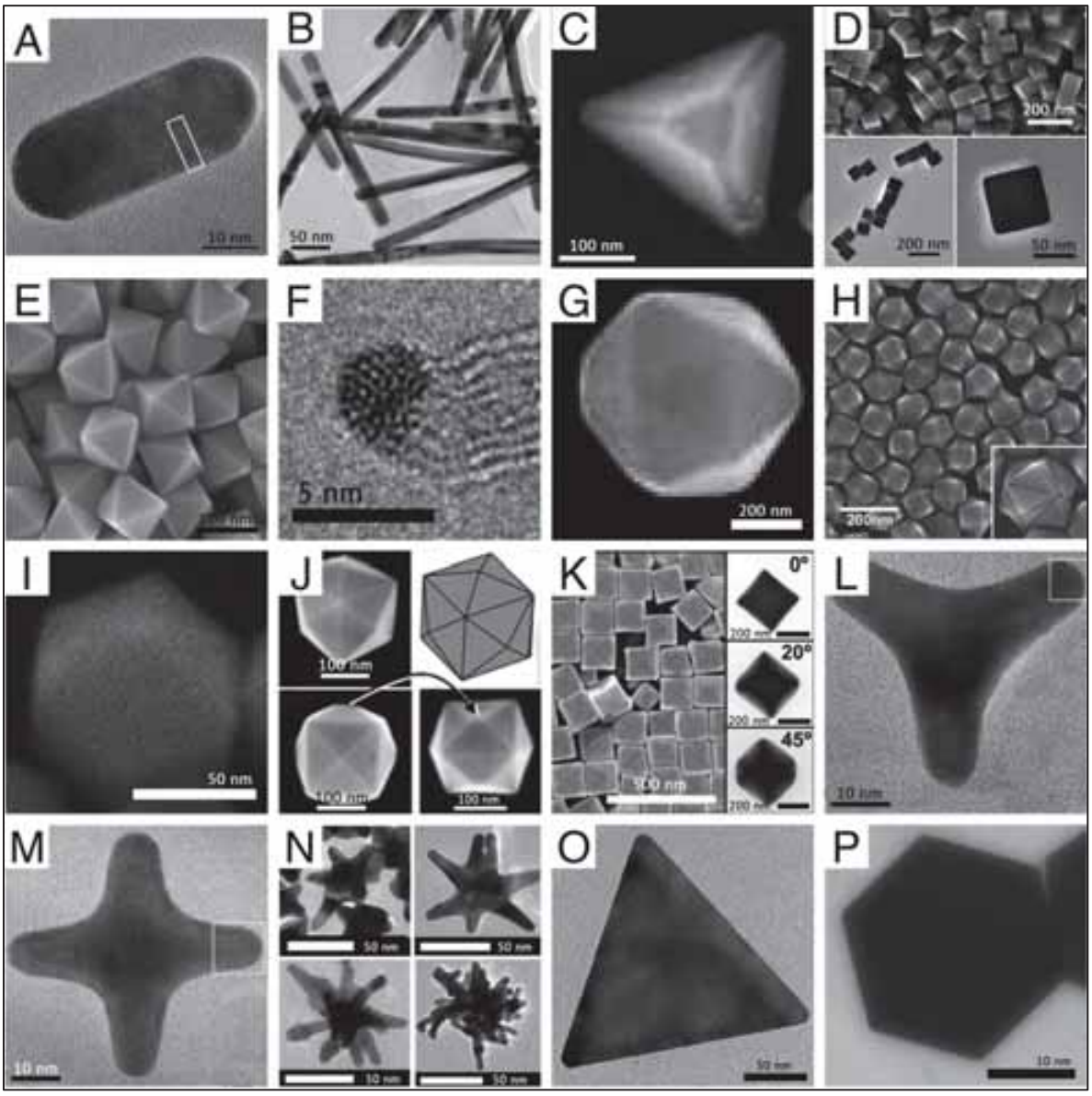

Figure II.1: The major classes of noble metal nanoparticle shapes seen through Transmission Electron Microscopy (TEM) and/or Scanning Electron Microscopy (SEM): A: gold octagonal single-crystal rod, **B:** gold pentagonally twinned rods, **C:** gold tetrahedron, **D:** palladium hexahedron (i.e., cube), **E:** gold octahedron, **F:** gold decahedron, **G:** gold icosahedron, **H:** gold trisoctahedrons, **I:** gold rhombic dodecahedron, **J:** platinum tetrahexahedron, **K:** gold concave hexahedron, **L:** gold tripod, **M:** gold tetrapod, **N:** gold star, **O:** gold triangular plate/prism, and **P:** gold hexagonal plate/prism nanoparticles. Adapted from **A:** Ref. **30**, **C & G:** Ref. **25**, **D:** Ref. **26**, **E:** Ref. **39**, **F:** Ref. **36**, **H:** Ref. **40**, **I:** Ref. **41**, **J:** Ref. **42**, **K:** Ref. **20**, **L & M**: Ref. **43**, **N:** Ref. **44**, **O:** Ref. **45**, and **P:** Ref. **46**.

II.1.1.3. Branched Nanostructures & Nanoplates

The third class of anisotropic nanoparticles comprises branched nanostructures (i.e., mono-, bi-, tri-, tetra-, penta-, and multi-pods; e.g. stars, spike-radiating, and dendritic shapes) (**Figure II.1L – N**).[3,7,27,44,47–51] However, highly branched structures are more difficult to synthesize reproducibly as they display a more complex structure. They are usually polycrystalline with different crystal domains between the core and the branches. Gold branches typically grow in the <110> direction (though other directions have been observed),[7,48,50,51] while platinum branches grow in the <112> direction.[27] The last distinct class of anisotropic nanoparticles comprises two-dimensional structures (i.e., nanoplates, nanoprisms).[3,13,27,45,52] Nanoplates are usually triangular or hexagonal in shape, though truncation is often observed (**Figure II.1O – P**). The surface area of nanoplates is dominated by {111} faces on top and bottom with edges of {211}, usually.

II.1.2. Seeded Growth Synthesis for Anisotropic Shapes

Over the past few decades, anisotropic metal nanocrystals have been prepared by a variety of synthetic approaches, which have become increasingly convenient while providing ever more precise control over nanoparticle shape.[1,3,7,8] The earliest anisotropic metal nanocrystals to be deliberately synthesized were probably nanowires and nanorods,[8] whereas nanoplates were the first to be implemented in a commercial use, as part of Kodak's photographic materials.[53] As early as the 1960s, metal and metal oxide nanowires ("whiskers") were prepared using the vapor-liquid-solid approach, a method that is still popular today for the synthesis of aligned nanowires.[54,55] By the early 1990s, however, many researchers had turned to electrochemical and photochemical methods for the synthesis of gold and silver nanorods/nanowires.[56–59] While these methods were effective for shape control, the accuracy and aspect ratio control provided by these approaches was limited, and the synthesis of anisotropic metal crystals was still largely limited to nanorods.

In the early 2000s, access to an unprecedented variety of anisotropic metal crystals (including rods, wires, stars, cubes, branched structures, and tetrahedra) became available when a new, convenient chemical synthesis approach, seeded growth in solution, was developed.[1,3,8,49,60,61] The seeded growth approach is a very versatile synthesis, and regardless

of which shape of nanoparticles is to be synthesized, or the identity of the metal core, the seeded growth syntheses of many different anisotropic metal nanoparticles are surprisingly similar.[1,8,14,27] Consequently, what seem like very minor changes in the seeded growth synthesis translate into significant differences in the morphology of the product nanoparticles.[1,8,12,49] This seeded growth approach involves the synthesis of small metal nanoparticle seeds (appearing spherical under electron microscopy), which are then placed in a growth solution containing additional gold monomer and shape-directing agents, and anisotropic growth begins.[49,60,61] In this way, nucleation and growth of the anisotropic crystals are temporally and physically separated, which permits very precise control over nanoparticle shape.[1,7,13,49,60–63] The morphology of the final product is governed by a variety of factors, including the size and shape of the seed, the concentration of the capping agents in the growth solution, and the ratio of the metal salt to reductant in the growth solution.[1,3,8,12,27,49] This approach provided, for the first time, a simple, scalable, and relatively high-yield approach to gold and silver nanorod synthesis, as well as unprecedented aspect ratio control.[1,49,60,61] As a result, the seeded growth approach has become probably the most commonly used synthetic approach for generating anisotropic metal nanoparticles (including gold, silver, platinum, and palladium nanoparticles).[1,8]

Of all the anisotropic metal nanoparticles that can be produced using the seeded growth approach, the synthesis of anisotropic gold nanoparticles has become probably the most extensively studied one.[1,3,8] An initial gold seed is first formed by the reduction of gold salt by sodium borohydride in the presence of a weakly binding ligand such as citrate or cetyltrimethylammonium bromide (CTAB).[1,3,8,49,60,61] A small aliquot of this seed solution is then added to the growth solution, which contains additional gold salt, CTAB, silver nitrate (optional for some nanoparticles, although essential for the growth of single-crystalline gold nanorods), and a weak reducing agent (such as ascorbic acid or hydroquinone).[1,3,8,49,60,61,64,65] These reagents interact synergistically to direct the shape-controlled growth of the seed. The original demonstrations of seeded growth in 2001 primarily focused on preparing spherical gold nanoparticles of precisely controlled diameter, and large aspect ratio gold nanorods.[60] By 2004, however, Sau et al. (among others) had demonstrated that a one-step, silver-assisted aqueous seeded growth synthesis (which used CTAB as the capping agent) could be

used to prepare a vast number of anisotropic gold nanoparticles, including single-crystalline rods (aspect ratios 1.5-4.0), tetrahedra, cubes, hexagonal plates, and branched structures.[49,60,61] The different shapes could be achieved simply by changing the relative amount of seed, silver nitrate concentration, and the ascorbic acid to gold salt ratio.[49] In more recent years, it has also been shown that the same seeded growth approach can be used to more subtly alter gold nanorod morphology ("overgrowth") or prepare complex nanoparticle morphologies that combine the basic morphology of gold nanorods with other shapes.[1,3,8,66,67] In these cases, previously prepared gold nanorods or platonic shapes (cubes or octahedra) are used as seeds to prepare more complex structures. The same general seeded growth approach that is used in the synthesis of gold nanoparticles has also been extended to other metals, such as silver or copper, and even platinum and palladium.[1,3,8,13,62,63] The principal difference among the seeded growth approaches used to prepare these different metal nanocrystals is the composition of the growth solution. While aqueous solutions of halide-surfactant complexes are the standard capping agents in the synthesis of gold and silver nanoparticles, platinum and palladium nanoparticles are more commonly synthesized using seeded growth approaches that occur in polyol solutions, using polymers (such as polyvinylpyrrolidone (PVP)) as capping agents (**Table II.1**). Platinum and palladium aqueous seeded growth syntheses using surfactants are also known.[63]

Table II.1: Common Seeded Growth Syntheses for Select Anisotropic Metal Nanoparticles

Metal	Morphology	Reaction Condition Summary	References
Gold	Spheres	$HAuCl_4$, CTAB, Ascorbic Acid, 3.0-12.0 nm seeds	68
	Single Crystal Rods	$HAuCl_4$, $AgNO_3$, CTAB, Ascorbic Acid, 1.5 nm seeds	69
	Twinned Rods	$HAuCl_4$, CTAB, Ascorbic Acid, 3.0 seeds	60
	Dumbbells	$HAuCl_4$, $AgNO_3$, CTAB, Ascorbic Acid, KI, HCl, 1.5 nm seeds	70
	Prisms	$HAuCl_4$, $AgNO_3$, CTAB, NaI, Ascorbic Acid, 4.0-6.0 nm seeds	71
Silver	Rods	$AgNO_3$, CTAB, KOH, Ascorbic Acid, 4.0 nm seeds	72
	Plates	$AgNO_3$, CTAB, Ascorbic Acid, 1.5 nm seeds	73
Platinum	Nanowire	K_2PtCl_4, CTAB, $NaBH_4$, water:chloroform	74
	Cube		75
Palladium	Tetrahadra/Octahedra	$Pd(acac)_2$/Na_2PdCl_4, Polyol, PVP, 5.0 nm seeds	76
	Nanoplates	Na_2PdCl_4, Fe(III), PVP, ethylene glycol	22

II.1.3. The Role of Halides in Gold Nanoparticle Seeded Growth

The mechanism by which the seeded growth approach accomplishes shape control is not yet well understood. Particularly, the importance of the halide anions as a shape-directing agent has only recently begun to be appreciated. Over the past five years, the growth mechanism of anisotropic gold nanoparticles has been the subject of much research (particularly the growth of gold nanorods), with the growth of the gold core being studied in detail by a variety of *in situ* and *ex situ* methods.[1,6,8,77–79] However, a detailed understanding of the chemical processes by which shape control is achieved remains elusive. For instance, the role of silver in the growth of gold nanorods remains the subject of much debate (see section II.2.6).[8,14,80] A variety of researchers have recently demonstrated that changes in the halide counterion (i.e., the use of cetyltrimethylammonium chloride, CTAC, or the introduction of potassium iodide to the synthesis) can completely change the morphology of the primary product.[12] For example, Smith et al. showed that low concentrations (< 3.0 ppm) of iodide

impurities present in CTAB would prevent the formation of gold nanorods in the silver-assisted synthesis.[18,19] The deliberate addition of iodide has also been used to alter the morphology of gold nanoparticles produced by the three-step seeded growth synthesis. If the iodide concentration in CTAB is above 50 μM, the formation of pentagonally twinned gold nanorods is inhibited, and the favored product becomes prisms/nanoplates instead. Several researchers have actually taken advantage of this to enable the synthesis of new anisotropic shapes (including prisms, trisoctahedra, and others) using growth solutions containing CTAC or a combination of CTAC/I^-.[12,81,82] Zhang et al. demonstrated that the use of CTAC versus CTAB as the surfactant in a silver assisted seeded growth synthesis could lead to the rational control of the shape of the products, under otherwise identical synthesis conditions. In this case, the use of CTAB led to the formation of tetrahexahedra, while the use of CTAC promoted the formation of concave cubes.[20] Mirkin et al. subsequently extended this study to show that the ratio of silver nitrate to halide and the selection of the appropriate halide counterion could be used to rationally prepare a variety of anisotropic gold nanoparticles.[12] These studies indicate that specific halides will lead to the preferential formation of different anisotropic shapes, under otherwise identical seeded growth conditions. It is thus clear that the nature of the halide counterion plays a crucial role in the growth processes of anisotropic gold nanoparticles, but it is not yet clear which halide-metal interactions are primarily responsible for shape control.

Completely understanding the role of halides in the synthesis of anisotropic nanoparticles is challenging because there are many different halide-metal crystal and halide-metal ion interactions (and these interactions may compete with each other, or act synergistically to effect shape control) that need to be accounted for in a seeded growth synthesis. Primarily, until last year, researchers have focused on the potential for halides to act as face-specific capping agents (a single type of metal crystal-halide interaction). However, there are many possible roles that halides could play in the synthesis of anisotropic gold nanoparticles. Potential metal-halide interactions fall into three broad categories: halide interactions with the growing metal crystal, halide interactions with ionic gold, and interactions with the ancillary reagents (e.g., silver nitrate and its underpotential deposition, UPD). More specifically, these interactions may include: the ability of the halide to change the reduction

potential of either Au(III) or Au(I) prior to seed addition, preferential halide binding to different gold crystal faces, the influence of the halide concentration on the shape of the CTA^+X^- micelle, and the effect of the halide on silver UPD, among others. Investigating any of these potential scenarios is challenging in a reaction mixture as complex as the milieu in which seeded growth occurs, and deciding whether a particular halide in a particular synthesis (e.g., bromide in the silver-assisted synthesis of gold nanorods) exerts shape control primarily through one of these roles, or a combination of several different roles is even more challenging. Nevertheless, in the past few years, several researchers have made significant strides in better articulating the often complex roles of halides in anisotropic gold nanoparticle synthesis.

Mirkin et al. investigated the role of halides, silver concentration, and growth rate on the final shape of gold nanoparticles (**Figure II.2**).[12] They found that halides primarily serve three roles during the synthesis of the specific shapes they investigated (which included tris-octahedra, concave cubes, prisms, and tetrahedra, but not gold nanorods): (1) the halides modulate the reduction potential of ionic gold prior to seed addition (**Figure II.2A**), (2) the halides passivate the gold nanoparticle surface (**Figure II.2A**), and (3) in the silver-assisted syntheses, the halides also modulate the extent of silver UPD (**Figure II.2B - C**). The UPD process is affected by both Ag^+ concentration (**Figure II.2B**) and the presence of halides (**Figure II.2C**). It is important to remember that many of their observations, while of crucial importance, are particular to certain solution conditions and it is not yet clear whether their results can be fully generalized to other syntheses.

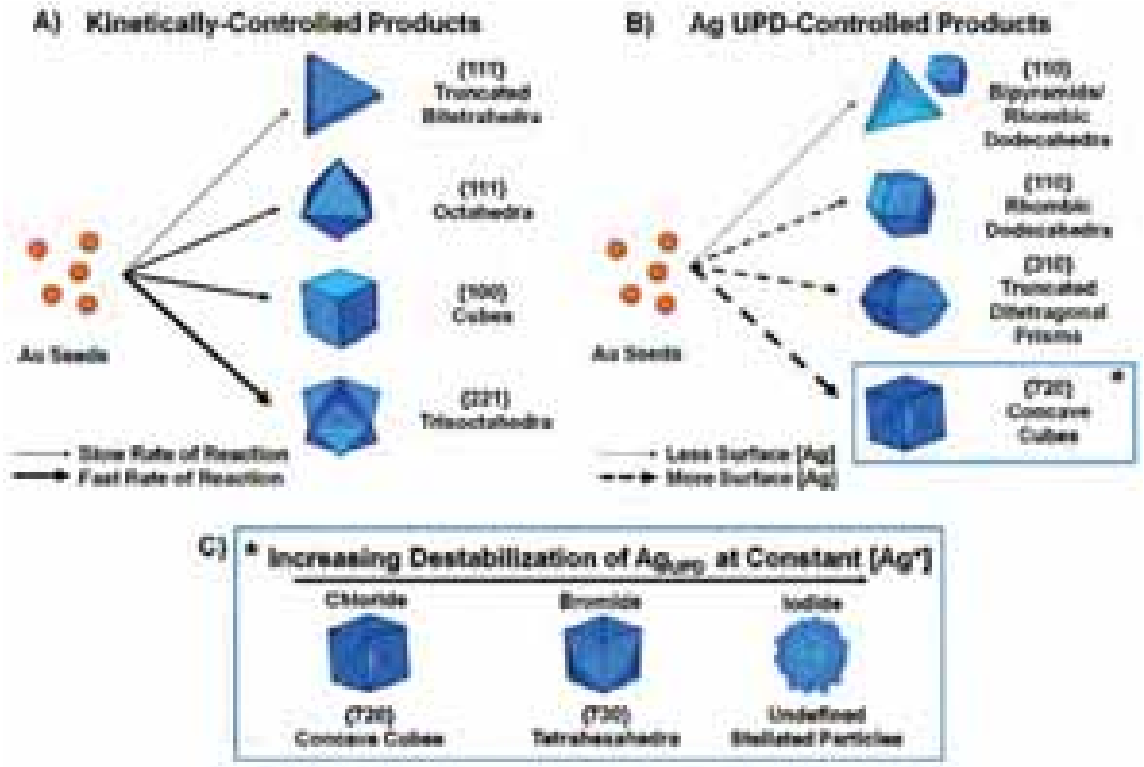

Figure II.2: Scheme illustrating the six rules proposed by Mirkin. Halides and silver ions can be used to direct the growth of gold seeds down different growth pathways to yield different shaped products. **A:** kinetically controlled products in the absence of silver ions; **B:** silver underpotential deposition-controlled products where the interactions of silver with the particle surface dictate product shape; **C:** effect of varying the stability of the silver UPD layer with high concentrations of chloride, bromide, or iodide in the growth solution, yielding concave cubes, tetrahexahedra, and stellated particles, respectively. Adapted from Ref. 12.

Mirkin et al. found that in the absence of silver larger halides (e.g., I^-) induce slower gold nanoparticle growth by altering the reduction potential of $[AuX_2]^-$ and by directly passivating the facets of the growing crystal, which correlates with the formation of gold nanoparticles with lower surface energy faces.[12] In the presence of silver, however, they conclude that the halides primarily exert shape control by controlling the rate/stability of silver UPD (affecting the mobility of silver atoms), and the manner of this control depends on the concentration of halides in solution following the trend of the interaction of gold and silver with the different halides: Ag_{UPD}-Cl > Ag_{UPD}-Br > Ag_{UPD}-I and Au-I > Au-Br > Au-Cl. When larger halides are only present in trace amounts, the stability of the silver UPD layer is somewhat decreased, leading to the formation of shapes with higher-energy facets. However,

when I^- or Br^- are present in high concentration, they prevent silver deposition on the particle surface, and this limits the number of shapes that can be generated.[12] They suggested that this concept allows a precise control over the growth rate and the surface chemistry, through a tight control over the concentrations of silver and halides.

II.1.4. New Developments: Do Halides Really Matter?

Although we have seen in the previous sections that halides appear to be essential for anisotropic growth, recent literature reports provide evidences that are in conflict with this concept. However, it should be noted that the conclusions are often contradictory and we therefore include a discussion here. For example, DuChen et al. systematically studied the effect of Cl^-, Br^- and I^- on the growth of citrate seeds both using CTAB and CTAC as surfactants.[45] The main conclusions are that Cl^- is unable to produce well-defined anisotropic architectures, while Br^- allows the system to evolve towards rod shape and the presence of I^- leads to the development of nanoprisms and hexagonal nanoplate morphologies. The authors proposed that passivation of low-index gold facets occurs because of adsorption of the different halides, with a strength that follows the order $Cl^- < Br^- < I^-$, which are likely to arise from the different redox potentials of the gold precursor in the presence of the different halide ligands, but no consideration was taken of the rates of reduction or growth. A completely opposite approach was taken by Huang and Chiu, who underlined that passivation of the surface of growing gold nanoparticles cannot explain the real mechanism of action of the halides, while the main contribution must be attributed to the different reduction and growth rates.[24] This claim was based on a systematic study of the growth of CTAC-capped seeds under different conditions (including silver-assisted and silver-free protocols), showing that it is possible to obtain a wide range of crystallographic habits by simply modulating the reaction rates involved in the synthesis. In particular, a faster growth rate leads to crystallographic habits characterized by higher index facets. However, this mechanism alone would not explain why the effect of halides significantly changes when Ag^+ ions are present. A combination of reaction kinetics and halide adsorption was recently claimed to determine reshaping upon silver coating, which was supported by density functional theory (DFT) calculations.[83] Nonetheless, Xiao and Qi provided an overview of

different gold nanocrystal syntheses where size, shape and crystal habit are determined by the use of different surfactants, without taking into consideration the role of the halide counterions.[32]

To obtain a more complete picture, we should also take in account synthesis methods involving the use of halide-free solvents and capping agents. This is often the case in the so-called polyol methods, where ethylene glycol or a higher polyol act as both solvent and reducing agent, almost invariably in the presence of PVP as a capping polymer.[25,28,39] In these procedures, it should be noted that the redox potential of PVP changes with temperature, which can be exploited to precisely control the reduction rate, ultimately controlling the final morphologies of the nanoparticles. Similar observations were made when dimethylformamide (DMF) was used instead of the polyols,[84] where variation of the reaction conditions (PVP and metal salt concentrations, temperature or presence of seeds) was found to lead to nanoparticles with different morphologies.[38,47] Although these syntheses do not involve the use of halide-containing surfactants, it is important to take in account that the gold precursor has always been $HAuCl_4$, and therefore the growth conditions are never halide-free. Additionally, when discussing the adsorption of halides on the particles surface, it must be kept in mind that the solvents have chemical and physical properties very different from water, as well as the capping strength of PVP, which cannot be compared with that of surfactants like CTAB. While halides have often been considered as spectator ions in these syntheses, Xia and co-workers have extensively discussed other effects, such as the role of chloride as an etchant for removal of twin planes.[50,85]

As discussed in the previous section, Mirkin et al. recently presented an excellent study on the effects of halides, both in presence and absence of silver. Despite the attempt of this paper to provide a global view of the "halide problem", the observations cannot be completely generalized because the study refers exclusively to the use of CTAC-capped seeds, which are significantly larger (7 nm or 40 nm) as compared to both to CTAB (< 2 nm) and citrate seeds (3.5 – 5 nm), and therefore most likely present a different surface chemistry.

An important consideration when dealing with the role of halides in gold nanoparticle synthesis is the discrimination between thermodynamic and kinetic products.[86] Kinetic considerations indicate that better-defined nanoparticles are generally formed when the

growth rate is slower (thereby allowing the system to reach the thermodynamic minimum energy, i.e. the thermodynamic product) while the nanoparticles are usually less anisotropic (AR < 1.5). However, kinetic products are typically characterized by fast growth and high anisotropy (AR >> 2). The reaction proceeds under thermodynamic control when the total surface energy of the system is minimized. In order to achieve this, the atoms deposited on the surface of the growing particles should be able to diffuse to the lowest-energy sites; this is possible only when the rate of diffusion is faster than that for atom deposition, otherwise the growth will proceed under kinetic control. It is interesting to note that in the latter case, halides do not seem to have a clear effect on the process. For example, Pallavicini et al. proposed the synthesis of branched gold nanoparticles using a zwitterionic surfactant without the addition of heavy halides like Br^- or I^-.[48,87] The same observation can be found in a totally different system like the surfactant-free nanostars reported by Yuan et al.[44] Both synthetic routes are silver-assisted, and the presence of Ag^+ is a key parameter to obtain the necessary symmetry break. The important message here is that it is essential to distinguish between the stabilization of certain facets to direct the synthesis towards a precise crystallographic habit and breaking the face-centered cubic symmetry to achieve anisotropic nanoparticles. This discrimination is not always clear in the literature, and can give rise to misunderstandings.

In the following sections the synthesis of nanoparticles with different shapes will be discussed in detail.

II.2. SYNTHESIS OF GOLD NANORODS

Gold nanorods have been the first successful example of anisotropic plasmonic nanostructure synthesized by wet-chemistry.[88] Since the early 2000's, gold nanorods have received increasing attention because of their tunable optical (plasmonic) properties, which render them ideal candidates for a wide range of applications, such as solar harvesting,[89] photovoltaics,[90] surface enhanced spectroscopies,[91,92] sensing[92–94] and therapy,[89,95] to name a few. The mechanism behind the formation of gold nanorods is still a matter of much interest, since a general mechanistic model would allow us to identify specific guidelines for the design of a synthetic pathway for each nanostructure.[3,12,96,97] Xia's group recently published a highly informative perspective article dealing with the distinction between thermodynamic and kinetic control during crystal growth.[86] An entire section of this paper is dedicated to the symmetry breaking event, a necessary step in the development of anisotropic structures, such as gold nanorods. The main message is that stabilization of crystallographic facets and anisotropic growth are different issues, the former being under thermodynamic control and the latter under kinetic control (see section II.1.4). Keeping this consideration in mind, it is not surprising that gold nanorod synthesis comprises both thermodynamic and kinetic control, which significantly increases the number of parameters that need be taken into account. This can be easily seen by considering that a gold nanoparticle colloid can be described by the average diameter alone, while for gold nanorods we need to consider length, thickness, aspect ratio (AR), reduction-yield (how much precursor gets reduced) and shape-yield (the proportion of formed particles that are nanorods). This consideration is translated in practice into the need for a higher degree of control throughout the growth process, which is of particular relevance when the goal is not simply the production of high-quality nanorods, but also a tight control on the actual AR to be produced.

As explained in the introduction, this was historically achieved through the introduction of the seeded-growth method (see section II.1.2). It is worth mentioning here that even though so-called 'seedless' methods have been reported, they are generally characterized by a lower product-quality and reproducibility. Furthermore, these methods require the addition of small amounts of a strong reducing agent, typically sodium borohydride, which leads to the *in situ* formation of seeds through partial reduction of the gold salt precursor into Au(0). It is also

important to decide whether you wish to prepare single crystalline or pentatwinned gold nanorods. Although both are rod-like nanoparticles, they have different dimensions, surface facets, twin defects, geometry, crystallographic habit and even composition (see section II.1.1.1). Pentatwinned gold nanorods display pentagonal cross-section, with {100} lateral facets, and {111} facets closing the crystal at the tips, they typically have larger dimensions and higher ARs, with longitudinal bands in the near infrared (NIR) range, and are synthesized by growth on citrate capped twinned seeds under "silver-free" conditions.[98] On the other hand, single crystal nanorods display smaller dimensions and ARs, the longitudinal plasmon band can be finely tuned from the visible into the NIR, and are grown using CTAB capped single crystal seeds, in the presence of silver nitrate.[99] There has been some controversy regarding their crystallographic habit, but it seems to be accepted by now that they show octagonal cross-section and high-index {520} lateral facets.[34] All together, these considerations impose significant differences in the respective synthetic protocols, each with different critical issues, which we analyze point by point in the discussion below. We analyze separately the various components of a typical gold nanorod synthesis.

II.2.1. The Seeds

In the context of this work, seeds are small nuclei (typically below 5 nm) made of gold, which serve as the starting point for the development of a more complex (anisotropic) structure.[3,100] It is thus obvious that a high quality seed solution is necessary to obtain high quality nanorods. Ideally, the seeds should be monodisperse and display the same crystallographic habit, which in practice is achieved by adding a strong reducing agent in excess (typically sodium borohydride, $NaBH_4$, 6-60 equivalent),[101] as fast as possible and under vigorous stirring. As a tip, when preparing a seed solution you should picture in your mind an *instantaneous* addition of the reductant to achieve the *simultaneous* production of all nuclei, homogenously distributed in the *entire solution volume*. Moreover, is important to remember that $NaBH_4$ is hygroscopic, and can react with the water contained in the air; therefore, is important to weigh it as fast as possible and to prepare it fresh every time. Two types of seeds can be used depending on the type of nanorods to be prepared: CTAB capped seeds are used for single crystal nanorods and citrate capped seeds for pentatwinned

nanorods. The former are single crystalline (**Figure II.3B**), with an average diameter below 2 nm, and their solutions appear light brown, i.e. they do not show any LSPR band (**Figure II.3A**); a red-pink shade would indicate the formation of bigger particles, which are likely to compromise the quality of the final product. Even though seeds are highly reactive, they can be stored between 27 and 29 °C for a couple of hours, which may also help to complete decomposition of the remaining borohydride ions. Citrate capped seeds are slightly bigger (*ca.* 3.5 nm on average) and therefore present the typical red color of gold colloids, with an LSPR band centered around 507 nm (**Figure II.3A**). Their larger dimensions also enhance their stability up to few days if stored in the fridge. It is important to point out that a mixture of crystallographic habits are usually obtained, comprising single crystalline, monotwinned and pentatwinned populations (**Figure II.3C**), which has a major impact on the usual low shape-yield in the synthesis of pentatwinned gold nanorods, typically around 30 %.

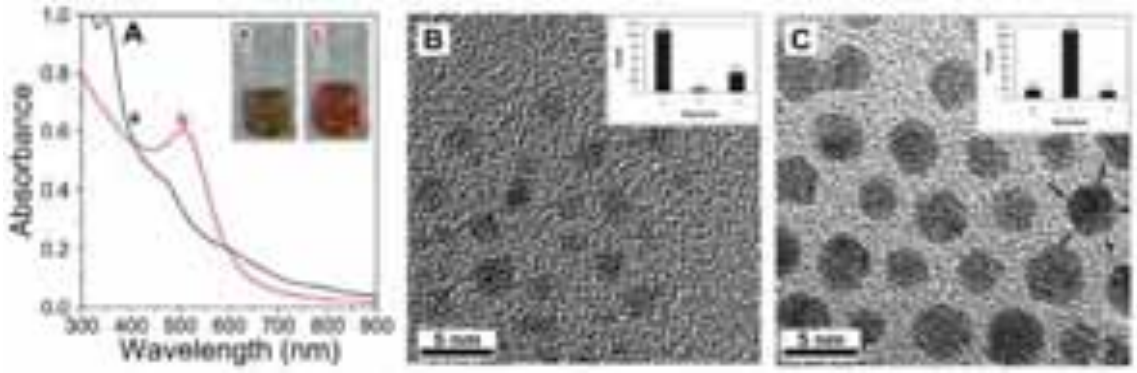

Figure II.3. gold seeds for the synthesis of single crystal and pentatwinned gold nanorods. **A:** UV-vis spectra of CTAB coated (a, black line) and citrate coated (b, red line) seeds. **Inset:** picture of a typical seed solution: CTAB coated (a, left) and citrate coated (b, right). **B-C:** High resolution transmission electron micrograph of single crystalline seed@CTAB and pentatwinned seed@citrate, respectively; the histograms show the counting for single crystal (S), twinned (T) and undefined (U) seeds. Adapted from Ref. 65.

II.2.2. The Surfactant

Originally, bromide-surfactant complexes were incorporated into the templated electrochemical synthesis of gold nanorods,[102–104] primarily because they were good electrolytes. By the time Jana et al. developed the original three-step seeded growth approach for pentatwinned gold nanorods, the choice of CTAB as a suitable surfactant for the synthesis of gold nanorods stems from the wealth of existing literature dealing with the rheology and phase behavior of its solutions, since at suitable concentrations CTAB was known to form rod-shaped micelles, which were expected to act as soft template that could direct the anisotropic growth of the gold nanorods.[14,31,59,60,105] This view slowly evolved into the hypothesis that CTAB acted as a face-specific capping agent, which would bind preferentially to the longitudinal faces of the developing gold nanorods, permitting faster reduction of gold atoms at the tips of the rod.[3,8,80] Similar roles for CTAB were proposed in the silver-assisted seeded growth of single-crystalline gold nanorods, with the caveat that silver also played a role in either the formation of the cylindrical micelles or the face-specific capping agent was some form of CTA^+-Br^--Ag^+ (see section II.2.6).[8,80] Numerous studies have been conducted with the aim of understanding the role of the surfactant on anisotropic growth, changing tail length[106] and head group[61] or using gemini surfactants,[107] among other variations. Between 2007 and 2010, however, several research groups reported that the bromide counterion was more important in directing the growth of gold nanorods (particularly in the silver-assisted growth procedure) than the surfactant, and that the presence of even relatively small impurities of other halides in the growth solution would completely inhibit gold nanorod growth.[16,17,77,108] For instance, Garg et al. showed that single-crystalline gold nanorods of comparable quality and yield could be grown in a growth solution that was only 1.0 mM in CTAB (just above CTAB's first critical micelle concentration) if the total bromide concentration of the solution was kept at 0.09 M or greater.[16] Bullen et al. studied the effect bromide concentration on gold nanorod growth kinetics, and found an inverse relationship between the concentration of bromide and the rate of gold nanorod growth, regardless of whether the bromide was primarily present as CTAB or KBr.[79] It is thus clear that the original dependence on CTAB for the synthesis of anisotropic gold nanoparticles was a serendipitous choice, but oddly, it seems that the halide

counterion may play a more significant role in controlling gold nanoparticle shape than the surfactant. Even though CTAB remains the most employed surfactant, we can identify three basic requirements to achieve rod-like shape:

- A quaternary ammonium surfactant head group that forms a complex with the gold salt precursor and modifies its redox potential.
- The presence of bromide as counter-ion: any attempt to synthesized single crystalline nanorods in either CTAC or benzyldimethylammonium chloride (BDAC) alone failed unless minute amounts of bromide ions (*ca.* 1 mM) are added to the reaction mixture, suggesting a key role of bromide ions in the symmetry breaking process.[109]
- A carbon tail that is long enough to stabilize the nanorods, but short enough to achieve solubility close to room temperature.[17]

II.2.3. The Gold Precursor

Tetrachloroauric acid, $HAuCl_4$, is widely used in gold nanoparticle synthesis. Therefore, three different oxidation states are involved: Au(III) in the precursor, Au(I) as intermediate, and Au(0) comprising the nanoparticles.[77] Au(III) is a d^8 soft metal center, forming square planar complexes. According to Ligand Field Theory, the complexation strength of Au(III) with halide ions follows the series: $I^- > Br^- > Cl^-$. Therefore, in the presence of CTAB the four chloride ligands in $[AuCl_4]^-$ will be eventually replaced by bromide ions from the surfactant:

$$[AuCl_4]^- \rightleftharpoons [AuCl_3Br]^- \rightleftharpoons [AuCl_2Br_2]^- \rightleftharpoons [AuClBr_3]^- \rightleftharpoons [AuBr_4]^- \quad \textbf{[II.1]}$$

which is reflected in a color change from pale yellow to dark-orange yellow, with a final absorption maximum at 396 nm.[110] Additionally, the $[AuBr_4]^-$ ions will form an ion-pair with the quaternary ammonium surfactant monomers which are neutral and therefore insoluble in water, requiring a surfactant concentration with a 60:1 ratio to ensure dissolution.[99] Both the $[AuCl_4]^-$ to $[AuBr_4]^-$ ligand exchange and the $[AuBr_4]^-$-CTA^+ complex formation will influence their redox potentials, which are cathodically shifted.[111] Such a variation in the redox potentials will influence the growth kinetics. Taking all this into account, it is

important to ensure not only that the gold salt has been completely dissolved, but also that ligand exchange has been completed. Moreover, an additional equilibrium needs to be considered between all three gold oxidation states, which can be pushed towards comproportionation or disproportionation reactions, depending on the relative stability of each species in the mixture:

$$Au^{3+} + 2Au^{0} \rightleftharpoons 3Au^{+} \quad \textbf{[II.2]}$$

In the growth solution, the most stable species is Au(I), meaning that the equilibrium is displaced towards the comproportionation between Au(III) and Au(0), i.e. gold nanorods (or other gold nanoparticles) will be oxidized in the presence of Au(III).[110–113] In this scenario, a central role is played by the reducing agent, as discussed below.

II.2.4. The Reductant

One of the key points in the seeded growth method is the use of a weak reducing agent, so that gold reduction takes place only on existing nuclei in solution, which also act as catalysts. Even though other reducing agents have been proposed,[64,114] the most popular choice is still ascorbic acid, AA.[115,116] Upon addition of AA to a growth solution containing a mixture of $HAuCl_4$ and CTAB, the reduction of Au(III) to Au(I) takes place, indicated by the solution turning colorless (the ligand-to-metal charge transfer band disappears for a d^{10} metal center as Au(I)). This is in fact an important step as it guarantees that when the seeds are injected into this growth solution their oxidation by the favorable comproportionation reaction (see section II.2.3) is avoided. It is also crucial that the reducing agent ***cannot*** complete the reduction of Au(I) into Au(0), i.e. secondary nucleation during the growth step is prevented. In fact, the seeds act as catalysts for the final reduction step, thereby inducing reduction of the Au(I) precursor on their surface only. Two possible mechanisms have been proposed: (1) a disproportionation reaction catalyzed by the seeds produces Au(0) and Au(III) (eq. **[II.2]** from left to right), the latter immediately being reduced again into Au(I) by remaining reductant,[117–119] and (2) the Au(0) surface drains electrons from the reductant and catalyzes the *in situ* reduction of Au(I).[99,120] It should be noted that AA features a pH-dependent reduction potential, being lower under acidic conditions and higher at more basic pH

values,[121] which has been applied to modulate gold nanorod growth. In fact, if the pH is above 9 AA will be able to reduce Au(I) into Au(0), even in the absence of seeds, thus compromising the seeded-growth mechanism.

Finally, another important issue involving the reductant is the reduction-yield. In fact, it is still unclear if the gold precursor is entirely reduced on the surface of the growing rods, and otherwise why this is the case.[8,122] In order to measure the reduction-yield in a more convenient way, it is useful to employ a simple spectroscopic analytical method based on the absorbance of light with a wavelength of 400 nm, which can be measured with a simple UV-vis spectrometer.[111,123] The idea is to select a wavelength where the main contribution to absorbance comes from absorption related to interband transitions in metallic gold,[69,124] which would thus be used to determine the amount of gold precursor that has been reduced, regardless of particle size and shape (note that large particles will display strong scattering so the accuracy of this method would be compromised in this case). Firstly, we used a standard protocol for the synthesis of citrate-capped seeds (i.e. using a strong excess $NaBH_4$ as reducing agent) at four different concentration of $HAuCl_4$ (the amount of citrate and $NaBH_4$ were adjusted consequently), to study the relationship between [Au^0] and absorbance at 400 nm. The high reduction power gives us the safety of a complete reduction of the gold precursor. The whole experiment has been repeated five times in order to calculate an average value and a standard deviation (**Figure II.4A - B**). A linear relationship was determined with a slope close to 2.4. In order to confirm the validity of this relationship for gold nanorods we carried out numerical BEM calculations[125] of the extinction spectra of nanorods with different ARs and dimensions. When the simulated spectra were normalized by particle volume (**Figure II.4C**), the extinction cross section (equivalent in practice to absorbance) at 400 nm was found to be identical for all geometries. We thus plotted (**Figure II.4D**) the absorbance at 400 nm as a function of nanorod volume, obtaining a perfectly linear relationship. This clearly demonstrates that all gold nanoparticles with the same volume will equally contribute to the measured absorbance at 400 nm. It is worth mentioning here that deviation from this relationship can be observed if the volume of the particles is too big and the scattering contribution to the extinction cross-section becomes significant. To further confirm the experimental evidences we characterized several gold nanorod samples

with different volumes and ARs by UV-vis spectroscopy and inductively coupled plasma mass spectrometry (ICP-MS) elemental analysis. As can be seen in **Figure II.4E**, the variation of absorbance at 400 nm for the different samples with the corresponding gold concentration determined by ICP-MS follows a linear trend with a slope of 2.4. Therefore, a value of 1.2 for the absorbance at 400 nm corresponds to an Au(0) concentration of 0.5 mM. Noteworthy, an absorbance at 400 nm below the expected value would indicate that part of the gold precursor remained in solution as Au(I), which in turn results in slow reshaping and spectral blueshift, as has been reported by many groups, when nanorods are aged for long periods of time. A simple centrifugation step can be used to remove the excess of reagents and enhance the long term stability of gold nanorods (even for years). We estimate the theoretically expected absorbance of a 0.5 mM solution of "nanometric" Au(0) starting from the value of extinction cross-section (for volume unity) that we obtained from the calculations:

$$\mathrm{A} = -\,\mathrm{Log}_{10}\, e^{-L\partial\tau} \quad \textbf{[II.3]}$$

where L is the optical path length (nm), σ is the scattering cross-section of a gold volumetric unity (nm^2), and τ is the volume fraction of gold (nm^{-3}). Using equation **[II.3]** we obtained a predicted absorbance of 1.1, in good agreement with the experimental value of 1.2. Overall, calculation and ICP-MS data confirm that:

- The reduction yield can be precisely estimated from the absorbance at 400 nm, regardless of the shape and size of the nanoparticles.
- An absorbance of 1.2 corresponds to $[Au^0]$ = 0.5 mM.
- During a standard gold nanorod preparation there is *quantitative reduction* of the gold precursor.

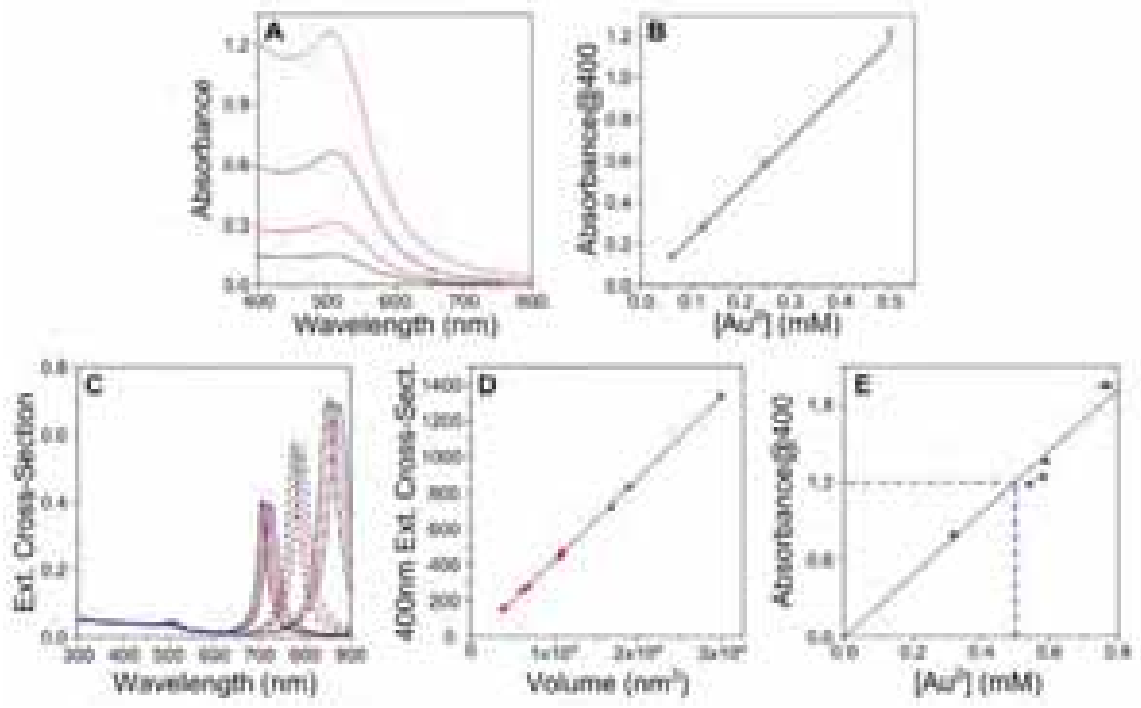

Figure II.4. Reduction-yield in gold nanorod synthesis. A: Example of UV-vis analysis of four citrate-seed samples prepared with different concentration of gold precursor: 0.0625 mM (black line), 0.125 mM (red line), 0.25 mM (blue line) and 0.5 mM (pink line). **B:** Graph showing the linear relationship (black line) between the concentration of the gold precursor and the absorbance at 400 nm, with a Pearson's coefficient $R^2 > 0.997$. Green circles represent the average values calculated after five repetitions. The error bars represent the standard deviations. **C:** Calculated extinction spectra for gold nanorods of different ARs and dimensions, normalized to the particle volume: AR = 3 (solid lines): 50x16.7 nm (black), 60x20 nm (red), 70x23.3 nm(blue); AR = 4 (dotted lines): 50x12.5 nm (black), 60x15 nm (red), 70x17.5 nm (blue); AR = 5 (dash-dotted lines): 50x10 nm (black), 60x12 nm (red), 70x14 nm (blue). Note that the absorbance at 400 nm is constant for all spectra. **D:** value of the extinction cross-section at 400 nm plotted against particle volume; the solid line is a linear interpolation to the data, with a Pearson's coefficient $R^2 > 0.999$. **E:** value of the absorbance at 400 nm of different gold nanorod colloids plotted against $[Au^0]$ obtained from ICP-MS analysis. The solid black line is a linear fit to the data, obtained by imposing a null y-intercept, with a Pearson's coefficient $R^2 > 0.994$. The blue lines confirm the relationship: $Abs_{400nm} = 1.2 \Leftrightarrow [Au^0] = 0.5$ mM.

II.2.5. Growth Kinetics

The growth of gold nanorods is characterized in general by a slow kinetics, meaning that several hours are needed to complete particle growth. Interestingly, significant differences can be found between pentatwinned and single crystal nanorods, thus involving different growth mechanisms. In the case of pentatwinned gold nanorods a constant redshift of the longitudinal plasmon band is observed during growth, suggesting a gradual increase in AR throughout the entire growth process (**Figure II.5A - B**).[99] Single crystal gold nanorods on the other hand display a more complicated behavior in which different groups agree in identifying two separate stages, which are reflected in changes of the optical spectra:[30,64,77,126] a fast redshift of the longitudinal band during the first minutes of growth, followed by a slow blueshift. The former is directly related to the increase of anisotropy that takes place at early stages of growth, whereas the latter is attributed to either isotropic growth[126] or reshaping of the nanorods tips.[30,77] In a related work we were able to distinguish these two different contributions (see section II.2.7.1);[110] briefly, we distinguished three different stages (**Figure II.5C - D**): initially the plasmon band quickly redshifts as the gold salt gets reduced (1), but then blueshifts (2), and the blueshift continues even after reduction is completed (3).[30,110] Transmission Electron Microscopy (TEM) analysis at the different stages (**Figure II.5e - g**) revealed that the growing particles initially show a dumbbell-like morphology but then reshape into "perfect" rods at the latest growth stage; calculations demonstrate that this reshaping can explain the blueshift of the longitudinal plasmon band.[30,77,127,128] Assuming that reduction takes place predominantly on the region of highest surface energy, i.e. at the tips of the growing rods, the freshly reduced gold atoms should migrate along the surface to form the most thermodynamically stable crystallographic habit. At a reaction temperature of 30 °C this process can take several hours to be completed.[86]

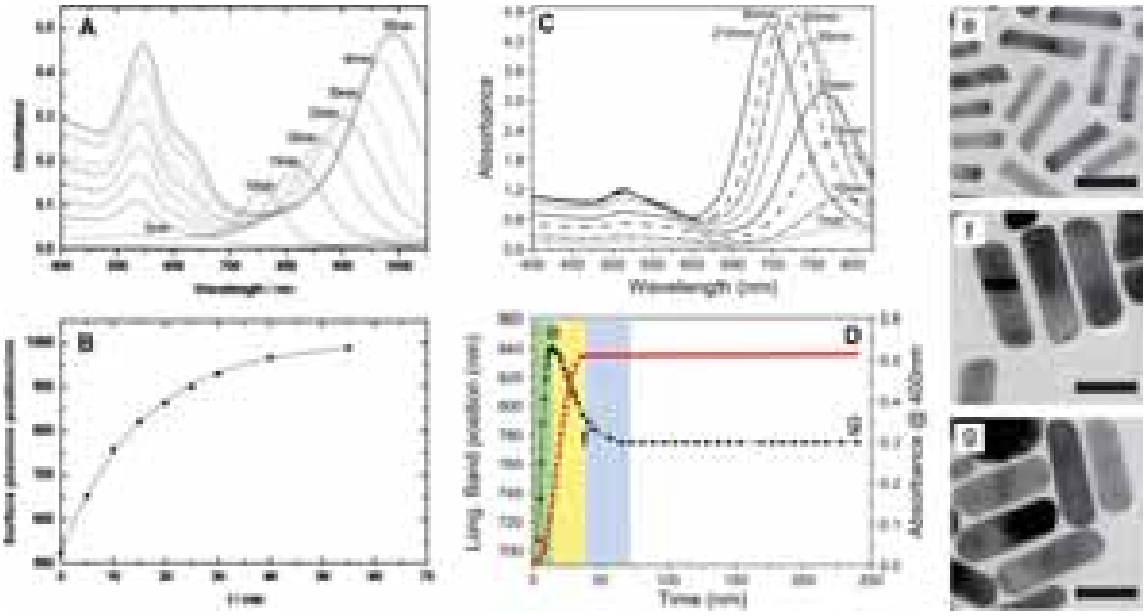

Figure II.5. Kinetic optical study of gold nanorod synthesis. A: UV-vis-NIR spectra of a growing pentatwinned gold nanorod solution. **B:** position of the longitudinal plasmon band as a function of time, where is evident a constant redshift (adapted from Ref. 99). **C:** UV-vis-NIR spectra of a growing single crystal gold nanorod solution. **D:** position of the longitudinal plasmon band (black) and value of the absorbance at 400 nm (red) as a function of time; three different stages are distinguished: redshift and reduction (green), blueshift and reduction (yellow) and blueshift no reduction (blue). **e-g**: TEM images of growing nanorods at different growth stages, as indicated in **D**: at the maximum red-shift of the longitudinal plasmon band **(e)**, at the end of reduction **(f)**, at the end of growth **(g)** (adapted from Ref. 110)**.**

II.2.6. Silver Ions

The specific role of silver ions in the synthesis of single crystal gold nanorods remains unclear. Three main mechanisms have been proposed: (1) UPD (see section II.1.3), (2) formation of a $Ag[BrCTA]_2$ complex that acts as a face-specific capping agent on the lateral facets of the growing seeds and (3) modification of CTAB micelle formation through silver-bromide interactions.[31,65,80,109,129] We deliberately leave out here a detailed mechanistic study of the role of silver, but rather concentrate our attention toward its practical consequences on synthetic protocols. The presence of Ag^+ ions is essential for the synthesis of single crystal gold nanorods, while it hinders the anisotropic growth of pentatwinned nanorods. In the latter case, the absence of silver as a surface active agent renders metal reduction "less" selective for nanorod tips. A lower temperature is thus required to slow down the reduction and diffusion of reduced atoms on the surface of the growing particles: typically, pentatwinned

gold nanorods are synthesized at 20 °C, which in turn imposes a limitation on the maximum CTAB concentration that can be used (8 mM *vs.* 100 mM for single crystal gold nanorods). On the contrary, for single crystal gold nanorods, the presence of silver simultaneously leads to higher selectivity for reduction on the tips (kinetically influencing the symmetry breaking) and stabilization of lateral facets (thermodynamically stabilizing the final product). In fact, gold nanorods can be synthesized at a much higher temperature, but moderate reaction temperatures are usually selected, again to slow down the reduction and achieve a narrower size distribution.

II.2.7. Characterization

The main techniques required for Au nanorod characterization are UV-vis-NIR spectroscopy and transmission electron microscopy (TEM). It is important to realize that they are complementary to each other and both of them should be used in all cases. In our opinion, there is a general tendency to overestimate the amount of information that can be derived from TEM analysis, and often optical data are neglected or even completely omitted. In practice, an optical spectrum can tell to an expert eye much more than a TEM image (**Figure II.6**): the full width at half maximum (FWHM) and the shape of the longitudinal LSPR band are excellent measures of size dispersion, while the plasmon band position gives us a quick estimate of the average aspect ratio, the nanoparticles concentration can be derived from the absorbance at 400 nm and the ratio between the maximum absorbance of the longitudinal and transverse LSPR bands, as well as the presence of a shoulder on the transverse band, are indications of the presence of by-products with different shapes (**Figure II.6A**). On the other hand, a TEM image can provide the particle dimensions with high accuracy, but if a fair reproduction of the three-dimensional morphology is required electron tomography should be employed.[130] It is also important to realize that a single TEM image is not the best way to demonstrate the absence of by-products, since shape segregation has been reported to occur during drying, meaning that the by-product will largely concentrate at a particular area of the grid (**Figure II.6B - C**).[131,132] It should be taken into account that, in order to obtain sufficient TEM statistics for the length, thickness and aspect ratio of nanorods, several images must be analyzed, ideally at different magnifications.[133]

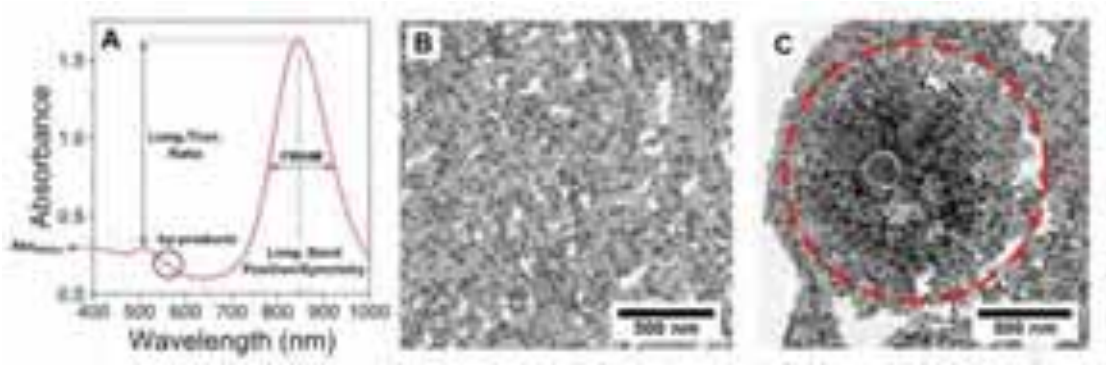

Figure II.6. A: Typical UV-vis-NIR spectrum of a single crystal Au nanorod colloid. In the image we indicate the parameters that are indicative of product quality. **B-C:** TEM images from the same TEM grid, showing the accumulation of isotropic material at a certain spot (red dotted circle). Is important to notice that the shape-yield that can be estimated from **B** and **C** is significantly different, *both being biased*.

II.2.8. Additives

The influence of different types of additives on the yield, homogeneity and reproducibility of gold nanorod synthesis has recently acquired major relevance. The nature of these additives (or co-factors) ranges from inorganic anions or cations to both aromatic and aliphatic molecules. Murray and co-workers have recently proposed sodium oleate and salicylic acids as additives to CTAB and to a binary surfactant mixture.[134] This allowed them to access unusual experimental conditions (i.e. lower seed concentration and higher silver to gold ratios), thereby leading to nanorods with larger dimensions, wide AR tunability and better product quality. In both cases the authors proposed a mechanism related to the intercalation of the additive within the CTAB bilayer surrounding the growing particles, which increases its stiffness and therefore improves the control over the symmetry breaking event.[135–137] However, it is important to realize that these additives can also interact in various other ways with the chemicals present in the growth medium. Interestingly, salicylic acid has been long known as an effective reducing agent for the preparation of gold nanoparticles.[138] This was also exploited by Malikova et al.[139] for the preparation of nanoprisms in aqueous media at high temperature, as well as by Luo,[140] who achieved an increase in the yield of nanoplates and their size by adding a certain amount of poly(diallyldimethylammonium chloride) to the growth solution. A systematic study of the influence of additives can supply new ideas and shed light on the mechanicistic aspects of gold nanorod synthesis that are still unresolved.

II.2.8.1. Tuning Gold Nanorod Synthesis Through Pre-reduction with Salicylic Acid

We have undertaken the study of the roles of 5-bromosalicylic acid (5-BrSA), as both co-factor and reducing agent for the Au(III)-to-Au(I) reduction step. Our results demonstrate that the use of 5-BrSA opens up the possibility of exploiting this double-reducing-agent-system to tune the AR of the formed particles, while significantly improving the yield of gold reduction. This may lead to new insights in the mechanistic aspects of the synthesis of anisotropic gold nanoparticles, while offering new strategies toward the control of their shape and dimensions. The reducing power of salicylic acids can also be exploited to perform an overgrowth reaction in a widely controllable way, with different compositions of the overgrowth solutions. In this way we demonstrate that Ag^+ ions help maintaining the nanorods anisotropy even after multiple overgrowth steps, thus avoiding a complete loss of anisotropy as registered in the case of silver-free overgrowth conditions.

The starting point of our discussion is an observation from ref. 136, regarding the reducing ability of salicylic acid: "The CTAB-additive-$HAuCl_4$ solution becomes colorless after being mixed for about 30 min without ascorbic acid. However, no gold nanorods are obtained unless […] ascorbic acid solution is added to the growth solution". Since the loss of color of the "CTAB-additive-$HAuCl_4$ solution" very likely indicates the reduction of Au(III) into Au(I) by "the additive", we studied the kinetics of Au(III) reduction by 5-BrSA in aqueous CTAB solution, by monitoring the changes in the UV-vis absorbance band of the Au(III)-CTAB complex (λ_{MAX} = 396 nm, inset **Figure II.7A**). It can be observed that the reduction proceeds rather slowly at room temperature (**Figure II.7**), thus providing us with the possibility to precisely select the amount of gold precursor that has been reduced into Au(I) prior to AA addition and to study how this affects the final nanorod product. The precise nature of the final reduction step is still under debate. Whereas some groups proposed a disproportionation mechanism[98] (catalyzed by the Au(0) surface), where three Au(I) ions would disproportionate into two Au(0) atoms and one Au(III) ion, other studies suggest that in the presence of CTAB, Au(III) and Au(0) would favorably undergo a comproportionation reaction.[99,141] In the former process, the reducing agent would act as a scavenger to reduce newly formed Au(III) into Au(I), and for this reason we believe that it is unlikely to be the main process in our system, since 5-BrSA should be able to carry out the same scavenging

process. As mentioned above, experimental evidence shows that 5-BrSA is unable to initiate nanorod growth. The synthetic process can thus be described through the following sequence (**Scheme II.1**): i) 5-BrSA is used to partially reduce Au(III) into Au(I) in a pre-reduction step; ii) AA is added to complete the reduction of Au(III); iii) pre-synthesized Au(0) spherical seeds are added, which catalyze the final reduction of Au(I) into Au(0), thereby initiating nanorod growth. It is important to point out that in all the presented experiments other parameters (such as Ag^+ concentration or pH) were kept constant.

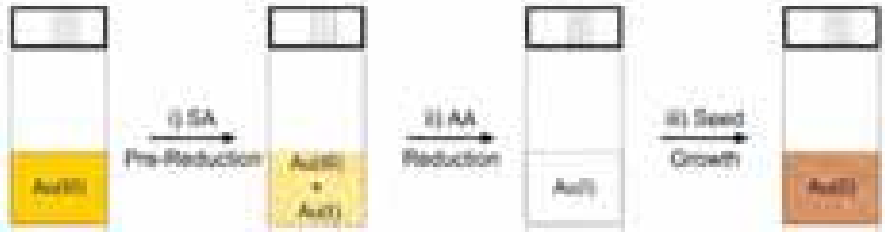

Scheme II.1. Description of experiments used for gold nanorods formation.

As can be seen in **Figure II.7A**, the pre-reduction time (monitored following the drop in absorbance at 396 nm, green dots in **Figure II.7A**) strongly affects the final AR of the nanorods (**Figure II.7B**). The longitudinal LSPR can be tuned between 850 and 650 nm for shorter and longer pre-reduction times, respectively, corresponding to AR values of 3.9 and 2.4, respectively (**Figure II.7C**). Note that size uniformity is hardly affected, as confirmed by the AR histograms (**Figures II.7C - E**). The pre-reduction time also affects significantly the reduction yield, i.e. the final amount of metallic gold. In order to quantify this parameter, we monitored the absorbance at 400 nm (see section II.2.4). Since using a cuvette with 1cm optical length, an absorbance of 1.2 at 400 nm corresponds to a quantitative reduction[141] (see section II.2.4), the percentage of unreacted Au(I) may be as high as 75% for the nanorods with the highest AR (shortest pre-reduction time). Assuming the absence of secondary nucleation, i.e. that an 'x' amount of seeds leads to a corresponding 'x' amount of nanorods, these data match with the average volume for a single nanorod, as calculated from TEM analysis (**Figure II.7F**), meaning that smaller rods are formed from the same number of seeds when the pre-reduction time is shorter.

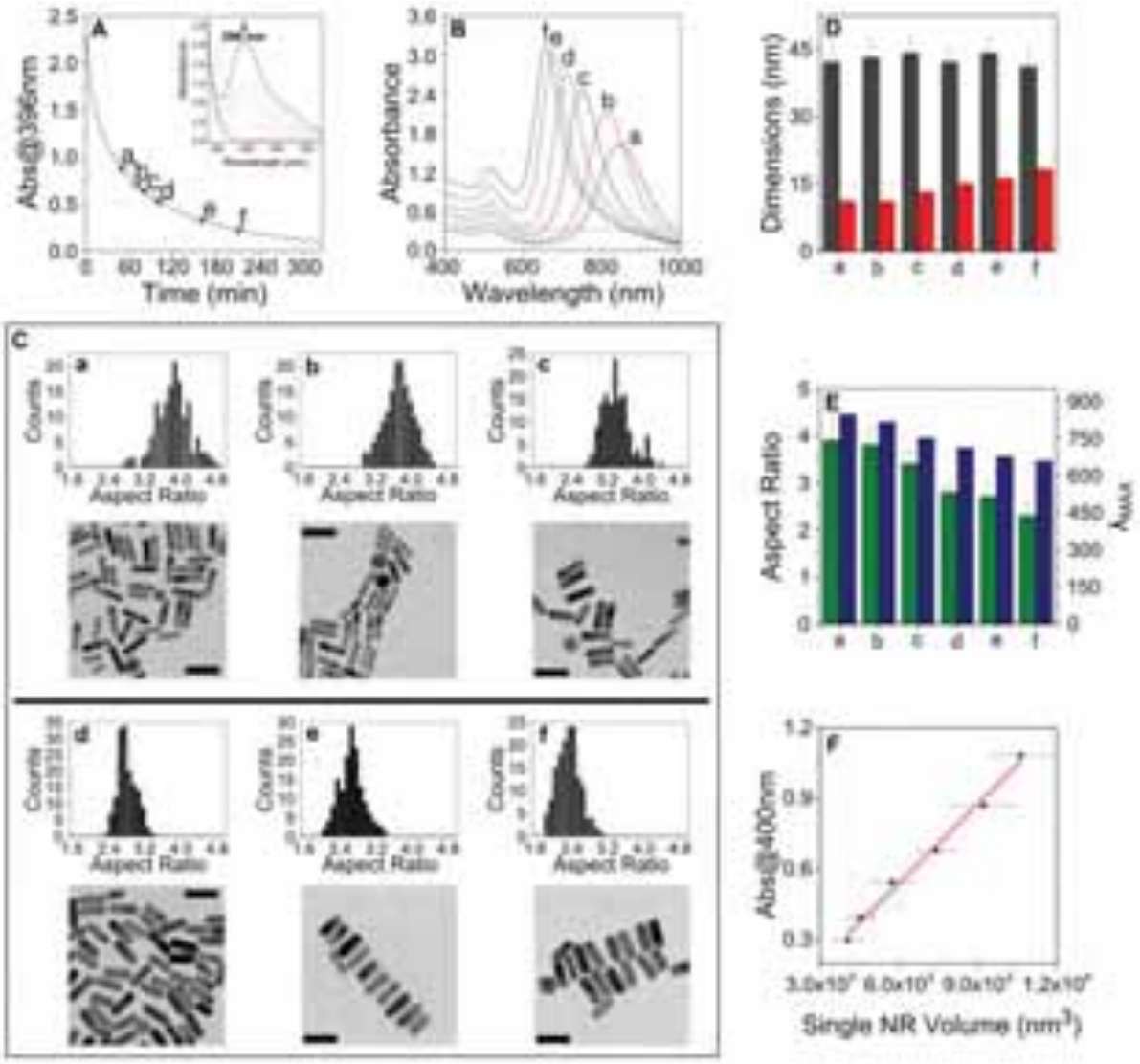

Figure II.7. The extent of pre-reduction by 5-BrSA affects both the AR and the amount of reduced gold. **A:** Kinetic study of the pre-reduction step (inset: full UV-vis spectra). **B:** UV-vis-NIR spectra of the various nanorod colloids obtained by changing the pre-reduction time. Abs_{396nm}: 0.88 (a); 0.71 (b); 0.64 (c); 0.53 (d); 0.33 (e); 0.22 (f) (UV-vis spectra were multiplied by the corresponding dilution factor). **C:** AR distribution analysis (top) and representative TEM images (bottom) of the samples shown in **B**. Scale bars: 50 nm. **D:** Length (grey) and thickness (red) of the nanorods in the samples shown in **B**. **E:** AR (green) and longitudinal LSPR band position (blue) of the samples shown in **B**. All the average data presented were obtained upon measurement of 150 nanorods from each sample. **F:** Correlation of the average single particle volume with the Au(0) yield for the sample shown in **B**, showing a Pearson's coefficient $R^2 > 0.988$.

To better understand the effect of pre-reduction time, we spectroscopically monitored nanorods growth. For this purpose we selected three different pre-reduction times corresponding to Abs_{396nm} = 0.75, 0.45 and 0.20. As shown in **Figure II.8**, regardless of pre-reduction time, we observed that the longitudinal LSPR initially redshifts, but then progressively blueshifts back, and this blueshift occurs to a larger extent when the pre-reduction time was longer. Additionally, the reduction is completed prior to the end of the blueshift (compare upper and lower plots in **Figure II.8A**), which clearly demonstrates that the blueshift is related to both reduction and reshaping. To correlate the optical behavior with size and shape evolution we arrested the growth of the nanoparticles by addition of excess dodecanethiol,[126,142] at three different stages: (*a*) at the time of maximum LSPR wavelength; (*b*) when gold salt has been totally consumed; (*c*) four hours after seed addition. In all cases, we observed that at stage *a* the nanocrystals have already acquired a well-defined rod-like shape, with similar values of length, width and volume (**Figure II.8C - E**). At stage *b*, the average nanorod volume was found to increase further for longer pre-reduction times, as more gold atoms were reduced. We observed that the highest AR is obtained for the rods prepared with the shortest pre-reduction time, i.e. with the largest amount of unreduced gold salt remaining in the growth solution. In agreement with the UV-vis analysis, the volume of the particles did not increase further at stage *c*. As the amount of added AA was constant for all reactions, gold reduction was faster for longer pre-reduction times, when less Au(III) was present in solution and more AA was involved in nanorod growth (**Figure II.8A**). Incidentally, reshaping of the nanoparticles can be noticed during the whole growth process, resulting in a progressive blueshift for all three samples, which is more pronounced for longer pre-reduction times. In addition, detailed shape inspection of the particles at stage *a* clearly showed that the nanorods obtained at longer pre-reduction times display a certain dumbbell-like morphology (**Figure II.8B**). Therefore, we postulate that the deviation from the ideal rod-like morphology is somehow correlated to the growth rate, and that this affects the final AR of the nanorods.

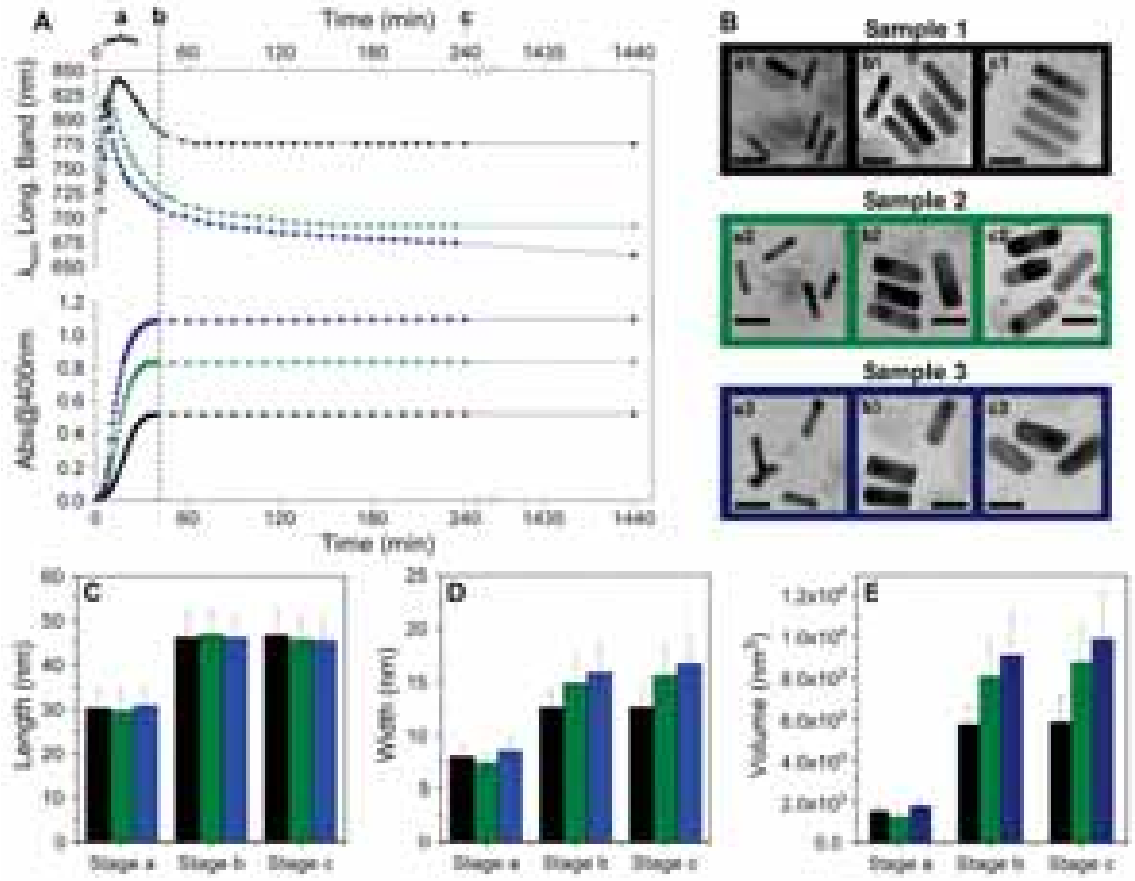

Figure II.8. Effect of the pre-reduction on the growth kinetics. A: Time traces of the longitudinal LSPR and the absorbance at 400 nm during the growth of gold nanorods after different pre-reduction times. Pre-reduction was stopped at Abs_{396nm} = 0.75 (sample 1, black), 0.45 (sample 2, green) and 0.20 (sample 3, blue). The vertical dashed line indicates the moment at which no further gold reduction was observed, whereas a, b and c correspond to the times at which the growth was arrested by thiol addition. **B:** TEM images for the three samples collected after addition of dodecanethiol. The labels indicate the different times at which growth was arrested (a, b, c) for each sample (1, 2, 3). Scale bars: 30 nm. **C-E:** Histograms relative to TEM analysis of length (**C**), width (**D**) and volume (**E**) for each sample (1 black, 2 green and 3 blue bars) and for each growth stage (a,b and c). The single particle volume is calculated from the average length and thickness obtained from TEM images (150 particles).

To further confirm the above conclusion, we devised a new set of experiments in which the concentration of AA was adjusted as a function of pre-reduction time, so that the total amount of electrons used in the reduction was fixed (**Figure II.9**). For example, when the pre-reduction time is increased, the fraction of Au(III) reduced to Au(I) by 5-BrSA is increased; from the absorbance at 396 nm we estimated the number of electrons corresponding to this increment and, according to this value, we reduced the amount of

added AA corresponding to the same number of electrons, keeping constant the total amount available for growth. For four different experiments, we found that both the AR and the kinetics of reduction and growth remain unchanged, i.e. the kinetic evolution of the absorbance at 400 nm and the longitudinal LSPR follow the same trend (**Figure II.9**). These results point again toward the importance of the growth rate to tune the final AR: by modifying the amount of AA to compensate the different extent of pre-reduction, identical initial conditions for nanorod growth were reproduced, and thus the same final product was obtained.

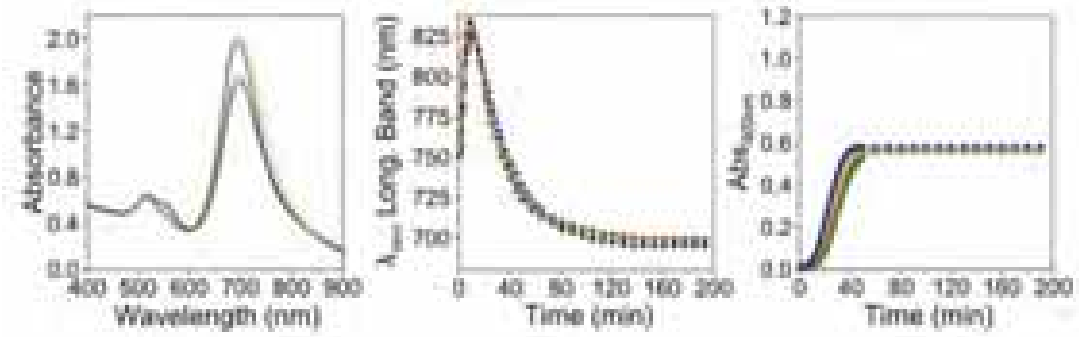

Figure II.9. Growth with a fixed total amount of electrons. UV-vis analysis (left panel) and time evolution of the longitudinal LSPR (central panel) and of the absorbance at 400 nm (right panel), relative to the experiment performed adjusting the amount of AA to the pre-reduction step. Growth started at Abs_{396nm}= 1.5 (black), 1.2 (blue), 0.7 (green), 0.5 (orange); the added volumes of AA 0.1M were 43.5µL, 37µL, 26µL, 21.5µL, respectively. All samples showed the same evolution, i.e. the same kinetics of reduction and growth and the same final AR.

One important point needs be clarified yet: one may claim that the tunability shown in **Figure II.7** can be only apparent, and in particular just correlated to the different yield in Au(0). Thus, to complete gold reduction and push all the samples to the same total amount of gold reduced, we added an additional amount of AA. Using again the correspondence between absorbance 1.2 at 400 nm and complete gold reduction (0.5 mM, see section II.2.4), the precise amount of AA that is required to complete gold reduction can be calculated (assuming a quantitative two-electron reaction). We exemplify this process with three different samples (prepared with different pre-reduction times) containing known amounts of unreacted Au(I), to which we added the corresponding amount of AA without any prior

washing. All three samples were indeed found to reach the same expected final absorbance at 400 nm of 1.2 (**Figure II.10A**). We also confirmed that, even when a significant excess of AA (up to 35%) was added, no further reduction was achieved (Abs_{400} did not increase). Additional confirmation was provided by calculation of the average nanorod volumes calculated from the dimensions determined by TEM (**Figure II.10B**). As expected, the volume increase was proportional in all cases to the amount of initially unreacted Au(I), and the final volume was equal for all samples, even though the AR was different (**Figure II.10C**). This indeed demonstrates that the tunability of the AR shown in **Figure II.7** was not an artifact created by the different yields in Au(0), and supports the assumption that the number of grown particles is related to the amount of seeds, regardless of other synthetic conditions. It is important to underline here that this possibility cannot be obtained just by changing AA concentration: in fact, in the standard synthesis the range of AA concentrations that lead to high yield and uniform nanorod is very narrow; moreover the final absorbance at 400 nm cannot be tuned in such a wide range.[69,143] In this respect, the two-reducing-agents system offers the chance to tune the final AR and Au(0) concentration by simply monitoring and selecting the pre-reduction step, thus resulting in a significant improvement of the reproducibility of the synthetic protocol.

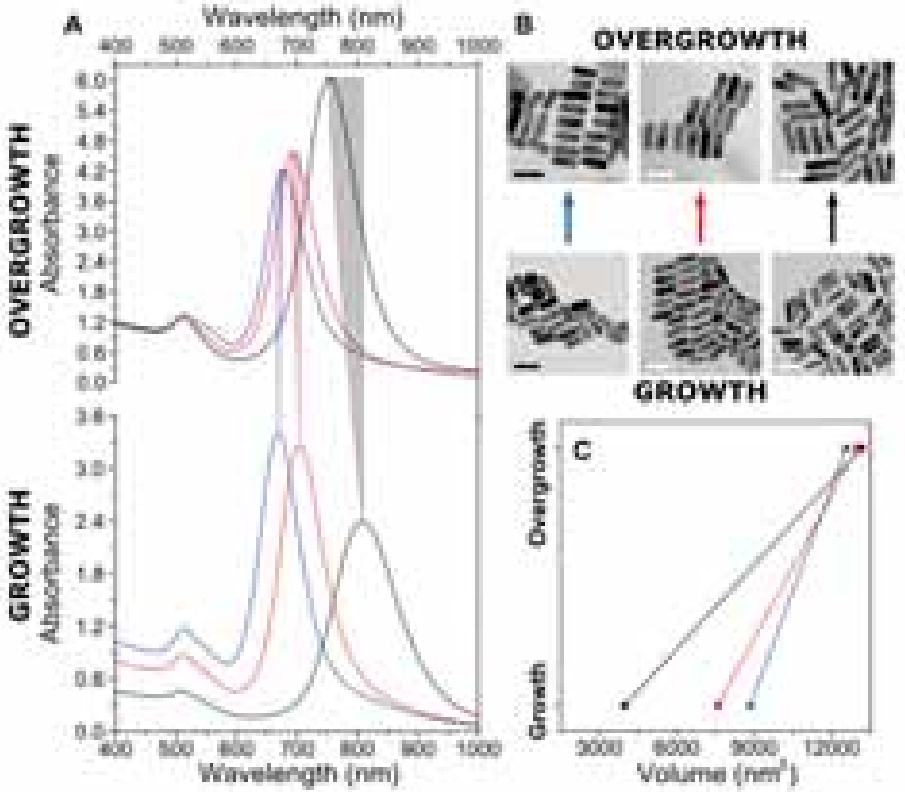

Figure II.10. Reduction of unreacted Au(I). A: UV-vis spectra, **B:** TEM images and **C:** average single nanorods volume registered after the addition of AA to three nanorod solutions prepared with different pre-reduction times as defined by Abs_{396nm}: 0.88 (black), 0.44 (red), 0.23 (blue). Note that the absorbance at 400 nm and the average single nanorod volume match upon overgrowth, whereas the longitudinal LSPR bands do not overlap. Scale bars: 50 nm. UV-vis spectra were multiplied by the corresponding dilution factor.

It is also important to study the effect of 5-BrSA concentration. The reduction rate of Au(III) to Au(I) decreases for lower 5-BrSA concentration, but tracking the reduction through the absorbance at 396 nm allowed us to initiate the reduction of Au(I) to Au(0) – upon AA addition – at the same starting conditions, i.e. the same amount of consumed electrons. This means that the pre-reduction time can be considered constant, as well as the concentration of AA. We carried out three experiments in which the concentrations of 5-BrSA were: 4.1, 2.3 and 0.9 mM. Whereas the absorbance at 400 nm reached the same value, the final position of the longitudinal plasmon band is shorter for lower concentrations of 5-BrSA (**Figure II.11A, C**). The nanorod dimensions confirmed the trend observed in the optical properties, indicating that smaller amounts of 5-BrSA lead to nanorods with a lower AR (**Table II.2**).

Once again, the reduction ends before the blueshift does, confirming the coexistence of isotropic growth and reshaping. TEM analysis upon thiol addition (**Figure II.11B**) confirmed that the initial well-defined nanorods (a1, a2, a3) progressively grow (volume increase) until the end of the reduction step (b1, b2, b3), after which the average volume per particle remains constant (c1, c2, c3; and **Figure II.11D**). Importantly, we observed that 5-BrSA also affects the reduction rate of Au(I) to Au(0). This effect cannot be explained with a change in the pH of the solution, since the difference is always lower than 0.35 pH units. Thus, besides changing the number of electrons provided to the system, larger amounts of 5-BrSA were also found to lead to a decrease in the rate of gold reduction (**Figure II.11A**). This suggests that 5-BrSA actively contributes to the growth, thereby revealing its role as co-factor. In fact, Murray and co-workers[136] attributed the role of salicylic acid to stabilization of the CTAB bilayer by the negatively charged aromatic additives. Molecular interactions between small additives and surfactant molecules facilitate the intercalation of such additives in the surfactant bilayer, which in turn improves its compactness. In such a scenario, the decrease of available catalytic surface slows down the overall reduction rate. We propose that tightly organized molecules on the lateral nanorod faces prevent mass transport (of metal salt) through the bilayer, thereby facilitating preferential metal reduction on the tips, and promoting anisotropic growth. This argument may also explain how oleic acid can help creating more robust systems that can stand different synthetic conditions, thereby leading to different sizes, ARs (or shapes) and crystallographic habits of the nanoparticles.[134]

Table II.2. TEM analysis details of the samples shown in **Figure II.11**. The AR decreases with [5-BrSA] due to a decreased length and an increased thickness. The data reported are the average of 150 measured nanorods.

	Sample 1 ([5-BrSA] = 4.1mM)	**Sample 2 ([5-BrSA] = 2.3mM)**	**Sample 3 ([5-BrSA] = 0.9mM)**
Length	53 ± 6	50 ± 4	43 ± 3
Thickness	16 ± 3	17 ± 3	17 ± 2
AR	3.3 ± 0.5	2.9 ± 0.4	2.6 ± 0.3

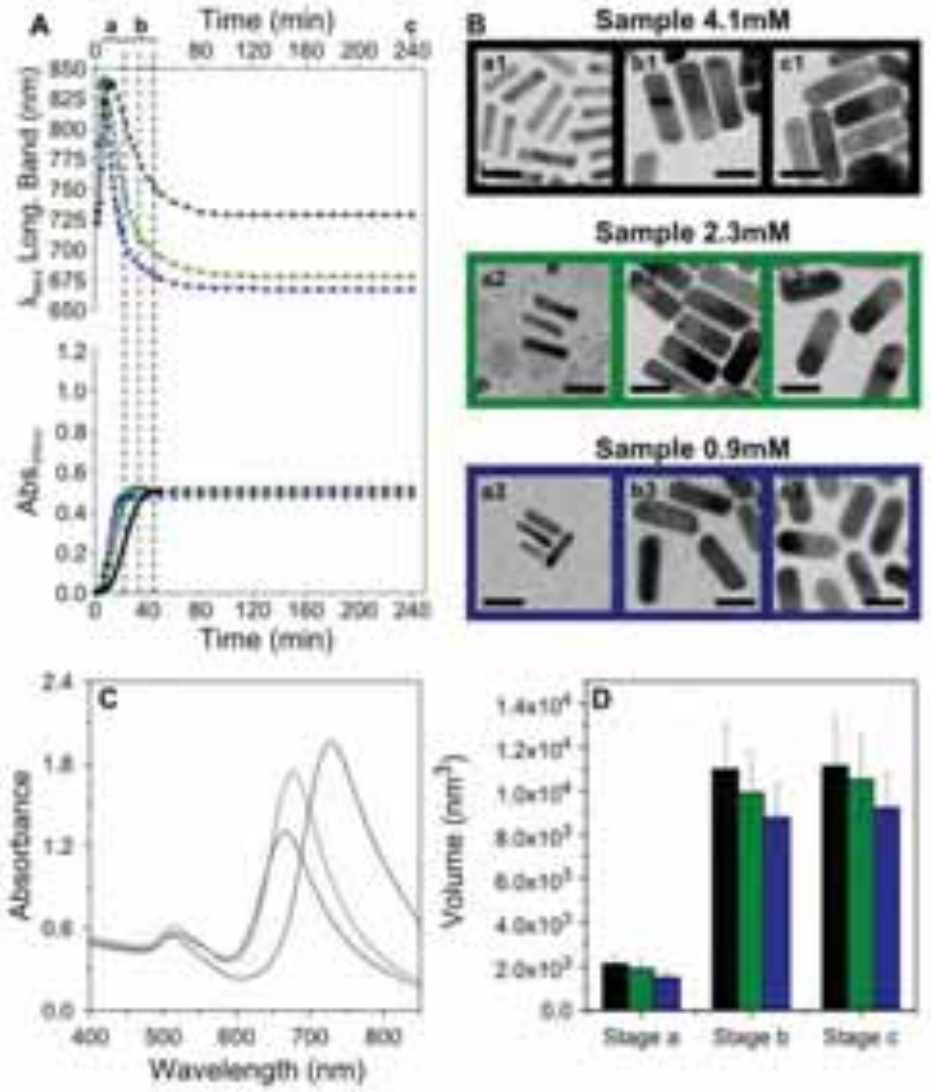

Figure II.11. Effect of 5-BrSA concentration. A: Time traces of the longitudinal LSPR and absorbance at 400 nm during the growth of gold nanorods using different 5-BrSA concentrations. [5-BrSA] = 4.1 mM (1, black), 2.3 mM (2, green) and 0.9 mM (3, blue). The three vertical dashed lines indicate the times at which no further gold reduction is observed for each sample, whereas a, b and c correspond to the times at which the growth was arrested by thiol addition. **B:** Representative TEM images for the three samples, collected after addition of dodecanethiol. The labels identify the three times at which the synthesis was stopped (a, b, c) and the imaged sample, 4.1 mM (1), 2.3 mM (2), 0.9 mM (3). Scale bars: 30 nm. **C:** UV-vis analysis of the three samples: 1 black, 2 green and 3 blue. **D:** Histograms relative to single particle volume analysis for each sample (1 black, 2 green and 3 blue bars) and for each growth stage (a, b, c). The single particle volume is calculated from the average length and thickness obtained from TEM images (150 particles).

II.2.8.1.1. Overgrowth

We identify as a major advantage of using 5-BrSA its inability to reduce Au(I) into Au(0), even in the presence of gold seeds. Therefore, solutions can be prepared containing Au(I) (complexed to CTAB) and chemically stable Au(0) seeds, thereby avoiding the problem of eventual comproportionation reactions, which lead to the dissolution of metallic gold particles when mixed with Au(III)-CTAB.[100,141,144] In this way, experimental protocols for the synthesis of core-shell nanoparticles can be facilitated. We demonstrate this by using preformed nanorods as seeds for additional growth (Overgrowth). The experimental procedure (see **Scheme II.2**) comprises the dispersion of gold nanorods in an overgrowth solution prepared by complete pre-reduction of Au(III) to Au(I) with 5-BrSA, followed by addition of AA. Note that the dispersion containing gold nanorods and Au(I) can be stored over extended periods of time without any sign of nanorod oxidation.

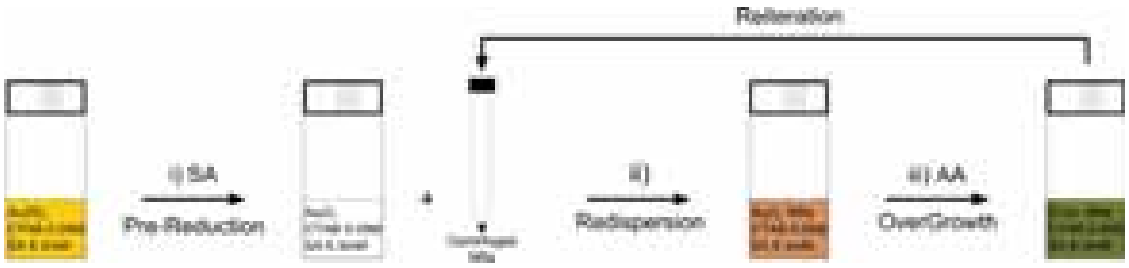

Scheme II.2. Description of the nanorods overgrowth process.

We exploited this possibility to further control the LSPR shift during overgrowth. In particular, we compared the influence of Ag^+ ions on the overgrowth process (**Figure II.12**): three solutions of nanorods with different ARs were centrifuged and redispersed in two different solutions of Au(I), one of which contained Ag^+ (0.096 mM); the amount of gold was the same as that used for initial nanorod growth (25 μmol of $HAuCl_4$), i.e. the concentration needed to reach an optical density of 1.2 at 400 nm. We observed in both cases a blueshift of the longitudinal LSPR, though not in the same extent, indicating that the AR of the resulting nanorods was higher in the presence of Ag^+, which was confirmed by TEM analysis, showing in this case longer and thinner nanorods (**Figure II.12** and **Table II.3**). This methodology offers the possibility of being implemented in multiple cycles, thereby opening new possibilities for tuning the dimensions of the nanorods.

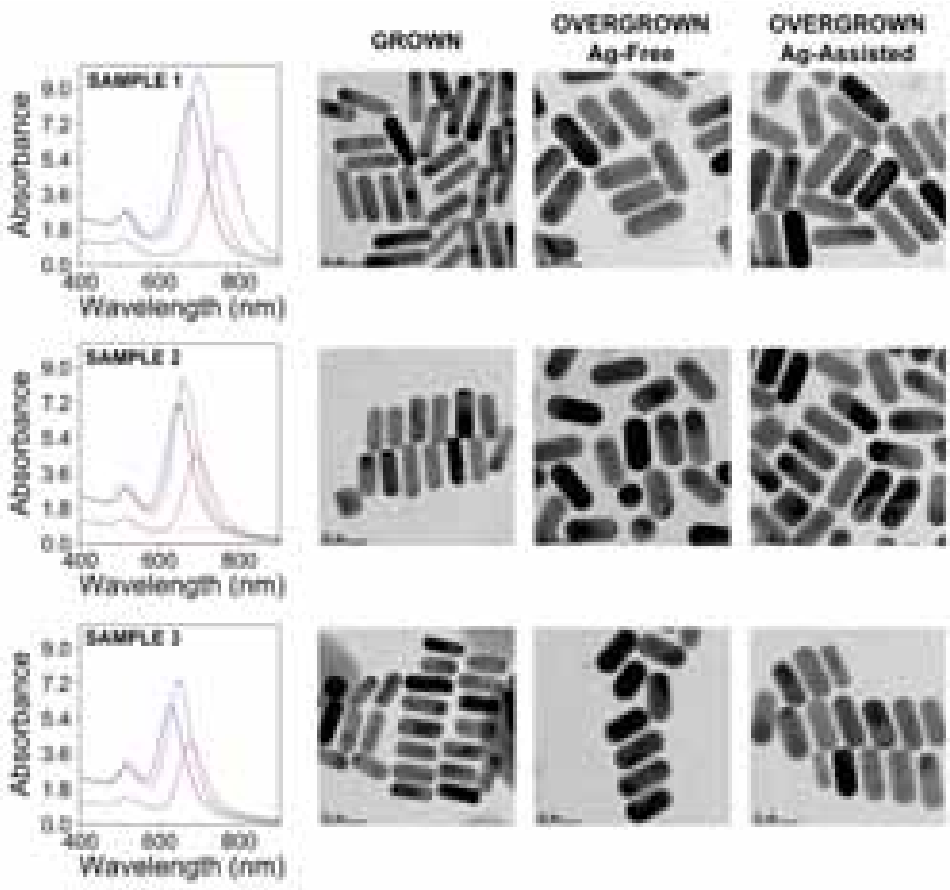

Figure II.12. Effect of Ag^+ on the overgrowth of gold nanorods. UV-Vis-NIR spectroscopy (left column, for the original sample (red line) and those overgrown under silver-assisted (pink line) and silver-free (blue line) conditions) and TEM analysis of the grown (second column), overgrown under silver-free (third column) and silver-assisted (right column) conditions, for three samples prepared using different pre-reduction times. Sample 1 (Abs_{396nm} = 0.80; top), Sample 2 (Abs_{396nm} = 0.44; middle) and Sample 3 (Abs_{396nm} = 0.23; bottom).

Table II.3. Details of TEM analysis of the samples summarized in **Figure II.12**. The data shown are the average over 150 particles, and are expressed as length, thickness and AR, each with its corresponding standard deviation.

	Sample 1	**Sample 2**	**Sample 3**
Grown (complete reduction)	58±4, 17±1, 3.5±0.4	51±4, 18±1, 2.8±0.3	47±3, 18±2, 2.6±0.3
Overgrown Ag-free	65±4, 24±1, 2.7±0.2	58±3, 26±1, 2.3±0.2	54±3, 26±2, 2.2±0.2
Overgrown Ag-assisted	68±4, 22±1, 2.9±0.2	60±4, 24±1, 2.5±0.2	57±3, 23±2, 2.4±0.2

II.2.8.1.2. Multicycle Silver-Free Overgrowth

The result of several growth cycles on preformed nanorods is depicted in **Figure II.13**. It can be clearly observed that after four overgrowth cycles performed under silver-free conditions the nanorods became essentially isotropic (**Figure II.13C**). The spectral evolution (**Figure II.13A**) agrees with that previously reported for a rod-to-octahedron transition,[112,145] which was again confirmed by TEM, showing a gradual increase in particle size (**Figures II.14 - 16** and **Table II.4**). It is important to note that the absorbance at 400 nm increases by 1.2 after each overgrowth cycle (up to 2.4, 3.6, 4.8 6.0), evidencing quantitative reduction of all additional gold ions in the growth solution.

II.2.8.1.3. Multicycle Silver-Assisted Overgrowth

When overgrowth was performed under standard silver-assisted conditions, the AR decreased from 3.0 to 2.4 after two cycles, but it then remained constant around this value (**Figure II.13C**). Optical analysis showed that the longitudinal LSPR remained around 700 nm despite of the increase in nanorod volume (**Figure II.13B, Figures II.14 - 16** and **Table II.4**). An additional observation concerns the ratio between longitudinal and transverse plasmon bands, since the band centered at 530 nm shows a significant absorbance increase. This can be rationalized considering two factors: first of all the larger diameter of the nanorods has been demonstrated by calculations to increase the contribution of the transverse LSPR to the optical profile.[146] Additionally, the samples were not purified prior to overgrowth, so that spherical impurities were overgrown along with the nanorods, thereby increasing their contribution to the absorbance of the low wavelength band. The stabilization of the AR points toward preferential adsorption of Ag^+ ions on the side facets of the growing nanoparticles, thereby enhancing the stability of the rod-like morphology. This can explain why the yield in nanorod formation increases when Ag^+ is added to the growth solution, and why under typical synthetic conditions it is difficult to obtain nanorods with high AR values, as compared to silver-free synthesis,[8] but additional experimental evidences may be needed to elucidate this point. The protocol we propose here sets no limitations on the composition of the overgrowth solution, and thus can in principle be applied to nanoparticles with different shapes or compositions, to ultimately tune their optical properties, size and morphology or to easily access bimetallic systems.

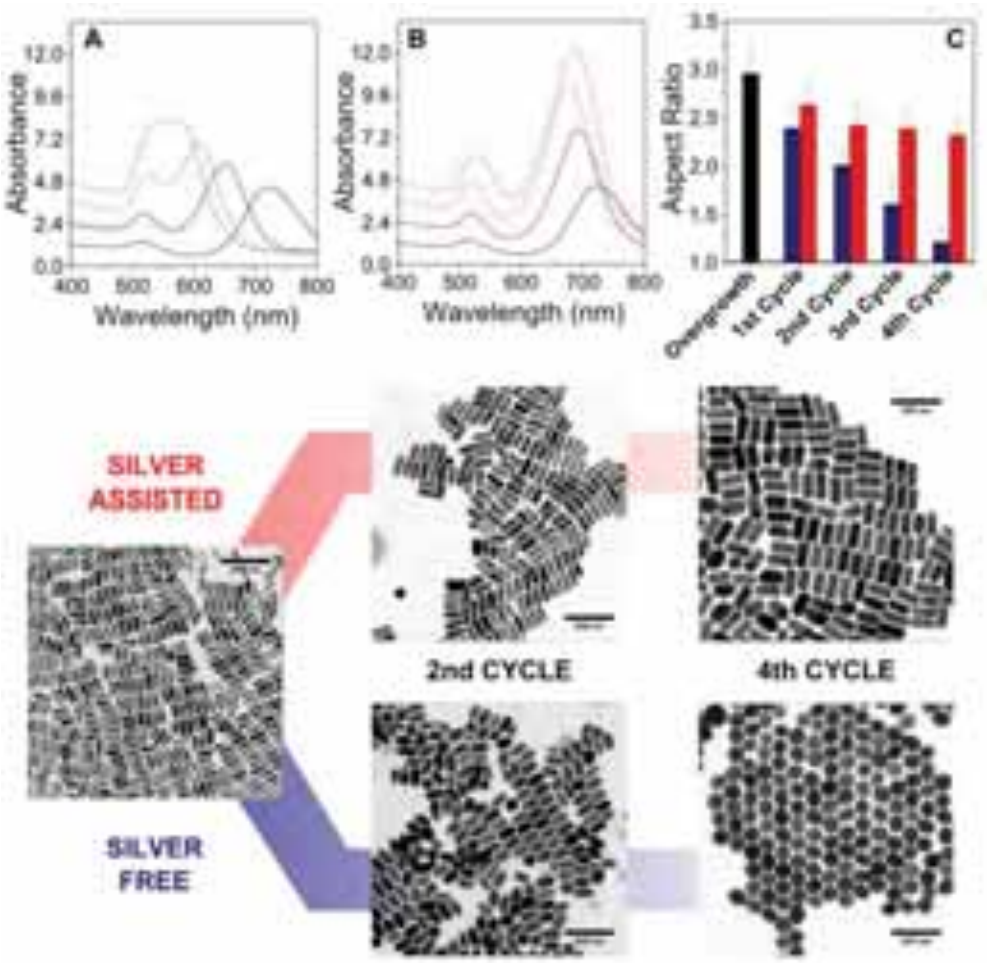

Figure II.13. Upper Panel: UV-vis-NIR spectra after each overgrowth step. **A:** Silver-free system; **B:** Silver-assisted system. The black spectra correspond to the common starting point for the overgrowth reactions (UV-vis spectra were multiplied by the corresponding dilution factor). **C:** Evolution of the AR for each overgrowth cycle in both silver-free (blue) and silver-assisted (red) systems. **Lower Panel:** TEM images showing the shape evolution from the initial sample (central-left image) after two and four cycles for silver-free (blue line) and the silver-assisted (red line) conditions. Scale bars: 200 nm.

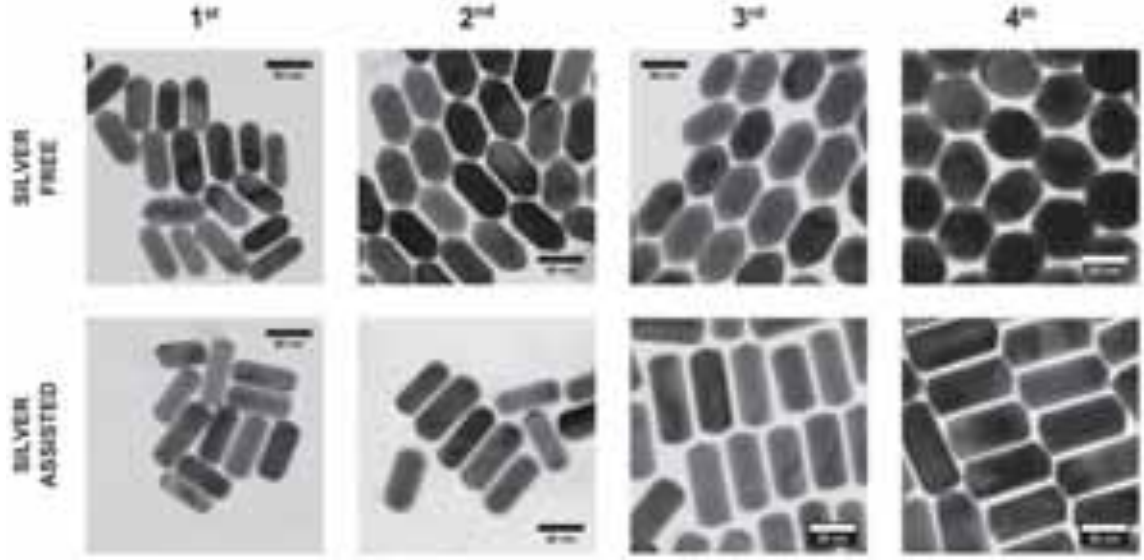

Figure II.14. Representative TEM images obtained at 100,000× magnification of the Multistep Overgrowth Experiment. The columns represent the different generations; the first row refers to silver-free conditions, the second row to silver-assisted ones.

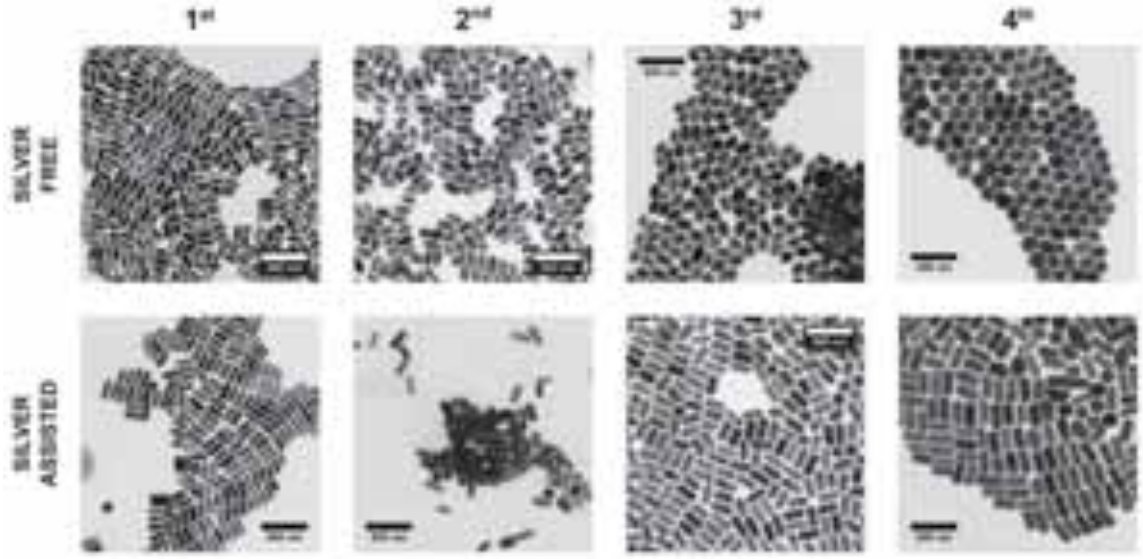

Figure II.15. Representative TEM images obtained at 25,000× magnification of the Multistep Overgrowth Experiment. The columns represent the different generations; the first row refers to silver-free conditions, the second row to silver-assisted ones.

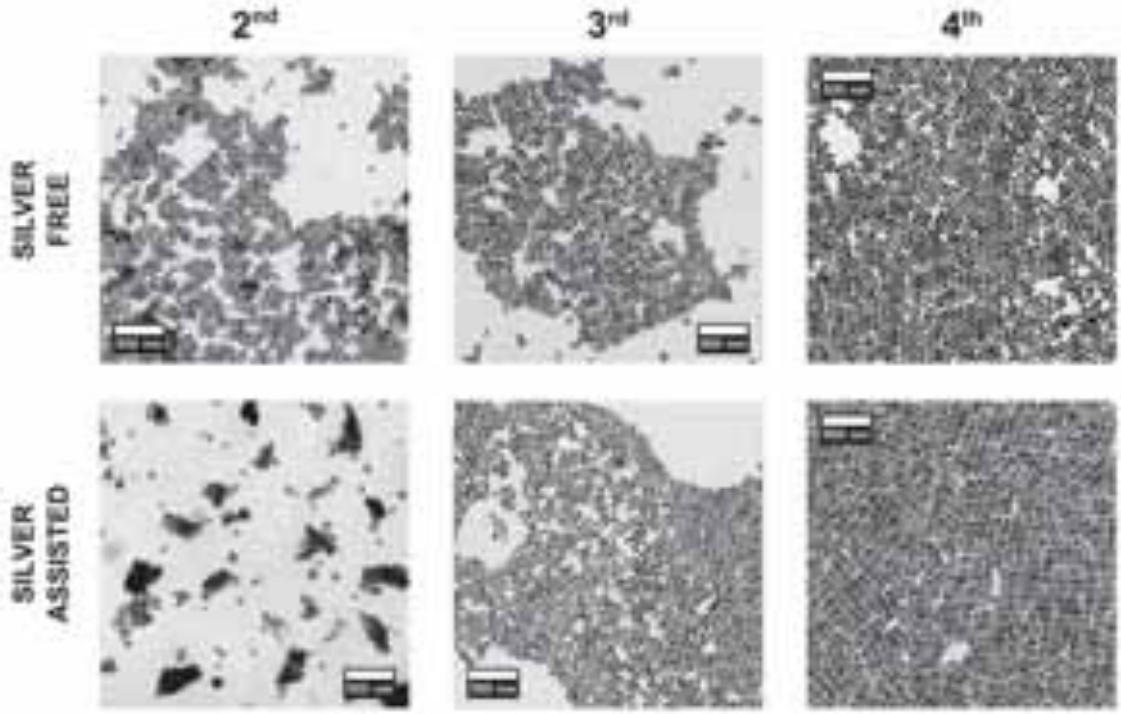

Figure II.16. Representative TEM images obtained at 8,000× magnification of the Multistep Overgrowth Experiment. The columns represent the different generations; the first row refers to silver-free conditions, the second row to silver-assisted ones.

Table II.4. Details of TEM analysis for the samples summarized in **Figure II.14-16**. The data shown are the average over 150 particles, and are expressed as length, thickness and AR, each with its corresponding standard deviation.

	Grown (common)	**1st Cycle**	**2nd Cycle**	**3rd Cycle**	**4th Cycle**
Ag-free	62±5, 21±2, 3±0.3	68±6, 29±2, 2.4±0.2	72±6, 36±3, 2.0±0.2	72±7, 46±6, 1.6±0.3	73±5, 61±6, 1.2±0.2
Ag-assisted		71±6, 27±3, 2.6±0.3	79±7, 33±3, 2.4±0.2	87±7, 37±2, 2.4±0.2	98±6, 43±2, 2.3±0.2

II.2.8.1.4. Conclusions

We have systematically studied the effect of 5-BrSA on the synthesis of gold nanorods, both as stabilizing co-factor and as pre-reducing agent. We showed that this two-reducing-agents system offers new possibilities toward tailoring the morphology and the optical properties of gold nanorods. We also showed that there is a direct relationship between the reduction yield and the total amount of electrons supplied to the system, thus demonstrating the possibility of quantitative gold reduction in silver-mediated nanorod synthesis. Our observations indicate that 5-BrSA influences the growth reaction both thermodynamically and kinetically, inhibiting the isotropic growth that contributes to the typically observed blueshift in gold nanorods synthesis. These results underline that the growth rate is an extremely important parameter in determining the morphology of the synthesized particles, in line with what has been recently proposed in the literature.[12,147,148] When reduction is not completed during synthesis, the system can be pushed into complete reduction through the addition of AA, without losing the possibility to tune the AR of the nanorods. Apart from the new mechanistic insights of these results, the reducing properties of 5-BrSA can be exploited to stabilize gold nanorods in Au(I) solution, thereby facilitating overgrowth. We demonstrated that overgrowth can be carried out in the presence of Ag^{+} ions, thereby stabilizing the anisotropy, i.e. avoiding a rod-to-octahedron transition, as registered in silver-free overgrowth. This suggests the possibility of tailoring the dimensions and optical properties of gold nanorods by selecting the appropriate conditions for overgrowth.

II.3. SYNTHESIS OF GOLD NANOTRIANGLES

Ultrasensitive detection,[149] metamaterials[150] and drug delivery[151,152] are prominent examples among a broad array of promising applications requiring a fine control on nanoparticle synthesis. Therefore, tuning the LSPR band position in the UV-vis-NIR region is the most important prerequisite for the successful application of a synthetic method.[48] In this context, gold nanotriangles stand out for their unique optical and plasmonic properties. However, the quality of available gold nanotriangles is still far away from that usually found for gold nanorods. The yield of common synthetic methods for gold nanotriangles is usually below 30 - 40% and the particles often show a broad size distribution. Indeed, in the existing synthetic protocols the nanotriangles usually have relatively big lateral dimensions,[45,153] and no synthetic protocols for the preparation of monodisperse gold nanotriangles below 100 nm are available in literature. Moreover, the stability of these nanoparticles against oxidation is low, and reshaping typically takes place few hours after their preparation.[154] All these factors have seriously hindered the application of gold nanotriangles for the development of plasmonic devices.

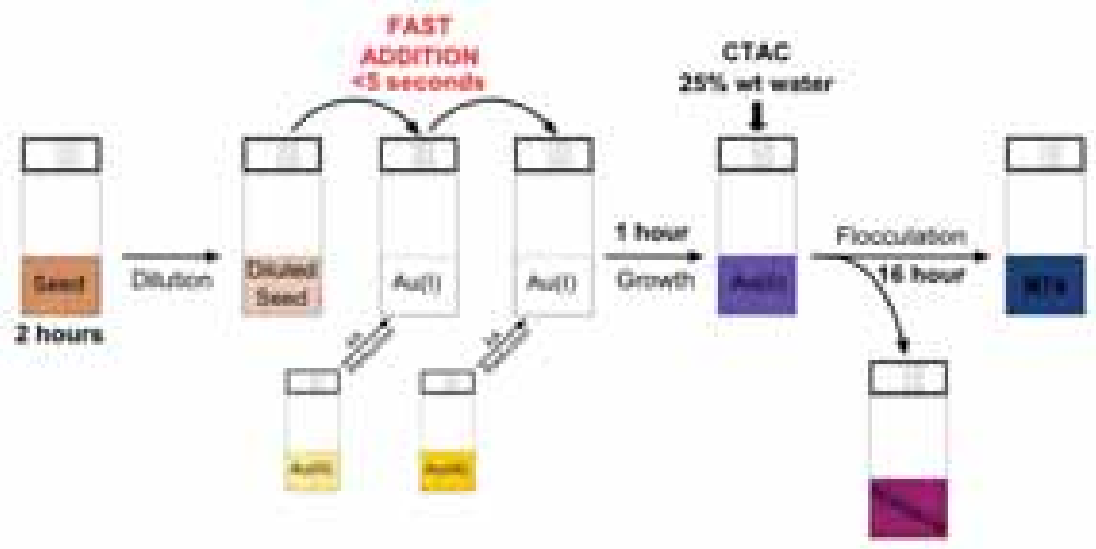

Scheme II.3: Scheme representing the overall procedure for the synthesis and purification of gold nanotriangles.

We demonstrate here that variations of these synthetic processes can yield gold nanotriangles with initial shape-yield higher than 50%, which can be further increased up to 95% after a

simple and fast purification step. This method additionally yields highly uniform gold nanotriangles, with a size dispersity down to 4%, and a wide tunability of the nanotriangle dimensions with edge lengths ranging from 50 to 150 nm, which translates into LSPR values from 630 to 740 nm. The proposed experimental approach for the synthesis of gold nanotriangles involves three consecutive steps: 1) generation of CTAC coated gold seeds, 2) fast addition of the generated seeds to a final growth solution and, 3) purification of the products (see **Scheme II.3**).

II.3.1. Synthesis of Gold Nanotriangles

The synthesis of gold nanotriangles is based on the seed mediated growth originally proposed by Mirkin and coworkers.[12] In this method, the presence of iodide anions in a silver-free growth solution triggers the anisotropic growth of the CTAC coated seeds. The initial gold seeds with a size of ca. 7 nm are first overgrown up to 40 nm in an intermediate growth step, and subsequently transferred to the final growth solution, yielding an overall shape-yield around 30%, with rather high size dispersity. Interestingly, we demonstrate that the shape-yield and size uniformity of the nanotriangles were significantly improved by overgrowing the seeds in the presence of iodide prior to transfer into the final growth solution, before the reaction was completed. It is important to mention at this point that in previous reports size tunability by overgrowth reactions was limited by the initial particle size, which was typically above 150 nm.[153] In the present work, small gold nanotriangles with edge lengths down to 60 nm were obtained for the first time, thereby leading to a significant improvement in size-tunability. This synthetic scheme comprising two growth steps is similar to that proposed by Jana and Murphy in 2001 for the early synthesis of gold nanorods,[155] in which the particles were transferred while the "intermediate" growth was still ongoing. Furthermore, the yield in nanotriangles was significantly increased (above 50%, **Figure II.17A, E - F**) by the "fast seed addition" and other modifications described in more detail in the Experimental Section (see section II.5.3.2.). The gold nanotriangles obtained in this way are considerably smaller (edge length 71±3 nm, **Figure II.18C**) and characterized by a low size dispersity (below 6%, see **Figure II.17E - F** and **Figure II.18**). High resolution TEM (HR-TEM) confirmed the {111} nature of the planar facets of the gold nanotriangles

(**Figure II.17D**). High resolution SEM (HR-SEM) analysis revealed the presence of a twin plane parallel to the most extended facets, leading to the formation of nanotriangles with a truncated-bipyramid morphology (see **Figure II.17C**), where also the lateral facets are of the {111} family. Strikingly, the introduction of the fast addition during seed overgrowth does not seem to affect the reproducibility of the synthetic protocol, even when the synthesis was scaled up to 250 mL. Regarding the stability of the gold nanotriangles over time, UV-vis monitoring was carried out to detect optical changes in the nanotriangle solution. In contrast with previous reports, the gold nanotriangles presented here were stable for at least 3 months and no reshaping was observed.

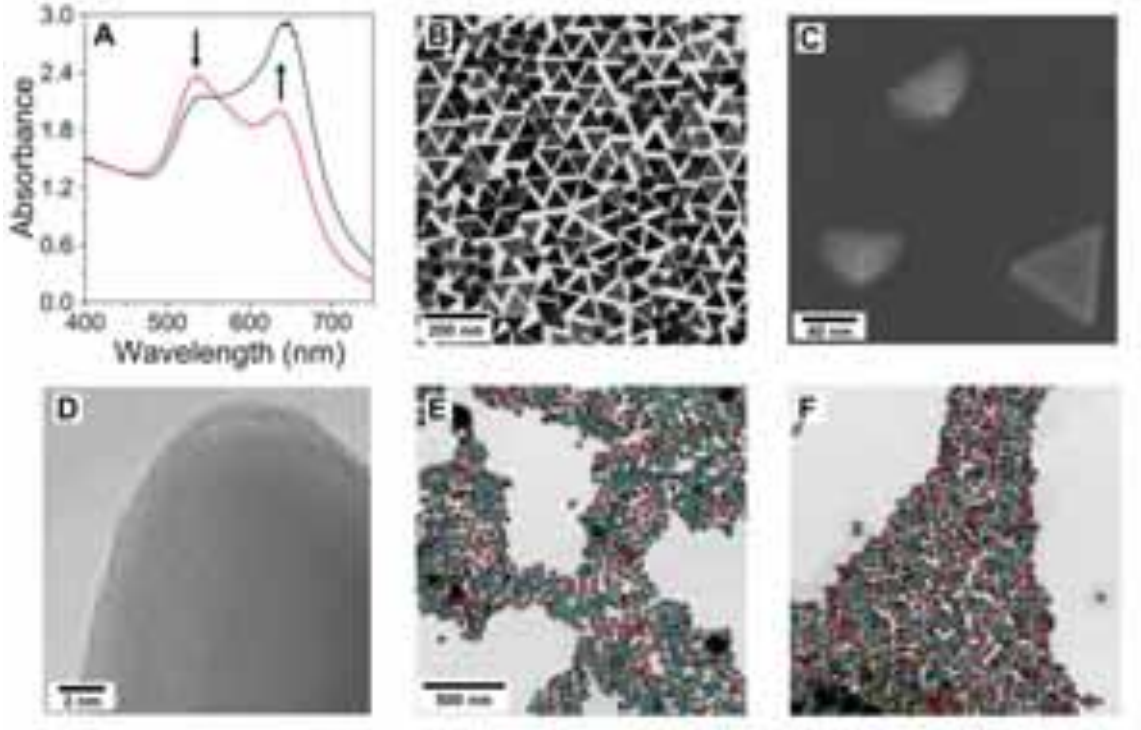

Figure II.17. Synthesis of gold nanotriangles. **A:** UV-vis spectra of samples obtained with (black line) and without fast addition (red line). Notice the different intensity ratio between the by-product band (isotropic nanoparticles, maximum around 520-530 nm) and the band corresponding to the nanotriangles (around 650 nm). **B:** TEM images of gold nanotriangles prepared with fast-addition. **C:** HR-SEM image of gold nanotriangles where a twin plane in the middle of the particle can be clearly distinguished. **D:** HR-TEM image of the area near a tip of an gold nanotriangle. **E-F:** TEM images of the products where the different shapes are labeled with different colors: by-products are labeled in cyan, horizontally positioned nanotriangles are labeled in red and vertically positioned nanotriangles (see below) are labeled in yellow. The scale bar is the same for both images. The shape yield of nanotriangles is 61.4% and 53.3% for **E** and **F**, respectively.

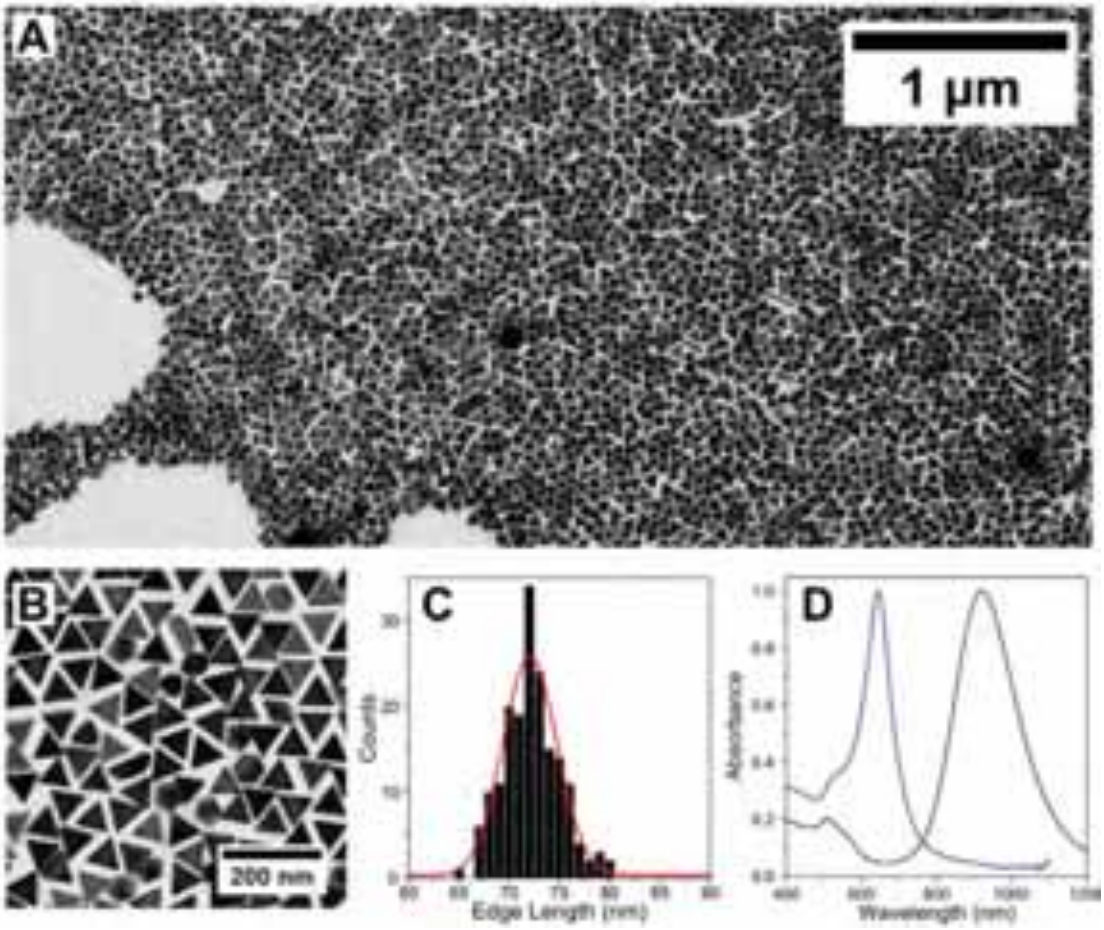

Figure II.18. A-B: TEM images of gold nanotriangle samples obtained by the synthesis procedure described without any further purification. **C:** dimension analysis (on 200 nanotriangles). **D:** comparison of the UV-vis spectra of nanotriangles (purified, section II.3.2) and nanorods (prepared by standard CTAB-Ag mediated synthesis[156]); the narrower band width for nanotriangles can be clearly appreciated.

Although a complete comprehension of the growth mechanism is beyond the aim of this work, our observations lead to some interesting reflections. The first observation is that, following the original procedure proposed by Mirkin et al., the seed overgrowth step is central for the formation of gold nanotriangles. In fact, in a control experiment where this step was skipped, both UV-vis and TEM analysis confirmed that almost no gold nanotriangles were obtained (**Figure II.19A - B**). Yet, what makes this step crucial is not clear - Is the growth pathway just influenced by the increased size of the seed? Does the different crystallographic structure of the bigger particles play a relevant role? Or do both

phenomena contribute equally? We found that the fast addition introduced here prevents the seed from growing completely prior to transfer into the growth solution, which suggests that the size of the particles used as seeds is not a crucial parameter, or at least that it is not the only one. Additionally, we achieved a significant increase in shape-yield by introducing a small amount of iodide in the overgrowth medium (see Experimental Section, section II.5.3.2.). Therefore, our experimental data suggest that this intermediate step may be relevant for the modification of the crystallographic structure of the seeds, which is crucial for the required symmetry breaking event.[65,100] This effect can be somehow verified by analyzing the overgrown seeds by both UV-vis spectroscopy and TEM analysis. A clear redshift of the plasmon band can be observed when iodide ions are present in the overgrowth medium (**Figure II.19C**), and we found a significant amount of seeds with triangular shape (**Figure II.19D - E**). To further confirm our observations, we directly synthesized the initial seeds in the presence of iodide. Interestingly, using these seeds, the overgrowth step is not necessary to achieve a final triangular shape, even if the quality of the sample in terms of size distriution is strongly affected (**Figure II.19F - G**). It is important to underline that, even though our results are not exhaustive, it is obvious that iodide has a strong effect on the shape of the seeds and on their further growth, which is essential to drive the symmetry breaking event towards the development of a triangular shape.

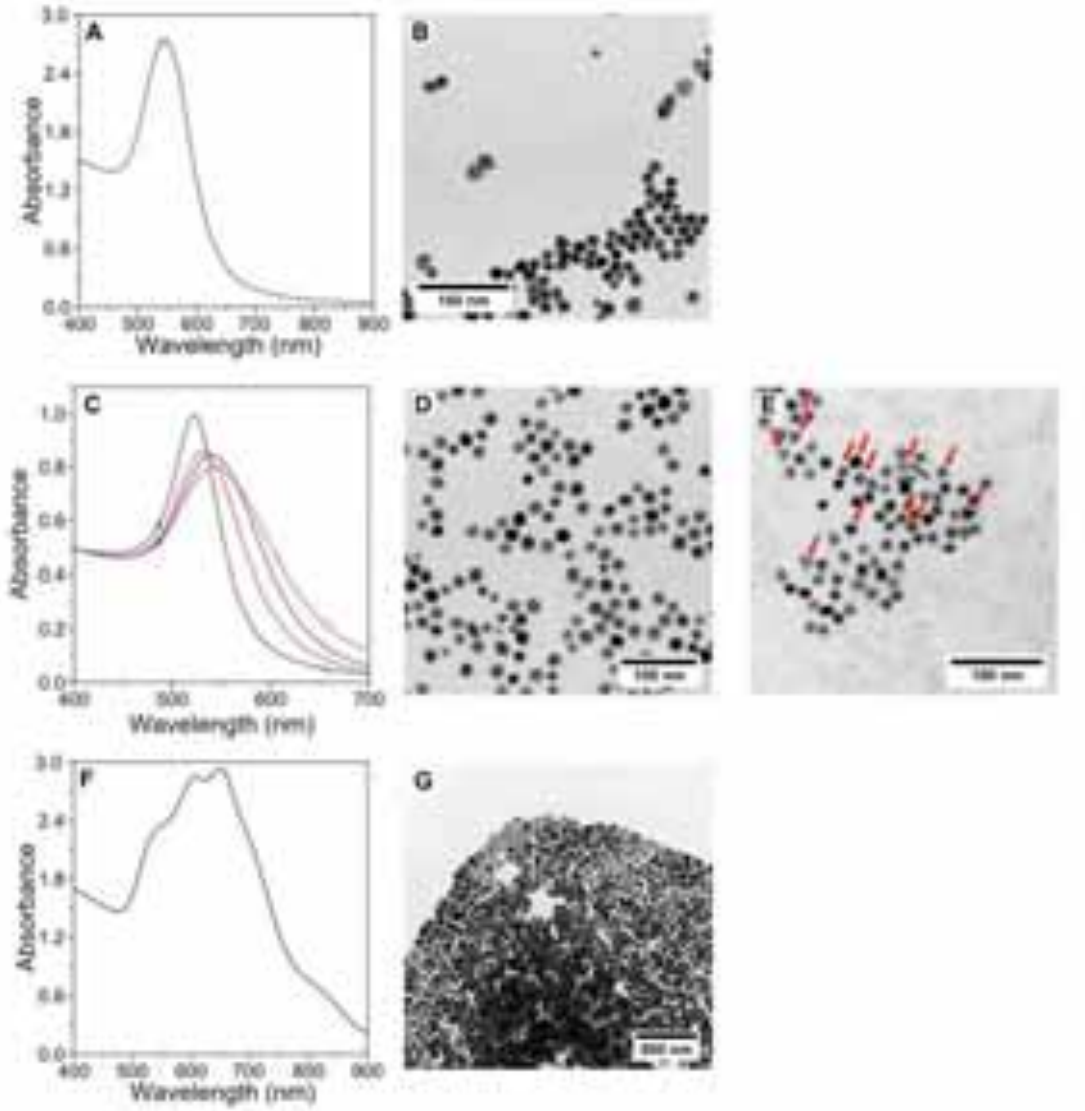

Figure II.19. Iodide effect on seed overgrowth. A: UV-vis spectrum of a gold nanotriangles solution grown using the initial seed@CTAC. Note that seeds were not overgrown. **B:** Representative TEM image of the same solution. **C:** UV-vis spectra of the fully overgrown seeds in the presence of different amounts of a 0.01 M NaI solution: 0 μL (black line), 15 μL (red line), 30 μL (blue line) and 60 μL (pink line). **D:** TEM image of seeds overgrown in the absence of iodide. **E:** TEM image of seeds overgrown in the presence of 60 μL of a 0.01 M NaI solution (pink line in **C**); seeds that clearly show a triangular shape are labeled with red arrows. **F:** UV-vis spectrum of an gold nanotriangles solution that was grown using seed@CTAC prepared in the presence of iodide. Note that seeds were not overgrown. **G:** Representative TEM image of the same solution, where triangular nanoparticles can be observed, but with a wide size distribution.

II.3.2. Nanotriangles Purification

Although both the yield and size distribution of the gold nanotriangles were improved by this synthesis method, still a significant amount of by-product particles are present, which may hinder the direct use of these nanotriangles for applications that require very high particle quality and narrow plasmon resonances. Several purification methods have been proposed,[157] including centrifugation,[158] electrophoresis,[159] selective oxidation[144] and depletion interaction forces.[160–162] Among these, the latter presents numerous advantages, as it can be readily scaled up, it is both shape and size selective, relatively fast and highly efficient. Depletion forces are attractive in nature but their origin is not particularly intuitive. They arise when colloidal particles are suspended at low concentration, in the presence of a more abundant population of smaller solutes (termed "depletant"), which are excluded from the space in between the larger particles, thereby reducing configurational entropy. In a nanoparticle colloidal suspension, surfactant micelles can be used as the depletant, creating an attractive force defined as:

$$|U| = \frac{2 \cdot r_m \cdot A \cdot N_{AV} \cdot (C - C_{cmc})}{AN} k_B T \quad \textbf{[II.4]}$$

where r_m, C_{cmc}, C and AN are the radius, the critical micelle concentration, the analytical concentration and the aggregation number of the surfactant, N_{AV} is Avogadro's number, and A is the area of interaction between two adjacent particles. In this way, nanoparticles with different size and shape can be selectively precipitated by changing the concentration of the surfactant.[81] This approach presents two important benefits: 1) the stability of the gold nanotriangles is not compromised at high CTAC concentrations (Indeed, CTAC can even enhance their stability), and 2) centrifugation is not necessary due to the nature of the CTAC stock solution (see Experimental Section at section II.5.1). This two highlighted aspects allowed us to purify gold nanotriangles in a simple and not time consuming way. Different CTAC concentrations were explored to find the optimal purification conditions, in which a high purity of the precipitate is achieved along with a good purification yield, i.e. a large proportion of the initial nanotriangles are precipitated. The results are summarized in **Figure**

II.20. The separation of the by-product (mainly isotropic particles) can be clearly appreciated by a significant color change of the solution from dark blue to indigo. Moreover the purification is highlighted by the change in intensity ratio between the two LSPR bands: indeed, the band centered at 520-530 nm (typical of isotropic particles) significantly decreased. The optimal procedure was found to correspond to a CTAC concentration of 0.15 M. As shown in **Figure II.20**, 0.125 M CTAC leads to highly pure gold nanotriangles, but in an extremely low amount, while using higher CTAC concentrations (from 0.175 to 0.4 M), the separation was not completed. In addition, a second purification step can be carried out, but the increment in purification yield is negligible compared to the amount of nanotriangles found in the supernatant (**Figure II.20E - F**). TEM analysis confirmed the separation of nanotriangles: while the supernatant mainly comprised different quasi-isotropic particles (**Figure II.20B**), the purity level of nanotriangles in the precipitate was higher than 90% (**Figure II.20D** and **Figures II.21-22**). Interestingly, this purification procedure is extremely robust and efficiently working regardless of the original nanotriangle shape-yield achieved in the synthesis. Therefore, the overall process results to be robust and highly reproducible.
Equation **[II.4]** was adapted for gold nanotriangles: [161]

$$|U| = \frac{2r_m l^2 \sqrt{3} N_0 (c - cmc)}{4Q} \, k_B T \quad \textbf{[II.5]}$$

where the area of interaction of the two particles is equal to $\frac{l^2 \cdot \sqrt{3}}{4}$, with l the edge of one nanotriangle. The 0.15 M concentration that we selected as the best choice corresponds to a value of $|U|$ equal to 9.8 k_BT (literature values of 0.001 M, 120, and 3 nm were used for CTAC critical micelle concentration, aggregation number and micelle radius, respectively[163,164]). This value is almost double the predicted value of 4 - 5k_BT, as proposed by Park et al.[161] This difference can be explained considering that the sides of the nanotriangles are not perpendicular to the most extended crystallographic facets, i.e. using the TEM images as a reference, the area of interaction is significantly overestimated.

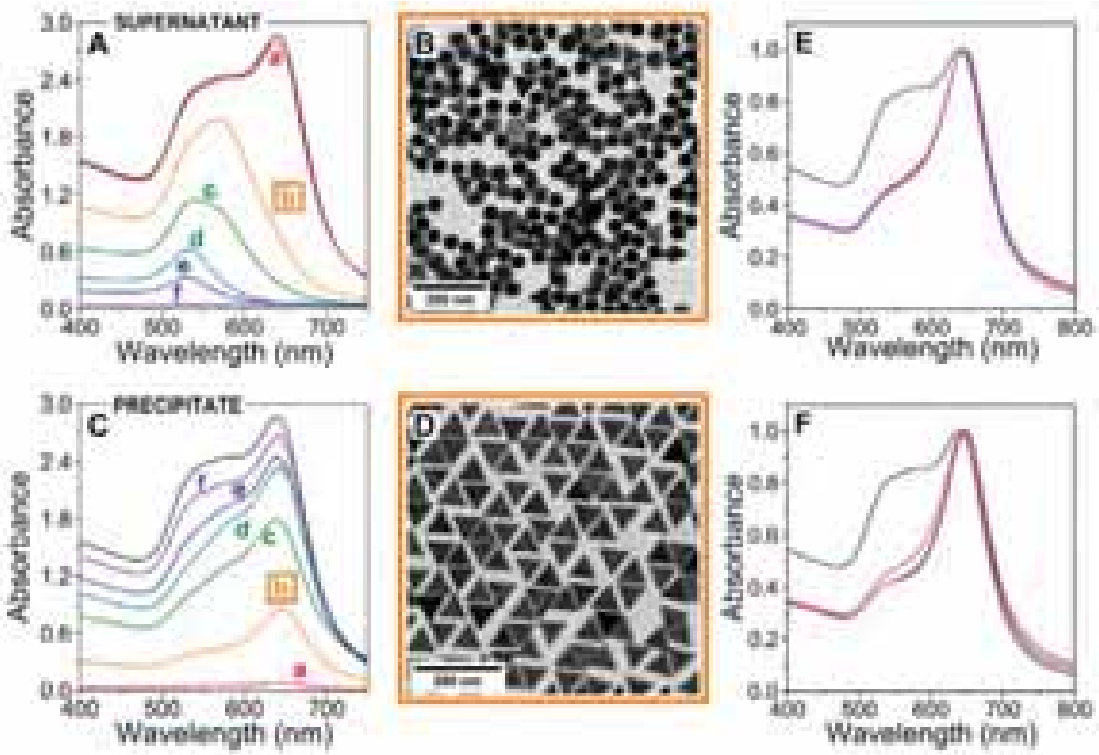

Figure II.20. Influence of CTAC concentration on the purification of gold nanotriangles. **A:** UV-vis spectra of the supernatant solutions: (a): 0.125 M, (b): 0.15 M, (c): 0.175 M, (d): 0.2 M, (e): 0.3 M, (f): 0.4 M. As expected, an increase in surfactant concentration leads to a more extensive flocculation/precipitation; the black line represents the original sample. **B:** TEM image of the 0.14 M (b) supernatant. **C:** UV-vis spectra of the precipitate after redispersion in 0.1 M CTAC solution, as indicated in A. Note the different intensity ratios between the two LSPR bands. **D:** TEM image of the 0.14 M (b) precipitate. Additional TEM images are provided in **Figures II.21-22**. **E:** UV-vis monitoring of gold nanotriangle precipitation at different times (spectra normalized at LSPR maxima): original (black line), 1 day (red line), 2 days (blue line) and 3 days (pink line). As shown, one night is enough to achieve complete separation. **F:** UV-vis spectra of consecutive purification procedures on the same sample (spectra normalized at LSPR maxima): original (black line), 1st purification (red line), 2nd purification (blue line) and 3rd purification (pink line). As can be seen, the quality is slightly improved by a second purification. However, it is important to remark that gold nanotriangle loss increases considerably during the second purification.

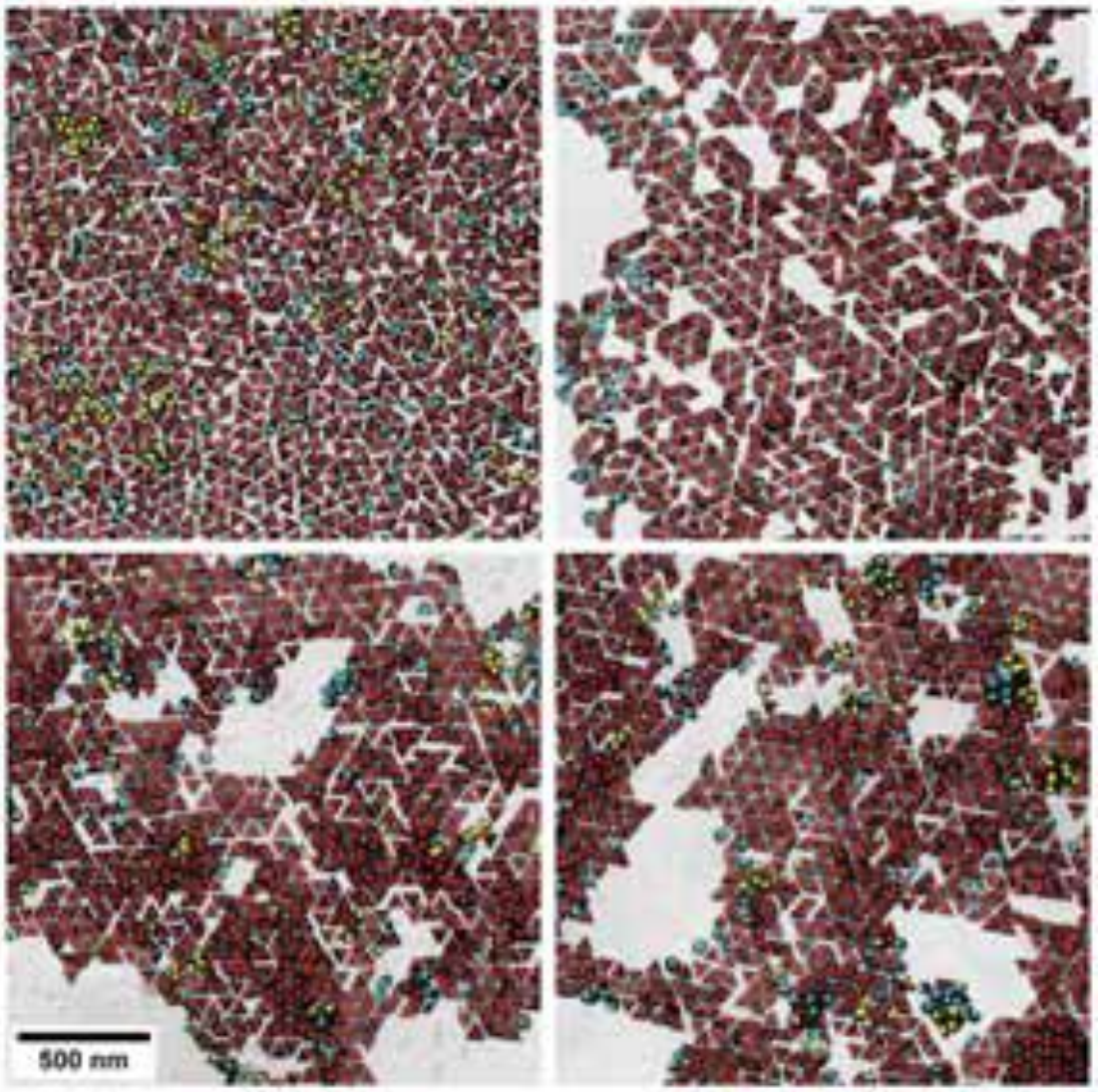

Figure II.21. Gold nanotriangle purification yield. Four TEM images representative of different samples obtained by the purification procedure described in the main text. Labels: by-products are labeled in cyan, horizontally positioned nanotriangles are labeled in red and vertically positioned nanotriangles are labeled in yellow. The scale bar is the same for the four images. In clockwise order the yield in nanotriangles is 91.0%, 95.5%, 92.7% and 94.0%, respectively. The magnifications of the images and the labels correspond to those used in **Figure II.17E - F** to facilitate the comparison.

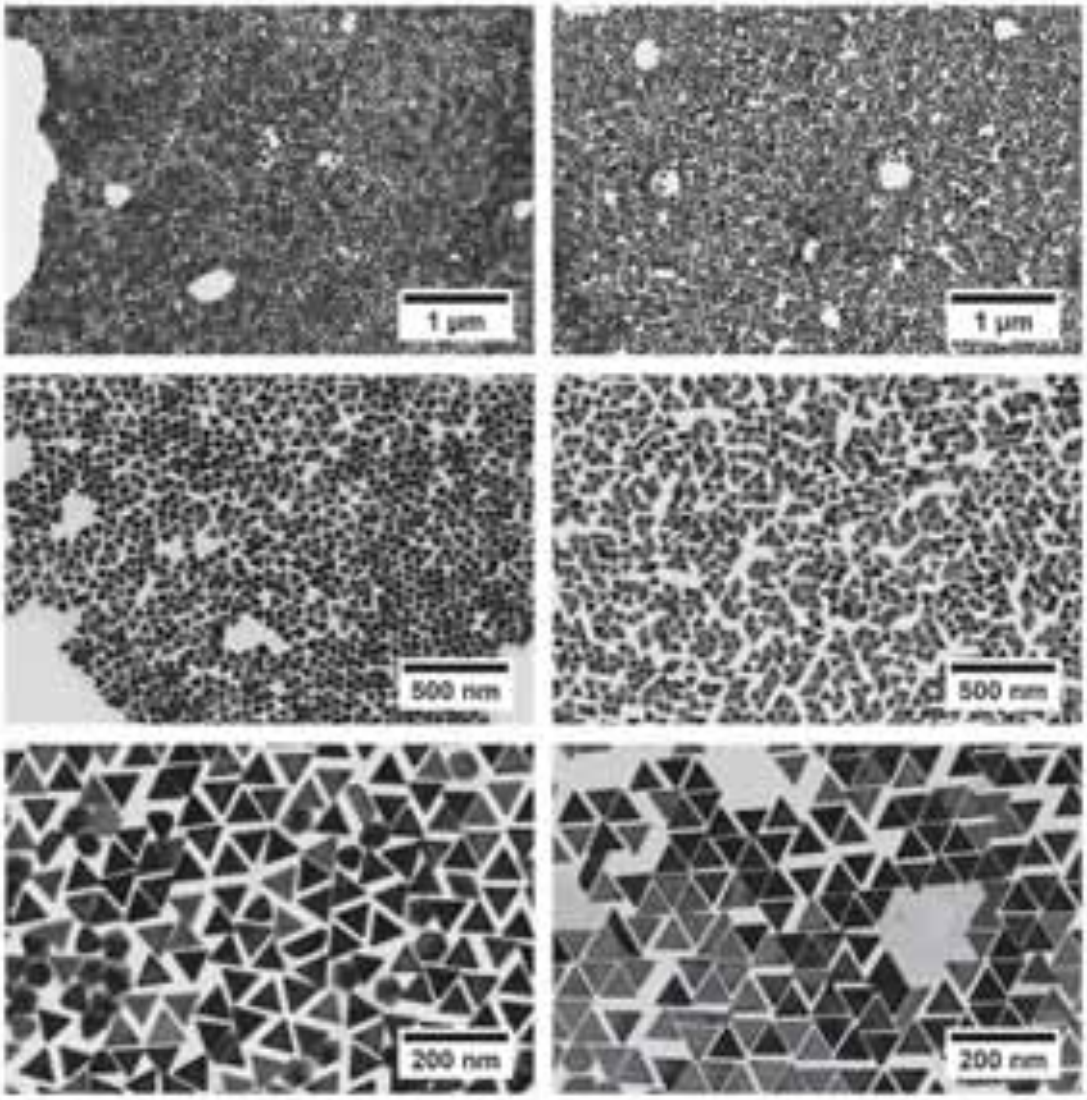

Figure II.22. TEM analysis of gold nanotriangle purification. Comparison between non-purified and purified gold nanotriangle samples (TEM images at various magnifications). Left panel: non-purified sample; right panel: purified sample.

II.3.3. Size Tunability

This improved synthesis method allowed us to explore the size tunability of gold nanotriangles. This objective was partially achieved by simply varying the amount of seed transferred into the growth solution by fast addition. In fact, reduction in the amount of seeds enabled us to increase the nanotriangles edge length up to 90 nm. However, further reduction

in seed concentration leads to increased size dispersity, from less than 6% up to 15%. This can be understood considering that the iodide/seed ratio is also varied; it is known that iodide can strongly bind to the gold surface, so that particle growth can be significantly affected.[12,45,148] Therefore, by lowering the concentration of iodide down to 50 μM (see Experimental Section, section II.5.3.2) the edge length of the nanotriangles further increased up to 150 nm (**Figure II.23**). As expected, this increase in edge length leads to a redshift of the plasmon band, (**Figure II.24A**). The purification procedure (see section II.3.2) could also be used for all the different gold nanotriangle sizes (**Figure II.24B** and **Figure II.25**). In all cases, purity higher than 90% and size dispersity as low as 6% were achieved. The CTAC concentrations used for each size, together with the calculated energy potential for the depletion interaction ($|U|$), are depicted in **Table II.5**. Interestingly, in all cases the energy values are around 9 k_BT, which means that this purification procedure could be applied to other flat nanoparticles of previously known dimensions. For this range of nanotriangles size the LSPR bands varied between 630 and 750 nm (**Figure II.24B**). A linear correlation was found between the nanotriangle dimensions and the maximum wavelength of the LSPR band (**Figure II.24C**).

Table II.5: TEM analysis of gold nanotriangles size for the samples shown in **Figures II.23** and **II.24**. The edge length was calculated as an average over 200 nanotriangles. The value of $|U|$ was calculated according to equation **[II.5]**.

Seed (μL)	Edge (nm)	Size Dispersity (%)	Area (nm^2)	[CTAC] (M)	$\|U\|$ (k_BT)
100	147 ± 10	6.68	9348	0.035	9.6
200	110 ± 5	4.66	5257	0.065	10.1
400	87 ± 5	5.89	3292	0.1	9.8
600	78 ± 6	6.05	2604	0.125	9.7
800	68 ± 3	4.02	1983	0.15	8.9
1200	59 ± 2	3.84	1513	0.2	9.1

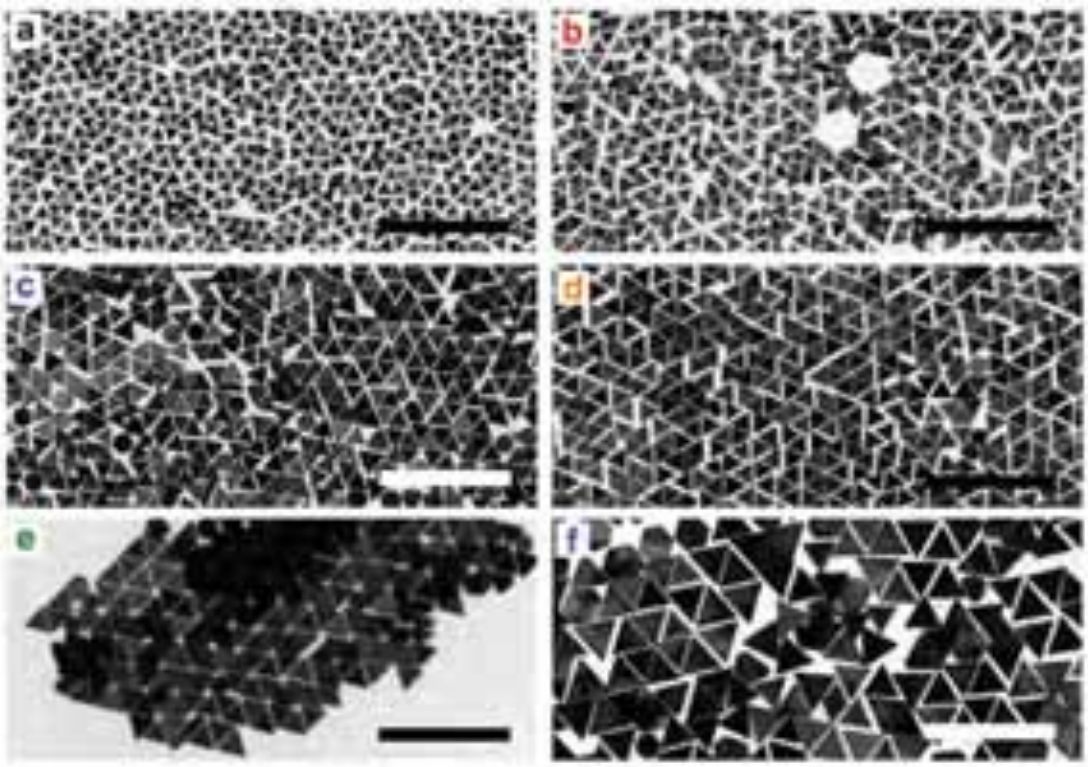

Figure II.23. Size-Tunability of gold nanotriangles – TEM analysis. TEM images of purified gold nanotriangles with increasing edge lengths. Sample b was prepared through the standard synthesis procedure depicted in Figure 1. a-f were prepared by using different amounts of seed solution transferred into the growth solution: 1.2 mL (a), 800 µL (b), 600 µL (c), 400 µL (d), 200 µL (e) and 100 µL (f). Scale bars: 500 nm.

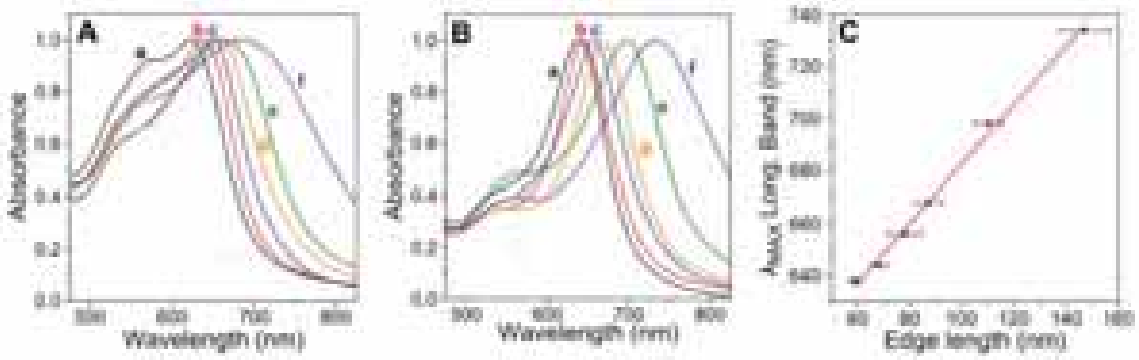

Figure II.24. A: UV-vis spectra of gold nanotriangles prepared using different amounts of seed: (a): 1.2 mL, (b): 800 µL, (c): 600 µL, (d): 400 µL, (e) 200 µL and (f): 100 µL. **B:** Spectra corresponding to the purified samples presented with the same labels. All the spectra are normalized at the LSPR maximum. **C:** Linear correlation between the edge length of the gold nanotriangles and the maximum of the LSPR band, with a Pearson's coefficient $R^2 > 0.994$.

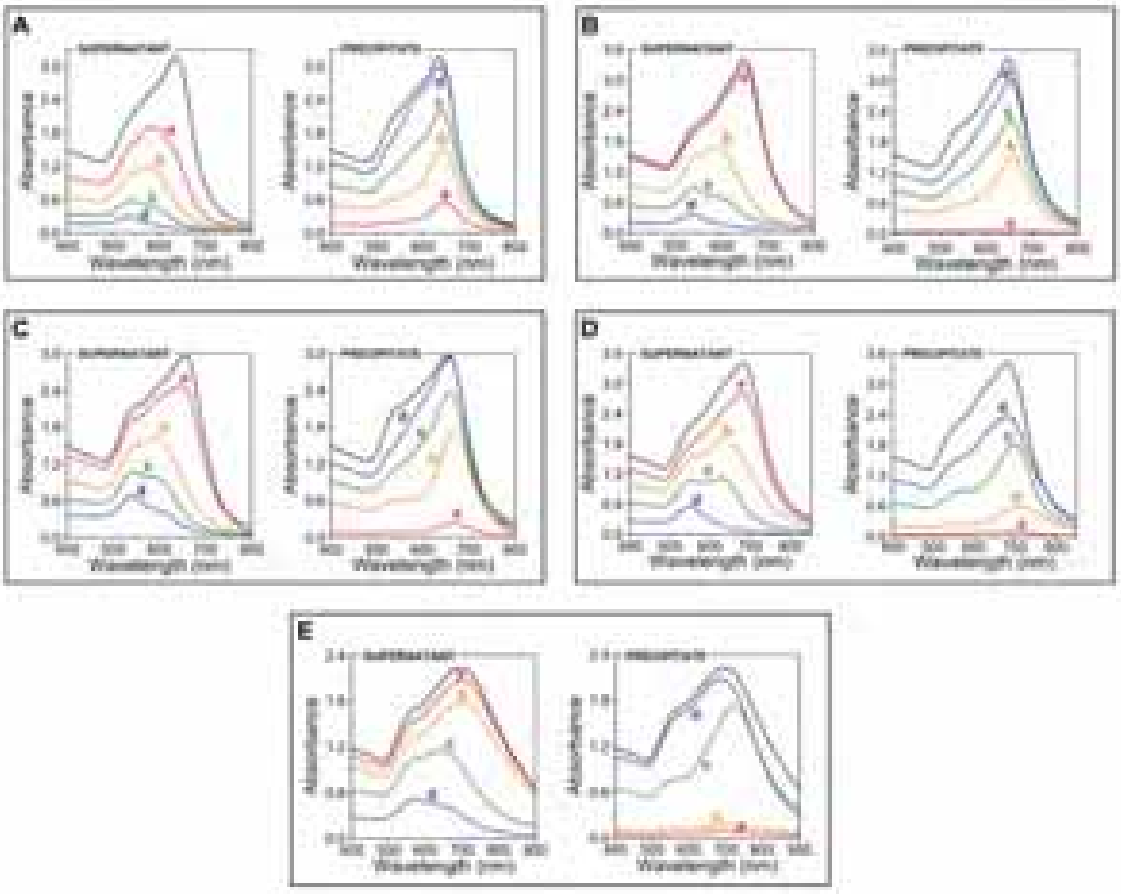

Figure II.25. Purification study on gold nanotriangles of different dimensions. In all the plots the black line represents the original sample. On the left side of each box: UV-vis spectra of the supernatant solutions after purification with different CTAC concentrations. On the right side: UV-vis spectra of the precipitate after redispersion. **A:** 1200 μL of seed: (a): 0.175 M, (b): 0.2 M, (c): 0.225 M, (d): 0.25 M. **B:** 600 μL of seed: (a): 0.1 M, (b): 0.125 M, (c): 0.15 M, (d): 0.175 M. **C:** 400 μL of seed: red (a): 0.085M, orange (b): 0.1M, green (c): 0.11M, blue (d): 0.125M. **D:** 200 μL of seed: (a): 0.035 M, (b): 0.05 M, (c): 0.065 M, (d): 0.085 M. **E:** 100 μL of seed: (a): 0.015 M, (b): 0.020 M, (c): 0.035 M, (d): 0.05 M.

The low LSPR wavelengths (typical literature values are above 1000 nm), together with the strong scattering that can be seen from the colloidal solution, suggests that the gold nanotriangles prepared with our method are rather thick, in agreement with Scanning Electron Microscopy (SEM) images (**Figure II.17C**). Similarly to what happens in the case

of short gold nanorods, the quadrupolar mode is not observed in the UV-vis analysis, as a consequence of the low AR of gold nanotriangles.[165] This observation was also confirmed by TEM analysis of vertically positioned nanotriangles, which revealed an average thickness of 30 nm (see **Figure II.26**).

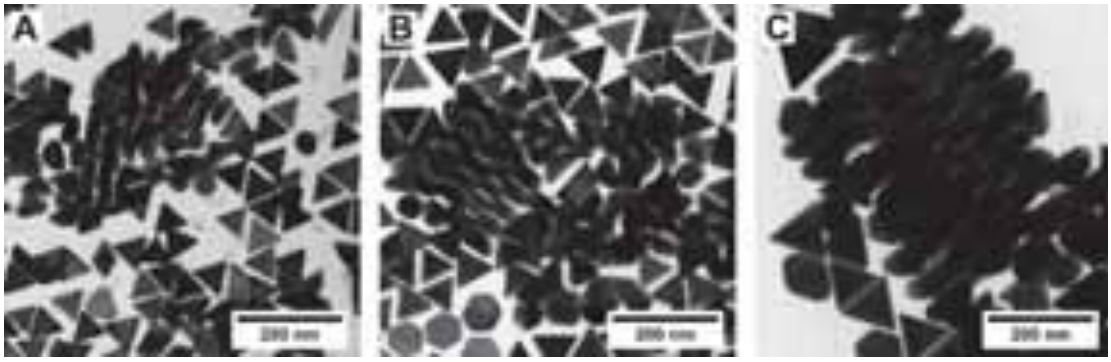

Figure II.26. TEM images showing vertically oriented nanotriangles of different sizes. Amount of seed added by fast addition: **A:** 1200 μL, **B:** 800 μL, **C:** 200 μL.

II.3.4. Conclusions

We demonstrated an improved synthesis of gold nanotriangles with sizes ranging from 50 to 150 nm edge length. In all cases the gold nanotriangles exhibited narrow size distribution, down to 3% standard deviation and a high shape-yield above 50%. A fast and simple purification step allowed separation of the byproducts, thereby reaching 95% nanotriangle shape-yield. The high quality of these solutions, together with the unique optical properties of the gold nanotriangles, renders them promising candidates for the development of nanoplasmonic devices.

II.4. SYNTHESIS OF SILVER-GOLD-SILVER BIMETALLIC NANOWIRES

The ability of plasmons to confine electromagnetic radiation on a subwavelength nanometer scale (see section I.2.1) holds great potential for a vast range of applications in optics, including metamaterials design,[166–168] biosensing,[169,170] therapeutics,[171,172] solar energy harvesting,[173] and photocatalysis.[174] Alongside the continued progress in the synthesis of noble metal nanoparticles with new exotic shapes and decreased size dispersity, the manufacture of bimetallic nanostructures represents an alternative strategy to enrich the library of plasmonic structures at our disposal.[147] Epitaxial seeded growth is one of the most widely used approaches for the preparation of such structures, where one or more metal precursors are reduced or co-reduced on the surface of a previously prepared core of a different metal.[175] The geometry of the obtained bimetallic system mainly depends on the lattice matching of the metal species involved,[176,177] on the seed morphology,[178] and on the growth mode on different crystallographic facets, which can be influenced by facet-specific capping agents.[23] The particular case of Au@Ag bimetallic nanoparticles has attracted much attention from the scientific community because of their complementary properties: while gold nanoparticles can be easily modulated in shape and size,[179–182] the lower optical losses of silver render a better plasmonic performance, for example in the amplification of weak optical processes such as Raman scattering,[183] fluorescence[184] and IR spectroscopy.[185] Among many other examples, Seo et al. reported the preparation of silver-gold-silver pentatwinned nanorods through epitaxial growth of silver on a pentatwinned gold nanorod core in an ethylene glycol solution of PVP.[186] Recently, Li et al. performed the same reaction in water,[187] which was further studied by Gómez-Graña et al. to elucidate the growth mechanism behind the formation of the silver shell using high-resolution electron microscopy in combination with DFT calculations.[182] It is important to underline that the production of high AR nanowires relies on the selective deposition of silver on {111} tip facets, whereas a similar overgrowth reaction with gold would lead to a decrease in AR, as previously reported.[113] Such elongated structures can be regarded as the plasmonic analogues of radiofrequency antennas, but with the resonance shifted into the vis-NIR range of the electromagnetic spectrum.[188] The most important prerequisites for a precise engineering of the plasmonic properties of noble metal nanoparticles are low size distribution and size

tunability. As maintaining a narrow size distribution becomes more difficult when anisotropy is increased, we developed, as we report here, the concept of *controlled living nanowire growth* for the production of monodisperse silver-gold-silver nanowires, by analogy with controlled living polymerization reactions (CLPR).[189] Controlling the addition of silver precursors by means of a syringe pump device, we managed to achieve a linear growth rate of silver on the gold cores. This procedure allowed us to prevent the nucleation of silver nanoparticles during nanowire growth, to significantly improve the size uniformity of the product, and to accurately predict the final dimensions of the bimetallic system. As a result, silver-gold-silver nanowire colloids were obtained which display up to nine well-defined plasmon resonance peaks spreading over the entire vis-NIR wavelength range, with a tight control on the total nanowire length up to several microns, corresponding to ARs above 100.

II.4.1 Controlled Living Nanowire Growth

To push the quality of silver nanowire synthesis beyond the existing limits, any side reactions and secondary nucleation should be suppressed completely. Thus, the aims in nanowire synthesis are similar to those in polymer synthesis, where a small size distribution index is desired. Consequently, we can apply the well-known concept of CLPR to a one-dimensional nanowire growth reaction. The criteria for CLPR as defined by IUPAC standards involve the complete suppression of termination and side reactions and a constant number of actively growing chains throughout the polymerization.[189] Furthermore, the initiation reaction should be much faster than the propagation reaction. As a consequence, the degree of polymerization –and thus the resulting chain length– is determined only by the ratio of monomer to initiator concentrations $P_n = [M_0] / [I_0]$. In the following, we introduce the concept of *controlled living nanowire growth*, which allows us to synthesize bimetallic silver-gold-silver nanowires with remarkably narrow size distributions and nanometer precision in length. As previously described by various groups, epitaxial silver overgrowth of pentatwinned gold nanorods in the presence of surfactants with chloride counter-ions leads to one-dimensional growth of bimetallic silver-gold-silver rods/wires.[182,187,190] This can be explained by the adsorption of chloride onto the lateral {100} facets resulting in less favored silver reduction. Consequently, silver is only reduced and deposited epitaxially on the {111}

facets at the nanorod tips, so the pentatwinned gold nanorod seeds can act as bifunctional initiators bearing two initiation sites. After deposition of the very first silver monolayer the initiator becomes an active species that is subsequently overgrown in one-dimensional fashion by continuous reduction of silver ions at the metal surface during nanowire growth. We identify the following requirements to obtain a living controlled nanocrystal growth mechanism: *(i)* the initiation of crystal growth takes place simultaneously and much faster than the continuous reduction of Ag^+ ions at the metal surface of the active species; *(ii)* all particles have to persist as active growing species for selective deposition of silver atoms throughout the complete experiment; and *(iii)* the reduction and deposition of silver must be quantitative, so that the growth of the particles is proportional to the amount of added silver precursor and a precise control over the final nanowire dimensions can be achieved.

(i) The first condition is met by using pentatwinned gold nanorods with a narrow size distribution as seeds, uncoupling completely nucleation and elongation. Furthermore, the *ex-situ* synthesis of the pentatwinned initiator guarantees a homogenous and simultaneous initiation at both ends upon addition of silver precursor. Consequently, the preparation of high quality pentatwinned gold nanorod seeds is of primary importance toward a precise growth of monodisperse silver-gold-silver nanowires. pentatwinned gold nanorods with average length of 210 ± 10 nm and width of 34 ± 1 nm were prepared as previously described by Pérez-Juste et al., with minor modifications (see Experimental Section, section II.5.4.1).[99] Since the presence of byproducts (nanoparticles with different shapes) ultimately limits the use of pentatwinned gold nanorods as seeds for silver overgrowth, a purification step was required to separate nanorods from other nanoparticles. Shape-dependent separation can be achieved by exploiting depletion interaction forces (see section II.3.2).[81,160,161,191,192] In our case the depletants are CTAC micelles; the choice of CTAC arises from its high water solubility compared to CTAB or BDAC; since CTAC only varies from CTAB in the counter-ion, the surfactant used for pentatwinned gold nanorod synthesis, and considering that it is present with a concentration as low as 8 mM, no washing is required prior to surfactant exchange, i.e. the required CTAC amount was added directly to the pentatwinned gold nanorod solution (see Experimental Section, section II.5.4.1.4). After screening various

[CTAC], a concentration around 0.1 M was found to lead to selective flocculation and precipitation of pentatwinned gold nanorods within 16 hours (**Figure II.27**). The purified pentatwinned gold nanorods show a shape yield around 99%, (**Figure II.27A - C**) and can be used as seeds after redispersion in 10 mM BDAC solution. As evidenced by UV-vis-NIR spectroscopy (**Figure II.27F**), the characteristic transversal and longitudinal dipolar, as well as longitudinal quadrupolar plasmon modes can be identified for the pure pentatwinned gold nanorod dispersion. Further inspection of the high-energy region reveals the presence of an octupolar mode as a shoulder below 600 nm (inset **Figure II.27F**). The narrow dipolar plasmon band, and the high intensity ratio between the dipolar and the transversal modes confirm the narrow size distribution of the pentatwinned gold nanorod seeds.

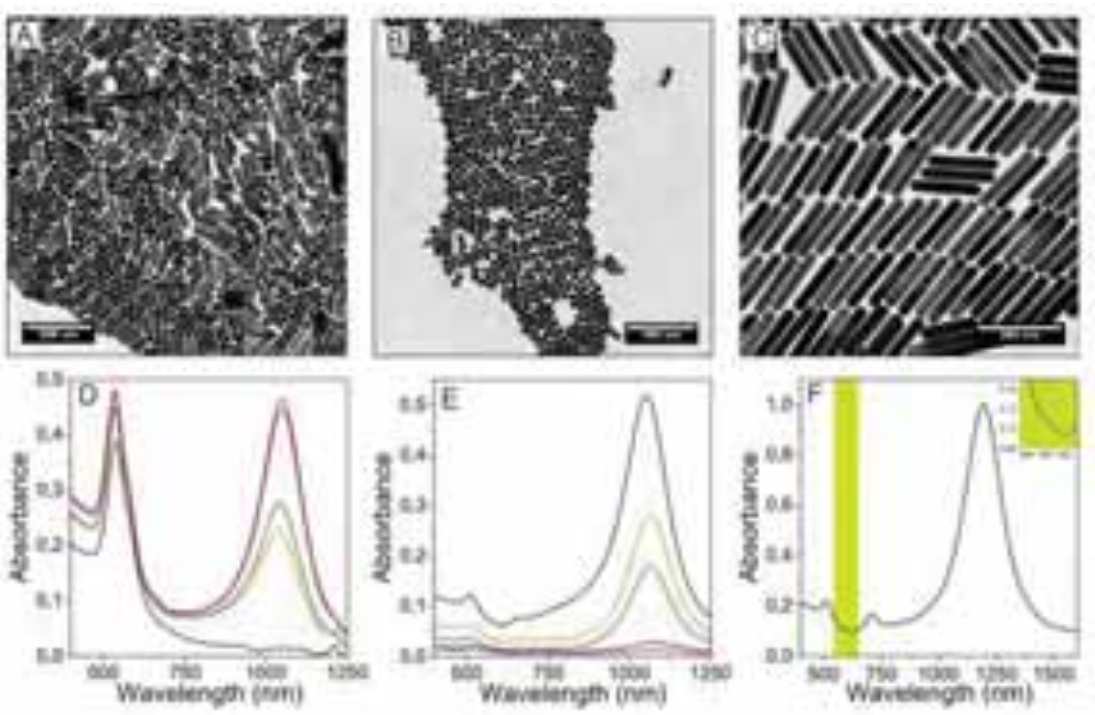

Figure II.27. Purified pentatwinned gold nanorod solution used as core for controlled living nanowire growth. A: TEM image of as-synthesized pentatwinned gold nanorods. **B:** TEM image from the supernatant containing the synthesis by-product. **C:** TEM image of purified pentatwinned gold nanorods. **D:** UV-vis analysis of the supernatant obtained 16 hours after addition of CTAC solutions; [CTAC]=0.12M (black curve), 0.10M (orange curve), 0.08M (green curve), 0.06M (blue curve) and 0.04M (red curve). **E:** UV-vis analysis of the precipitate obtained 16 hours after the addition of CTAC stock solution. The curve colors correspond to those in **D**. **F:** UV-vis spectra of a purified pentatwinned gold nanorods solution; **inset:** zoom of the highlighted area discerning the octupolar mode.

(ii) The second requirement can be fulfilled through careful adjustment of a low silver reduction rate to facilitate anisotropic growth.[142,147] Therefore, the silver overgrowth reaction conditions were set according to the following three conditions: (1) slow silver reduction at slightly acidic conditions and elevated temperature;[182] (2) BDAC as surfactant, which drastically reduces the reduction rate as compared to non-aromatic surfactants;[193] and most importantly, (3) continuous addition of silver nitrate and AA by means of a microfluidic pump setup from separated reservoirs. The continuous and slow addition prevents the accumulation of unreacted Ag^+ within the growth solution, which might lead to secondary nucleation and non-specific silver deposition.

UV-vis-NIR extinction spectra after various reaction times during nanowire growth were correlated with TEM images. All spectra were collected after transferring the nanowires into heavy water, so as to expand the detection range up to 2500 nm, avoiding the strong absorbance of water around 1350 nm (see Experimental Section, section II.5.4.2). We observed an initial blueshift of about 20 nm, along with a slight reduction of the overall AR when a thin silver layer (approximately 2 nm) grows on all facets (sides and tips). However, after coverage of the pentatwinned gold nanorod cores with this initial thin layer, silver deposits on the nanowire tips only. This results in a significant and gradual redshift of all plasmon modes, while multipolar, higher energy plasmon modes emerge as silver deposition continues. Optical extinction spectra of the resulting length-controlled silver-gold-silver nanowires are shown in **Figure II.28A-top**, along with representative TEM images for selected sizes (**Figure II.28D - G**), illustrating the strikingly high size homogeneity typically achieved by the growth method described above (see **Table II.6** and section II.4.2). In particular, the plasmon spectral features are narrow and mainly limited by intrinsic absorption and radiative losses, rather than by particle size dispersion (see section II.4.2). The corresponding BEM calculated extinction spectra (**Figure II.28A-bottom** solid lines) show an excellent agreement with the experimental spectra, as well as a gradually increasing similarity with spectra calculated for pure silver nanowires with the same overall dimensions (**Figure II.28A-bottom** dashed lines).

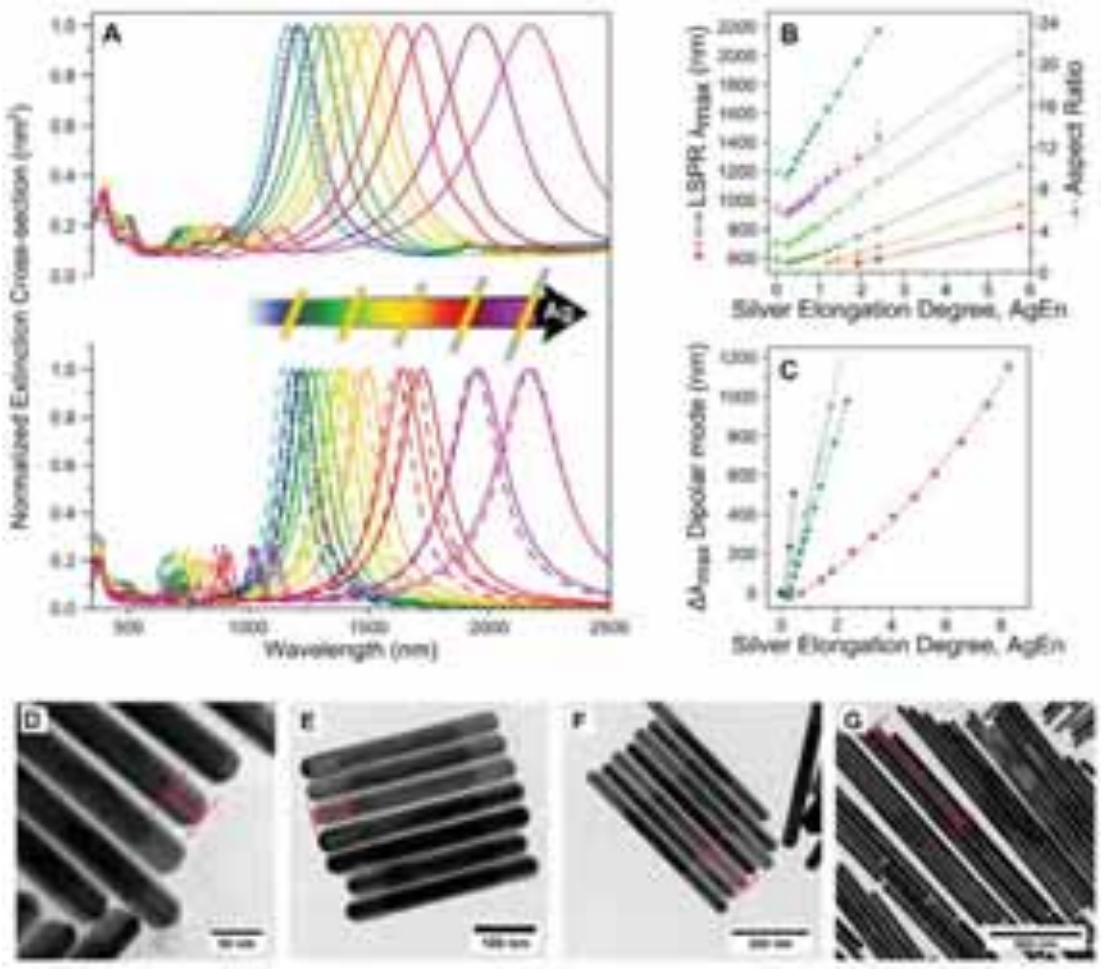

Figure II.28. Upper panel: Vis-NIR spectra recorded during silver growth; the pentatwinned gold nanorod core is displayed as a black dotted curve; Lower panel: calculated BEM extinction spectra of silver-gold-silver (solid curves) and pure silver (dashed curves) nanowires with dimensions corresponding to the experimental ones (same color code). **B**: Resonance wavelengths for the dipolar (cyan) and 2^{nd}-5^{th} order multipolar modes (green, dark green, orange, and red, respectively) *vs. AgEn.* The AR (purple) is also plotted for reference. Solid lines are linear fits to the data. The position of the corresponding modes for the pentatwinned gold nanorod cores are plotted as open symbols. **C**: Wavelength shift of the dipolar plasmon mode for growth with a faster addition rate (red), and for the standard rate on pentatwinned gold nanorods with different dimensions (180×34 nm, blue; 180×32 nm, green; 210×32 nm, cyan). The dashed grey line represents a theoretical estimation, using the silver-to-gold volume ratio in one nanowire as *AgEn*. The open black circle is the common origin. **D-G**: Representative TEM images at four different values of *AgEn*: = 0.72, 1.2, 2.4, 11.52, corresponding to a silver elongations per tip of 33±6 nm, 61±9 nm, 130±20 nm, and 660±90 nm, and a longitudinal dipolar plasmon resonances at 1405 nm, 1630 nm, and 2170 nm, respectively. The dipolar plasmon for G lies beyond our measurement spectral range.

(iii) The last requirement to achieve a living polymerization reaction (linear growth) can be met by selecting an addition rate that is slower than the reaction rate. In this way, a linear zero-order kinetic path is enforced and the resonance wavelengths of the longitudinal modes, as well as the corresponding ARs evaluated from TEM measurements (see **Table II.6**), turn out to scale linearly with time.

Table II.6. Summary of the TEM analysis relative to **Figure II.29A** and **II.31A**. It should be noticed that the nanowires thickness increases at early growth stages, but then remains constant throughout all the experiment. The last two samples (AgEn=3.82 and 8.59) are not shown in **Figure II.31A** for clarity.

AgEn	Thickness (nm)	Length (nm)	AR	Ag length per tip (nm)	λ_{MAX} Dipole LSPR (nm)
0	34 ± 1	210 ± 10	6.1 ± 0.4	//	1192
0.24	38 ± 1	220 ± 10	5.7 ± 0.5	3 ± 1	1170
0.36	38 ± 1	230 ± 10	6.0 ± 0.4	7 ± 2	1210
0.48	38 ± 1	240 ± 10	6.3 ± 0.5	17 ± 4	1281
0.60	38 ± 1	250 ± 20	6.7 ± 0.5	24 ± 4	1335
0.72	38 ± 1	270 ± 20	7.1 ± 0.5	33 ± 6	1405
0.84	39 ± 2	280 ± 20	7.3 ± 0.7	39 ± 8	1462
0.96	37 ± 2	300 ± 20	8.1 ± 0.7	50 ± 10	1514
1.20	38 ± 1	340 ± 20	8.9 ± 0.5	61 ± 9	1628
1.44	37 ± 2	360 ± 30	9.7 ± 0.9	75 ± 9	1736
1.92	38 ± 2	420 ± 30	11 ± 1	100 ± 10	1956
2.40	37 ± 2	470 ± 40	13 ± 2	130 ± 20	2170
5.76	38 ± 2	820 ± 90	21 ± 3	300 ± 40	//*
11.52	39 ± 3	1500 ± 200	39 ± 7	660 ± 90	//*

*The dipole resonance was redshifted beyond the detection limit of the instrument

Furthermore, as the conversion rate for silver is close to 100%, the linear shifts are directly proportional to the amount of added Ag^+. This proportionality is referred to in what follows as the *degree of silver elongation, AgEn*, defined as the molar ratio of added silver salt to gold seeds (i.e. $[Ag^+] / [Au^0]$), in analogy to the concept of *degree of polymerization*. We plotted in **Figure II.28B** the resonance wavelengths for all the longitudinal plasmons that were recorded within our measurement spectral range (from the dipolar mode up to the 5th order mode) *vs. AgEn*. Note that we discarded some high-energy spectral features that cannot be clearly resolved apart from the transverse mode. This plot clearly reveals a linear slope for all modes, up to ARs above 20 and *AgEn* value of almost 6. In other words, this plot indicates that the reaction proceeds according to zero order kinetics and that no termination or passivation occurs. The corresponding regression fits (solid lines) yield a Pearson R^2 above 0.999 for all the modes and for the AR. As a control experiment, we increased the rate of Ag^+ addition by a factor of 1.25. The resulting plasmon shifts were plotted in **Figure II.28C** (red dots), showing that the faster addition rate leads to non-linear shifts. Since the reaction does not comply with a slow addition rate, the apparent *AgEn* increases significantly faster than the plasmon band shift, which represents the actual growth rate. Furthermore, under these conditions, excess silver nitrate accumulates in solution, leading to secondary nucleation, formation of AgCl nuclei, non-specific deposition of silver on the growing particle surface, and uncontrolled increase of the reaction rate. All these effects reduce the amount of available silver ions for deposition on the nanowire tips and consequently compromise the linear growth and impair an accurate prediction of the final length of the produced silver-gold-silver nanowires. Interestingly, spherical particles with diameters around 500 nm were observed upon TEM inspection of the resulting colloid, which are likely due to crystallization of AgCl present in solution upon drying of the dispersion on the TEM grid (**Figure II.29**).

Table II.7. Summary of TEM analysis of nanowires obtained using a higher addition rate (see **Figure II.28C**). The selective deposition of silver is less efficient, as seen from a double increment of nanowires thickness compared to living growth conditions (see **Table II.6**).

AgEn	Thickness (nm)	Length (nm)	AR	Ag length per tip (nm)	λ_{MAX} Dipole LSPR (nm)
0	33.3 ± 0.9	182 ± 10	5.4 ± 0.3	//	1078
0.36	37 ± 2	193 ± 9	5.3 ± 0.4	5.1 ± 0.4	1061
0.73	38 ± 1	201 ± 11	5.3 ± 0.4	9.1 ± 0.7	1076
1.46	38 ± 2	208 ± 19	5.4 ± 0.6	13.0 ± 0.7	1143
1.84	39 ± 1	228 ± 12	5.8 ± 0.4	23 ± 2	1187
2.58	39 ± 2	266 ± 22	6.8 ± 0.6	42 ± 4	1288
3.33	40 ± 1	300 ± 19	7.6 ± 0.6	59 ± 4	1364
4.08	40 ± 1	313 ± 28	7.8 ± 0.9	65 ± 7	1468
4.84	39 ± 1	313 ± 23	8.1 ± 0.7	65 ± 6	1567
5.60	39 ± 2	362 ± 26	9.3 ± 0.9	90 ± 9	1685
6.54	39 ± 1	406 ± 23	10.5 ± 0.7	112 ± 7	1850
7.49	39 ± 1	451 ± 31	12 ± 1	134 ± 12	2036
8.26	39 ± 2	489 ± 28	13 ± 1.2	153 ± 14	2232
8.74	41 ± 2	898 ± 57	22 ± 2	358 ± 30	//*

*The dipole resonance was red-shifted beyond the detection limit of the instrument

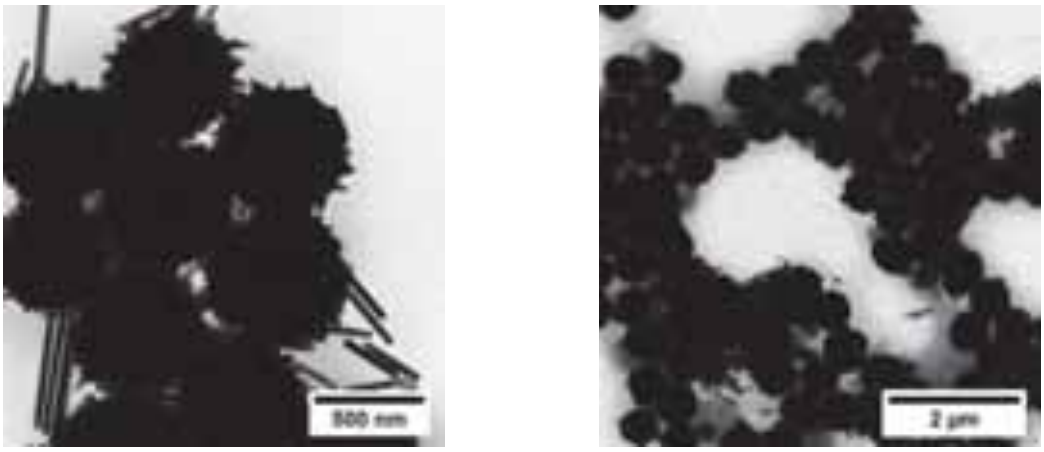

Figure II.29. AgCl particles observed upon drying when a higher addition rate was used for nanowire synthesis. The formation of these particles is likely due to accumulation of AgCl in the growth solution.

The generality of this method was confirmed by carrying out different experiments under *controlled living nanowire growth* conditions but starting with different pentatwinned gold nanorod core dimensions, which also led to linear growth and reproducible evolution of the plasmonic features (**Figure II.28C**). We used the silver to gold volume ratio of a single bimetallic nanowire as the *AgEn* parameter for BEM simulations (**Figure II.28A-bottom**), so as to estimate the theoretical linear behavior (dashed line in **Figure II.28C**). The observed deviation can be explained taking into account the presence of a small amount of gold byproducts (different particle shapes), on which silver is also reduced, as well as some uncertainty in the initial gold nanorod concentration, due to the purification step ($[Au^0]$ was estimated using the absorbance at 400 nm, see section II.2.4). The obtained agreement is a strong evidence that all added silver ions were reduced and selectively deposited on the silver-gold-silver nanowire tips. It is worth noting that we have not found any limitation in the final length of the nanowires, our longest experiment resulting in 3.4 μm nanowires (corresponding to a *AgEn* of 40.32) (**Figure II.30**).

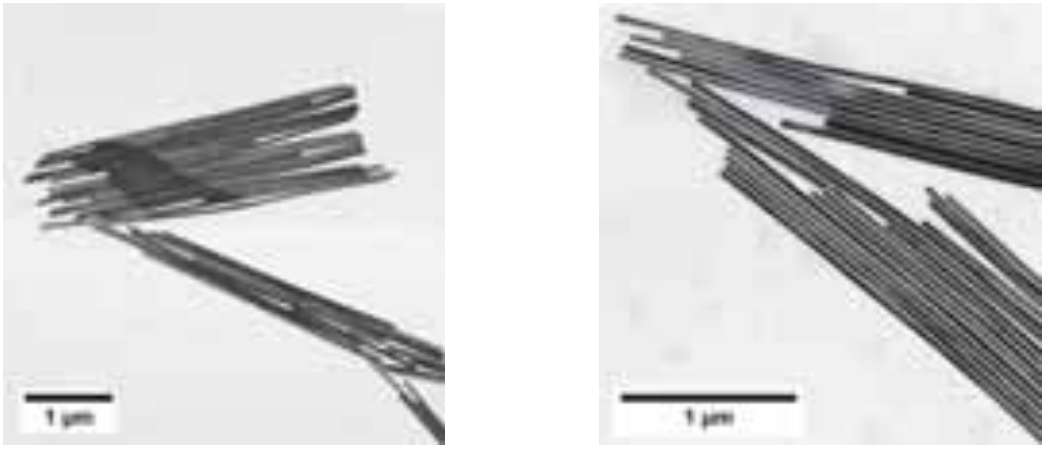

Figure II.30. TEM images of silver-gold-silver nanowires after 7 days of growth (AgEn=40.32). The average dimensions are: 3.4 ± 0.6 μm in length, 37 ± 2 nm in thickness, corresponding to an average Ag length per tip of 1.6 ± 0.2 μm, and AR of 90 ± 10.

II.4.2 Optical Quality of Silver-Gold-Silver Bimetallic Nanowires

The quality factor (Q-factor, i.e., the ratio of plasmon energy to spectral energy Full Width at Half Maximum, FWHM) is the characteristic figure of merit of any resonator, as it indicates how many oscillations are undergone by a particular oscillator. During silver elongation, the Q-factor of the dipolar mode decays exponentially (**Figure II.31B**), which can be explained considering that radiative coupling to the far-field increases with the length of the antenna, together with the relative dissipation, causing the peaks to broaden.[194] When comparing the experimental Q-factors with the ones obtained from the BEM simulated spectra of **Figure II.28A**, the calculated ones are found to be only 25% higher compared to the experimental ones. This clearly emphasizes the low size distribution of the samples. Interestingly, the decay slope is similar in both experiment and theory, suggesting again that there is no significant increase in the size distribution of silver-gold-silver nanowires during silver growth.

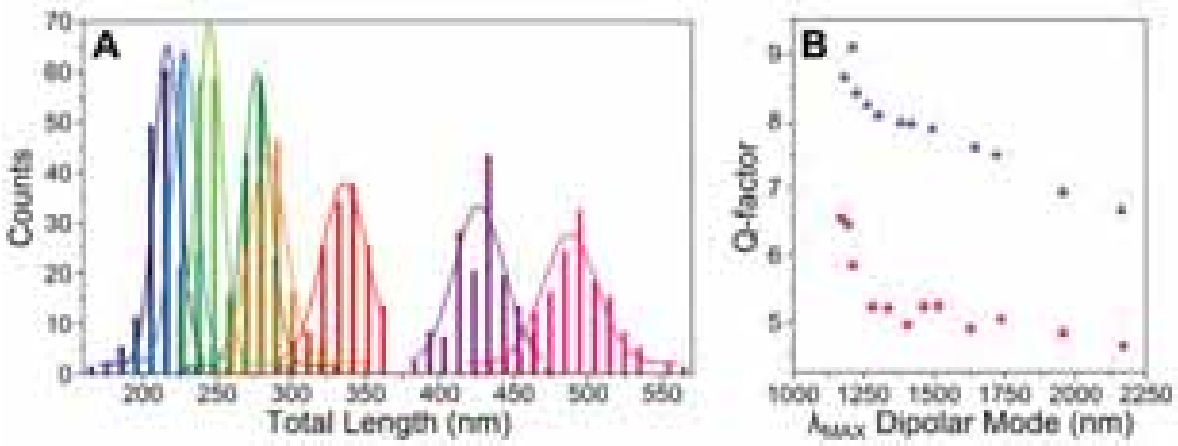

Figure II.31. A: Total length distribution histograms of the 8 samples discussed in **Figure II.28 and Table II.6**. The colors are the same as in **Figure II.28.** Histograms were obtained by measuring 150 nanorods for each sample. **B:** Experimental (pink diamonds) evolution of the Q-factor of the dipolar plasmon band as a function of its energy. This trend was confirmed by BEM calculations (blue triangles). The black circle is the Q-factor of the starting pentatwinned gold nanorods solution.

Overall, the resulting size distribution of the product is remarkably narrow and clearly emphasized by the narrowness of the plasmon bands in **Figure II.28A**. In order to achieve a more meaningful comparison between the widths of experimental and calculated spectra, we used TEM analysis to predict the contribution of the size ditribution to the FWHM, which is missing in the calculation. In fact, the FWHM of the experimental peaks is constituted by a Lorentzian component, intrinsically related to the nanoparticle properties, and a Gaussian component, related to the size distribution in the colloidal solution. The latter is what we normally evaluate using different techniques like TEM, dynamic light scattering (DLS) or small angle X-ray scattering (SAXS). The finite size distribution within each sample accounts for a moderate increase in FWHM of the observed plasmon features (**Figure II.32**). A more precise assessment is provided by comparing the wavelength width of the measured ($\Delta\lambda_{exp}$) and theoretical ($\Delta\lambda_{th}$) spectra, assuming that the excess in the former one originates from the finite size distribution of nanowire sizes for each given sample (ΔL). We then have $\Delta\lambda_{exp} \sim \Delta\lambda_{th} + m \cdot \Delta L$, where m is the slope of the plot of plasmon wavelength peak *vs.* nanowire length, extracted from **Figure II.28B**. In **Table II.9** the values of ΔL extracted from this analysis of the optical spectra (ΔL_{OPT}) are compared with the size distributions obtained from

TEM analysis (ΔL_{TEM}). The results show an acceptable agreement, considering that the number of nanowires measured by TEM for each sample is much smaller than those contributing to UV-vis-NIR spectra.

Table II.9. Total length distribution for silver-gold-silver nanowires with increasing elongation degrees *AgEn*, evaluated by TEM analysis (ΔL_{TEM}) and comparing experimental and calculated optical spectra (ΔL_{OPT}).

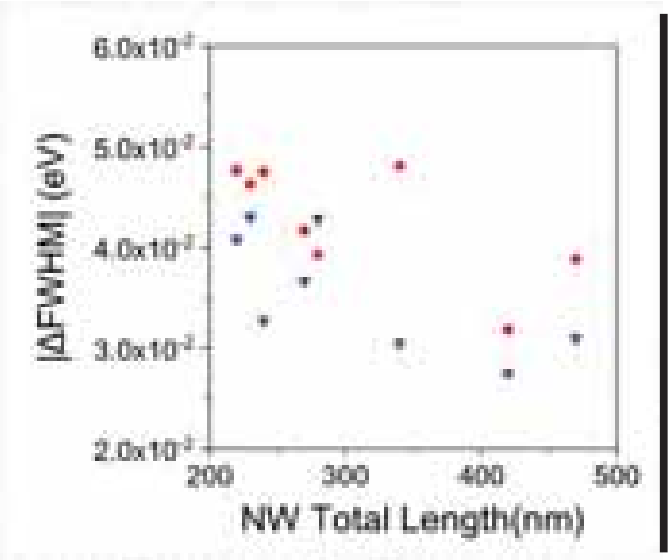

AgEn	ΔL_{TEM} (nm)	ΔL_{OPT} (nm)
0.24	20.3	17.6
0.36	19.5	18.7
0.48	19.8	24.3
0.72	21.9	27.5
0.84	29.2	29.7
1.20	36.3	29.7
1.92	39.8	34.2
2.40	42.9	39.1

Figure II.32. Increase in plasmon FWHM due to the finite size distribution of the nanowires. We compare the following two quantities: (1) difference of FWHM in experiment minus theory (red circles); (2) estimate of increase in FWHM extracted from the standard deviation of NW lengths observed in TEM images, multiplied by the derivative of the plasmon energy with respect to nanowire length (blue triangles). We only show results for the lowest-order plasmon mode. This figure confirms that the observed (moderate) increase in FWHM of experiment compared with theory is fully attributable to the finite distribution of nanowire lengths.

II.4.3 Conclusions

In conclusion, the synthesis of silver-gold-silver bimetallic nanowires has been largely improved by enforcing living growth conditions to the deposition of silver on the tips of pentatwinned gold nanorods, which allowed us to achieve high quality colloidal dispersions of nanowires with remarkably low size distribution. As a result, the plasmon bands observed in colloidal nanowire dispersions are much narrower than those reported for other types of both lithographic and colloidal nanoparticles within the same IR spectral range (see **Figure II.33**). The measured Q-factor is in fact reasonably close to that calculated for nanowires of well-defined size, and as we discuss above, the difference between these two is well explained in terms of the experimental finite size distribution, thus emphasizing our understanding of the optical response of the nanowires in terms of the local permittivities of gold and silver. The new protocol provides the opportunity to fine tune the nanowires length up to the micrometer scale (AR > 100), and the obtained optical antennas displayed a large number of plasmonic modes that spread over the entire UV-vis-IR region (up to 9 detectable modes directly in the colloidal suspension). The procedure opens up new possibilities for the exploitation of plasmon resonances in the near and mid IR regions.

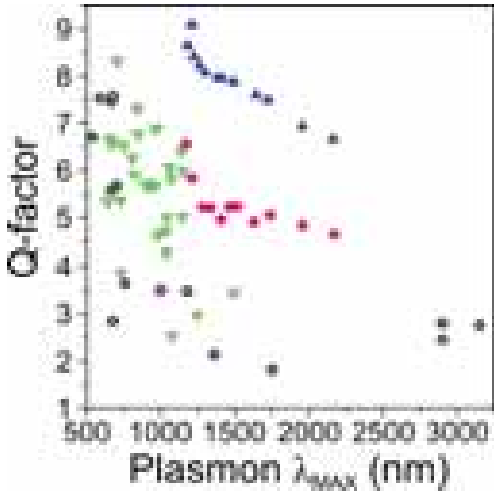

Figure II.33. Comparison of the quality factor of vis-NIR plasmons reported in the literature for different nanoparticles preparation: lithography (black opened circles) and wet-chemistry (green opened triangles). These are compared with those obtained here for silver-gold-silver nanowires, both experimentally (pink diamonds) and from calculations (blue triangles).

II.5. EXPERIMENTAL SECTION

II.5.1. Materials

Benzyldimethylhexadecylammonium chloride (BDAC), Hexadecyltrimethylammonium bromide (CTAB, ≥96%), Hexadecyltrimethylammonium chloride (CTAC, 25 wt % in water), 5-bromosalicylic acid (technical grade, 90%), hydrogen tetrachloroaurate trihydrate ($HAuCl_4 \cdot H_2O$, ≥99.9%), silver nitrate ($AgNO_3$, ≥99.0%), L-ascorbic acid (≥99%), sodium iodide (≥99.5%), dodecanethiol (≥98%), deuterium oxide (D_2O, 99.9 atom % D), trisodium citrate (≥98 %) and sodium borohydride ($NaBH_4$, 99%) were purchased from Aldrich. All the chemicals were used as received. Milli-Q water (resistivity 18.2MΩ·cm at 25 ºC) was used in all experiments. All glassware was washed with aqua regia, rinsed with water, sonicated three-fold for 3 min with Milli-Q water and dried before use.

II.5.2. General Tips for Gold Nanorods Synthesis (section II.2)

The following general practical tips can be of help in the synthesis of gold nanorods, both in terms of product quality and reproducibility of the results.

- *Stock Solutions*:

- $AgNO_3$ 10 mM (17 mg in 10 mL water) - freshly prepared every week, stored in the fridge protected from sunlight; use a plastic spatula or Pasteur pipette to weigh the salt, i.e. avoid contact with metal surfaces.
- AA 100 mM (176 mg in 10 mL water) – freshly prepared every week, stored in the fridge protected from sunlight.
- $HAuCl_4$ 50 mM – stored in the fridge and protected from sunlight, stable over long periods of time.
- NaI 10mM (17mg in 10mL water) – freshly prepared avery week.
- CTAB 0.1 M (1.82 g in 50 mL water – 30 ºC to dissolve) – stable over long periods of time.
- HCl 1M (10 mL of HCl 37% + 110 mL of water) – stable over long period of time.
- $NaBH_4$ 10 mM (7.6 mg in 20 mL water) – freshly prepared; as the powder is hygroscopic it should be weighed quickly.

- *Absorbance at 400 nm:* after each growth step, it is important to verify that the absorbance at 400 nm corresponds to the amount of gold precursor that has been reduced (see section II.2.4); this parameter is really important since it indicates the presence of unreacted Au(I), which can compromise the stability of the rods over time.

- *CTAB/CTAC foam:* when the solution is shaken by hand or stirred, CTAB or CTAC lead to foam formation. When adding a reagent with a micropipette, dip the micropipette tip sufficiently inside the foam to add the reagent directly in the solution; anything that goes into the foam itself will not mix properly in the growth mixture, affecting the overall synthetic conditions. Hand shaking may eventually put the solution in contact with the cap, so it must be thoroughly cleaned to avoid contamination.

- *Color shade and scale-up process:* it is important to remember that the timing, intensity and shade of the color appearance will change if the synthesis is scaled up, since the "optical path length" is increased.

II.5.3. Single Crystal Gold Nanorods Synthesis (section II.2)

II.5.3.1. Synthesis of Gold Seed@CTAB (section II.2.1)

The synthesis is performed in a water bath at 27-30 °C. After adding 25 μL of 50 mM $HAuCl_4$ solution to 4.7 mL of CTAB 0.1 M, the mixture is slowly stirred for 5 min: any sign of turbidity requires further stirring (see section II.2.2 and II.2.3). Then, 300 μL of a freshly prepared $NaBH_4$ 10 mM solution is rapidly injected under vigorous stirring (>1400 rpm). After 10-20 s the solution is mildly stirred (400 rpm) before use (light brown color, **Figure II.3A**).

N.B.: *The seed must be stored between 27 and 30 °C; a lower temperature will cause CTAB crystallization, whereas a higher temperature will induce further growth of the seed into bigger particles, thereby compromising seeded growth.*

II.5.3.2. Synthesis of Gold Nanorods (section II.2.8.1)

Gold nanorods are prepared by a modified version of the seeded growth method reported by Murray's group.[136] The process is carried out entirely at room temperature (ca. 25 °C).

II.5.3.2.1. Pre-reduction (values for 50 mL)

45 mg of 5-BrSa acid is added to 50 mL solution of CTAB 0.05 M. Once salicylic acid is completely dissolved (sonication helps), 480 μL of $AgNO_3$ 10 mM solution is added under mild stirring. After 15 min, 500 μL of $HAuCl_4$ 50 mM solution is added to the mixture under mild stirring. The pre-reduction of Au(III) to Au(I) by salicylic acid starts **immediately after addition**.

N.B.: *This reduction is highly sensitive to temperature: if warming up the solution was required to dissolve CTAB and 5-BrSA, wait until it cools down to room temperature before adding the gold salt (this can be a serious issue when you are dealing with large volumes).*

Pre-reduction can be easily monitored by optical spectroscopy: the $[AuBr_4]^-$ complex is orange, with an absorbance maximum at 396 nm, whereas $[AuBr_2]^-$ is colorless; therefore a reduction in absorbance at 396 nm corresponds to more Au(III) precursor being reduced to Au(I).

II.5.3.2.2. Growth (values for 50 mL)

The AR of the nanorods can be controlled through pre-reduction time: the more Au(III) you reduce by 5-BrSA, the lower the final AR will be. As a reference, an absorbance at 396 nm between 0.8 and 0.85 will result in a longitudinal plasmon band centered around 800 nm.

Immediately after reaching the desired value of absorbance at 396 nm the stirring speed is increased above 1000 rpm and 130 μL of AA 100 mM solution is added to the growth solution. The mixture turns colorless within few seconds. After stirring for 30 s 80 μL of seed solution is finally added to start the growth. After 30 s stirring is detained and the solution is left undisturbed for 4 hours.

N.B.: *The optical properties of the final product can be tuned via pre-reduction.*[110] *With an LSPR maximum around 800 nm the average dimensions are around 60x20 nm; the ratio between the longitudinal and transversal LSPR bands should be above 4.*

N.B.: *The absorbance at 400 nm is also dependent from the pre-reduction step. In this specific synthetic protocol, for a product with an LSPR around 800 nm, the absorbance at 400 nm is low, close to 0.4; consequently, almost 60 % of the initial Au(I) is left in solution. Even in the absence of AA, Au(I) will be reduced over time (a week or so) on the surface of your nanorods, leading to changes in AR and size dispersion. To avoid that, centrifuge the nanorods (9508 g, 20 min) within the first 24 h. It is important to stress here that low values of absorbance at 400 nm are typical of this specific synthetic process,*[110] *and not a general trend in single crystal gold nanorod synthesis: for example, in the method above, an absorbance of 1.2, corresponding to quantitative reduction, is typically achieved (see section II.2.4).*

II.5.3.3. Growth Arrest by Dodecanethiol Injection

NR growth was monitored by UV-vis-NIR spectroscopy. When the selected absorbance was reached, the growth was arrested by passivation of the nanorods surface by direct injection of excess dodecanethiol to the cuvette. For 3 mL nanorods solution, 100 µL of a 1 M dodecanethiol in acetone solution was used.

II.5.3.4. Reduction of Unreacted Au(I)

The fraction of unreacted Au(I) in solution was calculated by assuming 1.2 as the absorbance at 400 nm corresponding to complete reduction of the gold precursor into Au(0). The amount of 0.01 M AA solution required for the reduction (with 10% excess) was added under vigorous stirring using a syringe pump (model: WPI SP210IWZ); the average injection rate used was around 100 µL/h. This value can change significantly according to the volume, so that a total injection time around 6 hours was maintained. The overgrown samples were centrifuged (7000 rpm, 25 min, 29 ºC) and redispersed in an equal volume of 0.05 M CTAB.

II.5.3.5. Overgrowth Reaction (section II.2.8.1.1)

10 mL of a solution of CTAB (0.05 M), 5-BrSA (3.8 mM), $HAuCl_4$ (0.5 mM) and $AgNO_3$ (when present, 0.096 mM) was left undisturbed at room temperature until the reduction of the gold precursor to Au(I) was completed and the solution appeared transparent. This solution was then used to redisperse 10 mL of nanorods after two centrifugation steps (7000 rpm, 25 min, 29 ºC). The obtained mixture was stable at room temperature. AA (15% excess) was added under vigorous stirring using a syringe pump; the average injection rate was around 100 µL/h of 0.01M AA, but this value can significantly vary according to the volume, so that a total injection time around 6 hours was maintained. The samples were finally centrifuged (7000 rpm, 25 min, 29 ºC) and stabilized in 10 mL 0.1 M CTAB.

II.5.3.6. Multicycle Overgrowth Reaction (section II.2.8.1.2 - .3)

This process comprises a simple repetition of the previous overgrowth process. The samples (50 mL) were centrifuged twice and redispersed in 2x25 mL of a CTAB/5-BrSA/Au(I) solution (one with and one without Ag^+), to which AA was added with a syringe pump under vigorous stirring. After each cycle 5 mL of solution was separated for characterization. As the particle size increased, centrifugation was carried out at a lower speed, and the excess of AA was increased to ensure complete reduction: 1stCycle (15% excess, 5500 rpm, 20 min, 29 ºC), 2ndCycle (20% excess, 5000 rpm, 20 min, 29 ºC), 3rdCycle (25% excess, 4500 rpm, 15 min, 29 ºC), 4thCycle (30% excess, 4000 rpm, 15 min, 29 ºC).

II.5.4. Gold Nanotriangles Synthesis (section II.3)

II.5.4.1. Synthesis of Gold Seed@CTAC (section II.3.1)

The initial seeds were prepared by the standard CTAC/$NaBH_4$ procedure: 25 µL of a 0.05 M $HAuCl_4$ solution was added to 4.7 mL of 0.1 M CTAC solution; 300 µL of a freshly prepared 0.01 M $NaBH_4$ solution was then injected under vigorous stirring. Excess borohydride was consumed by keeping the seed solution for 2h at room temperature prior to use.

II.5.4.2. Synthesis of Gold Nanotriangles@CTAC (section II.3.1)

In a typical synthesis of 10 mL gold nanotriangles solution the following two growth solutions were prepared: 1) 1.6 mL of 0.1 M CTAC solution was added to 8 mL of Milli-Q water, followed by 40 µL of 0.05 M $HAuCl_4$ and by 15 µL of 0.01 M NaI solutions; 2) 125 µL of 0.05 M $HAuCl_4$ solution was added to 10 mL of 0.05 M CTAC, followed by 75 µL of 0.01 M NaI solution (reduced to 50 µL for bigger triangles, see section II.3.3). The first solution was used to grow the CTAC capped seed into larger nanoparticles, while the second solution was used as the nanotriangles growth batch. Before proceeding, the initial seed@CTAC solution was diluted 10 times in a 0.1 M CTAC solution. Subsequently, 40 µL and 100 µL of 0.1M AA solution were added to solutions 1 and 2 respectively, and both solutions were manually stirred until the complete transparency of the solutions was achieved, indicating Au(III) to Au(I) reduction. Finally, 100 µL of diluted seed@CTAC solution was added to solution 1 (and manually stirred for 1 second), and immediately 800 µL of this solution was added to solution 2 (and manually stirred for a few seconds). The gold nanotriangles dispersion was left undisturbed at room temperature for at least 1 hour (see **Scheme II.3**, for a schematic representation of the synthetic protocol). We observed that addition of 15 µL of 0.01 M NaI to solution 1 further improved the yield in nanotriangles obtained with the fast-addition procedure.

II.5.4.3. Purification of Gold Nanotriangles (section II.3.2)

After spectroscopic characterization, the gold nanotriangles dispersion was purified by addition of a selected amount of 25 wt% CTAC solution. Flocculation of the gold nanotriangles was completed overnight, the supernatant was then removed and the precipitated particles were redispersed in 5 mL of 0.1 M CTAC solution. Calculation of the amount of CTAC to be added to achieve purification requires taking into account the presence of CTAC used in the synthesis, for which the following equation is suggested:

$$V_x = \frac{V_{in}(C_{fin} - C_{in})}{C_{stock} - C_{fin}} \quad \textbf{[II.6]},$$

where V_x is the volume of CTAC stock solution (of concentration C_{stock}) needed to reach the desired final concentration C_{fin} from a solution of nanoparticles with an initial volume V_{in} and an initial concentration C_{in}.

II.5.5. Silver-Gold-Silver Bimetallic Pentatwinned Nanowires synthesis (section II.4)

II.5.5.1 Pentatwinned Gold Nanorods Synthesis (section II.4.1)

II.5.5.1.1. Seeds@Citrate

At room temperature (ca. 25 °C), 100 µL $HAuCl_4$ 50 mM is added to 20.0 mL of Na_3Cit 0.25 mM. 600 µL of a freshly prepared $NaBH_4$ 100 mM solution is rapidly injected under vigorous stirring (>1400 rpm). After 2 min the solution is kept under mild stirring (400 rpm) for 40 min at room temperature and for 15 min at 40-45 °C before use (red color, **Figure II.3A**).

N.B.: *The solution must be "clean"; in case black spots are floating around repeat the preparation. The UV-vis characterization shows a peak centered at 507 nm, with an absorbance at 400 nm around 0.6.*

II.5.5.1.2. Seeds@CTAB

12.5 µL of 0.05 M $HAuCl_4$ is added to a mixture of 3 mL of water and 2 mL of CTAB 0.1M. The solution is cooled down to 22 °C in a thermostatic bath. 12.5 µL 0.1 M AA is then added to the solution and shaken by hand; the mixture turns colorless in few seconds. Finally 835 µL of the Seeds@Citrate solution is added, shaken by hand and left undisturbed for 3 hours at 22 °C.

N.B.: *UV-vis characterization shows a peak centered at 522 nm, with an absorbance at 400 nm around 0.35.*

II.5.5.1.3. Synthesis of Gold Nanorods

CTAB (40 mL 0.1M) is added to 460 mL of water. 1.25 mL of $HAuCl_4$ 0.05 M solution is then added, the solution gently shaken and cooled down to 20 °C in a thermostatic bath. Subsequently, 1.56 mL of 0.1 M AA solution is added to the mixture, and the solution gently shaken until it turns completely colorless. Finally 650 µL Seeds@CTAB is added to the growing mixture; the solution is vigorously shaken by hand and then left undisturbed overnight at 20 °C.

N.B.: *Cooling down 500 mL of solution takes at least 30 minutes. The vis-NIR shows a longitudinal LSPR band around 1100 nm. The maximum achievable shape-yield is around 30 %, which can be verified through the optical spectra: the ratio between the longitudinal LSPR band in the NIR and the isotropic by-product plasmon centered around 530 nm should be ca. 1. The absorbance at 400 nm must be around 0.3, indicating a quantitative reduction of the gold precursor (0.125 mM).*

II.5.5.1.4. Purification of Pentatwinned Gold Nanorods

The solution is transferred to a test tube, so as to decrease the volume to base-surface ratio. Then, 70 mL of CTAC 25 wt % (~ 0.78 M) is added, with a final CTAC concentration around 0.1 M. The test tube is sealed and the solution is homogenized by turning the test tube upside-down several times. Precipitation of pentatwinned gold nanorods is completed within 16 hours (**Figure II.27**). The supernatant is then discarded using a pipette and the purified product can be easily redispersed in 20 mL of Milli-Q water.

N.B.: *Flocculation of the pentatwinned gold nanorods can be identified by vis-NIR spectroscopy after 20-30 minutes: the longitudinal band should disappear; but this does* ***not*** *mean that purification has been completed: plasmon coupling of the aggregated nanorods leads to disappearance of the band, but the deposition will still take several hours to be completed.*

N.B.: *The low shape-yield makes it difficult to actually see the precipitated nanoparticles. Therefore, extra care must be taken when the supernatant is discarded. An alternative would be leaving 20-25 mL of the supernatant, redispersing the precipitated nanorods by shaking and sonication of the test tube and transferring the remaining suspension into a smaller test tube, repeating the purification process overnight. With a smaller base-surface, the precipitated pentatwinned nanorods can be clearly appreciated as a black-gold patina.*

N.B.: *The amount of CTAC to be added depends on the AR and dimensions of the nanorods, which influence the area in eq.* ***[II.4]****; in order to start the flocculation a value of* $|U|$ *around 10* k_BT *must be achieved: smaller nanorods will thus demand a higher CTAC concentration. To calculate the amount of CTAC stock solution needed to reach a desired final concentration it is enough to solve equation* ***[II.6]****. We assume that the initial concentration was that of CTAB: even though CTAB and CTAC present different cmc values, we consider this an acceptable simplification considering the low concentration of CTAB used for the pentatwinned gold nanorod growth.*

II.5.5.2. Controlled Living Silver-Gold-Silver Nanowires Growth (section II.4.1)

20 mL of the purified pentatwinned gold nanorod solution containing 10 mM BDAC and 0.25 mM Au(0) was heated to 60 °C. $AgNO_3$ (0.004 M in water) and AA (0.016 M in 20 mM BDAC, in order to keep the BDAC concentration constant) were added continuously in separate syringes by a syringe pump (model: WPI SP210IWZ) with a rate of 0.24 equivalent of Ag(I) per hour (effective rate starting at 300 µL/h, equivalent calculated on the amount of Au(0)) under slow stirring at 60 °C. Samples of 1 mL were taken after defined time frames and the effective rate adjusted to maintain the rate of 0.24 equivalent of Ag(I) per hour during the whole experiment (see **Table II.9** for the effective rates). For UV-vis-NIR measurements beyond the water limit at around 1350 nm, the path length was reduced using a 1 mm cuvette and water was exchanged by deuterated water to reduce vibrational modes and consequently reduce overall extinction. The samples were washed 3 times by centrifugation (1000—3000 rpm) and redispersing in deuterated water

(concentrating the sample down to 400 µL) to allow UV-vis-NIR measurements in the range of 300—2500 nm in a 1 mm pathway cuvette to be performed.

Table II.9. Effective addition rates used for the experiment shown in Figure 1A. The starting volume was 20 mL, with $[Au^0]$ = 0.25 mM. For each sample we extracted 1 mL and adjusted the effective rate (µL/h, blue column) keeping constant the equivalent of ***Ag added per hour*** (orange column) at a value of **0.24**.

Sample	Au^0 (mol)	V $AgNO_3$ (mL)	Rate (µL/h)	Eqv. Ag per hour	time (h)	AgEn
1	5.00E-06	1.50E-01	**300.0**	**0.24**	0.50	0.12
2	4.75E-06	7.13E-02	**285.2**	**0.24**	0.75	0.18
3	4.51E-06	6.76E-02	**270.6**	**0.24**	1.00	0.24
4	4.27E-06	1.28E-01	**256.0**	**0.24**	1.50	0.36
5	4.03E-06	1.21E-01	**241.6**	**0.24**	2.00	0.48
6	3.79E-06	1.14E-01	**227.5**	**0.24**	2.50	0.6
7	3.56E-06	1.07E-01	**213.5**	**0.24**	3.00	0.72
8	3.33E-06	9.99E-02	**199.8**	**0.24**	3.50	0.84
9	3.10E-06	9.31E-02	**186.2**	**0.24**	4.00	0.96
10	2.88E-06	1.73E-01	**172.8**	**0.24**	5.00	1.2
11	2.66E-06	1.60E-01	**159.8**	**0.24**	6.00	1.44
12	2.45E-06	2.94E-01	**147.0**	**0.24**	8.00	1.92
13	2.25E-06	2.70E-01	**134.9**	**0.24**	10.00	2.4
14	2.06E-06	1.73E+00	**123.4**	**0.24**	24.00	5.76
15	1.91E-06	2.75E+00	**114.7**	**0.24**	48.00	11.15

II.5.6. Spectroscopic, and Structural Characterization

TEM images were collected with either a JEOL JEM-1400PLUS instrument operating at 120kV or a JEOL2010F FE-TEM instrument operating at 200kV, using carbon-coated 400 square mesh copper grids; all samples were centrifuged twice before dropping it on the TEM grid. SEM images were collected with an Ultra 55 FEG SEM, Zeiss operated at 10kV. SEM samples were prepared by spin-coating the collodial solutions on silicon substrates, previously cleaned with piranha solution. Optical extinction spectra were recorded using an Agilent 8453 UV-vis diode-array spectrophotometer, apart from the ones relative to silver-gold-silver bimetallic nanowires that were recorded using an Agilent Cary 5000 UV-vis-NIR spectrophotometer with deuterated water as solvent (see Experimental Section, section II.5.4.2). All the presented UV-vis spectra were multiplied by the respective dilution factors to facilitate comparison of the data.

II.6. REFERENCES

(1) Dreaden, E. C.; Alkilany, A. M.; Huang, X.; Murphy, C. J.; El-Sayed, M. A. *Chem. Soc. Rev.* **2012**, *41* (7), 2740–2779.
(2) Eustis, S.; El-Sayed, M. A. *Chem. Soc. Rev.* **2006**, *35* (3), 209–217.
(3) Grzelczak, M.; Pérez-Juste, J.; Mulvaney, P.; Liz-Marzán, L. M. *Chem. Soc. Rev.* **2008**, *37* (9), 1783–1791.
(4) Kennedy, L. C.; Bickford, L. R.; Lewinski, N. A.; Coughlin, A. J.; Hu, Y.; Day, E. S.; West, J. L.; Drezek, R. A. *Small* **2011**, *7* (2), 169–183.
(5) Kumar, S.; Nann, T. *Small* **2006**, *2* (3), 316–329.
(6) Langille, M. R.; Zhang, J.; Personick, M. L.; Li, S.; Mirkin, C. A. *Science* **2012**, *337* (6097), 954–957.
(7) Lim, B.; Xia, Y. *Angew. Chem. Int. Ed.* **2011**, *50* (1), 76–85.
(8) Lohse, S. E.; Murphy, C. J. *Chem. Mater.* **2013**, *25* (8), 1250–1261.
(9) Tao, A. R.; Habas, S.; Yang, P. *Small* **2008**, *4* (3), 310–325.
(10) Sardar, R.; Funston, A. M.; Mulvaney, P.; Murray, R. W. *Langmuir* **2009**, *25* (24), 13840–13851.
(11) Zhang, H.; Jin, M.; Xiong, Y.; Lim, B.; Xia, Y. *Acc. Chem. Res.* **2013**, *46* (8), 1783–1794.
(12) Langille, M. R.; Personick, M. L.; Zhang, J.; Mirkin, C. A. *J. Am. Chem. Soc.* **2012**, *134* (35), 14542–14554.
(13) Xia, Y.; Xiong, Y.; Lim, B.; Skrabalak, S. E. *Angew. Chem. Int. Ed.* **2009**, *48* (1), 60–103.
(14) Jana, N. R. *Small* **2005**, *1* (8-9), 875–882.
(15) Jin, R.; Charles Cao, Y.; Hao, E.; Métraux, G. S.; Schatz, G. C.; Mirkin, C. A. *Nature* **2003**, *425* (6957), 487–490.
(16) Garg, N.; Scholl, C.; Mohanty, A.; Jin, R. *Langmuir* **2010**, *26* (12), 10271–10276.
(17) Si, S.; Leduc, C.; Delville, M.-H.; Lounis, B. *ChemPhysChem* **2012**, *13* (1), 193–202.
(18) Smith, D. K.; Miller, N. R.; Korgel, B. A. *Langmuir* **2009**, *25* (16), 9518–9524.
(19) Smith, D. K.; Korgel, B. A. *Langmuir* **2008**, *24* (3), 644–649.
(20) Zhang, J.; Langille, M. R.; Personick, M. L.; Zhang, K.; Li, S.; Mirkin, C. A. *J. Am. Chem. Soc.* **2010**, *132* (40), 14012–14014.
(21) Wang, F.; Li, C.; Sun, L.-D.; Wu, H.; Ming, T.; Wang, J.; Yu, J. C.; Yan, C.-H. *J. Am. Chem. Soc.* **2011**, *133* (4), 1106–1111.
(22) Niu, W.; Li, Z.-Y.; Shi, L.; Liu, X.; Li, H.; Han, S.; Chen, J.; Xu, G. *Cryst. Growth Des.* **2008**, *8* (12), 4440–4444.
(23) Habas, S. E.; Lee, H.; Radmilovic, V.; Somorjai, G. A.; Yang, P. *Nat. Mater.* **2007**, *6* (9), 692–697.
(24) Huang, M. H.; Chiu, C.-Y. *J. Mater. Chem. A* **2013**, *1* (28), 8081.
(25) Kim, F.; Connor, S.; Song, H.; Kuykendall, T.; Yang, P. *Angew. Chem. Int. Ed.* **2004**, *43* (28), 3673–3677.
(26) Niu, W.; Zhang, L.; Xu, G. *ACS Nano* **2010**, *4* (4), 1987–1996.
(27) Sau, T. K.; Rogach, A. L. *Adv. Mater.* **2010**, *22* (16), 1781–1804.
(28) Wiley, B.; Sun, Y.; Mayers, B.; Xia, Y. *Chem. - Eur. J.* **2005**, *11* (2), 454–463.
(29) Quan, Z.; Wang, Y.; Fang, J. *Acc. Chem. Res.* **2013**, *46* (2), 191–202.
(30) Park, K.; Drummy, L. F.; Wadams, R. C.; Koerner, H.; Nepal, D.; Fabris, L.; Vaia, R. A. *Chem. Mater.* **2013**, *25* (4), 555–563.
(31) Murphy, C. J.; Thompson, L. B.; Chernak, D. J.; Yang, J. A.; Sivapalan, S. T.; Boulos, S. P.; Huang, J.; Alkilany, A. M.; Sisco, P. N. *Curr. Opin. Colloid Interface Sci.* **2011**, *16* (2), 128–134.
(32) Xiao, J.; Qi, L. *Nanoscale* **2011**, *3* (4), 1383–1396.
(33) Murphy, C. J.; Sau, T. K.; Gole, A. M.; Orendorff, C. J.; Gao, J.; Gou, L.; Hunyadi, S. E.; Li, T. *J. Phys. Chem. B* **2005**, *109* (29), 13857–13870.
(34) Carbó-Argibay, E.; Rodríguez-González, B.; Gómez-Graña, S.; Guerrero-Martínez, A.; Pastoriza-Santos, I.; Pérez-Juste, J.; Liz-Marzán, L. M. *Angew. Chem. Int. Ed.* **2010**, *49* (49), 9397–9400.
(35) Wang, Z. L.; Mohamed, M. B.; Link, S.; El-Sayed, M. A. *Surf. Sci.* **1999**, *440* (1-2), L809–L814.

(36) Montejano-Carrizales, J. M.; Rodríguez-López, J. L.; Pal, U.; Miki-Yoshida, M.; José-Yacamán, M. *Small* **2006**, *2* (3), 351–355.
(37) Rao, C. N. R.; Matte, H. S. S. R.; Voggu, R.; Govindaraj, A. *Dalton Trans.* **2012**, *41* (17), 5089–5120.
(38) Sánchez-Iglesias, A.; Pastoriza-Santos, I.; Pérez-Juste, J.; Rodríguez-González, B.; García de Abajo, F. J.; Liz-Marzán, L. M. *Adv. Mater.* **2006**, *18* (19), 2529–2534.
(39) Li, C.; Shuford, K. L.; Chen, M.; Lee, E. J.; Cho, S. O. *ACS Nano* **2008**, *2* (9), 1760–1769.
(40) Yu, Y.; Zhang, Q.; Lu, X.; Lee, J. Y. *J. Phys. Chem. C* **2010**, *114* (25), 11119–11126.
(41) Wu, H.-L.; Kuo, C.-H.; Huang, M. H. *Langmuir* **2010**, *26* (14), 12307–12313.
(42) Tian, N.; Zhou, Z.-Y.; Sun, S.-G.; Ding, Y.; Wang, Z. L. *Science* **2007**, *316* (5825), 732–735.
(43) Chen, S.; Wang, Z. L.; Ballato, J.; Foulger, S. H.; Carroll, D. L. *J. Am. Chem. Soc.* **2003**, *125* (52), 16186–16187.
(44) Yuan, H.; Khoury, C. G.; Hwang, H.; Wilson, C. M.; Grant, G. A.; Vo-Dinh, T. *Nanotechnology* **2012**, *23* (7), 075102.
(45) DuChene, J. S.; Niu, W.; Abendroth, J. M.; Sun, Q.; Zhao, W.; Huo, F.; Wei, W. D. *Chem. Mater.* **2013**, *25* (8), 1392–1399.
(46) Lin, G.; Lu, W.; Cui, W.; Jiang, L. *Cryst. Growth Des.* **2010**, *10* (3), 1118–1123.
(47) Kumar, P. S.; Pastoriza-Santos, I.; Rodríguez-González, B.; Abajo, F. J. G. de; Liz-Marzán, L. M. *Nanotechnology* **2008**, *19* (1), 015606.
(48) Pallavicini, P.; Chirico, G.; Collini, M.; Dacarro, G.; Donà, A.; D'Alfonso, L.; Falqui, A.; Diaz-Fernandez, Y.; Freddi, S.; Garofalo, B.; Genovese, A.; Sironi, L.; Taglietti, A. *Chem. Commun.* **2011**, *47* (4), 1315.
(49) Sau, T. K.; Murphy, C. J. *J. Am. Chem. Soc.* **2004**, *126* (28), 8648–8649.
(50) Zhang, H.; Xia, X.; Li, W.; Zeng, J.; Dai, Y.; Yang, D.; Xia, Y. *Angew. Chem. Int. Ed.* **2010**, *49* (31), 5296–5300.
(51) Guerrero-Martínez, A.; Barbosa, S.; Pastoriza-Santos, I.; Liz-Marzán, L. M. *Curr. Opin. Colloid Interface Sci.* **2011**, *16* (2), 118–127.
(52) Straney, P. J.; Andolina, C. M.; Millstone, J. E. *Langmuir* **2013**, *29* (13), 4396–4403.
(53) Kofron, J. T.; Booms, R. E.; Jones, C. G.; Haefner, J. A.; Wilgus, H. S.; Evans, F. J. Sensitized high aspect ratio silver halide emulsions and photographic elements, Patent US4439520A.
(54) Wagner, R. S.; Ellis, W. C. *Appl. Phys. Lett.* **1964**, *4* (5), 89.
(55) Ito, D.; Jespersen, M. L.; Hutchison, J. E. *ACS Nano* **2008**, *2* (10), 2001–2006.
(56) Yu; Chang, S.-S.; Lee, C.-L.; Wang, C. R. C. *J. Phys. Chem. B* **1997**, *101* (34), 6661–6664.
(57) Link, S.; Wang, Z. L.; El-Sayed, M. A. *J. Phys. Chem. B* **2000**, *104* (33), 7867–7870.
(58) Kim, F.; Song, J. H.; Yang, P. *J. Am. Chem. Soc.* **2002**, *124* (48), 14316–14317.
(59) Esumi, K.; Matsuhisa, K.; Torigoe, K. *Langmuir* **1995**, *11* (9), 3285–3287.
(60) Jana, N. R.; Gearheart, L.; Murphy, C. J. *Adv. Mater.* **2001**, *13* (18), 1389–1393.
(61) Nikoobakht, B.; El-Sayed, M. A. *Chem. Mater.* **2003**, *15* (10), 1957–1962.
(62) Liz-Marzán, L. M. *Chem. Commun.* **2012**, *49* (1), 16–18.
(63) Xiong, Y.; Xia, Y. *Adv. Mater.* **2007**, *19* (20), 3385–3391.
(64) Vigderman, L.; Zubarev, E. R. *Chem. Mater.* **2013**, *25* (8), 1450–1457.
(65) Liu, M.; Guyot-Sionnest, P. *J. Phys. Chem. B* **2005**, *109* (47), 22192–22200.
(66) Gou, L.; Murphy, C. J. *Chem. Mater.* **2005**, *17* (14), 3668–3672.
(67) Sohn, K.; Kim, F.; Pradel, K. C.; Wu, J.; Peng, Y.; Zhou, F.; Huang, J. *ACS Nano* **2009**, *3* (8), 2191–2198.
(68) Jana, N. R.; Gearheart, L.; Murphy, C. J. *Langmuir* **2001**, *17* (22), 6782–6786.
(69) Sau, T. K.; Murphy, C. J. *Langmuir* **2004**, *20* (15), 6414–6420.
(70) Grzelczak, M.; Sánchez-Iglesias, A.; Rodríguez-González, B.; Alvarez-Puebla, R.; Pérez-Juste, J.; Liz-Marzán, L. M. *Adv. Funct. Mater.* **2008**, *18* (23), 3780–3786.
(71) Millstone, J. E.; Wei, W.; Jones, M. R.; Yoo, H.; Mirkin, C. A. *Nano Lett.* **2008**, *8* (8), 2526–2529.
(72) Jana, N. R.; Gearheart, L.; Murphy, C. J. *Chem. Commun.* **2001**, No. 7, 617–618.
(73) Chen, S.; Carroll, D. L. *Nano Lett.* **2002**, *2* (9), 1003–1007.

(74) Song, Y.; Garcia, R. M.; Dorin, R. M.; Wang, H.; Qiu, Y.; Coker, E. N.; Steen, W. A.; Miller, J. E.; Shelnutt, J. A. *Nano Lett.* **2007**, *7* (12), 3650–3655.
(75) Niesz, K.; Grass, M.; Somorjai, G. A. *Nano Lett.* **2005**, *5* (11), 2238–2240.
(76) Lim, B.; Jiang, M.; Tao, J.; Camargo, P. H. C.; Zhu, Y.; Xia, Y. *Adv. Funct. Mater.* **2009**, *19* (2), 189–200.
(77) Edgar, J. A.; McDonagh, A. M.; Cortie, M. B. *ACS Nano* **2012**, *6* (2), 1116–1125.
(78) Personick, M. L.; Langille, M. R.; Zhang, J.; Mirkin, C. A. *Nano Lett.* **2011**, *11* (8), 3394–3398.
(79) Bullen, C.; Zijlstra, P.; Bakker, E.; Gu, M.; Raston, C. *Cryst. Growth Des.* **2011**, *11* (8), 3375–3380.
(80) Hubert, F.; Testard, F.; Spalla, O. *Langmuir* **2008**, *24* (17), 9219–9222.
(81) Scarabelli, L.; Coronado-Puchau, M.; Giner-Casares, J. J.; Langer, J.; Liz-Marzán, L. M. *ACS Nano* **2014**, *8* (6), 5833–5842.
(82) Chen, L.; Ji, F.; Xu, Y.; He, L.; Mi, Y.; Bao, F.; Sun, B.; Zhang, X.; Zhang, Q. *Nano Lett.* **2014**, *14* (12), 7201–7206.
(83) Gómez-Graña, S.; Goris, B.; Altantzis, T.; Fernández-López, C.; Carbó-Argibay, E.; Guerrero-Martínez, A.; Almora-Barrios, N.; López, N.; Pastoriza-Santos, I.; Pérez-Juste, J.; Bals, S.; Van Tendeloo, G.; Liz-Marzán, L. M. *J. Phys. Chem. Lett.* **2013**, *4* (13), 2209–2216.
(84) Pastoriza-Santos, I.; Liz-Marzán, L. M. *Adv. Funct. Mater.* **2009**, *19* (5), 679–688.
(85) Wiley, B.; Herricks, T.; Sun, Y.; Xia, Y. *Nano Lett.* **2004**, *4* (9), 1733–1739.
(86) Xia, Y.; Xia, X.; Peng, H.-C. *J. Am. Chem. Soc.* **2015**, 7947–7966.
(87) Casu, A.; Cabrini, E.; Donà, A.; Falqui, A.; Diaz-Fernandez, Y.; Milanese, C.; Taglietti, A.; Pallavicini, P. *Chem. - Eur. J.* **2012**, *18* (30), 9381–9390.
(88) Huang, X.; Neretina, S.; El-Sayed, M. A. *Adv. Mater.* **2009**, *21* (48), 4880–4910.
(89) de Aberasturi, D. J.; Serrano-Montes, A. B.; Liz-Marzán, L. M. *Adv. Opt. Mater.* **2015**, *3* (5), 602–617.
(90) Atwater, H. A.; Polman, A. *Nat. Mater.* **2010**, *9* (10), 205–213.
(91) Lal, S.; Grady, N. K.; Kundu, J.; Levin, C. S.; Lassiter, J. B.; Halas, N. J. *Chem. Soc. Rev.* **2008**, *37* (5), 898–911.
(92) Langer, J.; Novikov, S. M.; Liz-Marzán, L. M. *Nanotechnology* **2015**, *26* (32), 322001.
(93) Vigderman, L.; Khanal, B. P.; Zubarev, E. R. *Adv. Mater.* **2012**, *24* (36), 4811–4841.
(94) Hamon, C.; Liz-Marzán, L. M. *Chem. - Eur. J.* **2015**, *21* (28), 9956–9963.
(95) Webb, J. A.; Bardhan, R. *Nanoscale* **2014**, *6* (5), 2502–2530.
(96) Lohse, S. E.; Burrows, N. D.; Scarabelli, L.; Liz-Marzán, L. M.; Murphy, C. J. *Chem. Mater.* **2013**, 34–43.
(97) Niu, W.; Zhang, L.; Xu, G. *Nanoscale* **2013**, *5* (8), 3172–3181.
(98) Johnson, C. J.; Dujardin, E.; Davis, S. A.; Murphy, C. J.; Mann, S. *J. Mater. Chem.* **2002**, *12* (6), 1765–1770.
(99) Pérez-Juste, J.; Liz-Marzán, L. M.; Carnie, S.; Chan, D. Y. C.; Mulvaney, P. *Adv. Funct. Mater.* **2004**, *14* (6), 571–579.
(100) Gole, A.; Murphy, C. J. *Chem. Mater.* **2004**, *16* (19), 3633–3640.
(101) Carregal-Romero, S.; P r ez- uste, .; Herv s , P.; Liz-Marz n , L. M.; Mulvaney, P. *Langmuir* **2010**, *26* (2), 1271–1277.
(102) Martin, C. R. *Science* **1994**, *266* (5193), 1961–1966.
(103) Martin, C. R. *Chem. Mater.* **1996**, *8* (8), 1739–1746.
(104) Reetz, M. T.; Helbig, W. *J. Am. Chem. Soc.* **1994**, *116* (16), 7401–7402.
(105) Lin, Z.; Cai, J. J.; Scriven, L. E.; Davis, H. T. *J. Phys. Chem.* **1994**, *98* (23), 5984–5993.
(106) Gao, J.; Bender, C. M.; Murphy, C. J. *Langmuir* **2003**, *19* (21), 9065–9070.
(107) Guerrero-Martínez, A.; Pérez-Juste, J.; Carbó-Argibay, E.; Tardajos, G.; Liz-Marzán, L. M. *Angew. Chem. Int. Ed.* **2009**, *48* (50), 9484–9488.
(108) Sau, T. K.; Murphy, C. J. *Philos. Mag.* **2007**, *87* (14-15), 2143–2158.
(109) Almora-Barrios, N.; Novell-Leruth, G.; Whiting, P.; Liz-Marzán, L. M.; López, N. *Nano Lett.* **2014**, *14* (2), 871–875.
(110) Scarabelli, L.; Grzelczak, M.; Liz-Marzán, L. M. *Chem. Mater.* **2013**, *25* (21), 4232–4238.

(111) Rodríguez-Fernández, J.; Pérez-Juste, J.; Mulvaney, P.; Liz-Marzán, L. M. *J. Phys. Chem. B* **2005**, *109* (30), 14257–14261.
(112) Carbó-Argibay, E.; Rodríguez-González, B.; Pacifico, J.; Pastoriza-Santos, I.; Pérez-Juste, J.; Liz-Marzán, L. M. *Angew. Chem. Int. Ed.* **2007**, *46* (47), 8983–8987.
(113) Carbó-Argibay, E.; Rodríguez-González, B.; Pastoriza-Santos, I.; Pérez-Juste, J.; Liz-Marzán, L. M. *Nanoscale* **2010**, *2* (11), 2377–2383.
(114) Newman, J. D. S.; Blanchard, G. J. *Langmuir* **2006**, *22* (13), 5882–5887.
(115) Khan, Z.; Singh, T.; Hussain, J. I.; Hashmi, A. A. *Colloids Surf. B Biointerfaces* **2013**, *104*, 11–17.
(116) Zümreoglu-Karan, B. *J. Nanoparticle Res.* **2008**, *11* (5), 1099–1105.
(117) Ojea-Jiménez, I.; Romero, F. M.; Bastús, N. G.; Puntes, V. *J. Phys. Chem. C* **2010**, *114* (4), 1800–1804.
(118) Gammons, C. H.; Yu, Y.; Williams-Jones, A. E. *Geochim. Cosmochim. Acta* **1997**, *61* (10), 1971–1983.
(119) Kumar, S.; Gandhi, K. S.; Kumar, R. *Ind. Eng. Chem. Res.* **2007**, *46* (10), 3128–3136.
(120) Rodríguez-Fernández, J.; Pérez-Juste, J.; García de Abajo, F. J.; Liz-Marzán, L. M. *Langmuir* **2006**, *22* (16), 7007–7010.
(121) Gramlich, G.; Zhang, J.; Nau, W. M. *J. Am. Chem. Soc.* **2002**, *124* (38), 11252–11253.
(122) Orendorff, C. J.; Murphy, C. J. *J. Phys. Chem. B* **2006**, *110* (9), 3990–3994.
(123) Hendel, T.; Wuithschick, M.; Kettemann, F.; Birnbaum, A.; Rademann, K.; Polte, J. *Anal. Chem.* **2014**, *86* (22), 11115–11124.
(124) Rao, P.; Doremus, R. *J. Non-Cryst. Solids* **1996**, *203*, 202–205.
(125) García de Abajo, F. J. *Phys. Rev. Lett.* **1998**, *80* (23), 5180–5183.
(126) Yang, J. A.; Lohse, S. E.; Boulos, S. P.; Murphy, C. J. *J. Clust. Sci.* **2012**, *23* (3), 799–809.
(127) Maltzahn, G. von; Park, J.-H.; Agrawal, A.; Bandaru, N. K.; Das, S. K.; Sailor, M. J.; Bhatia, S. N. *Cancer Res.* **2009**, *69* (9), 3892–3900.
(128) Grochola, G.; Snook, I. K.; Russo, S. P.; *J. Chem. Phys.* **2007**, *127*, 194707.
(129) Jackson, S. R.; McBride, J. R.; Rosenthal, S. J.; Wright, D. W. *J. Am. Chem. Soc.* **2014**, *136* (14), 5261–5263.
(130) Bals, S.; Goris, B.; Liz-Marzán, L. M.; Van Tendeloo, G. *Angew. Chem. Int. Ed.* **2014**, *53* (40), 10600–10610.
(131) Lekkerkerker, H. N. W.; Tuinier, T. *Colloids and the Depletion Interaction*; Springer, 2011.
(132) Sánchez-Iglesias, A.; Grzelczak, M.; Pérez-Juste, J.; Liz-Marzán, L. M. *Angew. Chem. Int. Ed.* **2010**, *49* (51), 9985–9989.
(133) Murphy, C. J.; Buriak, J. M. *Chem. Mater.* **2015**, *27* (14), 4911–4913.
(134) Ye, X.; Zheng, C.; Chen, J.; Gao, Y.; Murray, C. B. *Nano Lett.* **2013**, *13* (2), 765–771.
(135) Dong, A.; Chen, J.; Vora, P. M.; Kikkawa, J. M.; Murray, C. B. *Nature* **2010**, *466* (7305), 474–477.
(136) Ye, X.; Jin, L.; Caglayan, H.; Chen, J.; Xing, G.; Zheng, C.; Doan-Nguyen, V.; Kang, Y.; Engheta, N.; Kagan, C. R.; Murray, C. B. *ACS Nano* **2012**, *6* (3), 2804–2817.
(137) Ye, X.; Gao, Y.; Chen, J.; Reifsnyder, D. C.; Zheng, C.; Murray, C. B. *Nano Lett.* **2013**, 2163–2171.
(138) Okamoto, S.; Hachisu, S. *J. Colloid Interface Sci.* **1977**, *62* (1), 172–181.
(139) Malikova, N.; Pastoriza-Santos, I.; Schierhorn, M.; Kotov, N. A.; Liz-Marzán, L. M. *Langmuir* **2002**, *18* (9), 3694–3697.
(140) Luo, Y. *Mater. Lett.* **2007**, *61* (6), 1346–1349.
(141) Rodríguez-Fernández, J.; Pérez-Juste, J.; Mulvaney, P.; Liz-Marzán, L. M. *J. Phys. Chem. B* **2005**, *109* (30), 14257–14261.
(142) Yang, Y.; Wang, W.; Li, X.; Chen, W.; Fan, N.; Zou, C.; Chen, X.; Xu, X.; Zhang, L.; Huang, S. *Chem. Mater.* **2013**, *25* (1), 34–41.
(143) Miranda, O. R.; Dollahon, N. R.; Ahmadi, T. S. *Cryst. Growth Des.* **2006**, *6* (12), 2747–2753.
(144) Khanal, B. P.; Zubarev, E. R. *J. Am. Chem. Soc.* **2008**, *130* (38), 12634–12635.
(145) Myroshnychenko, V.; Carbó-Argibay, E.; Pastoriza-Santos, I.; Pérez-Juste, J.; Liz-Marzán, L. M.; García de Abajo, F. J. *Adv. Mater.* **2008**, *20* (22), 4288–4293.

(146) Lee, K.-S.; El-Sayed, M. A. *J. Phys. Chem. B* **2005**, *109* (43), 20331–20338.
(147) Gu, J.; Zhang, Y.-W.; Tao, F. (Feng). *Chem. Soc. Rev.* **2012**, *41* (24), 8050.
(148) Huang, M. H.; Chiu, C.-Y. *J. Mater. Chem. A* **2013**.
(149) Rodr guez-Lorenzo, L.; lv arez-Puebla, R. A.; Pastoriza-Santos, I.; Mazzucco, S.; St p han, O.; Kociak, M.; Liz-Marz n , L. M.; Garc a de Abajo, F. J. *J. Am. Chem. Soc.* **2009**, *131* (13), 4616–4618.
(150) Liu, Q.; Cui, Y.; Gardner, D.; Li, X.; He, S.; Smalyukh, I. I. *Nano Lett.* **2010**, *10* (4), 1347–1353.
(151) Duncan, B.; Kim, C.; Rotello, V. M. *J. Control. Release Off. J. Control. Release Soc.* **2010**, *148* (1), 122–127.
(152) Wilczewska, A. Z.; Niemirowicz, K.; Markiewicz, K. H.; Car, H. *Pharmacol. Rep. PR* **2012**, *64* (5), 1020–1037.
(153) Millstone, J. E.; Métraux, G. S.; Mirkin, C. A. *Adv. Funct. Mater.* **2006**, *16* (9), 1209–1214.
(154) Banholzer, M. J.; Harris, N.; Millstone, J. E.; Schatz, G. C.; Mirkin, C. A. *J. Phys. Chem. C* **2010**, *114* (16), 7521–7526.
(155) Jana, N. R.; Gearheart, L.; Murphy, C. J. *J. Phys. Chem. B* **2001**, *105* (19), 4065–4067.
(156) Pérez-Juste, J.; Pastoriza-Santos, I.; Liz-Marzán, L. M.; Mulvaney, P. *Coord. Chem. Rev.* **2005**, *249* (17–18), 1870–1901.
(157) Kowalczyk, B.; Lagzi, I.; Grzybowski, B. A. *Curr. Opin. Colloid Interface Sci.* **2011**, *16* (2), 135–148.
(158) Xiong, B.; Cheng, J.; Qiao, Y.; Zhou, R.; He, Y.; Yeung, E. S. *J. Chromatogr. A* **2011**, *1218* (25), 3823–3829.
(159) Xu, X.; Caswell, K. K.; Tucker, E.; Kabisatpathy, S.; Brodhacker, K. L.; Scrivens, W. A. *J. Chromatogr. A* **2007**, *1167* (1), 35–41.
(160) Mao, Y.; Cates, M. E.; Lekkerkerker, H. N. W. *Phys. Stat. Mech. Its Appl.* **1995**, *222* (1–4), 10–24.
(161) Park, K.; Koerner, H.; Vaia, R. A. *Nano Lett.* **2010**, *10* (4), 1433–1439.
(162) Jana, N. R. *Chem. Commun.* **2003**, No. 15, 1950–1951.
(163) Aswal, V.; Goyal, P. *Phys. Rev. E* **2000**, *61* (3), 2947–2953.
(164) Malliaris, A.; Binana-Limbele, W.; Zana, R. *J. Colloid Interface Sci.* **1986**, *110* (1), 114–120.
(165) Payne, E. K.; Shuford, K. L.; Park, S.; Schatz, G. C.; Mirkin, C. A. *J. Phys. Chem. B* **2006**, *110* (5), 2150–2154.
(166) Kawata, S.; Ono, A.; Verma, P. *Nat. Photonics* **2008**, *2* (7), 438–442.
(167) Cortes, C. L.; Newman, W.; Molesky, S.; Jacob, Z. *J. Opt.* **2012**, *14* (6), 063001.
(168) Shalaev, V. M. *Nat. Photonics* **2007**, *1* (1), 41–48.
(169) Lu, G.; De Keersmaecker, H.; Su, L.; Kenens, B.; Rocha, S.; Fron, E.; Chen, C.; Van Dorpe, P.; Mizuno, H.; Hofkens, J.; Hutchison, J. A.; Uji-i, H. *Adv. Mater.* **2014**, *26* (30), 5124–5128.
(170) McLintock, A.; Cunha-Matos, C. A.; Zagnoni, M.; Millington, O. R.; Wark, A. W. *ACS Nano* **2014**, *8* (8), 8600–8609.
(171) Tonga, G. Y.; Saha, K.; Rotello, V. M. *Adv. Mater.* **2014**, *26* (3), 359–370.
(172) Tsai, M.-F.; Chang, S.-H. G.; Cheng, F.-Y.; Shanmugam, V.; Cheng, Y.-S.; Su, C.-H.; Yeh, C.-S. *ACS Nano* **2013**, *7* (6), 5330–5342.
(173) Mubeen, S.; Lee, J.; Singh, N.; Krämer, S.; Stucky, G. D.; Moskovits, M. *Nat. Nanotechnol.* **2013**, *8* (4), 247–251.
(174) Sarina, S.; Waclawik, E. R.; Zhu, H. *Green Chem.* **2013**, *15* (7), 1814.
(175) DeSantis, C. J.; Sue, A. C.; Bower, M. M.; Skrabalak, S. E. *ACS Nano* **2012**, *6* (3), 2617–2628.
(176) Fan, F.-R.; Liu, D.-Y.; Wu, Y.-F.; Duan, S.; Xie, Z.-X.; Jiang, Z.-Y.; Tian, Z.-Q. *J. Am. Chem. Soc.* **2008**, *130* (22), 6949–6951.
(177) Jin, M.; Zhang, H.; Wang, J.; Zhong, X.; Lu, N.; Li, Z.; Xie, Z.; Kim, M. J.; Xia, Y. *ACS Nano* **2012**, *6* (3), 2566–2573.
(178) DeSantis, C. J.; Skrabalak, S. E. *J. Am. Chem. Soc.* **2013**, *135* (1), 10–13.
(179) Li, N.; Zhao, P.; Astruc, D. *Angew. Chem. Int. Ed.* **2014**, *53* (7), 1756–1789.
(180) Ah, C. S.; Hong, S. D.; Jang, D.-J. *J. Phys. Chem. B* **2001**, *105* (33), 7871–7873.

(181) Hong, S.; Choi, Y.; Park, S. *Chem. Mater.* **2011**, *23* (24), 5375–5378.
(182) Gómez-Graña, S.; Goris, B.; Altantzis, T.; Fernández-López, C.; Carbo-Argibay, E.; Martínez, A. G.; Almora-Barrios, N.; Lopez, N.; Pastoriza-Santos, I.; Perez-Juste, J.; Bals, S.; Van Tendeloo, G.; Liz-Marzán, L. M. *J. Phys. Chem. Lett.* **2013**.
(183) Le Ru, E. C.; Grand, J.; Sow, I.; Somerville, W. R. C.; Etchegoin, P. G.; Treguer-Delapierre, M.; Charron, G.; Félidj, N.; Lévi, G.; Aubard, J. *Nano Lett.* **2011**, *11* (11), 5013–5019.
(184) Ming, T.; Chen, H.; Jiang, R.; Li, Q.; Wang, J. *J. Phys. Chem. Lett.* **2012**, *3* (2), 191–202.
(185) Bagheri, S.; Giessen, H.; Neubrech, F. *Adv. Opt. Mater.* **2014**, *2* (11), 1050–1056.
(186) Seo, D.; Yoo, C. I.; Jung, J.; Song, H. *J. Am. Chem. Soc.* **2008**, *130* (10), 2940–2941.
(187) Li, Q.; Jiang, R.; Ming, T.; Fang, C.; Wang, J. *Nanoscale* **2012**, *4* (22), 7070.
(188) Muhlschlegel, P. *Science* **2005**, *308* (5728), 1607–1609.
(189) In *IUPAC Compendium of Chemical Terminology*; Nič, M., ir t, ., Košata, B., enkins, A., McNaught, A., Eds.; IUPAC: Research Triagle Park, NC, 2009.
(190) Ahn, S.-H.; Kim, D.-S.; Seo, D.; Choi, W.; Yi, G.-R.; Song, H.; Park, Q.-H.; Kim, Z. H. *Phys. Chem. Chem. Phys.* **2013**, *15* (12), 4190–4194.
(191) Young, K. L.; Jones, M. R.; Zhang, J.; Macfarlane, R. J.; Esquivel-Sirvent, R.; Nap, R. J.; Wu, J.; Schatz, G. C.; Lee, B.; Mirkin, C. A. *Proc. Natl. Acad. Sci.* **2012**, *109* (7), 2240–2245.
(192) Mason, T. *Phys. Rev. E* **2002**, *66* (6).
(193) Tebbe, M.; Kuttner, C.; Mayer, M.; Maennel, M.; Pazos-Perez, N.; König, T. A.; Fery, A. *J. Phys. Chem. C* **2015**.
(194) Zhang, S.; Chen, L.; Huang, Y.; Xu, H. *Nanoscale* **2013**, *5* (15), 6985–6991.

CHAPTER

SELF-ASSEMBLY OF PLASMONIC NANOPARTICLES

III.1. INTRODUCTION

Self-assembly processes are ubiquitous in nature at all scales, from the formation of crystals to the creation of planetary systems.[1,2] In particular, living systems are clear evidence that very complex structures can be built by letting simple constituents organize themselves as dictated by their intrinsic properties;[3,4] even more important for life, these systems are constantly adapting to external stimuli (temperature, light, nutrients, among others) in a bundle of dynamic and integrated adaptive processes.[5] In fact in his famous lecture, Professor Richard Fayman already identified biological systems as the living proof-of-principle that the dream of a bottom-to-bottom approach for the fabrication of nanoscale devices is ultimately possible (see section I.1). Some examples of natural systems that are based on self-assembly can be found in **Figure III.1**: the colors of the wings of butterflies and the skin of chameleons both arise due to structural colors (**Figure III.1A - G**);[6–8] beetles crawl upside-down by adhesive fibers that are clustered and unclustered under their feet (**Figure III.1H - I**);[9] the high hydrophobicity of hairy plant leaves (also known as lotus effect, **Figure III.1J**);[10,11] the reversible underwater adhesion of setae-covered gecko feet;[12] even the packing of DNA inside the chromosomes (**Figure III.1K**).[13] To use the words of the Nobel Prize winner Albert Szent-Gyorgy "the nonstop beating and whirling of living systems are nature's answer to an electron looking for a place to rest";[14,15] from this statement we can understand how all self-assembly processes are driven by minimization of the free energy of the final assembled structure, which will exist in equilibrium or at least in metastable states (see section III.1.2.1).

By joining together the two concepts described above, i.e. the formation of ordered structures and the evolution towards an equilibrium state, brings us to a third important concept: self-assemblies are governed by the balance of attractive and repulsive interactions, such as van der Waals, Coulomb, hydrogen bonding or hydrophobic interactions to name a few.

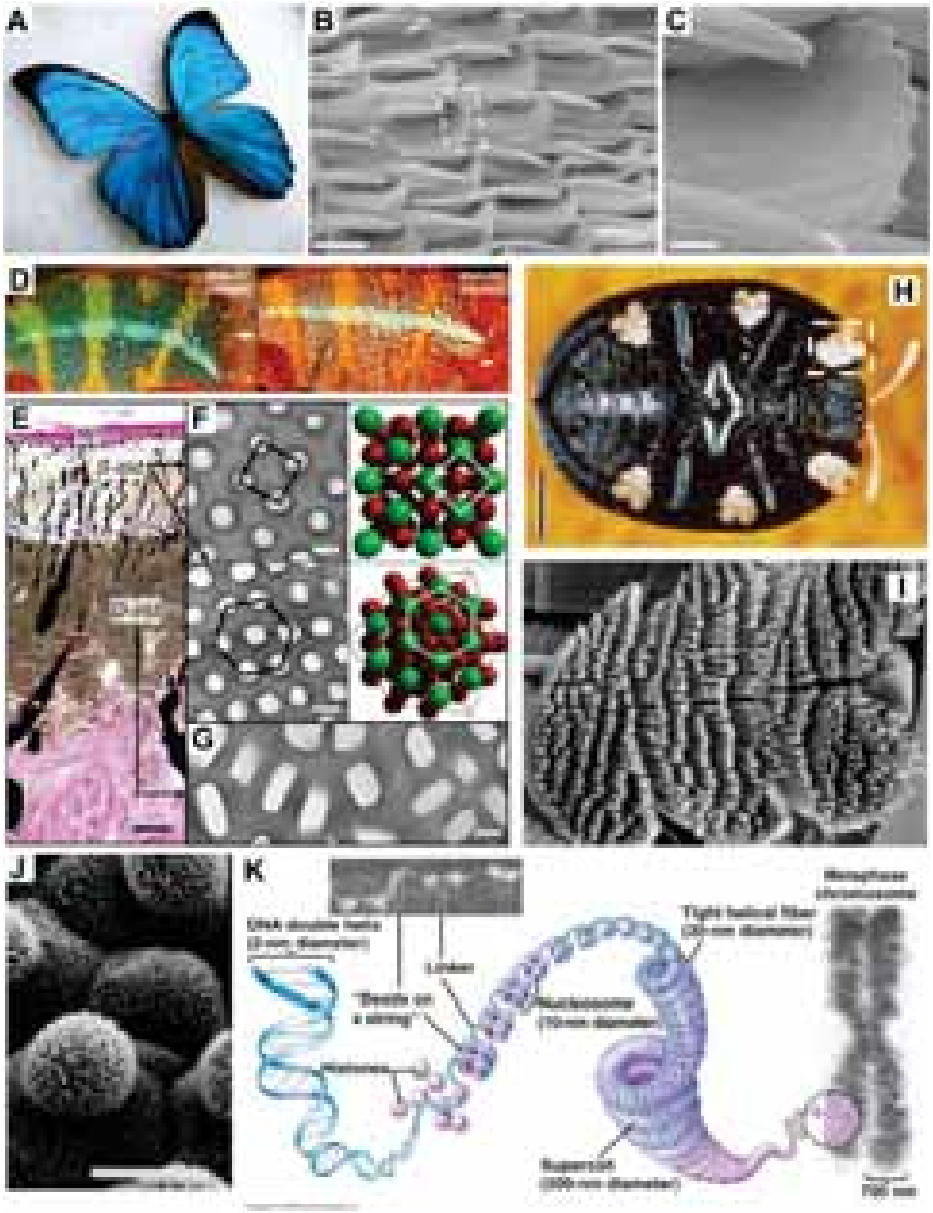

Figure III.1. A: Optical image of a *Giant Blue Morpho* butterfly. **B:** SEM image of scales in the colored wing region and **C:** close-up image of the curled region from which the color originates. **D:** Reversible color change for a male chameleon: during excitation (white arrows), background skin shifts from the baseline state (green) to yellow/orange. **E:** Haematoxylin and eosin staining of a cross-section of white skin showing the epidermis and the two thick layers of iridophores. **F:** TEM images of guanine nanocrystals in S-iridophores in the excited state and three-dimensional model of an fcc lattice (shown in two orientations). **G:** TEM image of guanine nanocrystals in D-iridophores. **H:** Ventral view of beetle, showing yellow tarsi. **I:** Close-up image of a normal tarsus. **J:** SEM image of the adaxial leaf water-repellent surface of *Colocasia Esculenta*. **K:** Graphical scheme representing the packaging of DNA inside chromosomes. Scale bars: **B:** 50 μm, **C:** 20 μm , **E:**20 mm. **F-G:** 200 nm. **H:** 1 mm. **I:** 100 μm. **J:** 20 μm. Adapted from **A:** Ref. 6**, B-C:** Ref. 7, **D-G:** Ref. 8, **H-I:** Ref. 9, **J:** Ref.11, **K:** Ref. 16.

From this perspective, supramolecular chemistry can be interpreted as self-assembly at the molecular level, and indeed, this field is often referred to as "molecular self-assembly", being able of creating ordered and complex molecular structures that are impossible to obtain through standard synthetic chemistry;[17,18] probably one of the most elegant examples is the synthesis of the Molecular Borromean Rings, proposed by F. Stoddart in 2012 (**Figure III.2.A**).[19,20]

Even though molecular self-assembly was the first one being developed in the 1980s,[17] there are many opportunities in its application to the nano-, micro- and even macroscale.[15,21,22] The interest has grown when self-assembly was recognized as one of the most general strategies toward the generation of ordered nanostructures,[1,15,23,24] with potential application in microelectronics[25], photonics[26,27] or near field optics,[28] among others. The last decade has seen an intense activity in the field, leading to the development of many different strategies for the production of ordered structures using nano- and micro- building blocks. Some of the most remarkable achievements are summarized in **Figure III.2.B - D**: Aizenberg et al. pursued a bio-inspired approach for the development of new materials based on the assembly of fibers presenting different stiffness, aspect ratio and surface chemistry (**Figure III.2.B**);[4,5] Grzybowski et al. concentrated on the Coulombian interaction between oppositely-charged nanoparticles to drive their self-assembly into micron-sized crystals that they proposed as chemical amplifiers for optical sensors (**Figure III.2.C**);[29–31] while Wang et al., and more recently Mirkin et al., explored the use of DNA coated nanoparticles for rational programmable self-assembly (**Figure III.2.D**).[32–37]

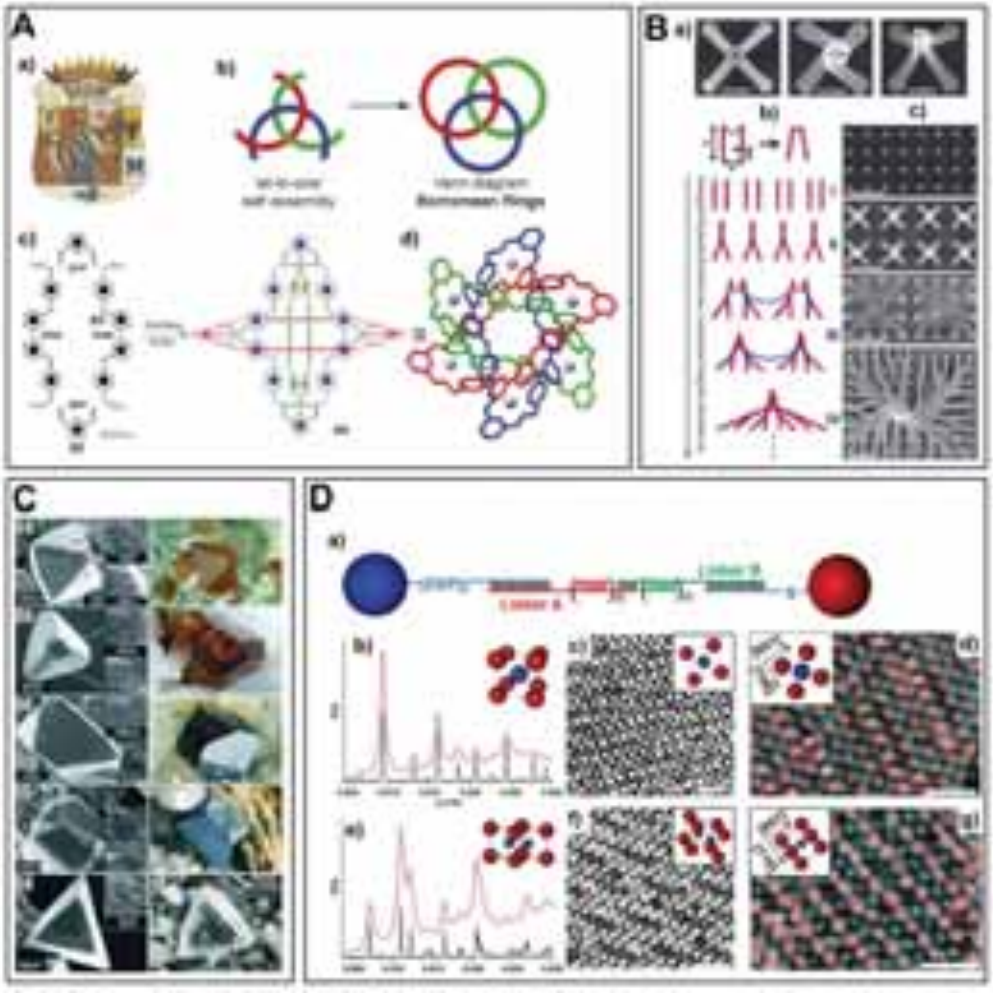

Figure III.2. A: Molecular Borromean Rings: a) The symbol of the Borromeo family of Renaissance Italy, the Borromean rings topology appears on their family crest. b) Schematic diagram showing the "all-in-one" approach to synthesizing molecular Borromean Rings. c) Synthesis of the Zn(II)-templated assembly (84) from $Zn(OAc)_2$, diformylpyridine (82), and the diaminobipyridine compound (83). d) Tubular representation of the solid-state structure of 84 with each individual ring colored red, blue, and green and the Zn(II) cations depicted as silver spheres. **B: Assembly of fibers into diverse shapes and hierarchical architectures:** a) Clusters of fibers connected at the tips (left), twisted into a chiral bundle (center), or zipped together (right). b) Schematic and c) corresponding SEM images showing the hierarchical assembly of fiber arrays into higher order chiral structures. **C: Diamond-like nanoparticle crystals.** The left column shows SEM images of diamond-like crystals formed from oppositely charged, 5 nm gold and silver nanoparticles. Insets zoom on the particles forming the faces of the crystals. The right column shows zinc-blend crystals (lattice isostructural with diamond) with similar morphologies. **D: Characterization of binary superlattices assembled from silver and gold nanoparticles**. a) Schematic illustration of the assembly of binary silver-gold nanoparticle superlattices where the linker lengths can be tuned by increasing *n*. b-c,e-f) SAXS patterns (and the corresponding unit cell) and STEM images of binary silver–gold nanoparticle superlattices that are isostructural with CsCl (b,c) and AlB_2(e,f). d-g) EDX elemental maps of AB- (d) and AB_2-type (g) binary lattices with the zone axis shown in the insets. Gold is shown in red and silver in blue. Scale bars: **B: a):** 1 μm, **b)** 4 μm. **D:** 100 nm. Adapted from **A:** Ref. 19**, B:** Ref. 38, **C:** Ref. 30, **D:** Ref. 35.

III.1.1. Definition of Self-Assembly

Self-assembly is an increasingly used notion within the scientific community. However, the term has often been misused in the literature, to the point that an exact definition of this phenomenon does not seem to be clear and straightforward.[39] In fact, the boundaries between self-assembly and other phenomena like molecular recognition, aggregation or complexation are more or less defined at the whim of whoever is using them.[15,40] Generally, self-assembly can be defined as the "autonomous re-organization of pre-existing disordered components into patterns or structures, without human intervention", but in this sense, the term self-assembly can be often exchanged with the more generic one *formation*.[1,41]

In order to clarify what self-assembly really is, we should keep in mind some important features that are essential for the definition.

1) The shaped structure must present a certain degree of order, at least at one scale. When the final structure presents different levels of order at different dimensions, each of which confers a new level of complexity and new properties to the structure, we speak about hierarchical self-assembly (e.g. the packaging compaction of DNA, **Figure III.1.K**).
2) The assembly is achieved through the balance between attractive and repulsive interactions, which can be divided into short-range (such as van der Waals, hydrophobic interactions[42] or hydrogen bonding[43]) and long-range ones (like capillarity or flow dragging);[44,45] the former are typically tuned modifying the coating of the nanoparticles while the latter are tuned by modifying the surrounding medium or through the introduction of a template (see section III.1.3).[46]
3) The existence of a design. The building blocks are chosen to obtain a particular structure, exploiting properties that are encoded in the building blocks themselves: concentration,[47] number of different building blocks,[48–50] surface chemistry[43,51–53] and shape[54] are the most important features that can be exploited for the design of a self-assembly experiment. The term "Directed" self-assembly is often used when referring to this concept.[41]

Considering the three above conditions, it seems clear that the most difficult task when dealing with self-assembly is the construction of the building blocks: in fact, if the appropriate interactions are correctly encoded, assembly should proceed by itself towards the most stable ordered structure. However, we still lack sufficient understanding of how to systematically encode such interactions directly into the building blocks to drive their assembly into ordered structures, particularly at the nanoscale.

III.1.2. Classification of Self-Assembly Modalities

Self-assembly is a very diverse phenomenon (see section III.1); consequently, it can be classified in many different ways, depending of which aspect of the process one decides to take into consideration.

III.1.2.1. Energy: Static and Dynamic Self-Assembly

From a thermodynamic point of view it is important to distinguish two different kinds of processes: static and dynamic self-assembly. In the first case the building blocks will self-assemble into the most stable ordered structure, reaching thermodynamic equilibrium, so that the ordered structure will be stable once formed. On the other hand, dynamic self-assembly (also called self-organization or dissipative self-assembly)[40] occurs in non-equilibrium systems and the order will fall apart once the external energy ceases to be dispensed, i.e. the assembly persists only if the system is dissipating energy.[1,40] This clearly complicates the picture[55–57] but can lead to the creation of assembled systems that are highly responsive and capable of a higher level of adaptability to environmental changes, capable of self-healing and can potentially self-replicate, as can be easily appreciated by observing a living cell.[58]

It is especially important to keep in mind the distinction between static and dynamic self-assembly, since the latter concept is often confused with the one of "reconfigurable" self-assembly (see section III.1.2.2.), where the system can be switched between multiple equilibrium states. While nowadays we have a consistent knowledge regarding static self-assembly, the study of dynamic self-assembly is still in its early stages; one of the few examples is the study proposed by Grzybrowski et al. for the assembly of gold nanoparticles functionalized with molecules carrying an azo-benzene moiety: this molecule exists in its

trans form, but is able to switch to *cis* upon irradiation with UV light, and return to the more stable form once the light source is switched off. When the ligands are in *cis* form the nanoparticles get organized into three-dimensional crystals, which are stable only under continuous UV-irradiation.[59]

III.1.2.2. Stability: Reversible, Irreversible and Reconfigurable Self-Assembly

As stated above (see section III.1), self-assembly is typically driven by the balance between attractive and repulsive interactions. In fact, this allows the system to assemble through a trial-and-error stochastic procedure, minimizing the defects through auto-correction. Consequently, self-assembly is generally seen as an easily reversible process, but this is not always the case. It is important to underline here that the distinction between reversible and irreversible can dramatically change depending on the considered conditions: crystallization appears as an irreversible process if compared to protein folding, but under suitable conditions also a crystal can be de-assembled into its original components.

More interesting is the case of self-assemblies that can respond to external stimuli, and either de-assemble, or reorganize into a different self-assembled structure.[41,60] A nice example of these responsive materials has recently been explored by our group: gold nanoparticles coated with a polystyrene/polyacrylic acid diblock-copolymer shell are able to respond to the composition of the solvent, forming clusters upon water addition and redispersing if water is removed.[42,61]

III.1.2.3.Dimensionality: 1D, 2D, 3D Self-Assembly

This classification is probably the most straightforward one. Examples of 1D and 2D assemblies can be found in the literature for a variety of different systems. For example, a high degree of control for the production of 1D assemblies has been achieved in a two-plate configuration, where particles are confined between two surfaces, one fixed and the other sliding at a specific distance, angle and speed,[49] or engineering wrinkles over a polydimethylsiloxane (PDMS) surface where the particles are drop-casted (**Figure III.3A**).[62,63] It is also possible to design 1D self-assembly in solutions, for example exploiting the different reactivity of a specific ligand as a function of the surface curvature,[52]

or combining amphiphilic nanorods and hydrophobic interactions.[64] Regarding 2D assemblies, many different groups demonstrated the formation of almost perfect assemblies at liquid-liquid or liquid-air interfaces, as well as by drop casting concentrated nanoparticle solutions on various substrates (**Figure III.3B** and section IV.2.3).[65–68] On the contrary, 3D constructs are only recently being explored.[44,46] The third dimension is particularly challenging, since it cannot be easily achieved through lithographic approaches. Even though supramolecular chemistry has been proposed for the "development" of the third dimension starting from a 2D assembly, the most promising results have been achieved using templated self-assembly (see section III.1.3), since it allows the creation of a 3D structure in a single step (see section III.2.1).

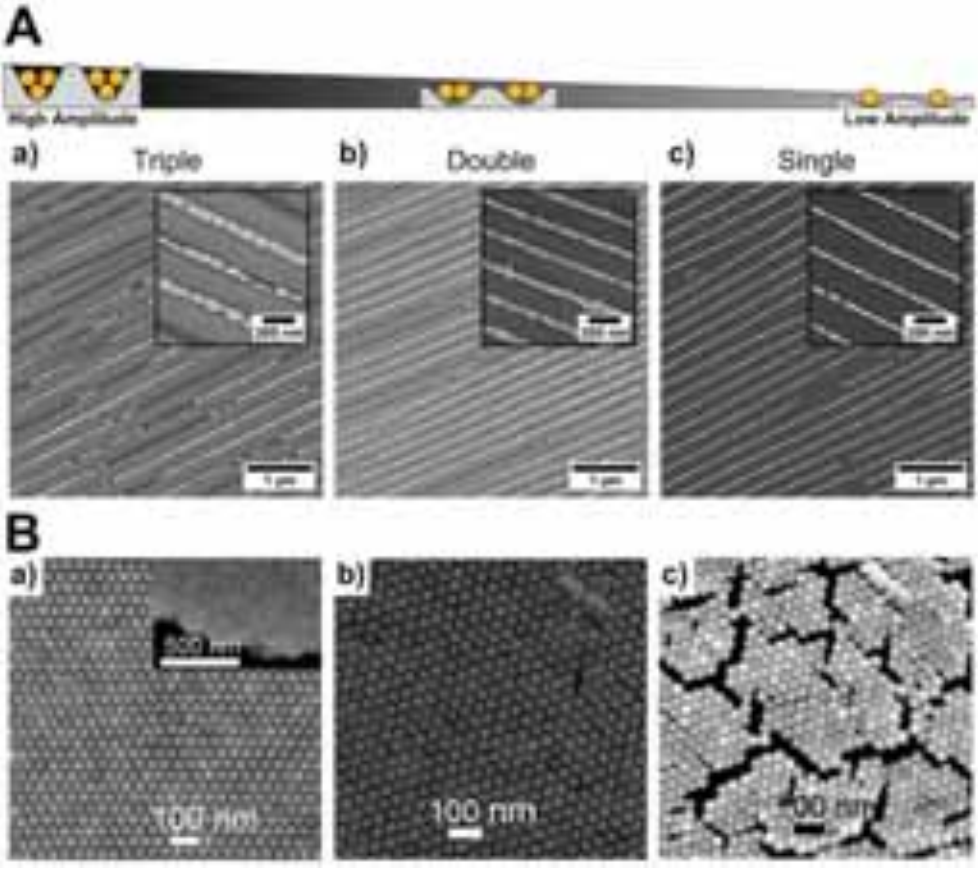

Figure III.3. A: Amplitude dependent linear assembly of bovine serum albumin functionalized gold nanorods into wrinkles using dip-coating. Organization of gold nanorods into a) triple lines, b) double lines, and c) single lines, decreasing the amplitude of the wrinkles. **B:** a) SEM images of vertical gold nanorod monolayer arranged in a hexagonal lattice. The edge-to-edge gap distance is 7.7 nm; the inset shows the monolayer feature. b-c) SEM images of the same vertical arrays before (b) and after (c) treatment by oxygen plasma. The edge-to-edge gap distance becomes sub-nanometer, 0.8 nm. Adapted from **A:** Ref. 63**, B:** Ref.69

III.1.2.4. Driving Force: Internal Forces, External Fields and Templated Self-Assembly.

As explained before (section III.1.2.1), self-assembly is a dissipative process triggered by different types of interactions between the building blocks. These interactions can arise from the particles themselves,[41,70–72] from an applied external field,[41,70] from a template,[46,73] or from entropic forces alone (phenomenological forces resulting from the entire system's statistical tendency to increase its entropy).[74,75]

III.1.2.4.1. Self-Assembly Triggered by Internal Forces.

In this case, the energy is dispensed through interactions between the building blocks, according to their size, shape and surface chemistry. The forces into play can be physical (e.g. hydrophobic or electrostatic interactions,[42,76] depletion attractions[44,77,78]), chemical (hydrogen bonding,[43] supramolecular chemistry,[79] formation of covalent bonds[80]) or biological (DNA,[36,37] antibody-antigen,[81,82] avidin-biotin[83,84]). For example Stoddart et al. demonstrated the formation of nanoparticle dimers, trimers, tetramers and linear chains triggered by the formation of pseudo-rotaxanes,[79] while Kumacheva et al. were able to assemble amphiphilic gold nanorods into different structures (including rings, chains, bundles and spheres) by simply changing the composition of the solvent.[64]

III.1.2.4.2. Self-Assembly Triggered by External Fields – Assisted Self-Assembly.

Various approaches have been developed to guide the self-assembly of nanoparticles exploiting the presence of an external field. We have already discussed some examples of self-assembly induced by light (section III.1.2.2), but other external forces have been successfully adopted, such as electric fields,[85] magnetic fields[86] or mechanical forces.[87,88] For example our group demonstrated that trapping gold nanorods inside a poly(vinyl alcohol) matrix it is possible to align them by simply stretching the matrix,[87] while more recently Klajn et al. triggered the assembly of cubic magnetic nanoparticles into well-defined double and triple helix suprastructures.[86]

III.1.2.4.3. Templated or Controlled Evaporative Self-Assembly

A template can be defined as any object serving as scaffold onto which the building blocks can be arranged into a structure presenting a morphology complementary to the one of the template.[41] Several approaches have been reported that combine soft lithography (for the preparation of the template) and evaporative self-assembly, which can be classified according to the dimensions of the pattern. Controlled evaporation within a pattern having dimensions of the order of magnitude of the particles has been used to form monolayers of discrete building blocks.[89–93] For example, Zhou et al. used an elastomeric template to selectively assemble single gold particles according to their shape and size, over several micrometers, using microcontact printing to transfer the particle monolayer onto a substrate of interest.[89] A second group of techniques comprises the use of patterns that have wider dimensions than the individual building blocks, from which supercrystals can be built.[94,95] In this respect, Thai et al. reported the assembly of gold nanorods into small supercrystals within a silicon pattern having different wettability properties.[94] Nanoparticles can also be evaporated directly on a substrate by using a template having significantly larger dimensions than the building blocks.[44,96–98] Large supercrystals have been built in this way, even through one-step processes, an interesting example being the work of Hamon et al., who reported the controlled evaporation of a suspension of gold nanorods in between micron-sized pillars on a substrate, resulting in a three-dimensional maze.[44]

III.2. SELF-ASSEMBLY OF PLASMONIC NANOPARTICLES: PROPERTIES AND APPLICATIONS

One reason behind the effort in designing and understanding self-assembled systems is the capability of these structures to show properties that are distinct to those of the building blocks.[72,99–101] Here we focus on the properties and applications of plasmonic nanoparticle assemblies. As we discussed in the introduction of this thesis (see section I.2.2), plasmonic properties of nanoparticles can be strongly influenced by nanoparticle mutual orientation and distance. In particular, when nanoparticles are close enough to each other (<10nm), near-field coupling occurs between the plasmon modes of neighboring nanoparticles. This

phenomenon strongly affects the energy of the resulting collective plasmon modes. For example, an end-to-end configuration leads to a redshift of the longitudinal plasmon band of gold nanorods, whereas a side-by-side configuration would lead to a blueshift.[102] Interestingly, the coupling of plasmon modes results in intense electric fields localized at the gap between two interacting particles, the so-called hot-spots.[103–106] In this scenario, the self-assembly of noble metal nanoparticles can be seen as "plasmon or hot-spot engineering", with promising applications for optical sensing of a variety of different analytes (heavy metals[107,108], oligonucleotides,[109] aminoacids,[110,111] proteins,[112] pathogens,[113] or toxins[81]), SERS,[69,103,104,114–118] metamaterials,[35,119,120] and photovoltaics,[121] or as nanoscale thermometers[122] or plasmon-rulers.[123] Control of interparticle spacing in self-assembled structures has been achieved through encapsulation with different shell thickness,[124] DNA interactions,[125] stimuli-responsive polymer coatings[126,127] or engineering the type and distribution of different ligands on the nanoparticle surface.[52,128] Another interesting optical property that can arise from nanoparticle assembly is plasmon chirality. Various groups, including Alivisatos, Kotov and Liz-Marzán have reported strong chiral effects in different plasmonic assemblies, including helically arranged gold nanorods,[129] and gold nanoparticles arranged in trimers, tetramers and tetrahedral clusters.[130,131] Apart from the optical properties described above, self-assemblies of metal nanoparticles present also interesting electronic properties for the design of nanoscale electronic devices. In particular, 2D assemblies of gold nanoparticles have been shown to conduct electricity.[132]

III.2.1. Hierarchical Self-Assembly of Gold Nanoparticles into Patterned Plasmonic Nanostructures

On the way toward the practical implementation of nanostructured devices, in parallel to the preparation of crystalline assemblies of nanoparticle building blocks, increasing interest has been placed on the design of multi-functional platforms. The surface chemistry and composition of such smart materials can be tuned to induce properties like localized heating, sensing, or target trapping and release on the same spot.[103,133–139] These systems have been used for ultratrace detection of molecular targets and show promise in various technologies ranging from medicine to homeland security.[104,140,141] Therefore, there is large interest in

combining the properties of nanostructured materials with an overall control of the topography in order to manufacture (bio)active surfaces. This emerging class of materials can interact with analytes of different sizes ranging from small proteins to living cells, thanks to the modulation of surface chemistry as well as the topography of the substrate. In this last case, the topography is an important parameter to direct the fate of living cells as it can modulate their adhesion, which is important e.g. in tissue engineering.[136,142,143] On the other hand, such implementation would require the fabrication of patterned surfaces with high throughput, which could be used in various fields such as non-fouling surfaces,[144] antimicrobial materials[145] or biosensor component design,[103,105,146] among others. Surface topography can be modulated by a variety of methods such as soft lithography, which allow a fine control over the morphology of pattern features. Nanofabrication techniques[147–150] such as stamping[151] or micro-molding in capillaries[152] have been explored for the assembly of polymers,[153] polystyrene beads,[154] inorganic particles,[149] as well as to perform chemical reactions *in-situ*.[152] Three of the major challenges toward the integration of nanoparticle superstructures into commercially viable applications are the simplification of the self-assembly process, reduced cost and scalability.[155] Unfortunately, improving the scalability often involves the use of more complex setups, in turn increasing the overall cost. The design of a technique combining these three aspects would thus be highly relevant in fields ranging from optoelectronics to the fabrication of bioactive surfaces.

Taking advantage of both gold nanoparticle self-assembly and the surface tunability of soft lithography techniques we present in this work a simple method that allows patterning arbitrary substrates with gold nanoparticle supercrystals over large areas through a one-step process. To tackle problems of reproducibility occurring in previously reported methods, we used an elastomeric template made of PDMS displaying arrays of micron-sized cavities that help regulating the evaporation of the gold nanoparticle colloid directly on a substrate of interest. We thereby achieved a high control over supercrystal morphology and thereby tuned the topography of the patterned substrate on the millimeter scale. We additionally demonstrate that the prepared supercrystals show high homogeneity and can be used for highly sensitive SERS detection. This multifunctional platform may result of high relevance for new strategies toward the design of point of care devices.

III.2.1.1. Preparation of Supercrystals

Nanoparticles of different shapes and sizes were synthesized as building blocks for the formation of supercrystal arrays. We prepared gold nanospheres of 17 ± 2 nm in diameter and two different types of gold nanorods with different dimensions. Smaller, single crystal gold nanorods (55 ± 6 nm length; 17 ± 2 nm width, **Figure III.4A - C**) were synthesized following a seed mediated process involving a pre-reduction step with 5Br-SA (see section II.2.7.1). This high yield synthesis developed by Murray and coworkers[156] and refined in the context of the present PhD thesis[157] leads to gold nanorods with narrow size distributions, which is crucial for high quality self-assembly.[103,158] Larger penta-twinned gold nanorods were synthesized as previously described by Pérez-Juste et al., and purified as described above (see section II.4.1).[159,160] In all cases CTAB was exchanged by (1-mercaptoundec-11-yl)hexa(ethyleneglycol) (MUDOL), a commercially available amphiphilic ligand bearing a thiol moiety. MUDOL has been reported to cap gold nanorods, and it is known to induce smectic order upon solvent evaporation.[44,161] Ligand exchange (see Experimental Section, section III.3.3) was confirmed by a 5 nm red-shift of the longitudinal plasmon band (**Figure III.4D**). In a typical experiment, nanorods were stabilized with 0.1 mM MUDOL together with residual CTAB in solution (below cmc) and remained well dispersed for weeks. However, the stability of the rods in solution was found to be dependent on the presence of a certain amount of CTAB: when the gold nanorods coated with MUDOL were diluted in an equal volume of water, fast aggregation occurred, resulting in a split of the longitudinal plasmon band into a double band with two peaks centered at 635 nm and 800 nm (**Figure III.4E**). This was attributed to preferential side-to-side aggregation of the nanorods and the corresponding plasmon coupling. When the initial amount of CTAB was recovered, complete disassembly was observed (**Figure III.4F**). This reversible aggregation has been previously reported by Xie et al.[161] and supports the replacement of CTAB by MUDOL, even if the positive surface charge of MUDOL coated nanorods (ζ = + 10 mV) indicates that some residual CTAB remains on the nanorods surface.[44]

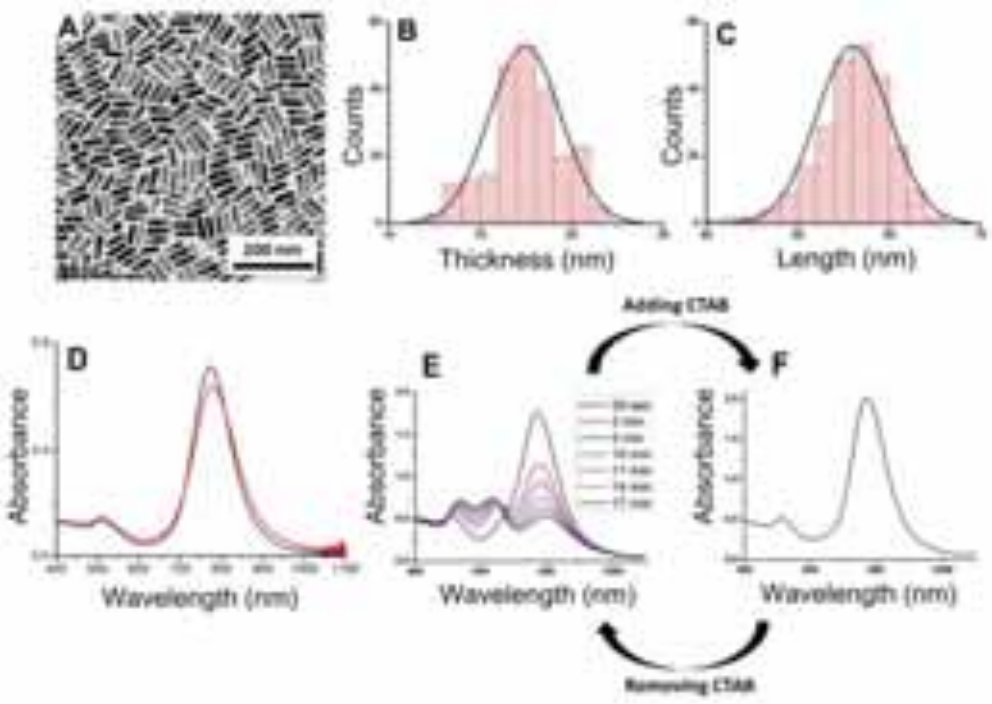

Figure III.4. Characterization of single crystal gold nanorods. A: Representative TEM image of as synthesized nanorods with mean length of 55 ± 6 nm, width of 17 ± 2 nm, and aspect ratio of 3.2 ± 0.4. **B-C:** Histograms of the width and length of the gold nanorods. Statistics were performed over 200 particles using a semi-automated procedure in the open access software Image J. **D:** UV-Vis spectra of a gold nanorod colloid before (black) and after (red) functionalization with MUDOL. A redshift of 5 nm was registered. **E-F:** UV-Vis spectra of gold nanorod colloids with varying CTAB concentration. **E:** 0.25 mM CTAB and 0.05 mM MUDOL: fast aggregation was observed within 17 min after dilution in an equal volume of water. **F:** 0.5 mM CTAB and 0.05 mM MUDOL: a stable dispersion was obtained. Addition of CTAB to the solution in **E** restores nanoparticle stability.

Standard CTAB coated gold nanorods form close packed structures upon drying only at high initial concentration ($[Au^0]$ = 1.5 mM), whereas no self-assembly into standing superlattices was noticed at lower concentrations, in agreement with previous reports.[162] In fact, CTAB coated gold nanorods possess a positive surface charge (ζ = +40 mV) inducing highly repulsive forces between adjacent gold nanorods during the drying process. On the other hand, the zeta potential of MUDOL rods was significantly lower (ζ = +10 mV) and self-assembly into standing supperlattices occurred even at low nanorod concentrations (i.e. below 1.5 mM). In order to compare the packed structures obtained with both ligands, the self-assembly of CTAB and MUDOL capped gold nanorods was compared in TEM at a Au(0) concentration of 1.5 mM. Evaporation was allowed to proceed for 4 - 6 hours in a

homemade setup (**Figure III.5A**). Whereas CTAB capped gold nanorods formed a net-like structure over large areas, MUDOL capped gold nanorods formed discrete islands of ≈ 2 μm in diameter (**Figure III.5B - E**). Although CTAB coated gold nanorods did show local organization, both lying and standing nanorods were observed. Conversely, all MUDOL coated gold nanorods seem to be standing. Therefore, all nanoparticles used for this work were functionalized with MUDOL using the same procedure.

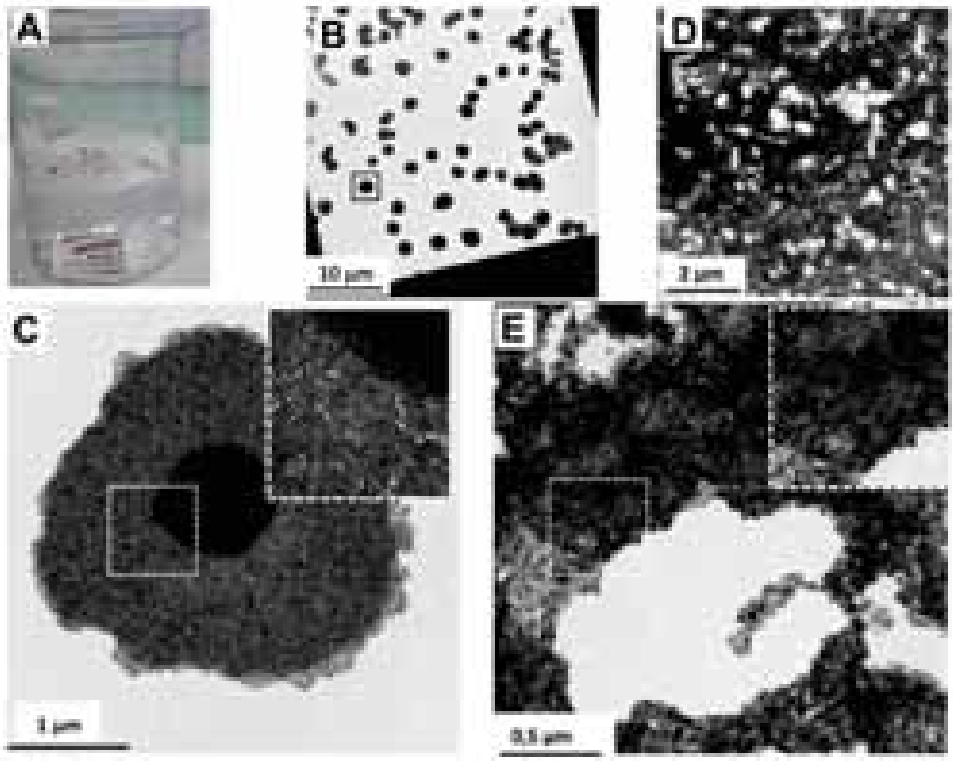

Figure III.5. Comparison of the self-assembly properties of MUDOL and CTAB coated nanorods by drop casting on TEM grids. A: Home-made setup used to slow down the evaporation of the solvent. Gold nanorods colloids were drop casted (10 μL) on a TEM grid inserted in a Petri dish. The support containing the drying droplet was carefully placed in a beaker which was half filled with water. The beaker was covered with a glass watch. Samples were completely dried after 4 - 6 h instead of 2 h in air. **B-C:** TEM images at different magnifications of MUDOL coated gold nanorod assemblies. The inset in **C** shows a homogeneous standing supperlattice. **D-E:** TEM images at different magnifications of CTAB coated gold nanorod assemblies. The inset in **E** shows a non-uniform organization of the nanorods but with a certain local order.

When gold nanorods self-assemble on a flat substrate by drop casting, supercrystals are formed upon drying with a random organization and a wide distribution of supercrystal sizes but mostly with circular shape. Additionally, due to the coffee stain effect,[163] the density of supercrystals is usually found to be larger at the edge of the drop (**Figure III.7B**). Aiming at

controlling the morphology (size and shape) as well as the local organization of the supercrystals, a PDMS template was used, which affected the evaporation of the solvent at certain places on flat substrates. The PDMS templates comprised an array of cavities with various shapes and sizes, but with a fixed depth of 4.8 μm (**Figure III.6**).

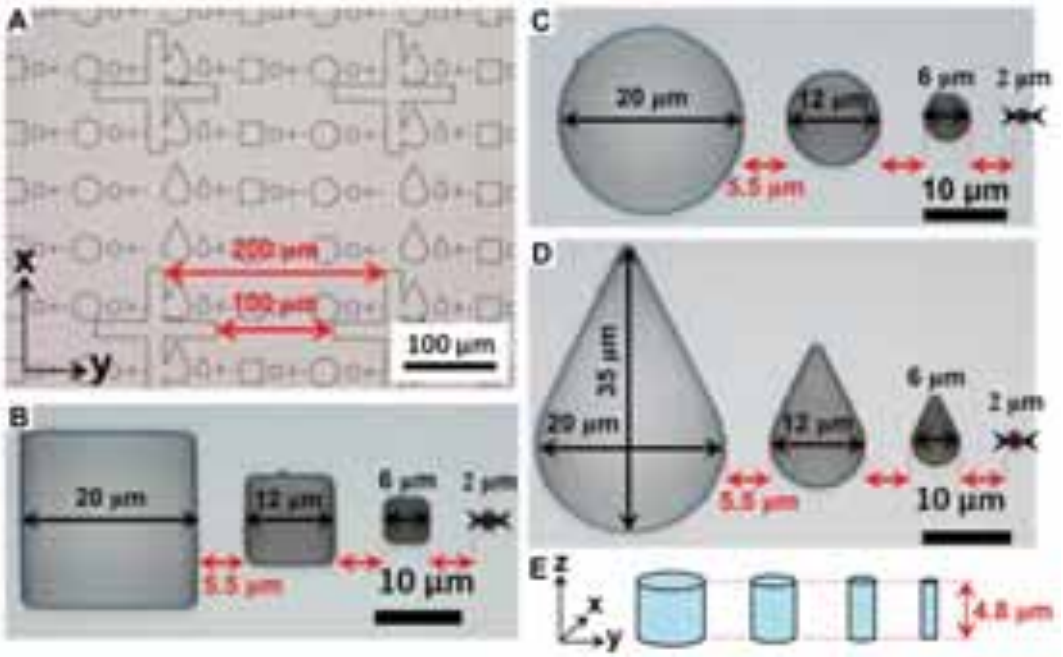

Figure III.6. PDMS template characterization. A: Optical microscopy image showing a general view of the template. The area comprised between the four crosses is $4 \cdot 10^4$ μm². **B-D:** Higher magnification optical microscopy images showing in detail the different cavity shapes: **B:** circles, **C:** drops, **D:** squares. **E:** Sketch showing that all cavities had a fixed depth of 4.8 μm.

We used initially a template displaying cavities with four different dimensions of 2, 6, 12, and 20 μm in diameter, in arrays of three different cavity shapes: circle, square and drop. For the formation of the assemblies, a drop of gold nanorod suspension was confined between the mould and a flat substrate (glass, silicon or carbon-coated TEM grids), and the system was then allowed to dry overnight under ambient conditions as schematically depicted in **Figure III.7A**. Subsequently, the PDMS template was carefully removed and well-defined supercrystal arrays were formed with dimensions that replicate those of the mould cavities (**Figure III.7C**). Interestingly, the relative orientation of the substrate, either being on the top or on the bottom of the assembly setup, did not seem to affect particle deposition and organization. It is important to note that the particles invariably deposited on the substrate

rather than on the PDMS template, presumably because of the wettability contrast between the hydrophilic substrate and the hydrophobic mould.

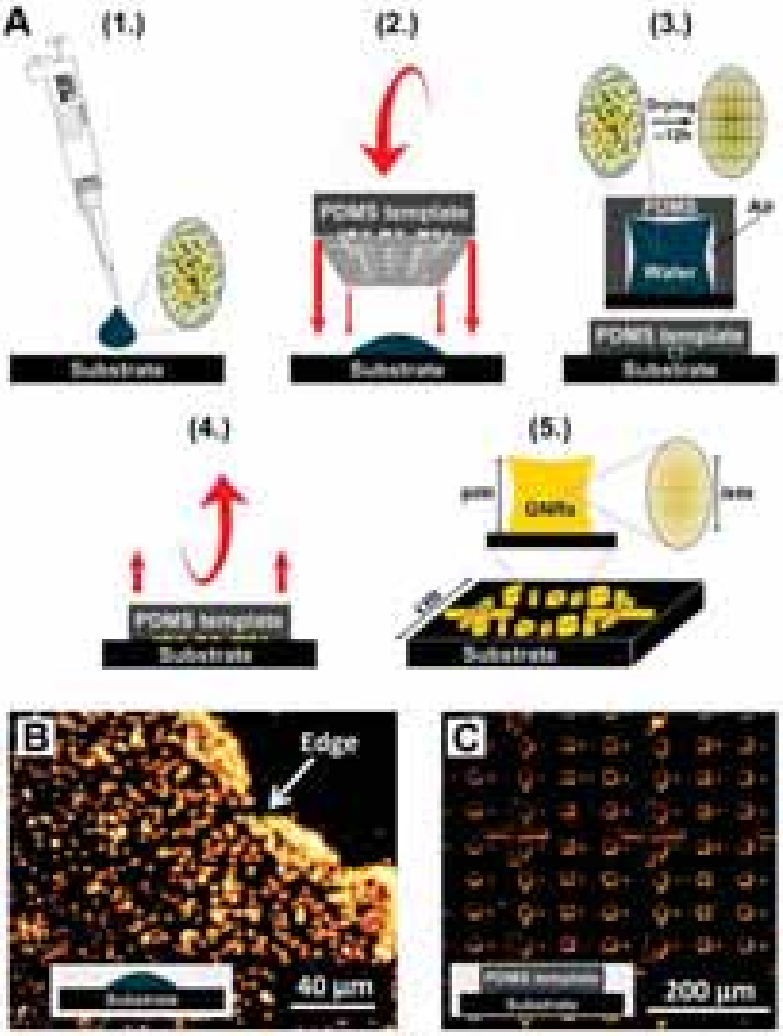

Figure III.7. A: Schematic view of the PDMS template-driven self-assembly process. (1.) A 2 µL gold nanoparticle suspension was drop casted with a micropipette on a substrate. (2.) Then a PDMS template displaying arrays of cavities was stamped on the system. (3.) The wetting properties of the suspension are modulated by the template and a meniscus is formed at the triple contact line between air, the solution and the substrate directing the final supercrystal shape. The system was allowed to dry for 12 h, allowing the crystallization of gold nanorods into smectic phases. (4.) The template was then removed and (5.) arrays of gold nanorods supercrystals were obtained over the substrate. All nanoparticles were functionalized with MUDOL. Different substrates were employed such as glass slides, silicon wafers or carbon-coated TEM grids. **B-C:** Dark field optical micrographs of gold nanorod supercrystals on glass obtained by drop casting (**B**) or by PDMS template driven self-assembly (**C**). Drop casting yielded a macroscale assembly determined by the coffee stain effect, resulting in accumulation of gold nanorods at the edge of the drop, as indicated by the white arrow.

Low magnification dark field optical microscopy images of the glass substrate demonstrate the long range order and the homogeneity of the micron-scale features within the array, meaning that the supercrystals were regularly patterned over the substrate at the millimeter scale (**Figure III.7C**). In comparison with the drop casting method, a remarkable improvement of the homogeneity and long-range order can be clearly observed. The assembly process resulted in an accurate reproduction of the geometry of the cavities in the PDMS mould, forming circles, squares and drop-shaped supercrystals (**Figure III.8A - B**). An additional observation is that the degree to which the cavities were filled, as well as the detailed morphology of the supercrystals, depends on the lateral dimensions of the cavities in the PDMS template. Whereas supercrystals formed in wider cavities of 20 and 12 μm displayed a middle hole, those assembled in smaller cavities 6 and 2 μm wide were fully packed with nanoparticles (**Figure III.8B - C**). It was also found that, except for the larger cavities (20 μm), the average size of the formed supercrystals was smaller than the initial cavity size. The supercrystals formed from the widest cavities however retained the size of the template cavity. We argue that confinement in smaller cavities increases the interaction between the aqueous dispersion and the hydrophobic template, leading to more constrained menisci and shrinkage during drying and self-assembly. In agreement with this interpretation, supercrystals usually displayed rounded profiles (**Figure III.8C**), which may be seen as reminiscent of a meniscus formed at the triple contact line between air, the solution and the substrate. PDMS is known to be hydrophobic with a water contact angle of ≈ 110°,[148] thus the gold nanorod suspension was likely not to fully wet the cavities and form a meniscus during assembly. We attempted to make supercrystals fitting better the cavity shapes by adding a surfactant to change the wettability of the aqueous colloid.[44,98] Polysorbate 20 was added to the gold nanorod colloid above its critical micelle concentration but no significant changes in the supercrystal shape were noticed. Another strategy would involve lowering the hydrophobicity of the mould, for example, by treating it with oxygen plasma prior to the assembly process, but such a detailed investigation was beyond the focus of the proof of concept study reported here.

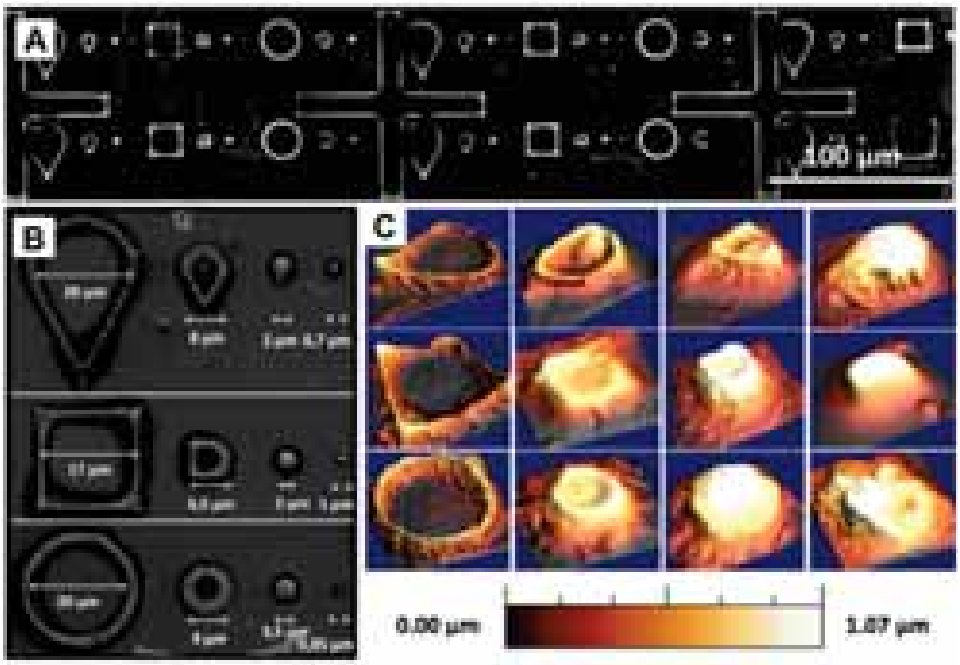

Figure III.8. Nanoparticle supercrystal arrays formed by PDMS template-driven assembly. The resulting arrays comprised supercrystals of different shapes and dimensions, ranging from 700 nm up to 20 µm. **A:** SEM of an array of gold nanorod supercrystals showing the long-range order of micron scale features on a glass slide, at device scale. **B:** SEM images at higher magnification showing the nanoscale topography of the substrate. The sizes are indicated below each supercrystal. **C:** Three dimensional atomic force microscopy topography plots of the supercrystals obtained from cavities with different shapes and sizes. A rounded hollow area is clearly visible on top of big supercrystals whereas smaller ones are full of particles.

PDMS template-driven assembly was applied to MUDOL capped gold nanoparticles with different morphologies, i.e. size and aspect ratio, which also resulted in the formation of supercrystals. We used spheres (17 nm, AR = 1), low aspect ratio gold nanorods (55×17 nm, AR = 3.2) and high aspect ratio gold nanorods (150×30 nm, AR = 5). In all cases, the macroscale organization was found to accurately reproduce the template geometry (**Figures III.9**). However, the degree of local order of the building blocks varied depending on their dimensions. Spheres and low aspect ratio nanorods formed hexagonal lattices regardless of the template geometry and dimensions (**Figures III.9A – D, K – M**). On the other hand, longer nanorods showed different organization depending on the size of the template cavity. Interestingly, we observed hexagonal packing when smaller cavities were used (**Figure III.9H - J**) but significantly less ordered assemblies for larger cavities, where both standing and lying gold nanorods were present in the superlattices (**Figure III.9E - G**). This effect is

probably related to the action of capillary forces inside the cavities affecting the assembly of this type of nanorods during drying. It should be noted however that such longer nanorods display pentagonal cross-section, which may also affect their self-assembly, as compared to single crystal nanorods, which have more rounded cross sections (see **Figure II.26C,** section II.4.1). Another possible reason behind the different local organization of the two types of nanorods is the change in aspect ratio, 3.2 vs. 5.[100] Overall, this last set of experiments demonstrates the versatility of the technique as it was applied to particles with different size and shape. Naturally, the organization of the nanoparticles within the supercrystals could be optimized for example by using more extended drying times,[103,105,162] perhaps employing evaporation chambers with controlled humidity and temperature. In the present work, we found that by using the PDMS templates, nanoparticle crystallization could be achieved within drying times in the range of 12h under ambient conditions.

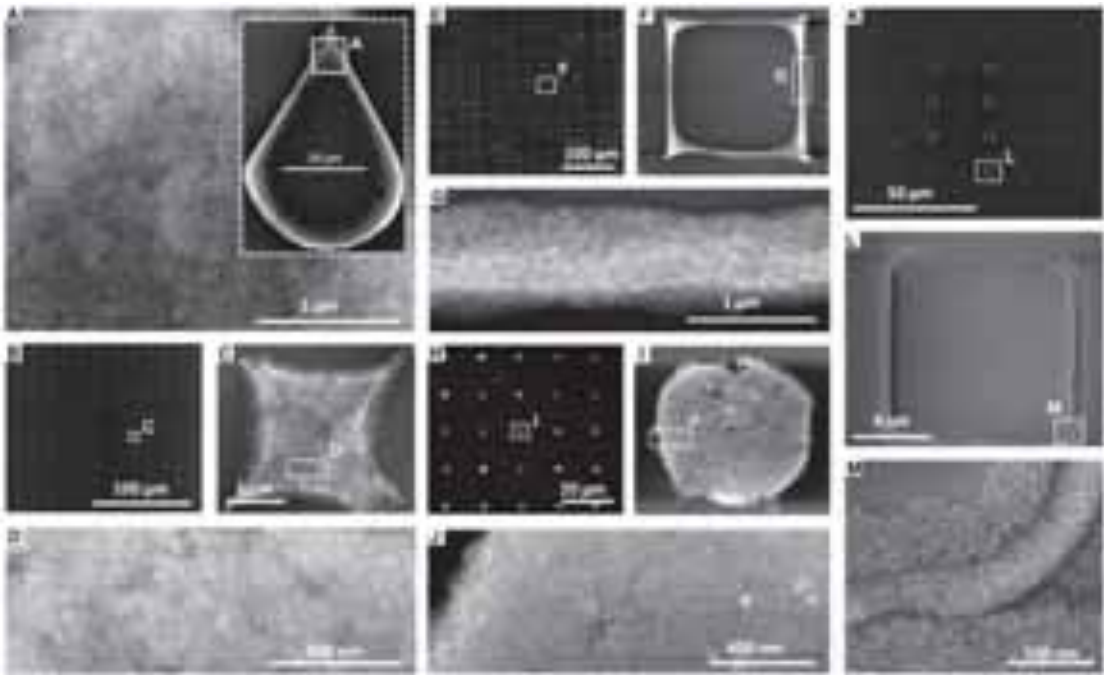

Figure III.9. Multiscale SEM characterization of patterned substrates obtained by PDMS driven self-assembly. Patterned substrates were obtained from colloidal solutions of gold nanoparticles of different shapes and dimensions: 55×17 nm single crystal nanorods (**A-D**), 150×30 nm penta-twinned nanorods(**E-J**), and 17nm nanospheres (**K-M**). Images were selected so as to represent supercrystals made from cavities with different size and shape: **A:** Drop-shaped cavity with 20 μm diameter; **B-D:** Square with 2 μm edge; **E-G:** Square with 20 μm edge; **H-J:** Circle with 6 μm diameter; **G-I:** Square of 6 μm in diameter.

The concentration of nanoparticles in the colloidal dispersion was found to have a strong influence on the formation of supercrystal arrays. We restricted this analysis to short gold nanorods (55×17 nm, AR = 3.2) because they form supercrystals with a homogeneous organization and also because they have been demonstrated to perform better than their spherical counterparts for sensing applications.[103] In the following, the gold nanorod concentration is expressed in molar concentration of Au(0), extracted from the absorbance at 400 nm (see section II.2.4).[157,164] Supercrystal arrays were prepared on silicon wafers using Au(0) concentrations in water of 15 mM, 75 mM and 375 mM. The top-views of the corresponding supercrystals are shown in **Figure III.10**.

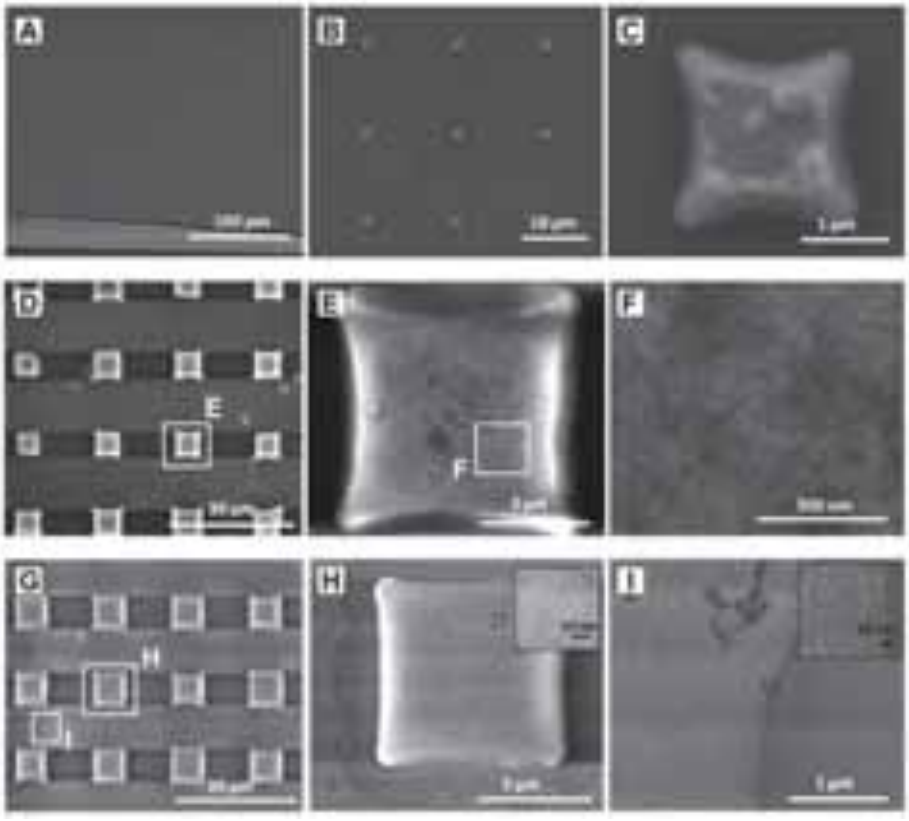

Figure III.10. Characterization of gold nanorod supercrystals obtained at different concentration. A-I: SEM images of patterned substrates obtained by PDMS-templated self-assembly on a glass slide. The initial gold nanorod concentrations (as [Au^0]) were: **A-C:** 15 mM; **D-F:** 75 mM; **G-I:** 375 mM. In the last case, a monolayer of gold nanorods was observed outside the limits of the cavities.

When the initial gold nanorod concentration was 15 mM and the cavities were large (20 μm in diameter), discrete supercrystals deposited as discontinuous lines along the edge of the

template structure (**Figure III.11A - B**). On the contrary, supercrystals with larger particle density were obtained when small cavities (2 μm diameter) were used. Interestingly, the height of these supercrystals (50-100 nm) corresponds to mono- and bi-layers of standing nanorods (**Figure III.12A - C**). Additional characterization was carried out by forming the supercrystal arrays on a TEM grid, which allowed us to determine a spacing of ca. 2 nm between nanorods, in agreement with the replacement of the CTAB bilayer with MUDOL (**Figure III.11C - F**); the value was further confirmed analyzing a supercrystal by atomic force microscopy (AFM, **Figure III.11G - I**).

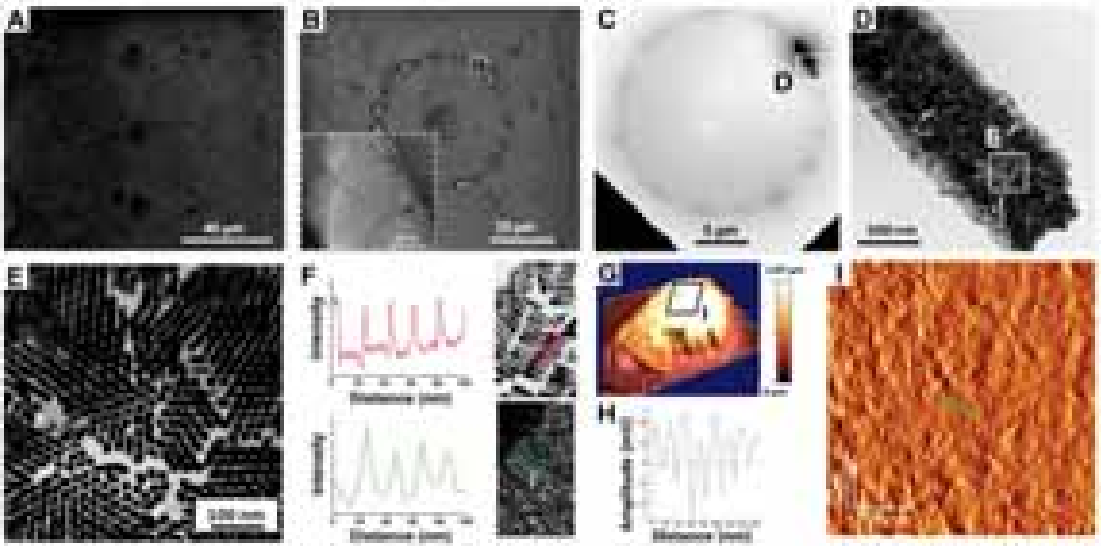

Figure III.11. A-B: SEM images at different magnifications of the structures obtained drying a gold nanorod colloid ([Au^0] = 15 mM) between a glass slide and a PDMS mould displaying circular holes. Discrete gold nanorod supercrystals are observed instead of a continuous line, which was however observed at higher nanorods concentration. **C-H:** Determination of internanorod spacing. **C-E:** TEM images at different magnifications of the structures obtained by drying the gold nanorod colloid between a TEM grid and a PDMS mould displaying circular holes. **F:** Plots of the intensity profiles used to measure the interparticle distance between lying (red) and standing (green) nanorods; an average value of 2 nm was found in both cases. **G:** Three dimensional AFM topography plots of a supercrystal obtained from cavities displaying drop geometry. **H:** Corresponding profile on the green line in **I**. The gold nanorod interdistance was determined to be 2 nm, in agreement with TEM analysis. **I:** AFM characterization of the surface at high magnification.

Increasing [Au^0] up to 75 mM induced the formation of uniform assemblies that follow the template geometry for all cavity sizes, which also contained a larger number of gold nanorod monolayers (height 1.2 μm, see **Figure III.12D - F**). Finally, for [Au^0] 375 mM, uniform assemblies were also observed, but gold nanorod monolayer deposition was also observed

outside the limit of the cavities (**Figure III.10G – I** and **Figure III.12I**). In this case, the height of the supercrystals was around 4 μm (**Figure III.12G – I**). The average number of layers was around 1-2, 20, and 70 for [Au^0] of 15 mM, 75 mM, and 375 mM respectively.

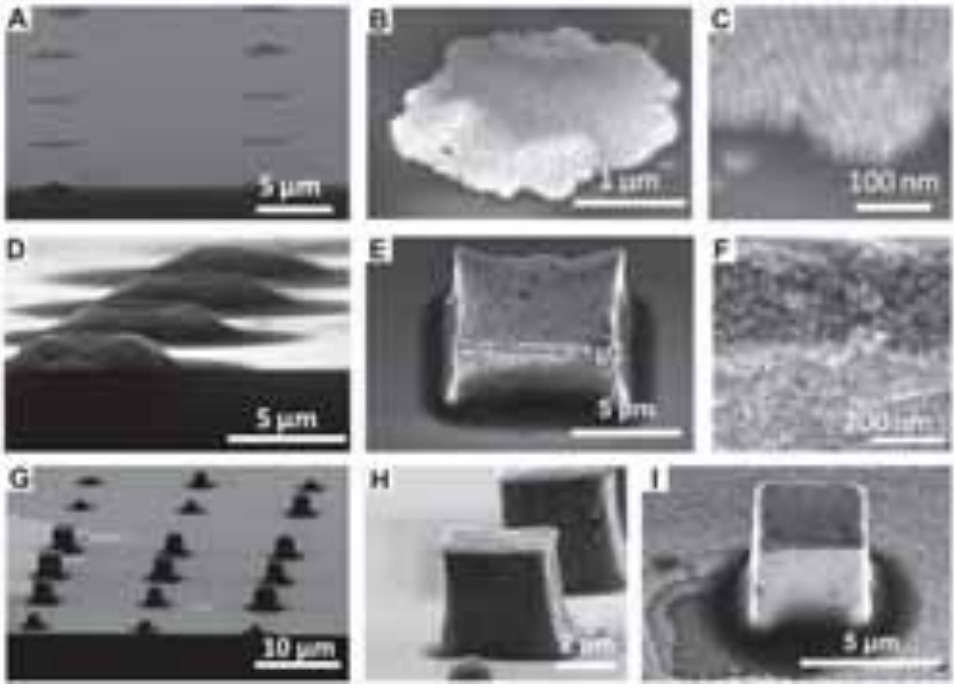

Figure III.12. SEM characterization at different magnifications of patterned substrates obtained at different gold nanorod concentrations; [Au^0] = **A-C:** 15 mM, **D-F:** 75 mM and **G-I:** 375 mM. Gold nanorod concentration is expressed as Au(0) molar concentration. Substrates were imaged with a tilt angle of 35°.

III.2.1.2. Supercrystals Internal Structure

Interestingly, hexagonal gold nanorod packing was observed not only at the top of the supercrystals but also on the other facets, suggesting preferential orientation of the rods perpendicular to the outer surfaces of the nanostructures (**Figure III.12F**). To investigate the organization of the building blocks inside the supercrystal, a detailed analysis of the internal structure was carried out by partial ablation of a supercrystal by means of focused ion beam (FIB) lithography, in combination with HR-SEM to image the corresponding supercrystal cross section. This Slice&View method allows 3D rendering of the sample structure (Experimental section, section III.3.9). An example of this analysis is shown in **Figure III.13.**

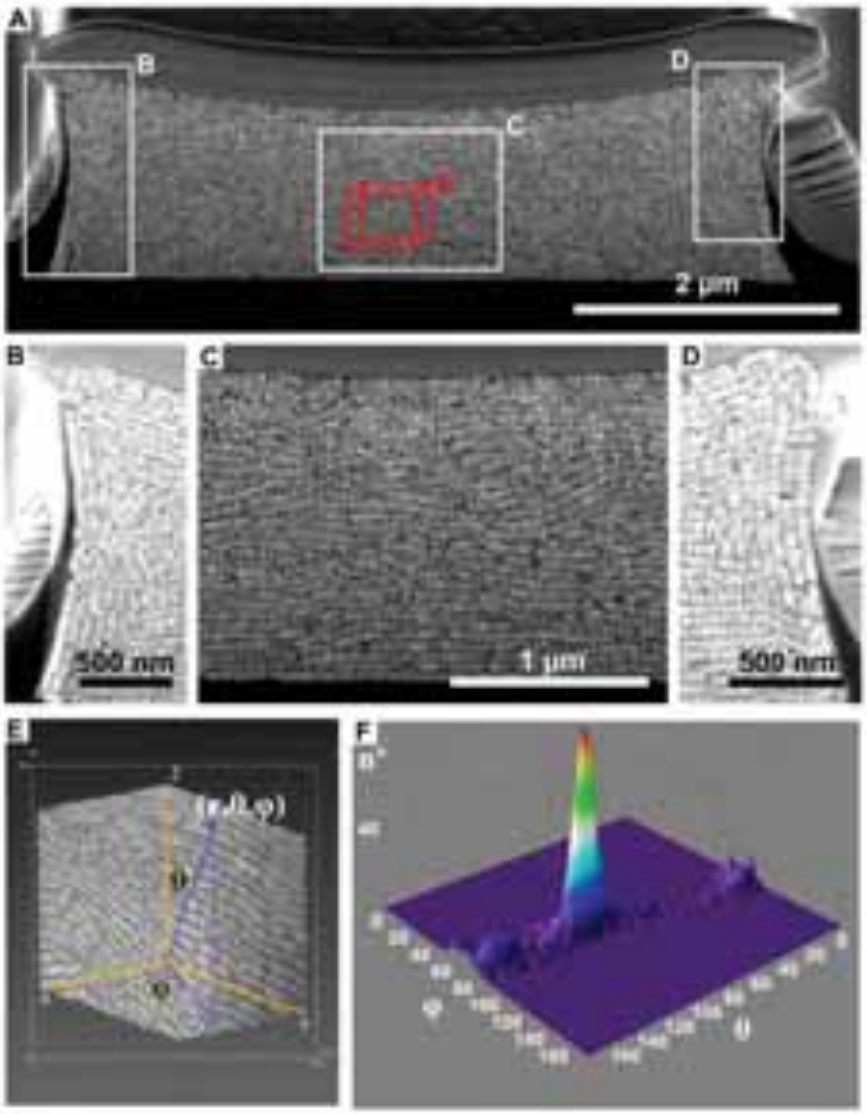

Figure III.13. FIB/SEM analysis of the internal structure of a gold nanorod supercrystal. **A:** SEM image of a supercrystal after FIB cutting. **B:** Higher magnification SEM image showing the organization of gold nanorods inside the supercrystal. The images were selected to display gold nanorod organization at both the center (**C**) and the edges (**B,D**) of the supercrystal. **E:** Three-dimensional reconstruction of a box within the supercrystal with a volume of 1.3 μm^3, showing a smectic organization. **F:** Orientation scattering maps obtained from **E**, revealing the distribution of rods orientation.

Most of the gold nanorods were found to be standing with their long axes perpendicular to the substrate, and a high degree of inter- and intra-lamellar long-range order was observed (**Figure III.13C**). However, we noticed a different local organization along the edges, where few gold nanorod layers were found to orient perpendicular to the lateral facets of the supercrystals (**Figure III.13B, D**). SEM images acquired from nearly two hundred

successive FIB slicing steps on the same supercrystal are combined to form a reconstruction of the internal structure in three dimensions (**Figure III.13E**). Image analysis was also carried out to obtain a more quantitative measure of the gold nanorods organization, resulting in orientation scattering maps that revealed an average orientation angle of the nanorods of 92 ± 8º with respect to the base of the substrate (**Figure III.13F**). Supercrystals with a height lower than 1 μm show no preferential gold nanorod orientation but small domains of parallel rods are observed (**Figure III.14C**); our interpretation is that as the concentration of gold nanorods is decreased, the larger amount of liquid within the same volume cavity leads to perturbations in the long-range order of the gold nanorod domains, likely resulting from convective and capillary forces in the liquid. When an even lower concentration of gold nanorods was used (forming supercrystals made of few gold nanorod layers, see **Figure III.12A – C**) the observed smectic organization is likely the result of reduced influence of the walls of the template cavity on the orientation of the nanorods (**Figure III.14D – E)**.

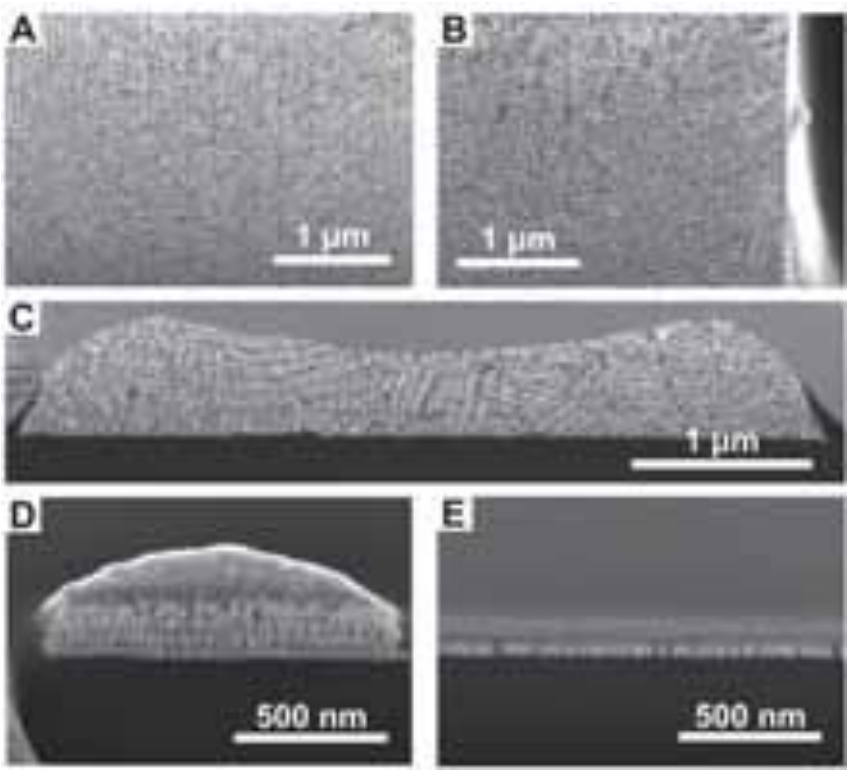

Figure III.14. Effect of gold nanorod concentration on the internal organization. SEM images of internal sections of gold nanorod supercrystals after cutting with FIB. The gold nanorod concentration is decreased as follows: **A-B:** 375 mM, **C:** 37 mM, and **D-E:** 8.3 mM.

Next, we studied the influence of the cavity dimension on the long-range order; decreasing the width of the square shaped template cavities down to 2 μm, we observed a significant decrease of the long range organization of the nanorods, which segregate into small organized domains, suggesting that the increased confinement for the self-assembly of smaller supercrystals decreases the ability of gold nanorods to reorganize inside the cavity (**Figures III.15)**

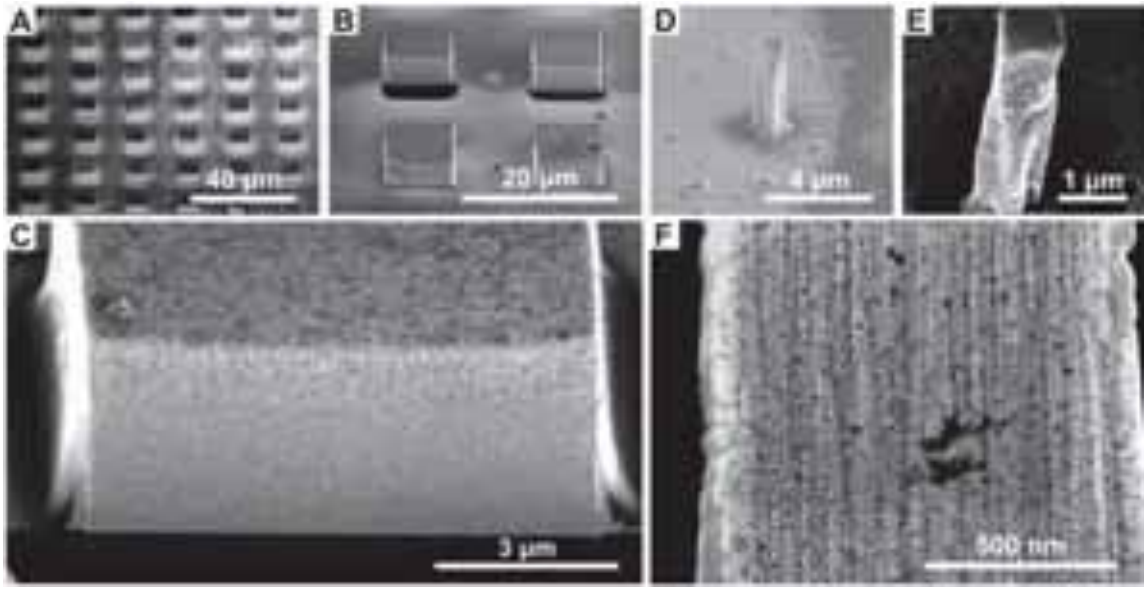

Figure III.15. Effect of cavity size on internal nanorod organization. A-C: SEM characterization of gold nanorod supercrystal nanostructure obtained from 12 μm cavities and initial [Au^0] of 375mM. Large domains of gold nanorods oriented in the same direction were observed. **D-F:** SEM Characterization of gold nanorod supercrystal nanostructure obtained from 2 μm cavities and initial [Au^0] of 375 mM. Local gold nanorod organization was observed.

Organization of gold nanorods into supercrystals is still a matter of debate due to the challenge of investigating *in situ* the crystallization process. However, the observation of the organization after drying gives valuable information on the parameters that have to be taken into account in order to obtain supercrystalline structures. Interestingly, the quasi-crystalline symmetry of MUDOL coated gold nanorod supercrystals has been attributed to the pre-formation of ordered lamellae of packed nanorods that can then self-assemble in a second step by a layer by layer process.[35] This ordering transition was proposed to take place once a critical particle density was reached during the evaporation of the solvent and was driven by

entropy as the interaction between particles is considered negligible.[74,165,166] The high concentration of gold nanorods used in this work hinders a direct observation of the assembly process by scattering techniques, but it is likely that a similar two-step process is at work. Thus, the observed organization at interfaces would result from monolayers forming at the air-water interface due the local higher evaporation rate.[167,168] Moreover, the supercrystal morphology seems to be reminiscent of the shape of the meniscus formed at the triple contact line between the air, the solution and the substrate. Consequently, the meniscus in the latter stage of the drying process applies pressure that can deform the supercrystal and affect the local organization.

III.2.1.3. Supercrystals SERS Performance

We selected 75 mM as the optimal concentration for the following experiments, since it leads to homogeneous deposition of nanorods for all cavity sizes, avoiding at the same time the deposition of nanorods outside the cavities. It should be noticed that such supercrystal size is difficult to obtain by other techniques unless very high gold nanorod concentrations are used. In the present work, the supercrystals height was modulated between 0.1 and 4 μm using moderate (between 15 and 375 mM) concentrations and the same mould in the self-assembly process. The Smectic B organization of the nanorods within the supercrystals is particularly suited for sensing applications as the high particle density maximizes hot-spot formation at multiple gaps between nanorods (see section III.2).[103,106] We proceed with the examination of the sensing properties of the nanoparticle supercrystals, on the basis of the well-known efficiency of these systems toward SERS.[103,105] In previous work, gold nanorod supercrystals for SERS detection were obtained by standard drop casting, resulting in non-uniform supercrystal arrays, which strongly hinders the reproducibility of the experiments. In this work, we took advantage of the uniform distribution of supercrystals on the substrate, as well as the smectic order of the nanorods and the control on the supercrystals morphology. Supercrystal arrays were prepared on a glass substrate, with the optimized concentration of 75 mM. The patterned substrates were then cleaned by oxygen plasma to remove the organic layer formed on top of the supercrystal surface, which would undoubtedly interfere with SERS detection (see Experimental Section, section III.3.7). Oxygen plasma etching time was

optimized to successfully remove the organic layer while avoiding any damaging or reshaping of the gold nanorods (which was observed for longer exposure times).

Crystal violet (CV) was selected as a model analyte for SERS detection and the measurements were carried out for supercrystals with different geometries. SERS images were acquired by mapping the spatial dependence of SERS intensity integrated over the Raman shift range 1618 - 1632 cm^{-1} (**Figure III.16A - C**). From these measurements we can clearly see that the analyte could be detected on the supercrystals only, confirming the signal enhancement by the plasmon excitation of the nanorod assembly. Importantly, only the chemical fingerprint of the analyte was measured and the SERS signal intensity was uniform throughout the supercrystals surface. Considering the low integration time of 500 ms and the low laser intensity (0.15 mW), an enhancement factor was determined of $3.1 \cdot 10^5$ at 633 nm. This should be taken as a lower estimate as CV molecules are likely to deposit also on the substrate outside the supercrystals. Interestingly, we did not notice any changes on the multiscale organization of the patterned substrates after Raman experiments and further cleaning, thus allowing its reusability.[103] Similar SERS experiments were carried out on supercrystals obtained with spheres and with large nanorods. Interestingly, we observed that larger nanorods (150×30 nm) provide higher signals, whereas spheres yield the lowest signals **(Figure III.16C - D)**. This may be related to both the larger dimensions and to the sharper tips of these nanorods. However, an accurate comparison between different systems is complicated, since the number of layers, the density of particles and therefore the density of hot spots is significantly different.

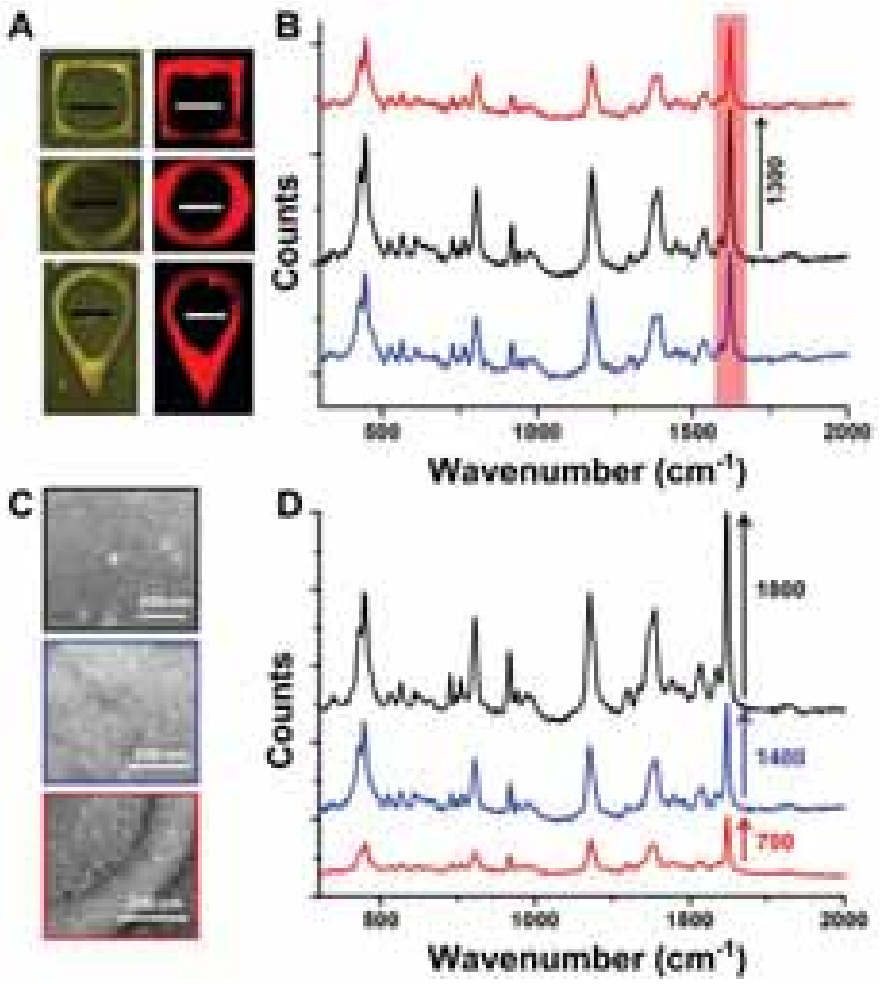

Figure III.16 A: Optical microscopy images (left) of gold nanorod supercrystals of different shapes and corresponding SERS images (right) obtained by mapping the intensity of the CV vibrational peak integrated over 1618 - 1632 cm^{-1} (red area in **B**). The scale bar on all images is 10 µm. **B:** Average SERS CV spectra acquired on supercrystals with different shapes: drops (blue), circles (black) and squares (red). **C:** representative SEM images of the areas analyzed in **D. D:** Comparison of CV SERS spectra measured on supercrystals obtained with different gold nanoparticle shapes: nanospheres (red), single crystal nanorods (blue), penta-twinned nanorods (black). For all SERS spectra, CV was dropcasted on the substrate at a concentration of 10^{-6} M in ethanol and dried under ambient conditions. The acquisition time was 500 ms and the laser power was ≈ 0.15 mW, with an excitation wavelength of 633 nm. Spectra were vertically shifted for the sake of clarity. The total number of counts is indicated by a black arrow corresponding to the intensity of the peak at 1626 cm^{-1}.

III.2.1.4. Conclusions

In summary, a simple and reliable technique was devised to obtain nanoparticle supercrystal arrays by confining a gold nanoparticle colloid between a patterned PDMS mould and a flat substrate. Self-assembly takes place in one step on arbitrary substrates such as TEM grids, silicon wafers and glass slides. The method only requires commercially available and inexpensive tools. The size, shape and height of the obtained supercrystals can be regulated by varying the mould cavity pattern and nanoparticle concentration. Overall, this technique is highly versatile and the morphology of the supercrystals can be tuned with unprecedented control on the macroscale. SEM and TEM revealed the hierarchical order of the nanoparticles up to the millimeter scale. Moreover a combination of FIB and HRSEM allow us to investigate the gold nanorod organization in the supercrystals; we were able to confirm their long range smectic order inside the supercrystals, and study the influence of nanorod concentration, cavity dimension and drying time over the long-range order. Well-defined supercrystals were obtained for all template geometries, opening new avenues for the future development of complex structures. Furthermore, the three-dimensional features obtained in this work cannot be produced by other bottom-up techniques.[155,169] The macroscale assembly of gold nanoparticles with different shapes and sizes was also demonstrated. We envision that the method can be applied to various colloids with different compositions such as semiconductor nanoparticles or proteins, for a broad range of applications. Herein, the patterned substrates were used as a sensing platform, with a SERS response that was homogeneous and intense for the various supercrystal sizes and shapes. The size of the obtained supercrystals allow the use of larger laser spot sizes and thus of portable Raman spectrometers. Moreover, the high chemical stability of gold nanorods allowed us to store the substrates for months, which is important for the eventual fabrication of point of care devices. Overall, the reproducibility, the fast optical read-out, the high sensitivity, together with the simplicity of fabrication, render these hierarchical assemblies appealing for the design of high-performance sensing platforms.

III.3. EXPERIMENTAL SECTION

III.3.1. Materials

(1-mercaptoundec-11-yl)hexa(ethyleneglycol) (MUDOL, 90%), Crystal Violet (CV, dye content ≥ 90 %), were purchased from Aldrich and used as received. Milli-Q water (resistivity 18.2MΩ·cm at 25 ºC) was used in all experiments. All glassware was washed with aqua regia, rinsed with water, sonicated three-fold for 3 min with Milli-Q water and dried before use.

III.3.2. Synthesis of Single Crystals and Penta-Twinned Gold Nanorods

The synthesis of single crystal and penta-twinned gold nanorods have been described in details in section II.5.3 and II.5.5 respectively.

III.3.3. MUDOL Functionalization of CTAB Coated Gold Nanorods (section III.2.1.1)

5 mL of freshly prepared gold nanorod solution was purified by centrifugation (7000 rpm, 40 min, 29 °C) from excess of CTAB and dispersed in an equal volume of Milli-Q water to reach a final surfactant concentration of 1 mM. Then, 5 mL of 0.2 mM MUDOL solution was mixed with the purified gold nanorod dispersion, shaken vigorously and left to incubate for 24h. The obtained MUDOL coated gold nanorods were stable for months. The concentration of gold nanorods is expressed as [Au^0], and was adjusted between 15 mM and 375 mM by centrifugation (7000 rpm, 40 min, 29 °C).

III.3.4. Fabrication of the PDMS Mould (section III.2.1.1)

The microtextured mould was manufactured in PDMS (Sylgard 184, Dow Corning), following standard soft lithography techniques.[148,170] The master was composed of pillars having different shapes and sizes on a 4 inch silicon wafer covered with SU-8 resin. PDMS (10:1 elastomer to curing agent) was cured at 70 °C for 2h.

III.3.5. 3D Gold Nanorod Self-Assembly (section III.2.1.2)

Patterned substrates were fabricated by drying a gold nanorod dispersion within an array of micron-sized cavities with a fixed height of 4.8 μm and varying side lengths and shapes. The nanorod synthesis was carried out on the liter scale with no loss of quality, which allowed the preparation of all substrates from the same gold nanorod batch. By adjusting the cavity size and shape of the template along with the particle concentration for a fixed volume, the morphology and height of the supercrystals can be tuned. Briefly, for all the substrates, a 2 μL drop of a gold nanorod colloid with the selected concentration was deposited on a silicon wafer and then covered by the microtextured PDMS template. The solvent was subsequently allowed to evaporate to dryness (with different drying time) and the template carefully removed resulting in the formation of arrays of gold nanorods supercrystals spread over millimeter-sized areas.

III.3.6. Preparation of the Gold Nanorod Supercrystal Substrates for SERS Spectroscopy Characterization (section III.2.1.3)

Substrates were cleaned with a combination of oxygen plasma (2 min, 0.4 mbar, 200 W) and UV/Ozone (1h). Oxygen plasma surface treatment was performed in a low pressure plasma system (PICO, Diener Electronic). UV/Ozone surface treatment was performed in a UV/Ozone Cleaner (ProCleaner). A solution of CV at 10^{-6} M in ethanol was drop casted on the substrate and dried under ambient conditions. SERS measurements were performed on a commercial confocal scanning Raman microscope (micro-Renishaw InVia Reflex system equipped with Peltier charge-coupled device (CCD) detectors) using a 100× objective (N.A. =0.85) with excitation wavelength of 633 nm, 1200 lines/mm diffraction grating. $P \approx 0.15$ mW, integration time 500 ms. Laser spot size was in the range of one micrometer in diameter.

III.3.7. Dark Field SEM and FIB Characterization (section III.2.1.2)

Dark field microscopy images were obtained using a Nikon Eclipse Ti-U inversion optical microscope. SEM images of gold nanorods were obtained using an Helios NanoLab 450S (FEI, The Netherlands) at accelerating voltage of 1 to 5 kV and beam current 100 pA. EDX analysis was performed at accelerating voltage 5 kV to 15 kV and beam current up to 1 nA. To obtain information about the internal structure of the supercrystals they were cross-sectioned by FIB and the sections were imaged by SEM. A platinum layer was locally deposited on the top of the supercrystal to avoid any collapse of the structures during the FIB process (**Figure III.26**). Typically a beam current of 50-100 pA at an accelerating voltage of 30 kV was used for cutting, and finish polishing current was 7 pA. To create three-dimensional reconstructions FIB tomography technique Slice&View was used. Series of slices were obtained automatically via FEI Auto Slice and View G2 software. The number of slices was about 200, with approximate slice thickness of 5 nm. The average time required for milling a series was about 7 hours. Further, the resulting series were processed with FEI Avizo software, which allows tilt correction and image alignment using cross-correlation. Image filtering was used to remove artifacts from the cutting with the ion beam. As a result, three-dimensional reconstructions of the supercrystals internal structure were obtained.

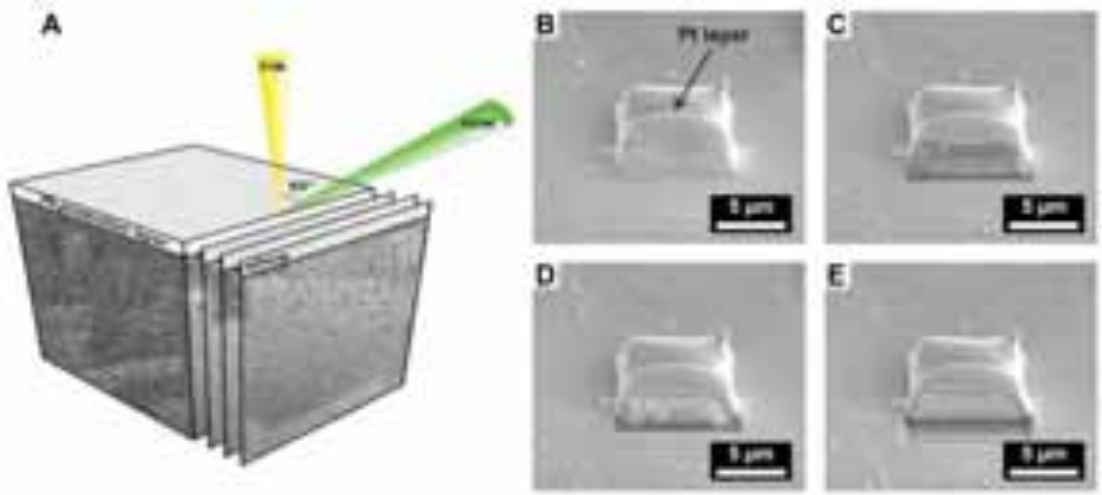

Figure III.26. A: schematic representation of the Slice&View technique used for the 3D reconstruction of the spatial organization of the gold nanorods within the supercrystals. **B-D:** series of SEM images taken at different stages of the FIB cutting. In **B**, the arrow indicates the protective Pt layer.

III.4. REFERENCES

(1) Whitesides, G. M.; Grzybowski, B. *Science* **2002**, *295* (5564), 2418–2421.
(2) Greenberg, R.; Brahic, A. *Planetary Rings* **1984**.
(3) Li, L.; Kolle, S.; Weaver, J. C.; Ortiz, C.; Aizenberg, J.; Kolle, M. *Nat. Commun.* **2015**, *6*, 6322.
(4) Monn, M. A.; Weaver, J. C.; Zhang, T.; Aizenberg, J.; Kesari, H. *Proc. Natl. Acad. Sci.* **2015**, *112* (16), 4976–4981.
(5) Grinthal, A.; Aizenberg, J. *Chem. Soc. Rev.* **2013**, *42* (17), 7072.
(6) Gorder, P. F. "Butterfly wings inspire new high-tech surfaces", http://phys.org/news/2012-11-butterfly-wings-high-tech-surfaces.html.
(7) England, G.; Kolle, M.; Kim, P.; Khan, M.; Munoz, P.; Mazur, E.; Aizenberg, J. *Proc. Natl. Acad. Sci.* **2014**, *111* (44), 15630–15634.
(8) Teyssier, J.; Saenko, S. V.; van der Marel, D.; Milinkovitch, M. C. *Nat. Commun.* **2015**, *6*, 6368.
(9) Eisner, T.; Aneshansley, D. J. *Proc. Natl. Acad. Sci.* **2000**, *97* (12), 6568–6573.
(10) Marmur, A. *Langmuir* **2004**, *20* (9), 3517–3519.
(11) Barthlott, W.; Neinhuis, C. *Planta* **1997**, *202* (1), 1–8.
(12) Stark, A. Y.; Badge, I.; Wucinich, N. A.; Sullivan, T. W.; Niewiarowski, P. H.; Dhinojwala, A. *Proc. Natl. Acad. Sci.* **2013**, *110* (16), 6340–6345.
(13) Richmond, T. J.; Davey, C. A. *Nature* **2003**, *423* (6936), 145–150.
(14) Szent-Gyorgyi, A. *Science* **1964**, *146* (3649), 1278–1279.
(15) Whitesides, G. M.; Boncheva, M. *Proc. Natl. Acad. Sci.* **2002**, *99* (8), 4769–4774.
(16) Copyright © 2015 Pearson Education, Inc. http://wps.pearsoncustom.com/wps/media/objects/4557/4666819/ebook/htm/chp11_4.htm
(17) Lehn, J.-M. *Angew. Chem. Int. Ed. Engl.* **1990**, *29* (11), 1304–1319.
(18) Philp, D.; Stoddart, J. F. *Angew. Chem. Int. Ed. Engl.* **1996**, *35* (11), 1154–1196.
(19) Forgan, R. S.; Sauvage, J.-P.; Stoddart, J. F. *Chem. Rev.* **2011**, *111* (9), 5434–5464.
(20) Chichak, K. S.; Cantrill, S. J.; Pease, A. R.; Chiu, S.-H.; Cave, G. W. V.; Atwood, J. L.; Stoddart, J. F. *Science* **2004**, *304* (5675), 1308–1312.
(21) Gross, R.; Dorigo, M. *Proc. IEEE* **2008**, *96* (9), 1490–1508.
(22) Harada, A.; Kobayashi, R.; Takashima, Y.; Hashidzume, A.; Yamaguchi, H. *Nat. Chem.* **2011**, *3* (1), 34–37.
(23) Klimov, V. I. *Science* **2000**, *290* (5490), 314–317.
(24) Sun, S. *Science* **2000**, *287* (5460), 1989–1992.
(25) Sirringhaus, H.; Kawase, T.; Friend, R. H.; Shimoda, T.; Inbasekaran, M.; Wu, W.; Woo, E. P. *Science* **2000**, *290* (5499), 2123–2126.
(26) Jenekhe, S. A. *Science* **1999**, *283* (5400), 372–375.
(27) Xia, Y.; Gates, B.; Yin, Y.; Lu, Y. *Adv. Mater.* **2000**, *12* (10), 693–713.
(28) Wu, M.-H.; Whitesides, G. M. *Appl. Phys. Lett.* **2001**, *78* (16), 2273.
(29) Kalsin, A. M. *Science* **2006**, *312* (5772), 420–424.
(30) Kowalczyk, B.; Walker, D. A.; Soh, S.; Grzybowski, B. A. *Angew. Chem. Int. Ed.* **2010**, *49* (33), 5737–5741.
(31) Kowalczyk, B.; Bishop, K. J. M.; Lagzi, I.; Wang, D.; Wei, Y.; Han, S.; Grzybowski, B. A. *Nat. Mater.* **2012**, *11* (3), 227–232.
(32) Mirkin, C. A.; Letsinger, R. L.; Mucic, R. C.; Storhoff, J. J.; others. *Nature* **1996**, *382* (6592), 607–609.
(33) Park, S. Y.; Lytton-Jean, A. K. R.; Lee, B.; Weigand, S.; Schatz, G. C.; Mirkin, C. A. *Nature* **2008**, *451* (7178), 553–556.
(34) Young, K. L.; Jones, M. R.; Zhang, J.; Macfarlane, R. J.; Esquivel-Sirvent, R.; Nap, R. J.; Wu, J.; Schatz, G. C.; Lee, B.; Mirkin, C. A. *Proc. Natl. Acad. Sci.* **2012**, *109* (7), 2240–2245.
(35) Young, K. L.; Ross, M. B.; Blaber, M. G.; Rycenga, M.; Jones, M. R.; Zhang, C.; Senesi, A. J.; Lee, B.; Schatz, G. C.; Mirkin, C. A. *Adv. Mater.* **2014**, *26* (4), 653–659.

(36) Dujardin, E.; Mann, S.; Hsin, L.-B.; Wang, C. R. C. *Chem. Commun.* **2001**, No. 14, 1264–1265.
(37) Jones, M. R.; Macfarlane, R. J.; Lee, B.; Zhang, J.; Young, K. L.; Senesi, A. J.; Mirkin, C. A. *Nat. Mater.* **2010**, *9* (11), 913–917.
(38) Grinthal, A.; Kang, S. H.; Epstein, A. K.; Aizenberg, M.; Khan, M.; Aizenberg, J. *Nano Today* **2012**, *7* (1), 35–52.
(39) Uskoković, V. *Adv. Colloid Interface Sci.* **2008**, *141* (1), 37–47.
(40) Halley, J. D.; Winkler, D. A. *Complexity* **2008**, *14* (2), 10–17.
(41) Grzelczak, M.; Vermant, J.; Furst, E. M.; Liz-Marz n , L. M. *ACS Nano* **2010**, *4* (7), 3591–3605.
(42) Sánchez-Iglesias, A.; Grzelczak, M.; Altantzis, T.; Goris, B.; Perez-Juste, J.; Bals, S.; Van Tendeloo, G.; Donaldson Jr, S. H.; Chmelka, B. F.; Israelachvili, J. N.; others. *ACS Nano* **2012**, *6* (12), 11059–11065.
(43) Ni, W.; Mosquera, R. A.; Pérez-Juste, J.; Liz-Marzán, L. M. *J. Phys. Chem. Lett.* **2010**, *1* (8), 1181–1185.
(44) Hamon, C.; Postic, M.; Mazari, E.; Bizien, T.; Dupuis, C.; Even-Hernandez, P.; Jimenez, A.; Courbin, L.; Gosse, C.; Artzner, F.; Marchi-Artzner, V. *ACS Nano* **2012**, *6* (5), 4137–4146.
(45) Ni, S.; Leemann, J.; Wolf, H.; Isa, L. *Faraday Discuss* **2015**, *181*, 225–242.
(46) Hamon, C.; Liz-Marzán, L. M. *Chem. - Eur. J.* **2015**, *21* (28), 9956–9963.
(47) Yabu, H.; Shimomura, M. *Adv. Funct. Mater.* **2005**, *15* (4), 575–581.
(48) Harris, D. J.; Hu, H.; Conrad, J. C.; Lewis, J. A. *Phys. Rev. Lett.* **2007**, *98* (14), 148301.
(49) Kim, H. S.; Lee, C. H.; Sudeep, P. K.; Emrick, T.; Crosby, A. J. *Adv. Mater.* **2010**, *22* (41), 4600–4604.
(50) Byun, M.; Hong, S. W.; Qiu, F.; Zou, Q.; Lin, Z. *Macromolecules* **2008**, *41* (23), 9312–9317.
(51) Lin, Z. *J. Polym. Sci. Part B Polym. Phys.* **2010**, *48* (24), 2552–2557.
(52) Walker, D. A.; Leitsch, E. K.; Nap, R. J.; Szleifer, I.; Grzybowski, B. A. *Nat. Nanotechnol.* **2013**, *8* (9), 676–681.
(53) Wang, D.; Nap, R. J.; Lagzi, I.; Kowalczyk, B.; Han, S.; Grzybowski, B. A.; Szleifer, I. *J. Am. Chem. Soc.* **2011**, *133* (7), 2192–2197.
(54) Gang, O.; Zhang, Y. *ACS Nano* **2011**, *5* (11), 8459–8465.
(55) Green, J. R.; Costa, A. B.; Grzybowski, B. A.; Szleifer, I. *Proc. Natl. Acad. Sci.* **2013**, *110* (41), 16339–16343.
(56) Tretiakov, K. V.; Szleifer, I.; Grzybowski, B. A. *Angew. Chem.* **2013**, *125* (39), 10494–10498.
(57) Zhang, R.; Walker, D. A.; Grzybowski, B. A.; Olvera de la Cruz, M. *Angew. Chem.* **2014**, *126* (1), 177–181.
(58) Fialkowski, M.; Bishop, K. J.; Klajn, R.; Smoukov, S. K.; Campbell, C. J.; Grzybowski, B. A. *J. Phys. Chem. B* **2006**, *110* (6), 2482–2496.
(59) Klajn, R.; Bishop, K. J. M.; Grzybowski, B. A. *Proc. Natl. Acad. Sci.* **2007**, *104* (25), 10305–10309.
(60) Klinkova, A.; Choueiri, R. M.; Kumacheva, E. *Chem. Soc. Rev.* **2014**, *43* (11), 3976.
(61) Grzelczak, M.; Sánchez-Iglesias, A.; Liz-Marzán, L. M. *CrystEngComm* **2014**, *16* (40), 9425–9429.
(62) Schweikart, A.; Fery, A. *Microchim. Acta* **2009**, *165* (3-4), 249–263.
(63) Tebbe, M.; Mayer, M.; Glatz, B. A.; Hanske, C.; Probst, P. T.; Müller, M. B.; Karg, M.; Chanana, M.; König, T. A. F.; Kuttner, C.; Fery, A. *Faraday Discuss* **2015**, *181*, 243–260.
(64) Nie, Z.; Fava, D.; Kumacheva, E.; Zou, S.; Walker, G. C.; Rubinstein, M. *Nat. Mater.* **2007**, *6* (8), 609–614.
(65) Dong, A.; Chen, J.; Vora, P. M.; Kikkawa, J. M.; Murray, C. B. *Nature* **2010**, *466* (7305), 474–477.
(66) Paik, T.; Murray, C. B. *Nano Lett.* **2013**, *13* (6), 2952–2956.
(67) Talapin, D. V.; Shevchenko, E. V.; Bodnarchuk, M. I.; Ye, X.; Chen, J.; Murray, C. B. *Nature* **2009**, *461* (7266), 964–967.
(68) Paik, T.; Diroll, B. T.; Kagan, C. R.; Murray, C. B. *J. Am. Chem. Soc.* **2015**, *137* (20), 6662–6669.
(69) Peng, B.; Li, G.; Li, D.; Dodson, S.; Zhang, Q.; Zhang, J.; Lee, Y. H.; Demir, H. V.; Yi Ling, X.; Xiong, Q. *ACS Nano* **2013**, *7* (7), 5993–6000.
(70) Li, F.; Josephson, D. P.; Stein, A. *Angew. Chem. Int. Ed.* **2011**, *50* (2), 360–388.
(71) Nie, Z.; Petukhova, A.; Kumacheva, E. *Nat. Nanotechnol.* **2010**, *5* (1), 15–25.
(72) Liu, K.; Zhao, N.; Kumacheva, E. *Chem. Soc. Rev.* **2011**, *40* (2), 656.
(73) Han, W.; Lin, Z. *Angew. Chem. Int. Ed.* **2012**, *51* (7), 1534–1546.

(74) Anders, G. van; Klotsa, D.; Ahmed, N. K.; Engel, M.; Glotzer, S. C. *Proc. Natl. Acad. Sci.* **2014**, *111* (45), E4812–E4821.
(75) Damasceno, P. F.; Engel, M.; Glotzer, S. C. *Science* **2012**, *337* (6093), 453–457.
(76) Grzybowski, B. A. *CrystEngComm* **2014**, *16* (40), 9368–9380.
(77) Park, K.; Koerner, H.; Vaia, R. A. *Nano Lett.* **2010**, *10* (4), 1433–1439.
(78) Baranov, D.; Fiore, A.; van Huis, M.; Giannini, C.; Falqui, A.; Lafont, U.; Zandbergen, H.; Zanella, M.; Cingolani, R.; Manna, L. *Nano Lett.* **2010**, *10* (2), 743–749.
(79) Olson, M. A.; Coskun, A.; Klajn, R.; Fang, L.; Dey, S. K.; Browne, K. P.; Grzybowski, B. A.; Stoddart, J. F. *Nano Lett.* **2009**, *9* (9), 3185–3190.
(80) Shibu Joseph, S. T.; Ipe, B. I.; Pramod, P.; Thomas, K. G. *J. Phys. Chem. B* **2006**, *110* (1), 150–157.
(81) Wang, L.; Zhu, Y.; Xu, L.; Chen, W.; Kuang, H.; Liu, L.; Agarwal, A.; Xu, C.; Kotov, N. A. *Angew. Chem. Int. Ed.* **2010**, *49* (32), 5472–5475.
(82) Chang, J.-Y.; Wu, H.; Chen, H.; Ling, Y.-C.; Tan, W. *Chem. Commun.* **2005**, No. 8, 1092.
(83) Caswell, K. K.; Wilson, J. N.; Bunz, U. H. F.; Murphy, C. J. *J. Am. Chem. Soc.* **2003**, *125* (46), 13914–13915.
(84) Salant, A.; Amitay-Sadovsky, E.; Banin, U. *J. Am. Chem. Soc.* **2006**, *128* (31), 10006–10007.
(85) Velev, O. D.; Bhatt, K. H. *Soft Matter* **2006**, *2* (9), 738.
(86) Singh, G.; Chan, H.; Baskin, A.; Gelman, E.; Repnin, N.; Král, P.; Klajn, R. *Science* **2014**, *345* (6201), 1149–1153.
(87) Pérez-Juste, J.; Rodríguez-González, B.; Mulvaney, P.; Liz-Marzán, L. M. *Adv. Funct. Mater.* **2005**, *15* (7), 1065–1071.
(88) Zhang, C.-L.; Lv, K.-P.; Cong, H.-P.; Yu, S.-H. *Small* **2012**, *8* (5), 648–653.
(89) Zhou, Y.; Zhou, X.; Park, D. J.; Torabi, K.; Brown, K. A.; Jones, M. R.; Zhang, C.; Schatz, G. C.; Mirkin, C. A. *Nano Lett.* **2014**, *14* (4), 2157–2161.
(90) Zhou, X.; Zhou, Y.; Ku, J. C.; Zhang, C.; Mirkin, C. A. *ACS Nano* **2014**, *8* (2), 1511–1516.
(91) Kuemin, C.; Nowack, L.; Bozano, L.; Spencer, N. D.; Wolf, H. *Adv. Funct. Mater.* **2012**, *22* (4), 702–708.
(92) Malaquin, L.; Kraus, T.; Schmid, H.; Delamarche, E.; Wolf, H. *Langmuir* **2007**, *23* (23), 11513–11521.
(93) Yin, Y.; Lu, Y.; Gates, B.; Xia, Y. *J. Am. Chem. Soc.* **2001**, *123* (36), 8718–8729.
(94) Thai, T.; Zheng, Y.; Ng, S. H.; Mudie, S.; Altissimo, M.; Bach, U. *Angew. Chem. Int. Ed.* **2012**, *51* (35), 8732–8735.
(95) Alba, M.; Pazos-Perez, N.; Vaz, B.; Formentin, P.; Tebbe, M.; Correa-Duarte, M. A.; Granero, P.; Ferré-Borrull, J.; Alvarez, R.; Pallares, J.; others. *Angew. Chem. Int. Ed.* **2013**, *52* (25), 6459–6463.
(96) Ahmed, S.; Ryan, K. M. *Nano Lett.* **2007**, *7* (8), 2480–2485.
(97) Yilmaz, C.; Cetin, A. E.; Goutzamanidis, G.; Huang, J.; Somu, S.; Altug, H.; Wei, D.; Busnaina, A. *ACS Nano* **2014**, *8* (5), 4547–4558.
(98) Vakarelski, I. U.; Chan, D. Y.; Nonoguchi, T.; Shinto, H.; Higashitani, K. *Phys. Rev. Lett.* **2009**, *102* (5), 058303.
(99) Thorkelsson, K.; Bai, P.; Xu, T. *Nano Today* **2015**, *10* (1), 48–66.
(100) Pietra, F.; Rabouw, F. T.; Evers, W. H.; Byelov, D. V.; Petukhov, A. V.; de Mello Donegá, C.; Vanmaekelbergh, D. *Nano Lett.* **2012**, *12* (11), 5515–5523.
(101) Wang, L.; Xu, L.; Kuang, H.; Xu, C.; Kotov, N. A. *Acc. Chem. Res.* **2012**, *45* (11), 1916–1926.
(102) Jain, P. K.; Eustis, S.; El-Sayed, M. A. *J. Phys. Chem. B* **2006**, *110* (37), 18243–18253.
(103) Alvarez-Puebla, R. A.; Agarwal, A.; Manna, P.; Khanal, B. P.; Aldeanueva-Potel, P.; Carbó-Argibay, E.; Pazos-Pérez, N.; Vigderman, L.; Zubarev, E. R.; Kotov, N. A.; others. *Proc. Natl. Acad. Sci.* **2011**, *108* (20), 8157–8161.
(104) Nie, S.; Emory, S. R. *science* **1997**, *275* (5303), 1102–1106.
(105) Gómez-Graña, S.; Pérez-Juste, J.; Alvarez-Puebla, R. A.; Guerrero-Martínez, A.; Liz-Marzán, L. M. *Adv. Opt. Mater.* **2013**, *1* (7), 477–481.

(106) Doherty, M. D.; Murphy, A.; McPhillips, J.; Pollard, R. J.; Dawson, P. *J. Phys. Chem. C* **2010**, *114* (47), 19913–19919.
(107) Yu, C.-J.; Tseng, W.-L. *Langmuir* **2008**, *24* (21), 12717–12722.
(108) D'Agostino, A.; Taglietti, A.; Bassi, B.; Donà, A.; Pallavicini, P. *J. Nanoparticle Res.* **2014**, *16* (10), 1–11.
(109) Elghanian, R.; Storhoff, J. J.; Mucic, R. C.; Letsinger, R. L.; Mirkin, C. A. *Science* **1997**, *277* (5329), 1078–1081.
(110) Wang, J.; Zhang, P.; Li, C. M.; Li, Y. F.; Huang, C. Z. *Biosens. Bioelectron.* **2012**, *34* (1), 197–201.
(111) Sudeep, P. K.; Joseph, S. T. S.; Thomas, K. G. *J. Am. Chem. Soc.* **2005**, *127* (18), 6516–6517.
(112) Lee, J.; Hernandez, P.; Lee, J.; Govorov, A. O.; Kotov, N. A. *Nat. Mater.* **2007**, *6* (4), 291–295.
(113) Parab, H. J.; Jung, C.; Lee, J.-H.; Park, H. G. *Biosens. Bioelectron.* **2010**, *26* (2), 667–673.
(114) Hou, J.; Zhang, H.; Yang, Q.; Li, M.; Song, Y.; Jiang, L. *Angew. Chem.* **2014**, *126* (23), 5901–5905.
(115) Fraire, J. C.; Pérez, L. A.; Coronado, E. A. *ACS Nano* **2012**, *6* (4), 3441–3452.
(116) Wei, W.; Chen, K.; Ge, G. *Adv. Mater.* **2013**, *25* (28), 3863–3868.
(117) Fan, M.; Andrade, G. F.; Brolo, A. G. *Anal. Chim. Acta* **2011**, *693* (1), 7–25.
(118) Lee, Y. H.; Lee, C. K.; Tan, B.; Rui Tan, J. M.; Phang, I. Y.; Ling, X. Y. *Nanoscale* **2013**, *5* (14), 6404.
(119) Kabashin, A. V.; Evans, P.; Pastkovsky, S.; Hendren, W.; Wurtz, G. A.; Atkinson, R.; Pollard, R.; Podolskiy, V. A.; Zayats, A. V. *Nat. Mater.* **2009**, *8* (11), 867–871.
(120) Garwe, F.; Huebner, U.; Clausnitzer, T.; Kley, E.-B.; Bauerschaefer, U. 2005; Vol. 5955, p 59550T – 59550T – 8.
(121) Mubeen, S.; Lee, J.; Singh, N.; Krämer, S.; Stucky, G. D.; Moskovits, M. *Nat. Nanotechnol.* **2013**, *8* (4), 247–251.
(122) Lee, J.; Govorov, A. O.; Kotov, N. A. *Angew. Chem.* **2005**, *117* (45), 7605–7608.
(123) Sönnichsen, C.; Reinhard, B. M.; Liphardt, J.; Alivisatos, A. P. *Nat. Biotechnol.* **2005**, *23* (6), 741–745.
(124) Kang, Y.; Erickson, K. J.; Taton, T. A. *J. Am. Chem. Soc.* **2005**, *127* (40), 13800–13801.
(125) Zheng, J.; Constantinou, P. E.; Micheel, C.; Alivisatos, A. P.; Kiehl, R. A.; Seeman, N. C. *Nano Lett.* **2006**, *6* (7), 1502–1504.
(126) Álvarez-Puebla, R. A.; Contreras-Cáceres, R.; Pastoriza-Santos, I.; Pérez-Juste, J.; Liz-Marzán, L. M. *Angew. Chem. Int. Ed.* **2009**, *48* (1), 138–143.
(127) Zhu, M.-Q.; Wang, L.-Q.; Exarhos, G. J.; Li, A. D. Q. *J. Am. Chem. Soc.* **2004**, *126* (9), 2656–2657.
(128) Frankamp, B. L.; Boal, A. K.; Rotello, V. M. *J. Am. Chem. Soc.* **2002**, *124* (51), 15146–15147.
(129) Guerrero-Martínez, A.; Auguié, B.; Alonso-Gómez, J. L.; Džolić, Z.; Gómez-Graña, S.; Žinić, M.; Cid, M. M.; Liz-Marzán, L. M. *Angew. Chem. Int. Ed.* **2011**, *50* (24), 5499–5503.
(130) Mastroianni, A. J.; Claridge, S. A.; Alivisatos, A. P. *J. Am. Chem. Soc.* **2009**, *131* (24), 8455–8459.
(131) Chen, W.; Bian, A.; Agarwal, A.; Liu, L.; Shen, H.; Wang, L.; Xu, C.; Kotov, N. A. *Nano Lett.* **2009**, *9* (5), 2153–2159.
(132) Teranishi, T. *Comptes Rendus Chim.* **2003**, *6* (8-10), 979–987.
(133) Chen, W.; Weng, S.; Zhang, F.; Allen, S.; Li, X.; Bao, L.; Lam, R. H.; Macoska, J. A.; Merajver, S. D.; Fu, J. *ACS Nano* **2012**, *7* (1), 566–575.
(134) Wang, S.; Liu, K.; Liu, J.; Yu, Z. T.-F.; Xu, X.; Zhao, L.; Lee, T.; Lee, E. K.; Reiss, J.; Lee, Y.-K.; others. *Angew. Chem. Int. Ed.* **2011**, *50* (13), 3084–3088.
(135) Yu, Z. T. F.; Aw Yong, K. M.; Fu, J. *Small* **2014**, *10* (9), 1687–1703.
(136) Engel, Y.; Schiffman, J. D.; Goddard, J. M.; Rotello, V. M. *Mater. Today* **2012**, *15* (11), 478–485.
(137) Moyano, D. F.; Rotello, V. M. *Langmuir* **2011**, *27* (17), 10376–10385.
(138) Alam, R.; Lightcap, I. V.; Karwacki, C. J.; Kamat, P. V. *ACS Nano* **2014**, *8* (7), 7272–7278.
(139) Alvarez-Puebla, R. A.; Liz-Marzán, L. M. *Chem. Soc. Rev.* **2012**, *41* (1), 43.
(140) Golightly, R. S.; Doering, W. E.; Natan, M. J. *ACS Nano* **2009**, *3* (10), 2859–2869.
(141) Aćimović, S. S.; Ortega, M. A.; Sanz, V.; Berthelot, J.; Garcia-Cordero, J. L.; Renger, J.; Maerkl, S. J.; Kreuzer, M. P.; Quidant, R. *Nano Lett.* **2014**, *14* (5), 2636–2641.

(142) Arnold, M.; Schwieder, M.; Blümmel, J.; Cavalcanti-Adam, E. A.; López-Garcia, M.; Kessler, H.; Geiger, B.; Spatz, J. P. *Soft Matter* **2009**, *5* (1), 72–77.
(143) Ofir, Y.; Moran, I. W.; Subramani, C.; Carter, K. R.; Rotello, V. M. *Adv. Mater.* **2010**, *22* (32), 3608–3614.
(144) Mérian, T.; Goddard, J. M. *J. Agric. Food Chem.* **2012**, *60* (12), 2943–2957.
(145) Vasilev, K.; Cook, J.; Griesser, H. J. *Expert Rev. Med. Devices* **2009**, *6* (5), 553–567.
(146) Kwiat, M.; Elnathan, R.; Kwak, M.; de Vries, J. W.; Pevzner, A.; Engel, Y.; Burstein, L.; Khatchtourints, A.; Lichtenstein, A.; Flaxer, E.; others. *J. Am. Chem. Soc.* **2011**, *134* (1), 280–292.
(147) Gates, B. D.; Xu, Q.; Stewart, M.; Ryan, D.; Willson, C. G.; Whitesides, G. M. *Chem. Rev.* **2005**, *105* (4), 1171–1196.
(148) Qin, D.; Xia, Y.; Whitesides, G. M. *Nat. Protoc.* **2010**, *5* (3), 491–502.
(149) Henzie, J.; Barton, J. E.; Stender, C. L.; Odom, T. W. *Acc. Chem. Res.* **2006**, *39* (4), 249–257.
(150) Vakarelski, I. U.; Marston, J. O.; Thoroddsen, S. T. *Langmuir* **2013**, *29* (16), 4966–4973.
(151) Zhan, Z.; Lei, Y. *ACS Nano* **2014**, *8* (4), 3862–3868.
(152) Xia, Y.; Kim, E.; Whitesides, G. M. *Chem. Mater.* **1996**, *8* (7), 1558–1567.
(153) Kim, E.; Xia, Y.; Whitesides, G. M. *Nature* **1995**, *376* (6541), 581–584.
(154) Kim, E.; Xia, Y.; Whitesides, G. M. *Adv. Mater.* **1996**, *8* (3), 245–247.
(155) Xu, L.; Ma, W.; Wang, L.; Xu, C.; Kuang, H.; Kotov, N. A. *Chem. Soc. Rev.* **2013**, *42* (7), 3114.
(156) Ye, X.; Jin, L.; Caglayan, H.; Chen, J.; Xing, G.; Zheng, C.; Doan-Nguyen, V.; Kang, Y.; Engheta, N.; Kagan, C. R.; Murray, C. B. *ACS Nano* **2012**, *6* (3), 2804–2817.
(157) Scarabelli, L.; Grzelczak, M.; Liz-Marzán, L. M. *Chem. Mater.* **2013**, *25* (21), 4232–4238.
(158) Guerrero-Martínez, A.; Pérez-Juste, J.; Carbó-Argibay, E.; Tardajos, G.; Liz-Marzán, L. M. *Angew. Chem. Int. Ed.* **2009**, *48* (50), 9484–9488.
(159) Pérez-Juste, J.; Liz-Marzán, L. M.; Carnie, S.; Chan, D. Y. C.; Mulvaney, P. *Adv. Funct. Mater.* **2004**, *14* (6), 571–579.
(160) Mayer, M.; Scarabelli, L.; March, K.; Altantzis, T.; Tebbe, M.; Kociak, M.; Bals, S.; García de Abajo, F. J.; Fery, A.; Liz-Marzán, L. M. *Nano Lett.* **2015**, *15* (8), 5427–5437.
(161) Xie, Y.; Guo, S.; Ji, Y.; Guo, C.; Liu, X.; Chen, Z.; Wu, X.; Liu, Q. *Langmuir* **2011**, *27* (18), 11394–11400.
(162) Ming, T.; Kou, X.; Chen, H.; Wang, T.; Tam, H.-L.; Cheah, K.-W.; Chen, J.-Y.; Wang, J. *Angew. Chem. Int. Ed.* **2008**, *47* (50), 9685–9690.
(163) Deegan, R. D.; Bakajin, O.; Dupont, T. F.; Huber, G.; Nagel, S. R.; Witten, T. A. *Nature* **1997**, *389* (6653), 827–829.
(164) Scarabelli, L.; Sánchez-Iglesias, A.; Pérez-Juste, J.; Liz-Marzán, L. M. *J. Phys. Chem. Lett.* **2015**, *6* (21), 4270–4279.
(165) Frenkel, D. *Nat. Mater.* **2015**, *14* (1), 9–12.
(166) Onsager, L. *Ann. N. Y. Acad. Sci.* **1949**, *51* (4), 627–659.
(167) Routh, A. F. *Rep. Prog. Phys.* **2013**, *76* (4), 046603.
(168) Erbil, H. Y. *Adv. Colloid Interface Sci.* **2014**.
(169) Zhang, S.-Y.; Regulacio, M. D.; Han, M.-Y. *Chem. Soc. Rev.* **2014**, *43* (7), 2301–2323.
(170) McDonald, J. C.; Duffy, D. C.; Anderson, J. R.; Chiu, D. T.; Wu, H.; Schueller, O. J. A.; Whitesides, G. M. *Electrophoresis* **2000**, *21* (1), 27–40.

CHAPTER

IV

CHARACTERIZATION OF PLASMONIC NANOMATERIALS

IV.1. INTRODUCTION

As discussed in the previous chapters of this thesis, the last two decades have witnessed impressive advances in the synthesis of a vast range of nanoobjects with new and intriguing optical properties. This calls for the development of new characterization techniques that enable the analysis of nanometric systems with increasing degree of detail.[1–5] In particular, understanding the plasmonic properties of noble metal nanostructures requires the study of their optical properties and their correlation with particle size, shape, composition and surface chemistry.[1,2,6] This need becomes especially relevant toward the analysis of single particles or ordered self-assembled structures as compared to colloidal solutions (see section IV.2). Within the wide variety of characterization techniques, a classification can be made into three main categories: microscopy, spectroscopy and scattering analysis.[7] Before proceeding to a brief overview of the most common techniques, it is important to distinguish between near-field and far-field analysis. In fact, most plasmonic effects are confined in close vicinity to the nanoparticle surface (much less than one wavelength, see section I.2.3); therefore, techniques that are able to probe them are classified as near-field techniques, while in the case of a far-field measurement, the optical properties of the sample are detected far (several wavelengths) away from it. This concept is particularly important, since the relationship between near- and far-field measurements is often not trivial.

IV.1.1 Microscopic Analysis

The main issue when dealing with microscopic analysis of nanosystems is obviously their size, which is generally well below the diffraction limit of an optical microscope. For this reason electron microscopy has developed as the most common family of techniques that allow the direct visualization of nanoparticles (**Figure IV.1A**).[8,9] Transmission electron microscopy (TEM) and scanning electron microscopy (SEM) have significantly evolved towards high resolution power (HR-TEM and HR-SEM), currently being able to image the periodic distribution of atoms in a crystalline lattice. Furthermore, when fast electrons are focused on a sample, different signals are generated (**Figure IV.1B**). Those signals can be used to further characterize the specimen, thereby giving rise to additional characterization

methods based on electron microscopy, such as Energy Dispersive X-ray Spectroscopy (EDX or EDS), which allows for elemental analysis of the imaged nanoparticles.[10,11] However, even the highest resolution does not change the fact that TEM produces a two-dimensional (2D) projection of a three-dimensional (3D) object. To overcome this important drawback, electron tomography has been significantly improved and adapted to inorganic materials (**Figure IV.1C**).[12] In a typical tomography experiment, a so-called tilt series of images is taken sequentially by tilting the sample holder by few degrees, followed by processing through suitable mathematical algorithms into a 3D reconstruction of the real object (**Figure IV.1C**). Over the years, many electron microscopy techniques have been extended to the third dimension, and even atomic resolution was recently demonstrated.[13] Despite the huge amount of information that can be retrieved using electron microscopy, one major drawback of this set of techniques is the need for working in ultra-high vacuum conditions. Even though environmental TEM and SEM try to overcome this problem, the conditions are anyway severely restricted.[14,15]

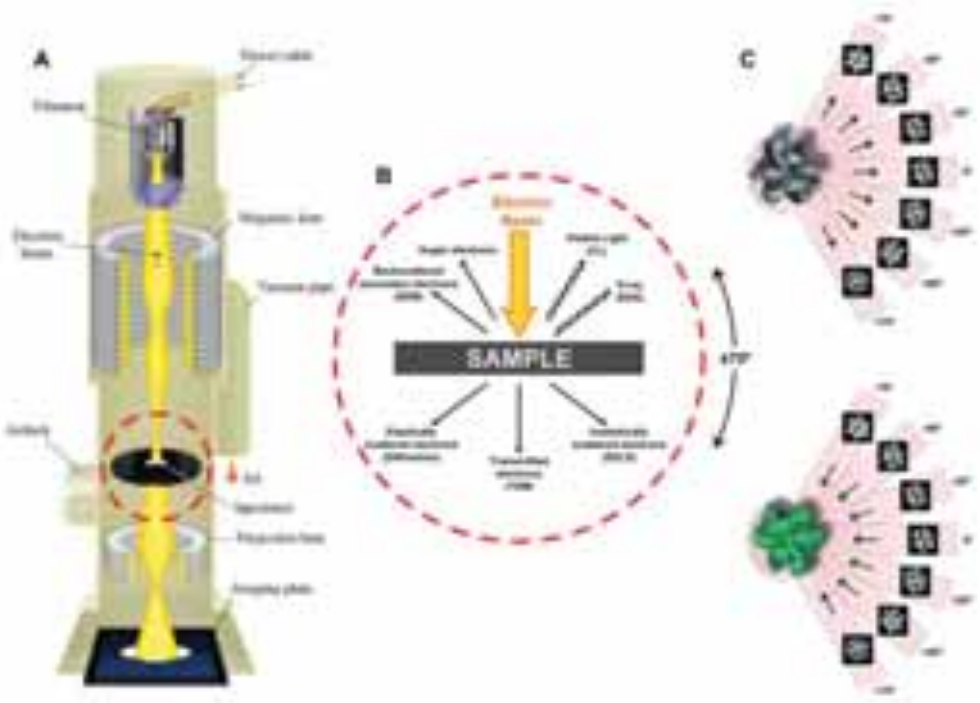

Figure IV.1 A: Schematic representation of a typical transmission electron microscope. **B:** Schematic view of the specimen area with a list of the different signals deriving from the interaction between the electron beam and the sample. **C: top:** example of the acquisition of a tilt-series; **bottom:** back-projection of the images along their original acquisition directions. **C** adapted from Ref. 12.

IV.1.2. Spectroscopic Analysis

In this second group we include commonly used techniques such as UV-vis and fluorescence or photoluminescence spectroscopies. In fact, since the optical properties of nanoparticles are extremely sensitive to any kind of modification in the nanoparticle size, shape, surface chemistry and environment (see section I.2.2), optical data become extremely useful in many cases, such as monitoring of ligand exchange reactions, aggregation, growth or coating of nanoparticles, etc.[16–18] Another important spectroscopic technique is X-ray photoelectron spectroscopy (XPS), which can provide detailed information on nanoparticle elemental composition, electronic/oxidation state and surface ligands.[19–21] It should be noted however that XPS is a surface sensitive technique, so the analysis is restricted to the most external atomic layers. Interestingly, it has been demonstrated that plasmonic optical information can be accessed using fast electrons, like those employed in electron microscopy.[22–30] Two main techniques were developed from this observation: cathodoluminescence (CL)[31–34] and electron energy loss spectroscopy (EELS).[35–37] In these techniques, a fast electron (typically travelling at half the speed of light) is focused onto or close to the nanostructure of interest. The electron is capable of transferring energy to the nanostructure via electromagnetic interaction: more specifically, the electric field carried by the electron strongly resembles a plane wave of white light travelling in the direction of the electron path,[8,38] i.e. it is spatially localized and spectrally broadband, in perfect opposition to the spatially isotropic and monochromatic plane waves commonly used in photonic excitation.[29] Consequently, these two excitations show two important differences: i) through fast electrons it is possible to excite both bright and dark plasmonic modes; ii) electron excitation provides high spatial resolution.[8] EELS analyzes the plasmon-electron interaction through the slowdown experienced by the electron (dispersing them as a function of their energy with a magnetic prism), while CL detects the emitted light resulting from the interaction (using a concave mirror to transmit the signal to a spectrometer, **Figure IV.3A**). Interestingly, theoretical considerations indicate a strong parallelism between EELS and light extinction on one hand and CL and light scattering on the other (see section IV.2.1.2).[8] Two crucial advantages of these techniques are the possibility of reaching atomic resolution, and the fact that both techniques can be applied while analyzing the structural properties of the nanoobject through

Scanning TEM (STEM), therefore directly providing a correlated optical and structural study (see section IV.2).[39,40]

IV.1.3. Scattering Analysis

Compared to molecules, nanoparticles scatter light much more efficiently (up to 5 orders of magnitude), which can be exploited for their characterization, both in colloidal solution and in the dried state. Dynamic light scattering (DLS or photon correlation spectroscopy) uses the scattering of laser visible photons to investigate nanoparticles diffusion in solution, thereby being able to determine their size and, through application of a voltage, their surface potential.[41–43] Small angle X-ray scattering (SAXS) exploits X-rays instead to retrieve structural information, and if complemented with small angle neutron scattering (SANS) it can also allow us to investigate the ligand layer surrounding the particles, since neutrons display a higher cross-section, rendering them sensitive to lighter elements such as carbon, oxygen or nitrogen.[44,45] Another important technique that is becoming standard in the characterization of plasmonic systems is dark field spectral microscopy (DFM), which combines optical microscopy (**Figure IV.2B**) with scattering analysis (**Figure IV.2C**).[2,5,46–48] The basic idea behind DFM is depicted in **Figure IV.2**. A high numerical aperture condenser equipped with a circular block at the lens is coupled with an objective presenting a lower numerical aperture. In this configuration only light that is scattered by the specimen can reach the objective and consequently the detector (**Figure IV.2A**). This signal is ultimately collected and analyzed with a high sensitivity spectrophotometer. The main advantages of DFM are the ability of working in ambient condition (both dry and in liquid), and the very high signal-to-noise ratio, which allows single particle experiments, whereas the principal drawback is the lack of resolution, so that DFM analysis is often coupled to electron microscopy (see section IV.2).

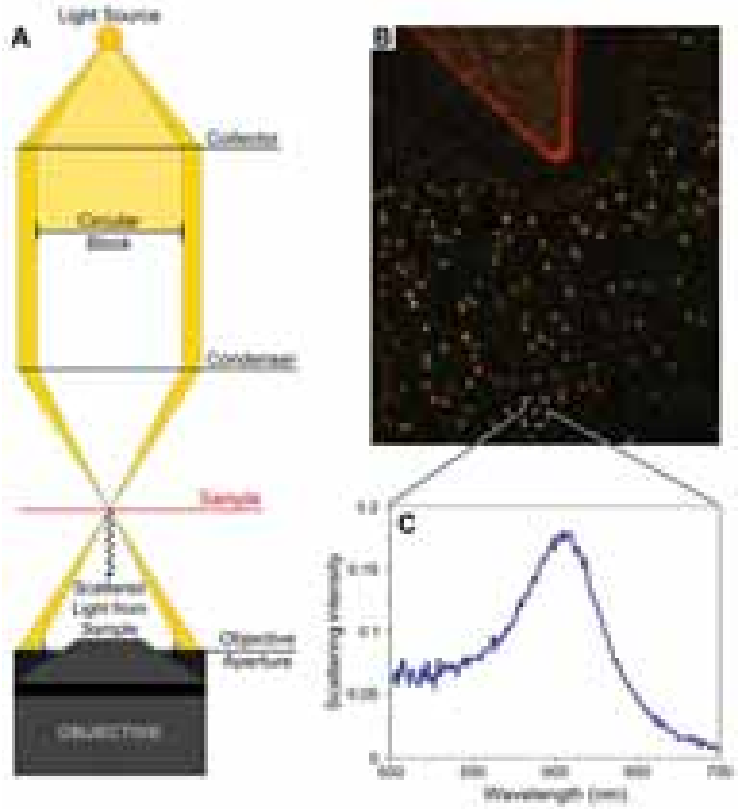

Figure IV.2 A: Schematic representation of a typical dark field microscope. **B:** Representative DFM image of a sample of gold nanoparticles spin coated over and indexed substrate. **C:** Optical spectroscopic analysis of one of the bright dots in **B**.

IV.2. STRUCTURALLY CORRELATED SPECTROSCOPY

Despite the significant advances that have been achieved in the bottom-up synthesis of plasmonic nanoparticles, there are intrinsic differences between nanosynthesis and "standard" organic synthesis. Whereas the *product* of an organic reaction is made of identical (molecular) components, this does not apply in nanochemistry, where there is always a certain distribution of sizes and morphologies within a nanoparticle population. In organic synthesis, ensemble measurements are always representative of the properties of each constituent molecule, while in nanosynthesis this is not necessarily true.[2] For example, Sherry et al. observed that single silver nanocubes present two well defined LSPRs, which are not resolved in ensemble spectra, where the quadrupolar mode is only barely observable as a shoulder. [49,50]

The scenario is further complicated by differences between near-field and far-field: the classical optical concepts of extinction, absorption, and scattering are no longer sufficient to describe optical phenomena at the nanoscale. Instead, the spatial and spectral distributions of photonic eigenmodes have been recognized to play an important role when interpreting experimental outputs delivered by numerous near-field techniques.[22,24,26,27,31,51–53] Likewise, concepts such as the local density of states (LDOS)[54] or alternative descriptions in terms of modal decompositions[55] have become relevant for understanding nanoscale resolved experiments, including scanning near-field optical microscopy,[56,57] thermal radiation scanning tunneling microscopy,[58] EELS[23,25,36,57,59–62] and CL.[25,32,60,63] Nevertheless, the physics embodied in optical extinction, absorption, and scattering phenomena should hold to some extent at the nanometer scale. In other words, we still need to understand how a nanostructure absorbs and scatters electromagnetic waves at subwavelength scales.

In conclusion, the possibility of correlating structural and optical properties at the level of a single nanoobject is crucial toward understanding and development of optical phenomena at the nanometer scale.

IV.2.1. EELS and CL of Single Gold Nanotriangles

EELS and CL, which proved to be outstanding tools for studying surface plasmons with superior spatial resolution, even in the most complex systems,[64] are both suitable candidates for single particle optical correlated studies.[8] Basically, the electromagnetic nature of the electron-sample interaction allows us to explore the optical response of the nanostructure. In particular, CL relates to the ability of the nanostructure to scatter the evanescent electromagnetic field carried by electrons in the far-field, whereas EELS probes the sum of radiative losses (i.e., CL) plus energy that is inelastically absorbed by the materials involved. This close relationship between fast electron-based spectroscopies and optical properties has been emphasized in qualitative interpretations of EELS and CL experiments in terms of either absorption, extinction, or scattering.[33,65–68] However, the apparent connection between EELS and extinction on the one hand, and CL and scattering on the other hand, which is also suggested by modal decomposition analysis in the case of spheres,[8,25,32,36,60–64] has not been addressed theoretically in a general case. From the experimental viewpoint, we remark that

combined EELS/CL experiments on the same nanoobject and in the same environment are still missing, precluding a fair, exact comparison of both extinction and scattering at the nanometer scale, as well as clear evidence of the intimate relationship between traditional optics-based measurements and subwavelength-resolved electron-beam spectroscopies.

In this work, we present experimental and theoretical evidence that spatially resolved EELS and CL experiments performed on the same individual metallic nanoparticles allow us to directly disentangle radiative and non-radiative modes on a single particle basis. We also show that EELS and CL are closely connected to optical extinction and scattering phenomena at the nanometer scale. We further demonstrate that dipolar surface plasmon modes, as measured by both techniques, may appear to have different resonance energies although they give rise to similar intensity spatial distributions. Simulations clearly show that such spectral differences between EELS and CL are also present in light extinction and scattering. As a consequence, the main spectral differences between extinction and scattering observed when examining individual nanoparticles as a whole via far-field spectroscopies are qualitatively maintained upon nanoscale inspection within individual nanoaprticles through EELS and CL. We formulate modal decompositions in the quasi-static limit for CL, as well as for optical extinction and scattering, and compare them to a previously derived formula for EELS. This helps us to understand in simple terms the role of dissipation that we report in both experiments and simulation, which affects extinction and scattering phenomena in distinct ways.

IV.2.1.1. Correlated EELS/CL Study on Single Small Gold Nanotriangles

Gold triangular nanoprisms were synthesized using the protocol described in section II.3.1;[69,70] In this study two batches of nanoprisms were used. The first one[70] consists of highly uniform equilateral 60 nm edge long, 30 nm thick nanoprisms deposited on a graphene sheet. The second one[69] consists of 80 - 200 nm edge long (and varying thickness) nanoprisms drop-casted on a thin carbon film. Such nanoparticles are chosen for their high crystallinity which leads to well-defined resonances both in EELS[71] and CL,[72] and because the surface plasmon modes that dominate their optical response have been thoroughly discussed in the literature.[62,65,71,73] In particular, in small nanoprisms the modes are rather

simple[73] and well-described in the quasi-static limit.[62,65] Additionally, the mode energies lie within the experimental range that is accessible with our CL detection system (above 1.2 eV). However, these nanoparticles yield extremely weak CL signals, which might explain why no spatially resolved CL experiments have been previously reported on objects of such a small size. Experiments were performed using a STEM fitted with home-made EELS detection[26] and high efficiency CL detection systems,[74] as presented in **Figure IV.3A** (see Experimental Section, section IV.3.3). Such a microscope generates a sub-nanometer electron beam that can be scanned over the region of interest. At each sampling point, a morphological high angle annular dark field (HAADF) signal is recorded simultaneously with an EELS and/or a CL spectrum. At the end of the scan, both an HAADF image and a complete set of spatially resolved spectra are collected and can be accurately compared. Alternatively, such a set of spatially-resolved spectra can be viewed as a collection of energy filtered maps, which show the spatial distribution of the recorded signal at constant energy (see examples below). In these experiments, EELS and CL datasets are acquired sequentially because the experimental illumination conditions are drastically different for both spectroscopies, with electron beam currents typically two orders of magnitude higher for CL experiments (around 1 nA) than for EELS experiments (around 10-20 pA). Furthermore, typical acquisition times for EELS are 5 to 10 times shorter than for CL. This emphasizes the much higher interaction cross-sections when measured by EELS as compared to CL. As the purpose is to directly compare both techniques, extreme care was taken in calibrating both spectrometers. Further details can be found in the Experimental section (section IV.3.3). We systematically checked that the electron beam did not alter the prisms or the substrate during the scans, and we discarded all experiments in which this happened. We stress that we performed measurements on the very same triangles and environment, thus allowing us to unambiguously compare both physical signals (EELS and CL). This is in stark contrast to previously published CL and EELS measurements performed on related but dissimilar nanoprticles,[34] as even slight changes in dimensions or environment can significantly shift energies,[6] and thus impair any quantitative comparison between CL and EELS. We simulated spatially-resolved EELS and CL probabilities, as well as extinction and scattering cross-sections, using the retarded BEM,[75] which allowed us to account for the particle

morphologies[65] and, when appropriate, to model carbon substrates. The dielectric function of gold and amorphous carbon were taken from optical data.[76,77] When needed, in order to increase the effect of dissipation, the imaginary part of the dielectric functions were modified as described in Ref. 64 (see Simulations section IV.4.1). As a first illustration, **Figure IV.3B** presents the HAADF image and colored maps obtained from spatially-resolved EELS and CL experiments performed on a 60 nm wide triangle lying on a graphene sheet. Total acquisition times for the whole experiments are 157 s for CL and 16 s for EELS. In the color maps, the color and intensity of each pixel can be related to the energy and amplitude of a locally measured resonance.[78] These maps clearly show that two main excitations, located at the tips (lower energy excitation, yellowish color) and at the sides (higher energy excitation, greenish color) of the nanoprism, were measured in EELS, while only the low energy one was observed in CL. It is worth noting that such maps can be generated on the fly right after acquisition without resorting to the more lengthy procedures required for quantitative analysis as described below.

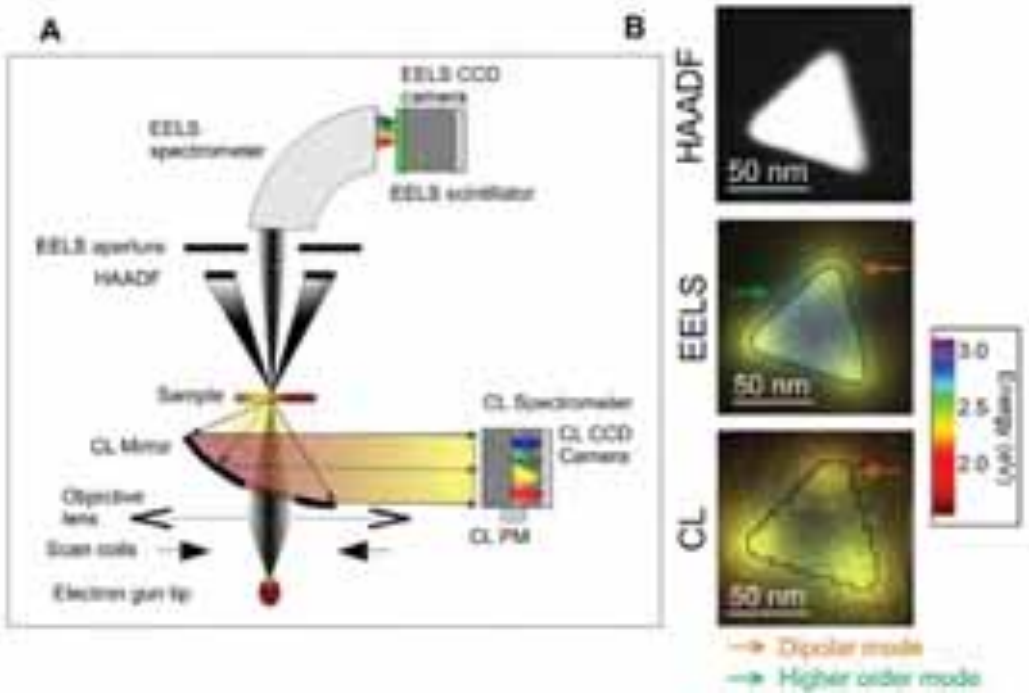

Figure IV.3: A: Scheme of a STEM equipped with EELS and CL detection systems. **B:** Combined HAADF imaging (top), EELS (middle) and CL (bottom) spatially resolved datasets. Total acquisition times were 157 s for CL and 16 s for EELS. In the case of EELS, the spectra were first deconvoluted and normalized. CL and EELS images were generated by coloring each filtered map of the datasets according to its energy, weighting each pixel of the maps by its intensity and summing all the resulting images. This simplified representation of the EELS and CL datasets shows that the EELS data exhibit both dipolar and higher order modes, while the CL data exhibit mainly the dipolar mode. The black lines superimposed on the maps indicate the prism shape as obtained in the HAADF image.

In order to quantitatively analyze the features already suggested by **Figure IV.3B**, we show in **Figure IV.4A** the EELS (blue) and CL (red) spectra corresponding to an electron probe located at the tip (T) and side (S) of the nanoprism. The filtered maps of **Figure IV.4B** display the spatial variations of the EELS (blue framed maps) and CL (red framed maps) signals averaged over two narrow (50 meV wide) energy windows centered on the resonances revealed in the EELS spectra. Beyond such filtered maps, we analyze the surface plasmon modes probed by both techniques by processing and fitting each spectrum of the datasets to a sum of Gaussian functions.[79,80] By doing so, each Gaussian peak can be associated with an optical mode.[6,26,34,57,64,79,80] An intensity map of a given mode is then retrieved by assigning to each image pixel the peak amplitude measured in the spectrum that

is recorded at the corresponding electron probe position. Such amplitude maps are shown in **Figure IV.4C**, and correspond to modes resonating at the energies associated with the maxima visible in the EELS and CL spectra. Data analysis based on such fitting techniques allows us to lift the ambiguities generally found in filtered maps, in which the origin of a given intensity change cannot be clearly identified, as it can result from a peak energy change or the tail of a neighboring intense mode.[8,72]

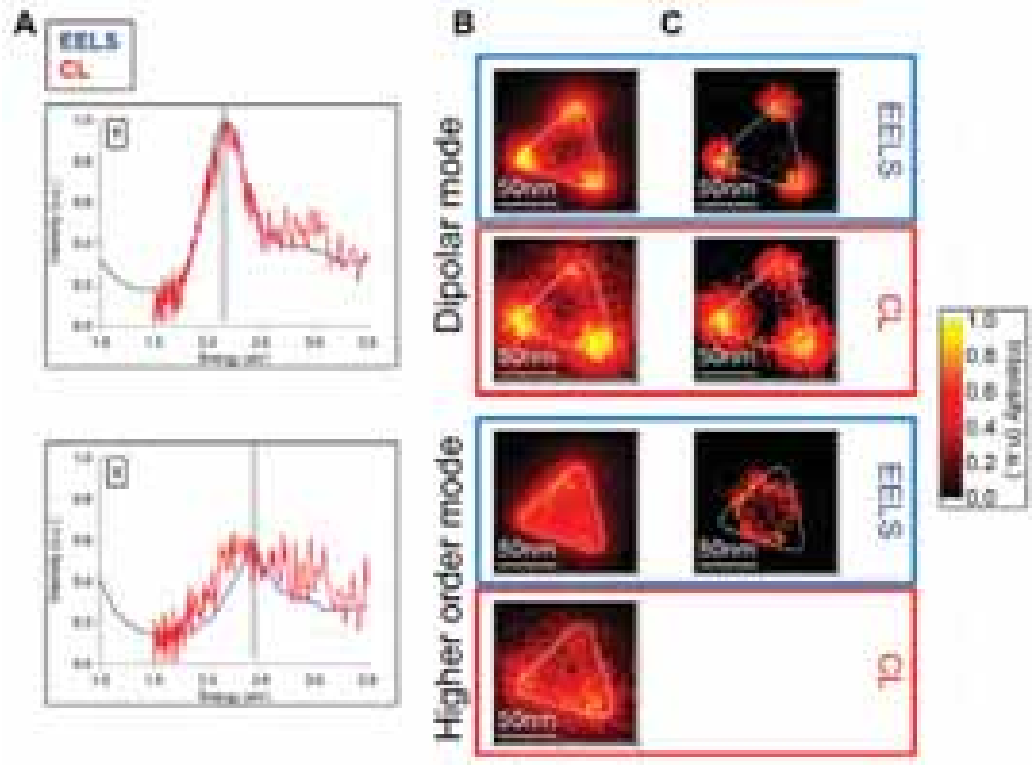

Figure IV.4. A: EELS (blue) and CL (red) spectra taken at the low left tip (T) and left side (S) of the 60 nm long, 30 nm thick prism deposited on a graphene sheet shown on **Figure IV.3**. The vertical gray windows indicate the spectral ranges considered when building the energy filtered and fitted maps. The spectra were averaged on 9 (EELS) and 25 (CL) pixels of the datasets. **B:** EELS and CL maps filtered around the energy of the EELS/CL maxima shown on the T and S panels of **A. C:** Fitted amplitude maps corresponding to the dipolar (EELS and CL) and higher order (EELS only) modes. EELS and CL were independently normalized to their own maxima. The white lines superimposed on the maps indicate the prism shape as obtained from the HAADF image.

As previously demonstrated,[65,73] the two dominant modes that appear in the EELS data correspond to a low-energy dipolar mode (d), with charge density peaking at the tips, and a higher-energy non dipolar mode (ho), with charge density peaking at the tips and edges (see insets of **Figure IV.5A**). The non –dipolar mode, here loosely denoted as higher order mode, has been historically referred to as quadrupolar[73] but has been recently recast as hexapolar.[62] When averaging over the three tips and sides, we note that these modes are resonant at $E_{EELS}^{d,exp}$ = 2.16 ± 0.02 eV and $E_{EELS}^{ho,exp}$ = 2.41 ± 0.02 eV. Strikingly, the CL data exhibit just the dipolar mode (resonant at $E_{CL}^{d,exp}$ = 2.18 ± 0.02 eV), as implied by the featureless spectrum and map filtered at the higher order mode energy, which shows only a background intensity without any spatial variations. We also note that the spatial distributions of EELS and CL intensities are similar for the dipolar mode, as suggested by previously reported separate EELS[26,65,71] and CL[72] experiments. These conclusions confirm the above qualitative analysis based on **Figure IV.3B**. The darkening of the higher order mode in CL is corroborated by the simulations shown in **Figure IV.5**. Considering the absolute energy values, the agreement between simulations and experiments is quite satisfactory without taking into account any substrate. More precisely, they show that the dipolar mode is resonant at $E_{EELS}^{d,sim}$ = 2.20 ± 0.005 eV in EELS and $E_{CL}^{d,sim}$ = 2.17 ± 0.005 eV in CL. Furthermore, the higher order mode appears as an additional clear peak at $E_{EELS}^{ho,sim}$ = 2.41 ± 0.005 eV in EELS, while it is barely visible in CL. The small energy difference between the EELS and CL dipolar resonances, which lies within the experimental error bars, is discussed in further detail below (section IV.2.1.2). Moreover, we note that the FWHM of the calculated EELS and CL resonances ($\sigma_{EELS}^{d,sim}$ = $\sigma_{CL}^{d,sim}$ = 230 ± 5 meV) are in good agreement with those obtained from the CL measurements ($\sigma_{CL}^{d,exp}$ = 245 ± 20 meV) but slightly smaller than those of the EELS measurements ($\sigma_{CL}^{d,exp}$ = 260 ± 20 meV). We attribute this effect to the lower experimental energy resolution of EELS as compared with CL.

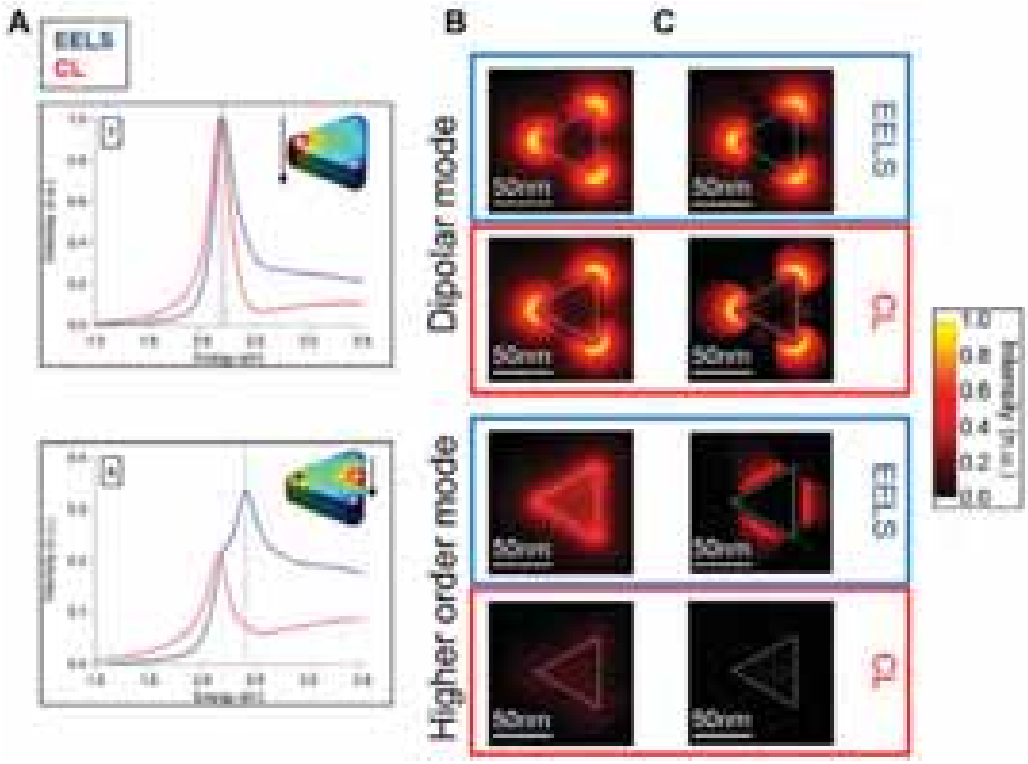

Figure IV.5. A: Simulated EELS (blue) and CL (red) spectra calculated at the tip (T) and side (S) of a 60 nm long, 30 nm thick prism surrounded by vacuum. The vertical grey windows indicate the spectral ranges considered when building the energy filtered and fitted maps of **B** and **C**. **Insets:** surface charges induced by a fast electron beam located at the tip and side (represented as arrows) at the energies of the corresponding EELS maxima. **B** Simulated EELS and CL maps filtered around the energy of the EELS and CL maxima. **C** Simulated fitted amplitude maps corresponding to the dipolar (EELS and CL) and higher order (EELS only) modes. EELS and CL are independently normalized to their own maxima. The white lines superimposed on the maps indicate the prism shape.

The remarkable agreement between the experimental and calculated CL FWHM thus confirms the weak influence of the graphene sheet on the actual measurements. The absence of any higher order mode within the CL dataset is a direct experimental demonstration of the drastically different character of EELS and CL signals, which has been theoretically anticipated for several years.[8,25,38] CL only probes the radiative modes, which are dipolar modes for small objects, while EELS probes all the modes.

IV.2.1.2. Differences Between EELS/Extinction and CL/Scattering Measurements

We now focus on a more systematic comparison between EELS and CL measurements of dipolar modes in small nanoprisms, before drawing a parallel with optical extinction and scattering. In the case shown in **Figure IV.4** and **Figure IV.5** (small, graphene-supported particles), the dipolar energy positions as measured in EELS and CL are very similar. However, the situation is different when considering larger nanoprisms on carbon films. Although the spatial distributions of EELs and CL intensities are rather similar in both spectroscopies just as for the smaller triangles, a difference arises for the resonance energies (**Figure IV.6**).

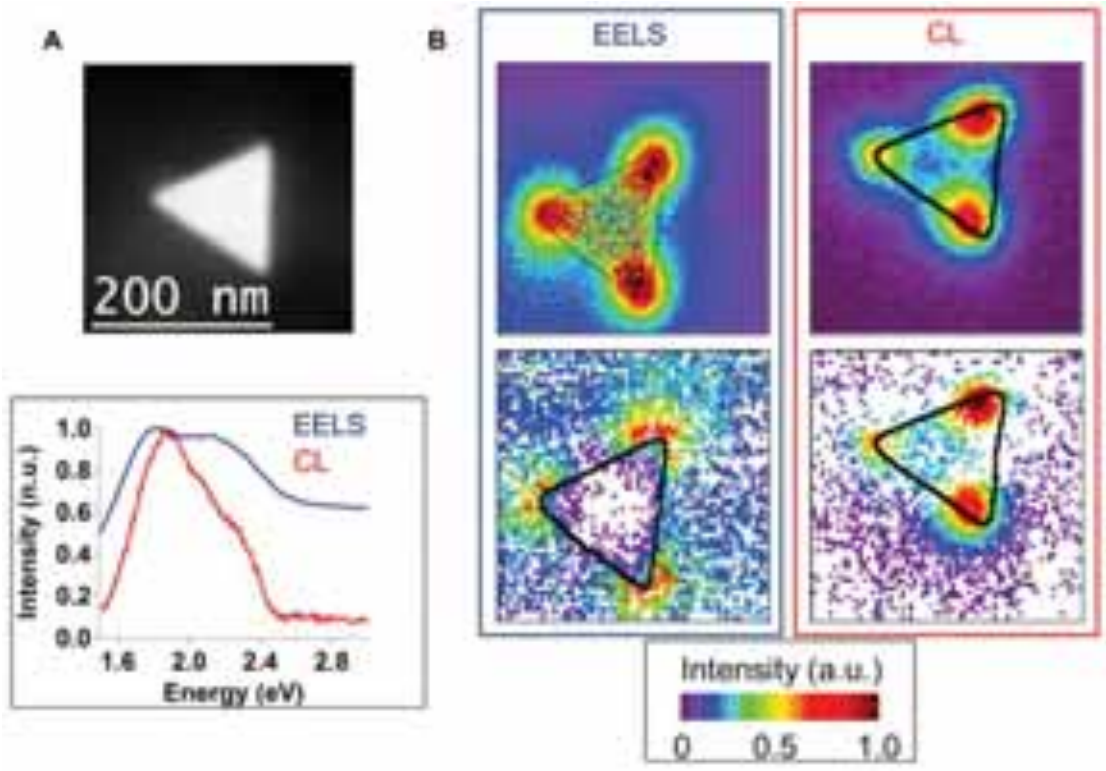

Figure IV.6. A: HAADF image of a gold triangular nanoprism. Experimental EELS (blue) and CL (red) spectra corresponding to electron probe positions located at the upper tip. **B:** EELS and CL maps obtained at the energies of the main EELS and CL maxima (top). Fitted amplitude maps corresponding to the peaks resonant at the energies of the main EELS and CL maxima (bottom).

Figure IV.7A shows experimental EELS and CL spectra recorded when the electron probe is located at the tip of a nanoprism lying on a carbon foil. Although associated with the same dipolar mode, the FWHM are larger in this case than for the small triangle lying on graphene. Similar shifts and increased broadening are measured repeatedly on nanoprisms lying on a carbon foil, and are reminiscent of extinction and scattering phenomena. Indeed, as a very simple example, **Figure IV.7B** shows calculated extinction and scattering spectra superimposed on calculated EELS and CL tip spectra for an individual small nanoprism. The resemblance between EELs (CL) and extinction (scattering) is remarkable around the resonances. In particular, extinction is also blueshifted with respect to scattering, and the shift is the same as between EELS and CL.

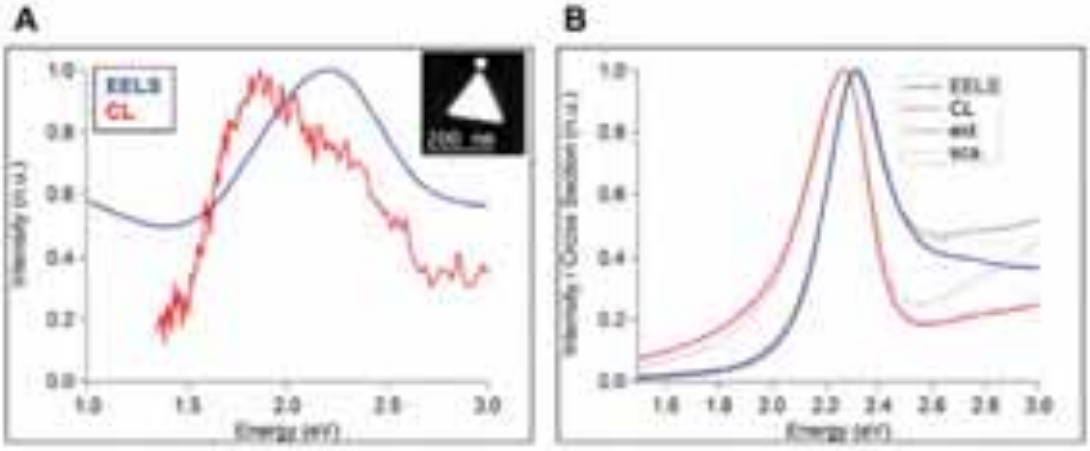

Figure IV.7: A: Measured EELS (blue) and CL (red) spectra taken at the tip of a 140 nm edge long gold nanoprism lying on a carbon foil. Inset: HAADF image of the nanoprism. The white disk indicates the electron beam position. **B**: Calculated extinction (black dotted line) and scattering spectra (grey dotted line) superimposed to calculated EELS (blue) and CL (red) tip spectra for a single small nanoprism of 50 nm edge length, 50 nm thickness surrounded by vacuum. In the case of the optical cross-sections, the light propagation direction is chosen perpendicular to the prism, and the polarization is parallel to one of the edges.

In order to seek deeper and more intuitive understanding of these observations, we adopted, in collaboration with the group of Professor F.J. Garcia de Abajo (ICFO, Barcelona), an analytical approach derived from the non-retarded BEM formalism in the quasi-static limit (See Appendix at the end of the thesis for more detailed description and the complete derivation).[23,36,57,58,61] This formalism enables a direct comparison between the quantities measured by optical and fast electron based spectroscopies through simple analytical

expressions. In particular, the absorption and scattering cross-sections can be shown to reduce to $C_{abs}(\omega) = \sum_{i=d} A_{i,abs}\omega Im\{f_i(\omega)\}$ and $C_{sca}(\omega) = \sum_{i=d} A_{i,sca}\omega^4|f_i(\omega)|^2$, where $A_{i,abs}$ and $A_{i,abs}$ are energy-independent prefactors and:

$$f_i(\omega) = \frac{\lambda_i + 1}{\lambda_i - \lambda(\omega)} \quad \textbf{[IV.1]}$$

In this expression, λ_i is a real eigenvalue characterizing mode i, and $\lambda(\omega) = (1 + \varepsilon(\omega))/(1 - \varepsilon(\omega))$ contains the dielectric function of the metallic object $\varepsilon(\omega)$. The physical meanings of the spectral function $f_i(\omega)$ and of λ_i can be found in references 57, 23 and 8. In the modal decompositions, the sums run over all the dipolar modes of the system. Obviously, the extinction and absorption cross-sections are the same,[81] as the scattering cross-section vanishes in the quasi-static limit. Thus, the physics of the extinction is driven by absorption, and we can place extinction and absorption on an equal footing. Furthermore, it has been shown that EEL probability at point $\vec{R}_\perp$ in a plane perpendicular to the electron beam (along z) reduces to:[57]

$$\Gamma_{EEL}(\vec{R}_\perp, \omega) = A_{EEL} \sum_i Im\{f_i(\omega)\} \left|\tilde{\phi}_i\left(\vec{R}_\perp, \frac{\omega}{v}\right)\right|^2 \quad \textbf{[IV.2]}$$

where A_{EEL} is an energy-independent prefactor and $\tilde{\phi}_i(\vec{R}_\perp, q_z)$ is the Fourier transform of the eigenpotential of mode $\phi_i(\vec{R}_\perp, z)$ along the beam direction. In a similar way, one can write the CL probability as:

$$\Gamma_{CL}(\vec{R}_\perp, \omega) \approx \sum_{i=d} A_{i,CL}\omega^3 |f_i(\omega)|^2 \left|\tilde{\phi}_i\left(\vec{R}_\perp, \frac{\omega}{v}\right)\right|^2 \quad \textbf{[IV.3]}$$

where $A_{i,CL}$ is an energy-independent prefactor. In contrast to EELS, the sum only runs over the dipolar modes (i.e., the only ones that contribute to radiation in the small particle limit).
Eq.s **[IV.2]** and **[IV.3]** show that for a given dipolar mode *i*, the spatial dependences are the same in EELS and CL, as observed experimentally and in the simulations. They have a well-defined physical meaning, given by the spatial modulations of $\left|\tilde{\phi}_i(\vec{R}_\perp, \omega/v)\right|^2$. Furthermore, the above expressions clearly reveal that the spectral profiles of both EELS and

absorption/extinction are proportional to the same spectral function $Im\{f_i(\omega)\}$. Likewise CL and scattering are both proportional to $|f_i(\omega)|^2$. This finding constitutes a generalization to an arbitrary shape of a well known result in the special case of a small sphere,[8,25,81] and explains in simple terms why EELS and extinction on the one hand, and CL and scattering on the other are so closely related.

Indeed, although both the square modulus and the imaginary part of $f_i(\omega)$ have the exact same maximum energies in the absence of dissipation, they shift when dissipation is present. For instance, by inserting a Drude model expression $\varepsilon(\omega) = 1 - \omega_p^2/(\omega^2 + i\ \omega)$ (ω_p being the bulk plasmon energy and a damping term) into eq. **[IV.1]**, one finds the following Lorentzian-type expressions for the imaginary part and square modulus of $f_i(\omega)$:

$$Im\{f_i(\omega)\} = \frac{\tilde{\omega}_i^2 \omega}{^2\omega^2 + (\omega^2 - \tilde{\omega}_i^2)^2} \quad \textbf{[IV.4]}$$

$$|f_i(\omega)| = \frac{\tilde{\omega}_i^4}{^2\omega^2 + (\omega^2 - \tilde{\omega}_i^2)^2} \quad \textbf{[IV.5]}$$

where $\tilde{w}_i = \sqrt{1+\lambda_i}\,\omega_p/\sqrt{2}$ is the well-known non-dissipative surface plasmon energy, which has a simple dependence on λ_i in the Drude model. Because with this analytical dielectric constant $Im\{f_i(\omega)\} \propto \omega|f_i(\omega)|^2$, it is clear that these two quantities do not have the same resonance energies.

This is consistent with the observation that the maximum oscillation amplitude of a driven harmonic damped oscillator (which corresponds to the maximum dipole moment, and can thus be connected to the light emission induced either by light or fast electrons) occurs at a lower frequency than the maximum energy transfer.[82] Such an effect has been invoked to explain the spectral shifts between near-field probe and far-field spectra,[83] and has already been reported theoretically for extinction and scattering.[84] These expressions also predict that the magnitude of the shift increases with the amount of dissipation, which is in agreement with the fact that a shift is measured between EELS and CL only on large particles lying on a carbon foil. As a further investigation of such spectral shifts, **Figure IV.8A** shows the

magnitude of the EELS-CL shifts as measured on different particles. We sort these particles into four different groups: very small particles (60 nm edge long) lying on a graphene sheet (type 1), and larger particles of various sizes (90 nm, 130 - 150 nm, and 160 nm edge long) lying on a carbon foil (types 2, 3 and 4). We can speculate two different reasons to explain the shifts: large particle sizes and/or absorbing substrate. We thus performed additional BEM simulations for gold nanoprisms with different sizes, with and without sparsely or highly dissipative carbon substrates (see Simulations, section IV.4.1). For simplicity, we keep a constant AR of 2, and vary the edge length. The output is summarized in **Figure IV.8B**. For a given size, the substrate either induces or increases the spectral shift between EELS and CL by an amount related to its dissipating influence, in accordance with the quasi-static theory. We stress that the exact energy positions and shifts depend both on the size of the object and the absorption properties of the substrate, which makes any truly quantitative comparison between experiments and simulations extremely difficult. In particular, the thickness of most of the objects, as well as the exact dielectric properties of the substrates and the environment, are unknown. As a matter of fact, the magnitude of the shift is always much larger in experiments than in simulations, which we tentatively attribute to an underestimate of dissipation. However, it is striking that the calculated trend is in qualitative agreement with the experiment (compare **Figure IV.8A** and **Figure IV.8B**). Interestingly, this trend cannot be captured by our model when describing the metal with a simple Drude model. In particular, taking into account the right energy dependent prefactors of the modal decompositions, eqs. **[IV.4]** and **[IV.5]** imply that a dipolar mode would induce a CL (scattering) resonance blueshifted relative to its corresponding EELS (extinction) resonance, which is contrary to what is observed in most cases. Nevertheless, the complete trend is qualitatively recovered by the model, not only for EELS and CL but also for extinction and scattering, when introducing tabulated gold dielectric function[76] into eq. **[IV.1]** (see **Figure IV.8C**). This points out the importance of taking into account interband transitions in gold in this energy range to accurately describe the difference between absorption and scattering phenomena. This trend can be summarized as follows: the shift between EELS/extinction and CL/scattering whose magnitude increases with the dissipation level, is increasingly negative below typically 1.6 eV, where gold behaves as a good Drude metal, and

increasingly positive above 1.8 eV, where it is dominated by its interband transitions.[85] The quasi-static modal decompositions are thus capable of generally explaining the close similarities between EELS and extinction shown in recent experiments[86] and call for an experimental comparison of CL and scattering to confirm their predicted resemblance.

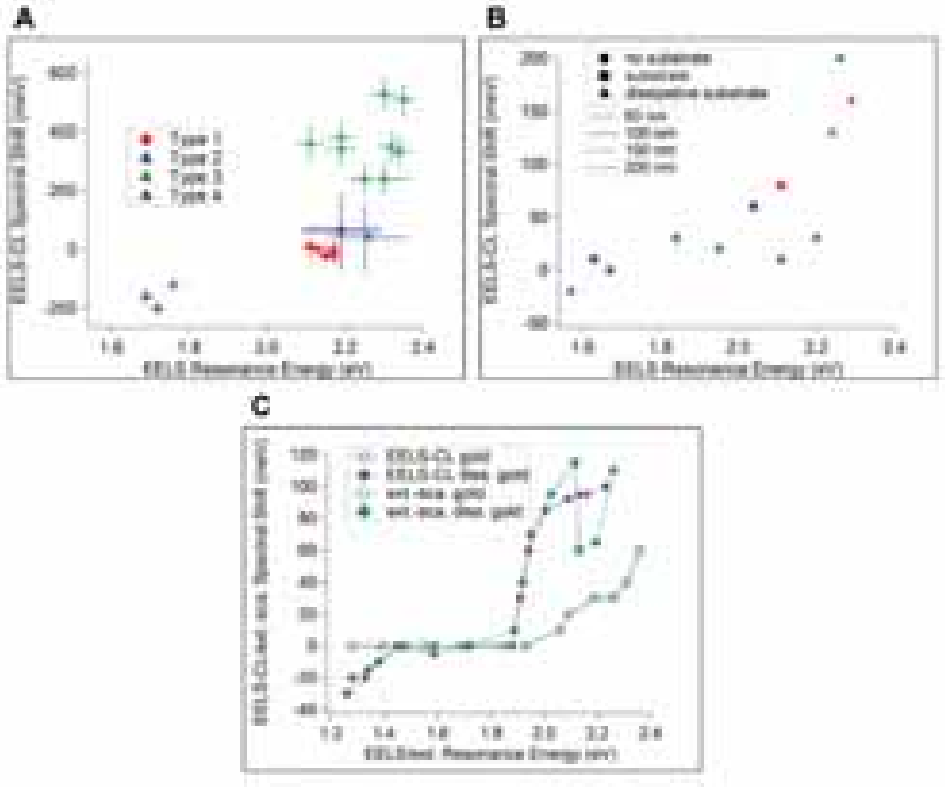

Figure IV.8. A: EELS-CL spectral shifts as measured at the tips of several gold nanoprisms. The naoprisms are color-sorted in four different types. Type 1: small 60 nm edge long nanoprisms lying on a graphene sheet. Type 2: 90 nm edge long nanoprisms lying on a carbon foil. Type 3: 130-150 nm edge long nanoprisms lying on a carbon foil. Type 4: 160 nm edge long nanoprisms lying on a carbon foil. **B:** EELS-CL spectral shifts as obtained from tip spectra of gold nanoprisms of various sizes simulated within the retarded BEM framework, with and without sparsely or highly dissipative carbon substrates. The nanoprisms have a constant AR of 2, and the numbers in the caption correspond to the edge lengths. **C:** Spectral shifts between EELS and CL (round purple symbols), and extinction and scattering (diamond green symbols), predicted within the quasi-static modal decomposition model described in the text when using the dielectric function of Ref [76]. The resonances are calculated for various dipolar modes of gold objects with tabulated dissipation (open symbols) and increased dissipation simulated by multiplying the imaginary part of the tabulated dielectric function by a factor of 5 (solid symbols). The resonance energies are tuned by changing the eigenvalue λ_i (see text). Note that tin the case of low dissipation, there is no visible difference between EELS (CL) and extinction (scattering).

IV.2.1.3. Conclusions

In conclusion, we reported spatially resolved EELS and CL measurements on the very same gold nanoprisms. The results allowed us to directly sorting out radiative and non-radiative plasmon modes. We showed that a radiative mode, depending on the size and substrate, may be clearly observable at different resonance energies in both EELS and CL. These results are in agreement with fully retarded BEM electromagnetic simulations, which also indicate that such spectral differences originate in dissipation and are similar to those observed between optical extinction and scattering. These observations are explained using a modal decomposition analysis, which allow us to link the macroscopic concepts of extinction and scattering to spatially resolved EELS and CL experiments. We expect that these conclusions can be extrapolated to larger particles, for which similar retarded modal decompositions are needed to deal with more delocalized surface plasmon modes. We further hope that the present work sheds some light on the experimental retrieval of spectral and spatial information of plasmons.

IV.2.2. EELS Characterization of the Plasmonic Properties of Silver-Gold-Silver Nanowires

Like their radiofrequency counterparts, optical antennas are characterized by several multipolar plasmon oscillations, which can be separated into bright and dark modes, depending on their ability to couple efficiently (bright) or not (dark) to incident/scattered far-field radiation.[87,88] While the former can be exploited in the development of signal processing devices[89] and Raman/IR/fluorescence-based sensors, the latter is useful for enhanced absorption spectroscopy and photothermia.[90] In order to efficiently engineer the near-field electromagnetic confinement and implement the application of optical antennas, it is useful to have a detailed understanding of the relationship between the antenna structure and the spatial/spectral distributions of the different plasmon modes.[8,35] In this respect, the near-field properties of pure gold and silver nanorods have been investigated by different research groups, both theoretically[88,91] and experimentally, using different imaging techniques that exploit either resonant optical illumination (e.g., DFM,[92,93] apertureless scanning near-field optical microscopy,[94–96] and photoemission electron microscopy[52,97]) or fast electrons (CL[31] and EELS[53,87,98,99]). In contrast, detailed studies of the plasmon near-field behavior of Au@Ag bimetallic nanostructures have not been reported. Rodríguez-González et al. studied the effect of a silver shell on the plasmonic behavior of gold nanodumbbell cores, describing a complex plasmonic scenario where the transversal mode of the core-shell system cannot be directly related to an equivalent silver nanorod.[100] To the best of our knowledge, the only available study of the plasmonic properties of silver-gold-silver nanorods is the work by Ahn et al. using DF spectroscopy, which indicated no influence of the gold core.[93]

IV.2.2.1. Structural and Optical Far-Field Characterization of Silver-Gold-Silver Nanowires

In this work we performed a correlated sctructural and optical study on two different silver-gold-silver nanowire samples (see section II.4.1) displaying significantly different nanowire lengths to discuss the influence of the penta-twinned gold nanorod core on the optical properties of the bimetallic particles. We analyzed the optical extinction spectra from

nanowires in heavy water solution (**Figure IV.9**) and carried out a detailed EELS analysis (**Figures IV.10 – 11 and IV.13 - 14**). Both experimental methods were supported by BEM calculations. The first sample had *AgEn* = 0.5, corresponding to a total aspect ratio of 6.7, and 25 nm silver extending beyond each tip of the penta-twinned gold nanorod core. We compare in **Figure IV.9A** the vis-NIR spectrum (black solid curve) with the calculated extinction spectrum of a nanowire with the average dimensions, either containing the penta-twinned gold nanorod core (red-dotted curve) or being made of pure silver (blue dash-dotted curve). The simulations reveal in this case a clear influence of the penta-twinned gold nanorod core on all the plasmon modes, particularly in the short wavelength (high energy) region. The second sample corresponds to *AgEn* = 5.3, aspect ratio 25, and 360 nm of silver from each tip. The 3D reconstructed volume of the two samples obtained by the total variation minimization (TVM)[101] technique, applied to a tilt series of HAADF-STEM images (**Figure IV.9 B, D**) clearly shows that the penta-twinned gold nanorod core is located in the center, with 2 nm of silver on the lateral facets (also considered for the simulations). The pentagonal cross section of the particle – characteristic for penta-twinned nanorods – is preserved, as evidenced by the cross section in **Figure IV.9B,D**. Remarkably, the low polydispersity of the synthesized silver-gold-silver nanowires allowed us to detect nine LSPR bands in solution (**Figure IV.9C**), and we find again a good agreement with the BEM simulated extinction spectrum. In this case however, the differences between simulations with and without the gold core are significantly smaller and mainly observed in the high-energy region. It should be noted that the permittivities of silver and gold are well described through a common Drude expression $\varepsilon(\omega) = \varepsilon_b - \omega_p^2/\omega(\omega+i\gamma)$ in the IR region, where the so-called classical plasma energy is given by $\hbar\omega_p \sim 9$ eV,[38] as determined by the density of *s* conduction electrons (i.e. the same in both metals, because each atom contributes with one *s* electron and their atomic densities are nearly identical). The difference between these two metals lies in the level of losses ($\hbar\gamma$ = 25 meV for silver and 71 meV for gold) and in the background screening produced by *d*-band polarization (ε_b = 4 in silver and 9.5 in gold). Consequently, in the infrared spectral region (i.e. $\lambda > \sim$1000 nm), the second term dominates in the Drude expression, the precise value of ε_b becomes irrelevant, and both silver and gold behave in a similar fashion, except that the latter produces more inelastic optical losses

(through a larger damping rate γ). Besides these intrinsic material properties, which lead to similar optical behavior in the NIR, there is a geometrical effect associated with the nanowire: for a given mode order (e.g. the lowest-order dipolar mode), the wavelength shifts deeper into the IR with increasing nanowire length, and eventually the mode size becomes comparable to λ/2, giving rise to a relatively larger contribution of radiative damping, which again makes the two metals look more similar. These considerations explain why the silver-gold-silver bimetallic nanowires have similar properties to those of pure silver nanowires with the same outer geometry, particularly for infrared modes and high AR (**Figure II.27** in section II.4.1).

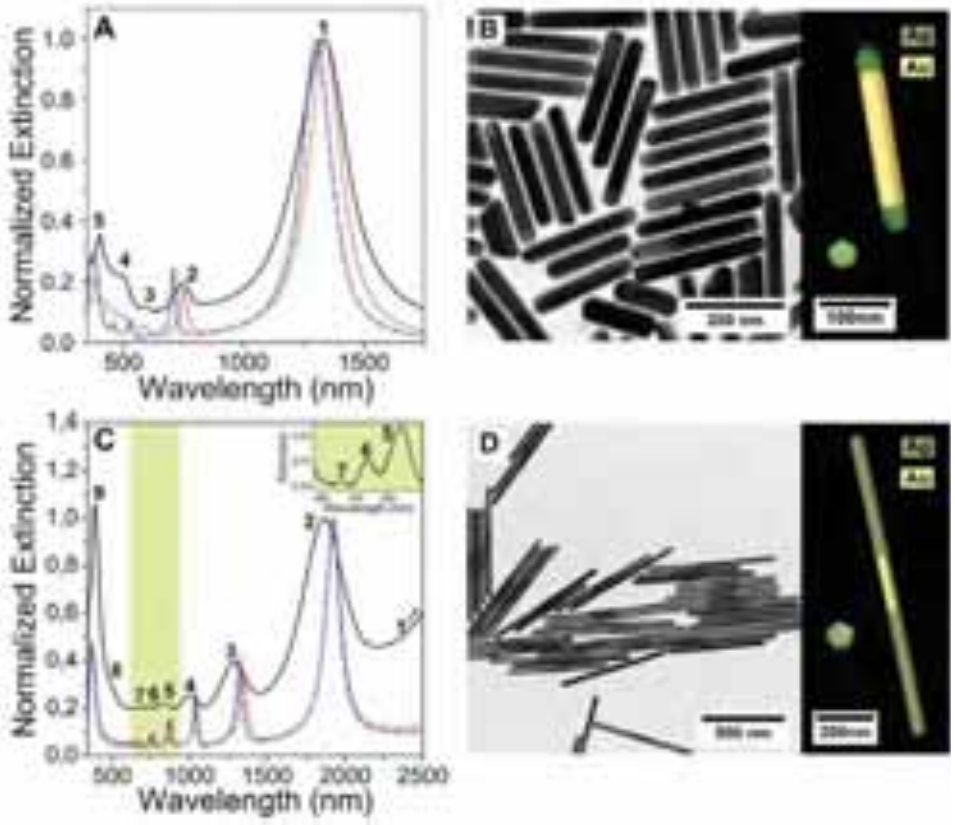

Figure IV.9. A: vis-NIR spectrum of a colloid of short (*AgEn* = 0.5) silver-gold-silver nanowires (black line) compared to simulated spectra in the presence (red) and absence (blue) of the penta-twinned gold nanorod core. **B:** Representative TEM image showing the narrow size distribution of the prepared bimetallic nanowires. **C,D:** Same as **A,B** for a sample of longer nanowires (*AgEn* 5.3). **Inset of C:** zoom of the highlighted area discerning high order modes 5, 6, and 7. At the right subpanels of **B** and **D**, 3D TEM visualizations of the reconstructed nanowires are presented (green and yellow correspond to silver and gold, respectively), both from one tip (left) and along their length (right).

IV.2.2.2. EELS Near-Field Analysis of Single Silver-Gold-Silver Nanowires

To confirm these observations, we carried out a detailed near-field study by EELS, also supported by BEM calculations. Plasmon mapping confirmed the symmetry and standing-wave nature of the modes under study. We summarize in **Figure IV.10 - 11** the results for the short nanowires (*AgEn* = 0.5): all of the extinction bands observed in the far-field vis-NIR spectrum are also found in EELS (**Figure IV.10A – 11A**). The spatial distribution of the plasmons clearly indicates the even or odd nature of each mode: modes (1-3) are the dipolar, quadrupolar, and octupolar longitudinal modes, respectively, while modes (4-5) are the accumulation of several modes (see below).

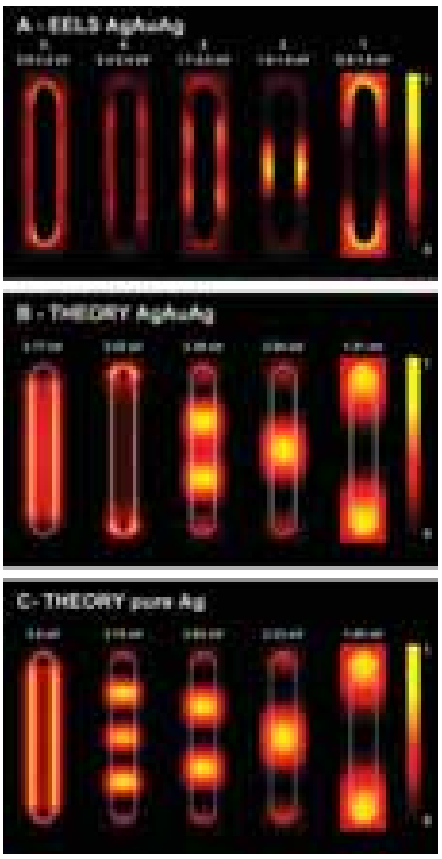

Figure IV.10. A: spatial distribution of plasmon modes for a short silver-gold-silver nanowire (*AgEn* = 0.5) as measured by EELS; the numbers refer to the same modes as in the vis-NIR spectrum of **Figure IV.9A**. **B:** BEM simulations of EELS maps associated to the plasmon modes shown in **A**, for a nanowire containing the penta-twinned gold nanorod core. **C:** Simulations for a silver nanowire with the same dimensions. The simulated maps are normalized to the maximum intensity in each case. The silver (gold) surface is indicated with solid (broken) white lines in the calculated maps.

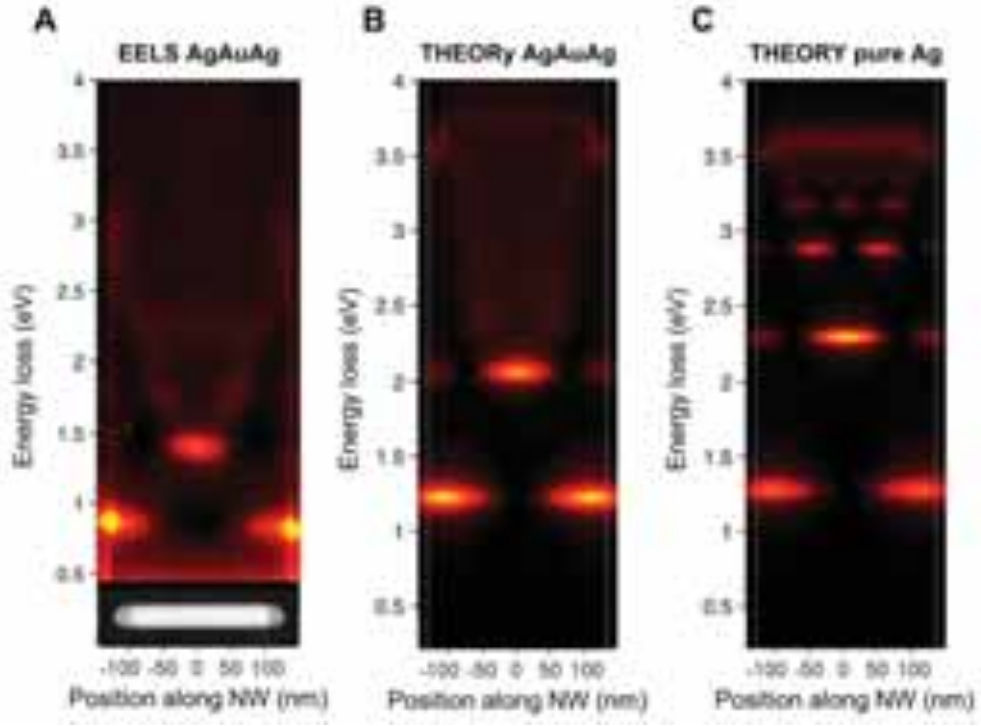

Figure IV.11. A: Experimental and **B-C:** calculated EELS data as a function of energy for a short silver-gold-silver nanowire (*AgEn* = 0.5), both with (**B**) and without (**C**) penta-twinned gold nanorod core.

Incidentally, only odd modes can be excited using light incident with its electric field parallel to the nanowire, in contrast to EELS in which even modes are also excited due to the multipolar character of the electron exciting field. This conclusion can be actually extended to nanowires of arbitrary orientation relative to the externally applied field when they are sufficiently small as to neglect retardation effects (e.g. an $\exp(i2\pi r/\lambda)$ dependence on position r and light wavelength λ). However, we are dealing here with long nanowires, with lengths that are comparable to λ, so there is strong retardation and this is the reason why our optical spectra reveal modes with both odd and even symmetry.[31,33,90,95] The EELS experimental maps were compared to numerically computed maps using BEM. Simulations were carried out both in the presence (**Figure IV.10B – 11B**) and in the absence (**Figure IV.10C – 11C**) of the penta-twinned gold nanorod core. Although the agreement between theoretical and experimental plasmon energies in the optical measurements is excellent (**Figure IV.9A**), the EELS modes are noticeably redshifted with respect to theory, presumably because of the

effect of the substrate, which is not accounted for in our simulations. However, the features in the measured and calculated EELS spectra are in good mutual agreement (see **Figure IV.12**), and we argue that the spatial distribution of the plasmon excitation should not be too sensitive to the observed shift.

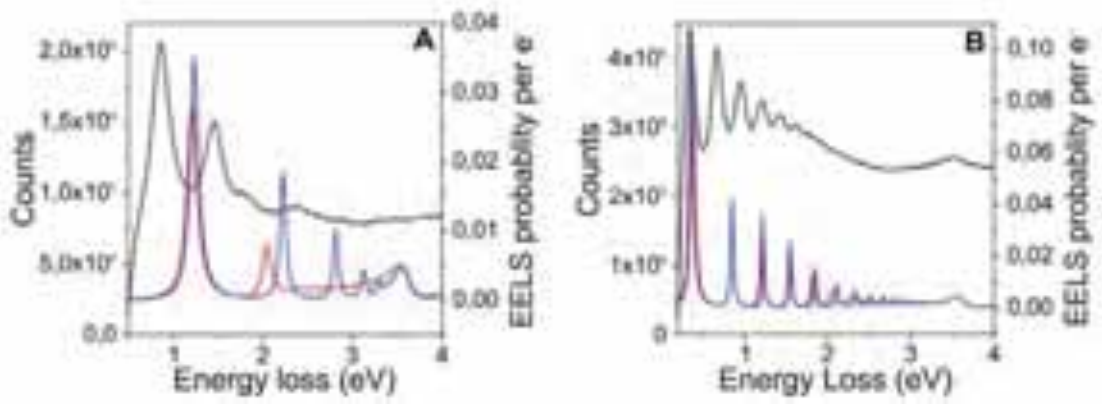

Figure IV.12. Experimental EELS spectra (black) and calculated spectra, in the presence (red) and absence (blue) of the gold core. The Experimental spectra were background corrected to eliminate the zero loss peak. **A:** *AgEn*=0.5. **B:** *AgEn*=5.3.

This intuition is corroborated when comparing modes of the same symmetry, which yield very similar spatial distributions in theory and experiment. It is important to keep in mind that the highest-order modes observed in EELS (modes 4 and 5 in **Figure IV.10**) are in fact the accumulation of several modes, which are integrated over the finite energy range covered within the energy-filtered images. Note that we are instead showing monochromatic maps in the calculations, so that these high-order maps are understandably different from those experimentally acquired. Additionally, the number of plasmon modes (an infinite, discrete set) has an accumulation point towards the electrostatic planar surface plasmon (signaled by ε_1=1 in vacuum), as they undergo fast oscillations, so that the surface is locally seen as flat. This explains the rather uniform distribution of the observed map at that energy (3.7 eV for the silver-vacuum interface). The theoretical calculations also allow us to explore the role of the penta-twinned gold nanorod core in the plasmonic response, which essentially produces a redshift of the plasmon energies along with additional broadening in the EELS spectra (see **Figure IV.12**). It is thus not surprising that the silver nanowire has better-defined higher-order modes (second maps from the left in **Figure IV.10B, C**).

For a long nanowire (**Figure IV.13 - 14**, *AgEn* = 5.3), EELS characterization did allow us to identify the dipolar longitudinal mode (1), as well as six additional multipolar modes (2—7 corresponding to increasing order, i.e. number of sign changes in the associated induced charge along the wire), whereas the last two peaks (8-9) correspond to an accumulation of several modes, as discussed above for short nanowires. In this case, the effect of the penta-twinned gold nanorod core is qualitatively similar, but nearly marginal for low energy modes. In particular, the lowest-order dipolar plasmon involves high plasmon strength (larger enhancement of the near-field) near the nanowire tips, and consequently the near-field plot looks nearly identical for the calculated silver-gold-silver (**Figure IV.13B – 14B**) and the pure silver nanowire (**Figure IV.13C – 14C**), also in excellent agreement with the experimental EELS maps (**Figure IV.13A – 14A**).

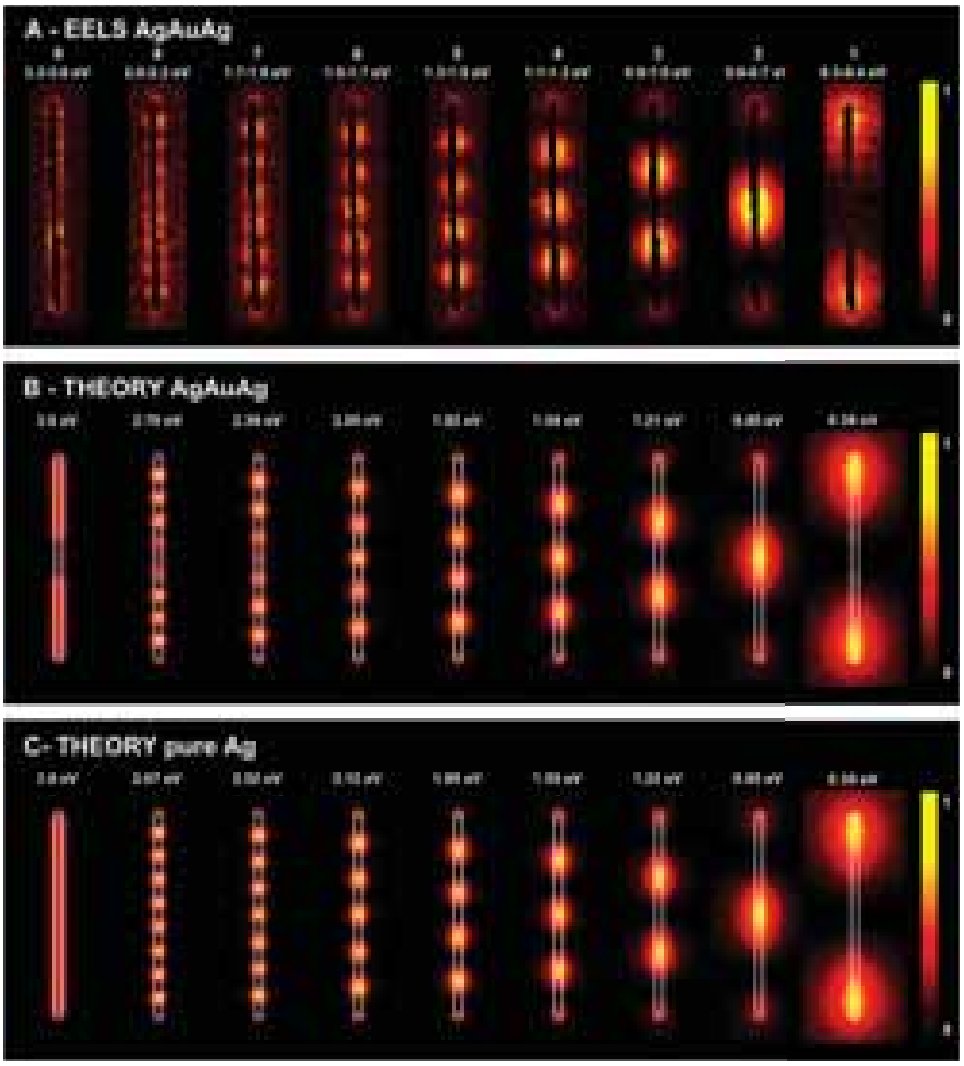

Figure IV.13. A: spatial distribution of plasmon modes for a long silver-gold-silver nanowire (*AgEn* = 5.3) as measured by EELS; the numbers refer to the same modes as in the vis-NIR spectrum of **Figure IV.9C. B:** BEM simulations of EELS maps associated to the plasmon modes shown in **A**, for a nanowire containing the penta-twinned gold nanorod core. **C:** Simulations for a silver nanowire with the same dimensions. The simulated maps are normalized to the maximum intensity in each case. The silver (gold) surface is indicated with solid (broken) white lines in the calculated maps.

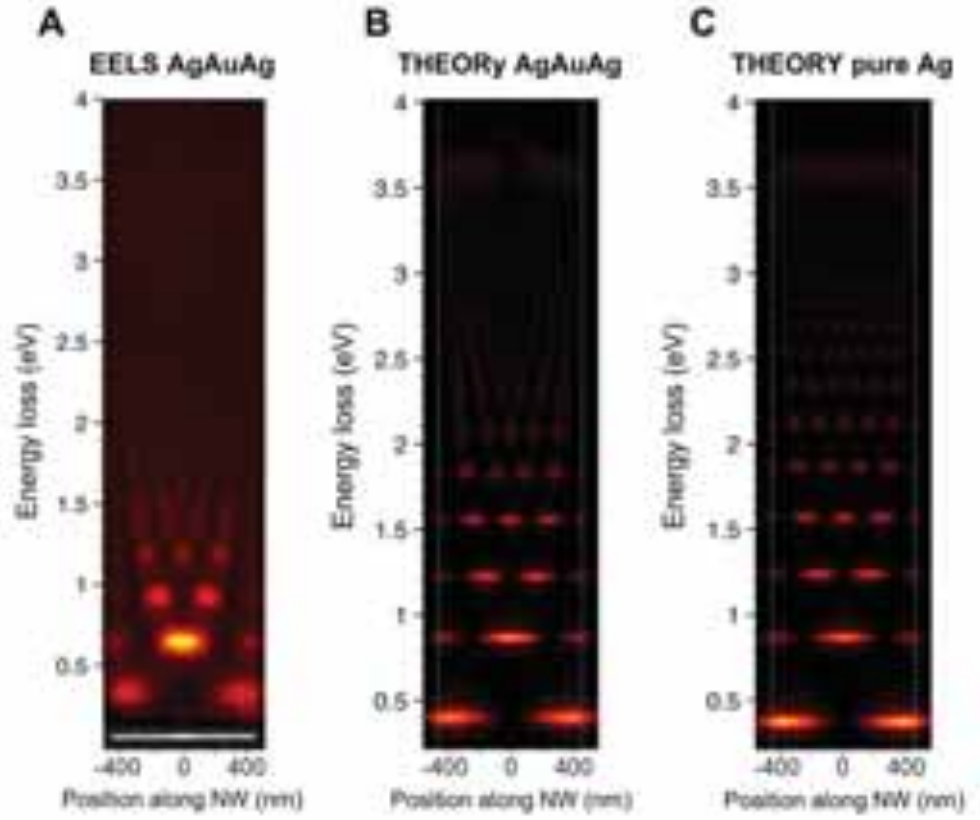

Figure IV.14. A: Experimental and **B-C:** calculated EELS data as a function of energy a long silver-gold-silver nanowire (*AgEn* = 5.3), both with (**B**) and without (**C**) penta-twinned gold nanorod core.

Since the NIR response of gold and silver is similar, as they both behave as Drude's metals, and interband transitions contribute marginally in this spectral region, the low energy plasmon position should not change significantly between a pure gold and a pure silver nanowire; nonetheless we expect to observe additional broadening in the case of gold, since it shows higher intrinsic damping losses compared to silver (71 vs 21 meV). In **Figure IV.15** we investigate this point with a new set of calculations relative to pure gold nanowires. In conjunction with a higher broadening, we observed a reduction in the plasmon extinction cross-section.

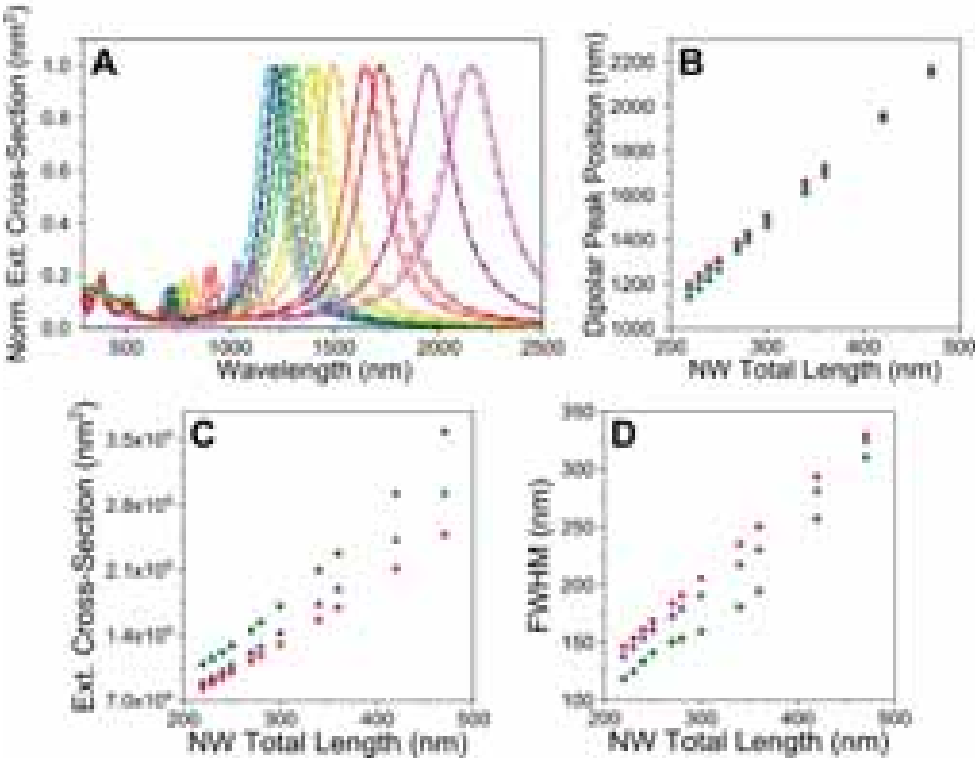

Figure IV.15. A: calculated (BEM) extinction spectra of silver-gold-silver (solid curves) and pure gold (dashed curves) nanowires with dimensions corresponding to the experimental ones (same color code used in **Figure II.27A**, see section II.4.1). Comparison between pure gold (red circles), pure silver (green diamonds) and bimetallic silver-gold-silver nanowires (blue triangles); **B:** dipolar peak position, **C:** Extinction cross-section and **D:** FWHM.

Subsequently, the penta-twinned gold nanorod core can only be identified in the higher-order modes, which involve a large intensity in the central nanowire region, while their high energies involve very different and relatively moderate values of the dielectric functions of the two metals. Interestingly, the second-order mode, which also has a large weight in the center of the nanowire, appears at a sufficiently low energy as to feel a similar response from both gold and silver, as we argued above, and consequently, the calculated energies of this mode in the long nanowires are similar with and without the penta-twinned gold nanorod core. For such low order modes, the nanowire acts as a whole plasmonic entity. On the contrary, the vacuum/silver interface plasmon is both experimentally and theoretically localized on the silver parts only. For this mode, corresponding to high wave vectors (short

wavelengths), the plasmons feel differently each metal, and consequently the gold and silver parts act as two separated plasmonic entities in this regime.

IV.2.2.3. Conclusions

The role of the gold cores on the optical response of silver-gold-silver nanowires was carefully investigated by EELS, and we demonstrated that it does not interfere with plasmon propagation along the nanowire surface, whilst its influence is limited to higher energy modes. The procedure opens up new possibilities for the exploitation of plasmon resonances in the near and mid IR regions.

IV.2.3. Collective Plasmonic Properties in Few- Layer Gold Nanorod Supercrystals

The precise correlation of structure and optical properties becomes more and more complicated when dealing with large-assemblies instead of single nanoparticles, due to the large amount of interactions between the building blocks. As we demonstrated in section III.2.1, supercrystal structures made of gold nanorods are particularly interesting in plasmon enhanced spectroscopies, like SERS.[102–108] In fact, the strong electric fields needed for the enhancement of the otherwise extremely weak Raman scattering signals can be achieved by inducing coupling of plasmon modes between closely spaced nanoparticles, creating so-called "hotspots" (see section I.2.3).[102,109–112] Previous studies showed that among all possible gold nanorod packing and orientation, 3D supercrystals are among the most promising architectures for enhancing Raman scattering.[113–115] Indeed, the intralamellar hexagonal order maximizes the number and density of the formed hotspots and their homogeneous distribution permits more reproducible and quantitative SERS measurements. During recent years, several research groups reported the detection of relevant bioanalytes using gold nanorod supercrystals as SERS substrates, with a detection limit ranging from nanomolar to picomolar concentrations, which confirms the suitability of these structures toward biosensing.[114,116,117] For example, Xion et al. demonstrated femtomolar detection of food contaminants on a gold nanorod monolayer.[116] Our group has shown attomolar detection of scrambled prions in blood and serum, supported on micron-scale supercrystals containing a large number of stacked gold nanorod layers.[114] Even though a relationship between the height of the supercrystal (i.e. the number of stacked rods layers) and the EF of those architectures was suggested, a systematic study including detailed simulations is still lacking. Therefore, a better understanding of such effects is of great interest and would pave the way toward optimized architecture design. We carried out a careful SERS investigation on supercrystals comprising different numbers of stacked layers. This systematic study relied on the fabrication by drop casting of highly organized gold nanorod assemblies, thanks to surface coating with MUDOL (see section III.2.1.1).[118–120] Correlated SEM/STEM and AFM analyses, as well as Raman scattering spectroscopy were used to characterize the organization and optical properties of the supercrystals, respectively. Importantly, the experimental results are supported by an *ad hoc* implementation of the full-wave numerical

method recently introduced in the context of nanoplasmonics,[121] which is based on the surface integral equation-method of moments (MoM) and the multilevel fast multipole algorithm (MLFMA).[121–123] It must be emphasized that rigorous modeling of such large-scale, densely-packed nanoparticle arrangements is highly challenging. We exploited here the repetition pattern, taking into account the periodicity inherent to these structures but without resorting to infinite-structure approximations, which would omit edge effects.[122] Overall, the dramatic reduction in computational cost (regarding both runtime and memory) achieved with this method allowed us to simulate supercrystals composed of tens of thousands of gold nanorod building blocks, thereby allowing us to accurately predict the scattering response from a complex plasmonic system with dimensionally realistic simulation boxes (for more details see Simulations, section IV.4.3).

IV.2.3.1. Preparation of Gold Nanorod Supercrystals

Gold nanorods (58 ± 5 nm long; 17±2 nm thick) were synthesized and coated with MUDOL according to previously reported protocols (see section III.2.1 and III.4.3).[18,118–120,124] This procedure facilitates the formacion of gold nanorod supercrystals upon drying after drop casting; importantly, not only all gold nanorods were found to orient perpendicular to the substrate, but the obtained supercrystals were found to be rather uniform in terms of lateral dimensions, with an average quasi-circular shape of 4 μm diameter regardless of the initial gold nanorod concentration, expressed as [Au^0] (see section II.2.4). Within the same casting experiment, a larger number of stacked layers were usually found closer to the edge of the drop, most likely because of the well-known coffee stain effect. In general, supercrystals were obtained containing between one and twenty monolayers, depending on initial rod concentration. For example, supercrystals prepared with an initial concentration of [Au^0] = 3 mM displayed between one and five layers inside the coffee ring (**Figure IV.16**). The high level of organization of the nanorods and the homogeneous distribution of the supercrystals are fundamental for the realization of this work.

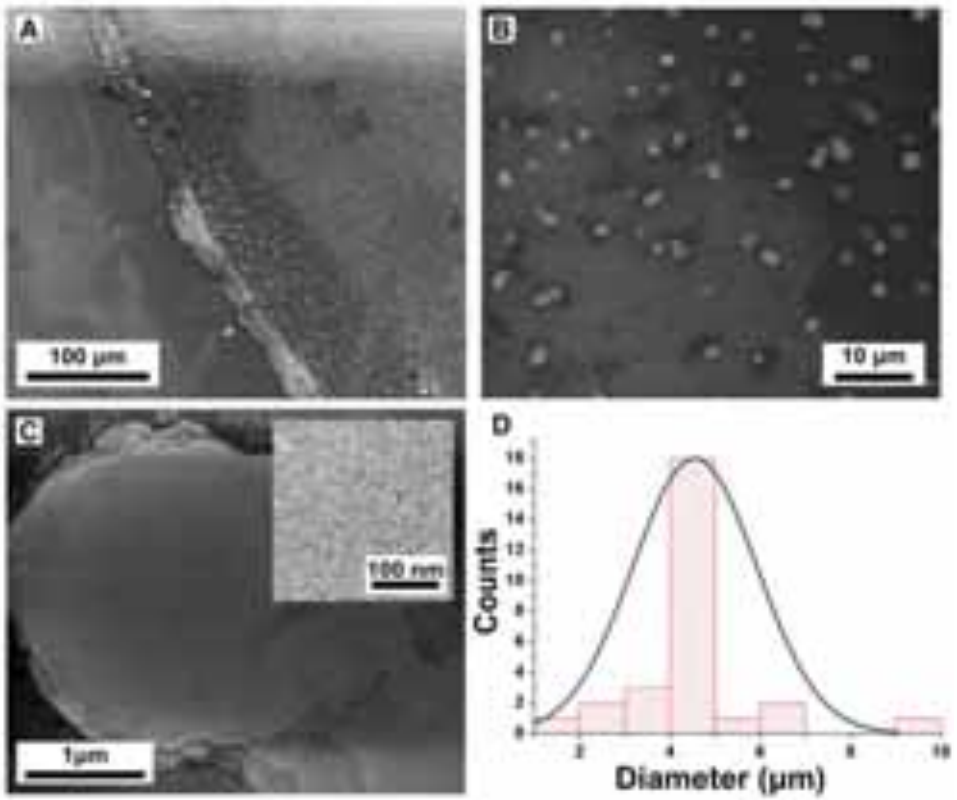

Figure IV.16. Characterization of MUDOL coated gold nanorod supercrystals obtained by dropcasting of a colloid with [Au^0] = 3 mM. A-C: Representative SEM images of MUDOL coated gold nanorod supercrystals at different magnifications. **D:** Histogram of supercrystal diameters showing an average diameter of 4.51 µm. CTAB and MUDOL concentrations were below the cmc and 0.1 mM, respectively.

IV.2.3.2. Correlated Structural and Optical Characterization of Supercrystals

The structure and local organization of the nanorods within supercrystals was thoroughly investigated, as summarized in **Figure IV.17**. The hexagonal intra-lamella order of the nanorods was observed by SEM (**Figure IV.17A**), AFM, HAADF-STEM and electron tomography (**Figure IV.17B - F**). AFM images revealed a small degree of roughness at the surface of the supercrystals, which may arise from a slight polydispersity in the length of the gold nanorods or from some roughness in the glass support. In HAADF-STEM however, the substrate roughness was considerably lower and additionally allowed the precise determination of the separation distances between adjacent nanorods within a single layer, which was found to be 2 nm (**Figure IV.17C**). Remarkably, Moiré interference patterns in

images of multilayers were observed due to a small degree of rotational offset between two neighboring layers,[125,126] demonstrating the quasi-crystalline symmetry of the gold nanorod multilayer assemblies. The 6 fold symmetry in a hexagonal lattice implies that each 30° rotation is equivalent to a 0° rotation, therefore the Moiré patterns in **Figure IV.17D-E** correspond to a misorientation angle of 8° and 18°, respectively. Three-dimensional characterization of the supercrystals by electron tomography confirmed the misorientation of the gold nanorod layers, as well as ABA-type stacking, which will be used as an input for modeling studies or during the interpretation of optical properties. The Moiré interference patterns were found to be different from one supercrystal to another, meaning that the misorientation angle between two layers was not always the same (**Figure IV.17D, E**). A similar aperiodicity has been reported for semiconductor (CdS) nanorod supercrystals, suggesting a strong similarity in the formation mechanism for semiconductor and gold nanorod supercrystals. Ryan and coworkers explained the formation of CdS nanorod superstructures by a primary assembly of ordered sheets in solution followed by a layer-by-layer process in which each monolayer would randomly settle on top of another, which may well be the case here (see section III.2.1.2).[125]

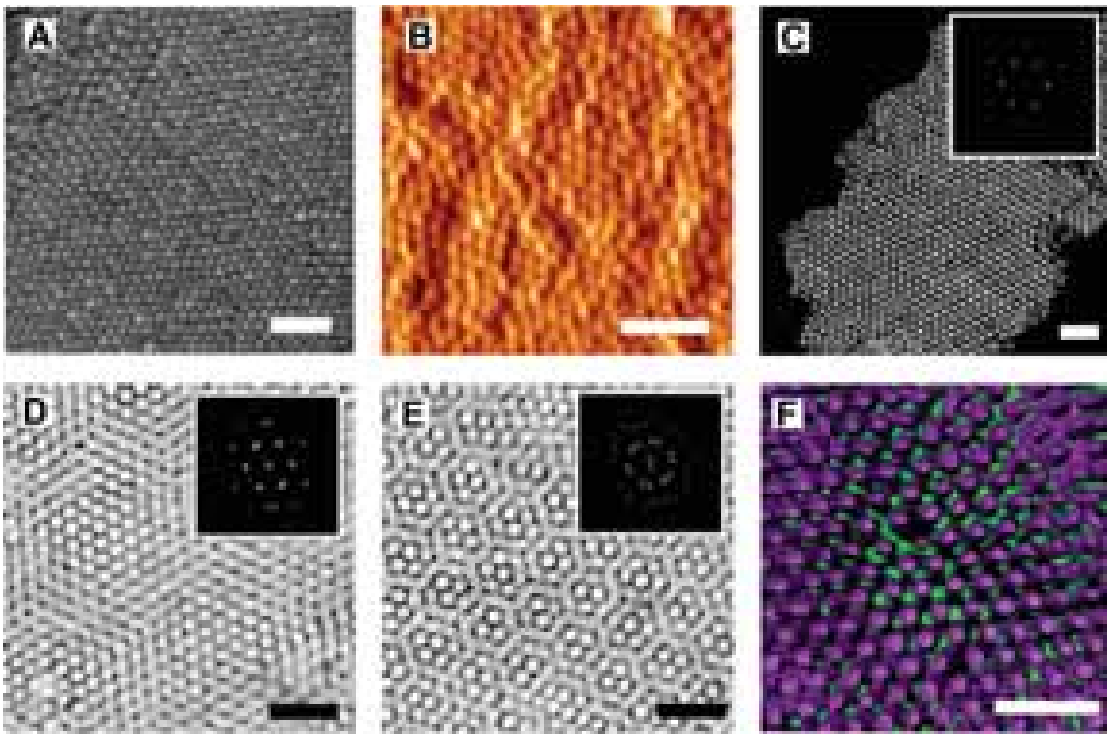

Figure IV.17. Characterization of gold nanorod supercrystals. A: SEM image of the top surface of a supercrystal. **B:** AFM image of a supercrystal surface. **C-E:** HAADF-STEM images of different supercrystals, standing on a SiN film, including a monolayer **(C)** and two different bilayers (**D - E)**. Insets are FFT patterns of the images. Moiré patterns result from a small angular misorientation between neighboring gold nanorod sheets that can be determined from the corresponding FFT. **F:** Electron tomography reconstruction image of a gold nanorod bilayer showing the top layer in purple and the bottom layer in green. All scale bars are 100 nm.

Next, aiming at the study of the optical properties of gold nanorod supercrystals, DFM, EELS and SERS measurements were conducted. It should be mentioned that the DFM measurements were not conclusive and thus are not represented here. Likely, the nanorods are too close to each other, so that the (multi)layer systems behave as a continuous film in far-field. Nonetheless, the optical properties of the supercrystals were described by means of EELS and SERS so as to map the spatial distribution of the plasmon modes and the electric field enhancements, respectively. The EELS experiments were carried out on monolayers and bilayers and hotspots could be clearly identified at the gaps between nanorods. A strong peak for monolayers located around 500-550 nm was noted (**Figure IV.18**), whereas three peaks were observed in the case of the bilayer, one around 500-550 nm and two other that were red-shifted toward 690-890 nm (**Figure IV.19**).

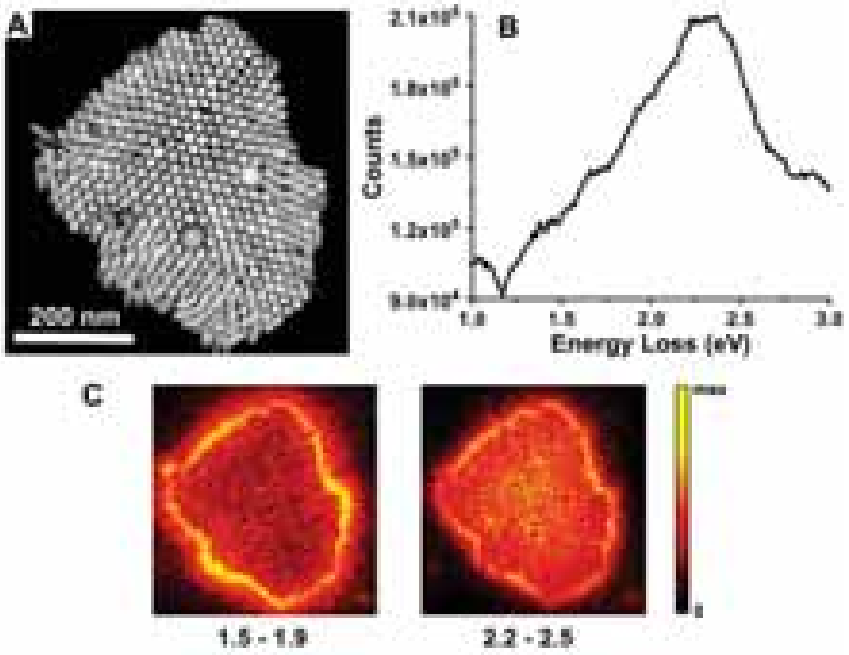

Figure IV.18. EELS plasmon mapping of a gold nanorod monolayer. A: HAADF-STEM image of a gold nanorod monolayer on a SiN film. **B:** EELS spectrum showing one strong peak at 2.1-2.5 eV and a shoulder at 1.5-1.9 eV. **C:** Plasmon maps showing the plasmon modes present in the spectrum presented in **B**.

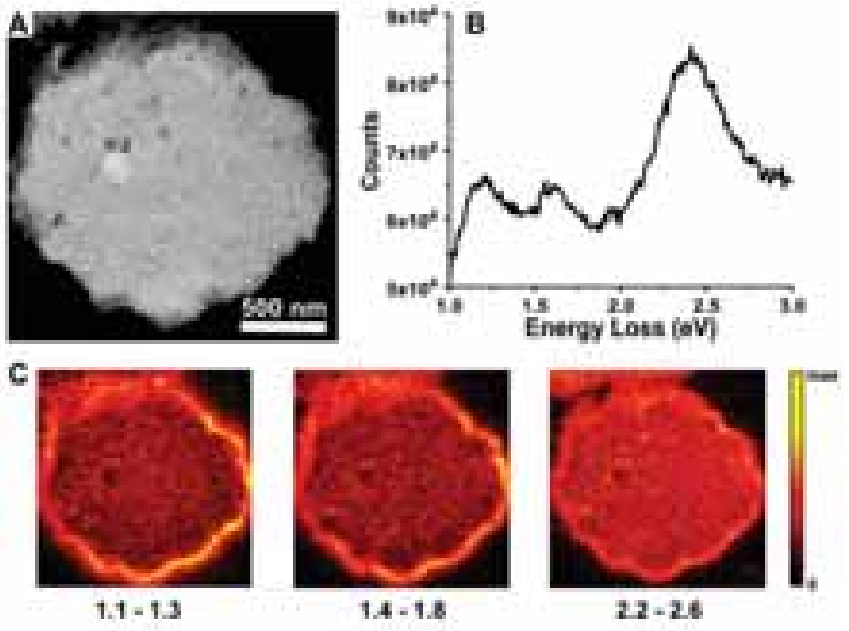

Figure IV.19. EELS plasmon mapping of a golf nanorod bilayer. A: HAADF-STEM image of a bilayer assembly of gold nanorods standing on a SiN film. **B:** EELS spectrum showing three peaks at 2.2-2.6 eV, 1.4-1.8 eV and 1.1-1.3 eV. **C:** Plasmon maps showing the plasmon modes present in the spectrum presented in **B**.

Although interpretation of these results is far from straightforward, a clear difference can be appreciated between the optical properties of monolayers and bilayers, which is likely related to field enhancement distributions as discussed below. Before proceeding with SERS analysis, the substrates were cleaned by Ar^+ plasma treatment to remove organic material deposited on top of the supercrystals, which could interfere with the measurements. Details and comparison between different cleaning procedures are provided in the Supporting Information **(Figure IV.20)**.

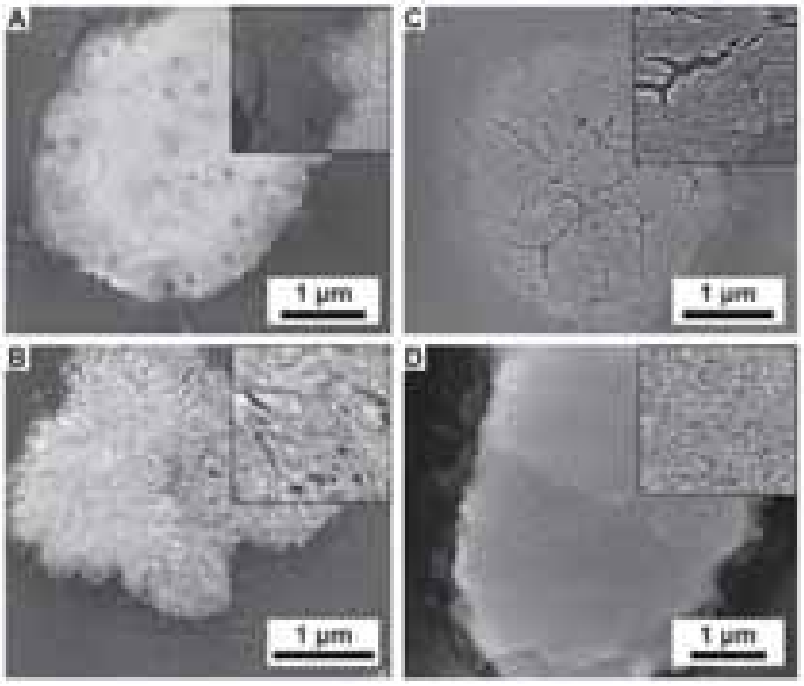

Figure IV.20. Comparison of cleaning processes by SEM. A: As prepared supercrystals. **B:** Supercrystals after one hour UV/O_3; formation of defects on the surface was observed as previously reported.[116] **C:** Supercrystals after O_2 plasma (200 W, 0.4 mbar O_2, 30 sec); a lot of defects and aggregates were found. **D:** Supercrystals after Ar cleaning (4W, 24 mbar Ar, 30 min).

The optical properties of the supercrystals were further investigated through their SERS performance, as shown in **Figure IV.21**. Crystal violet (CV) was selected as a model analyte because of its well-known chemical and physical features. After plasma cleaning, CV was drop casted on the supercrystals and SERS mappings were recorded at various positions of the substrate. CV deposition was considered to be uniform, taking into account the small region of interest, so that all supercrystals were similarly covered by the analyte as required for a meaningful comparison of the SERS intensities. Importantly, the SERS measurements were performed prior to structural characterization, as both the electron beam in SEM and the tip in AFM could eventually charge, contaminate or damage the surface of the supercrystals. This systematic optical and structural characterization was carried out on a large number of supercrystals with different numbers of layers on the same drop casted sample. We focused on supercrystals containing up to three layers. **Figure IV.21A** shows a schematic representation of the mono-, bi- and tri-layered supercrystals and their systematic characterization by SEM, AFM, and SERS. In particular, height profiles measured in AFM were found to be in agreement with multiple values of the average gold nanorod length, thereby confirming the lamellar order within the supercrystals and allowing us to precisely determine the number of layers in each gold nanorod supercrystal. Indeed, heights of 58 nm, 117 nm and 174 nm were measured precisely corresponding to one, two and three times the average rod length, respectively (**Figure IV.21B**). All measurements were performed at an excitation wavelength of 633 nm, which matches the absorption band of CV, meaning that we actually measure SERRS (see section I.2.3). SERRS images were acquired by mapping the spatial dependence of SERRS intensity integrated over the shift range of 1618-1632 cm^{-1}, corresponding to the most intense vibrational peak of CV. Remarkably, in all cases the SERRS signal intensity was uniform throughout the entire supercrystal surface and only the chemical fingerprint of CV was detected, with an average maximum intensity of 700 counts (**Figure IV.21C**). Note that the intensity of the signal was relatively high taking into account the small integration time (500 ms) and low laser power (0.01 mW) used in this experiment. Another important issue that needs to be considered is the presence of edge effects, which can significantly affect the collection and interpretation of the SERRS data. In this respect it is important to underline that the laser spot size (λ = 633 nm) was around 1 μm in diameter,

i.e. substantially smaller than the dimensions of the supercrystals. The hexagonal packing of the nanorods was confirmed in all cases on the top layer of the supercrystals (**Figure IV.17**).

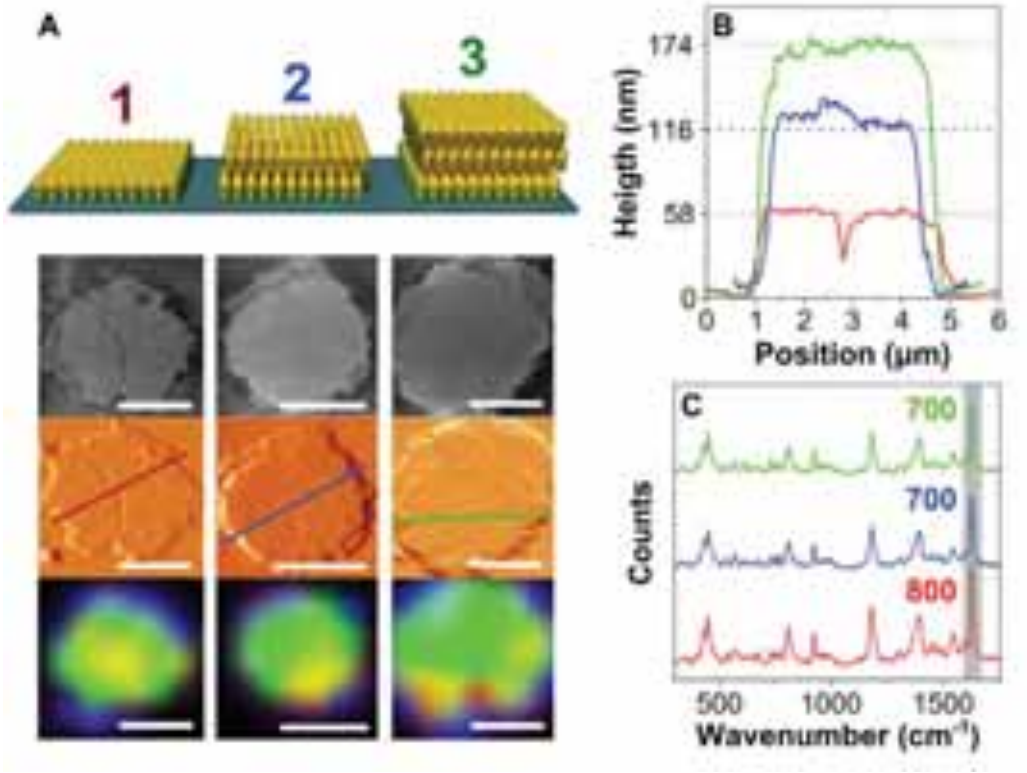

Figure IV.21: Optical characterization of mono-, bi- and tri-layered gold nanorod supercrystals. **A:** Schemes depicting mono, bi and tri-layered supercrystals together with (top to bottom): SEM, AFM and SERRS images. SERRS images were obtained by mapping the SERRS intensity of the crystal violet vibrational peak over 1618-1632 cm^{-1}. Scale bars are 2 μm on all nine images. **B:** Height profiles of a monolayer (red), a bilayer (blue) and trilayer (green) along the lines shown on the AFM image in **A**; the dotted lines indicate the expected values for mono-, bi- and trilayers. **C:** Average SERRS spectra of crystal violet measured on a monolayer (red), bilayer (blue) and trilayer (green). The shaded grey column indicates the integrated spectral range for generating SERRS images in **A**. Concentration of CV solution was 10^{-6} M, acquisition time was 500 ms, and laser power at the sample was ≈0.01mW at an excitation wavelength of 633 nm.

Although small height variations were noted on the supercrystal surface by AFM, these did not impact the measured SERRS signal. On the other hand, anomalously higher intensity spots in the SERRS mapping images corresponded to spherical byproducts or randomly oriented gold nanorods on the supercrystal upper surface (**Figure IV.22**), which may lead to the presence of additional plasmon modes.

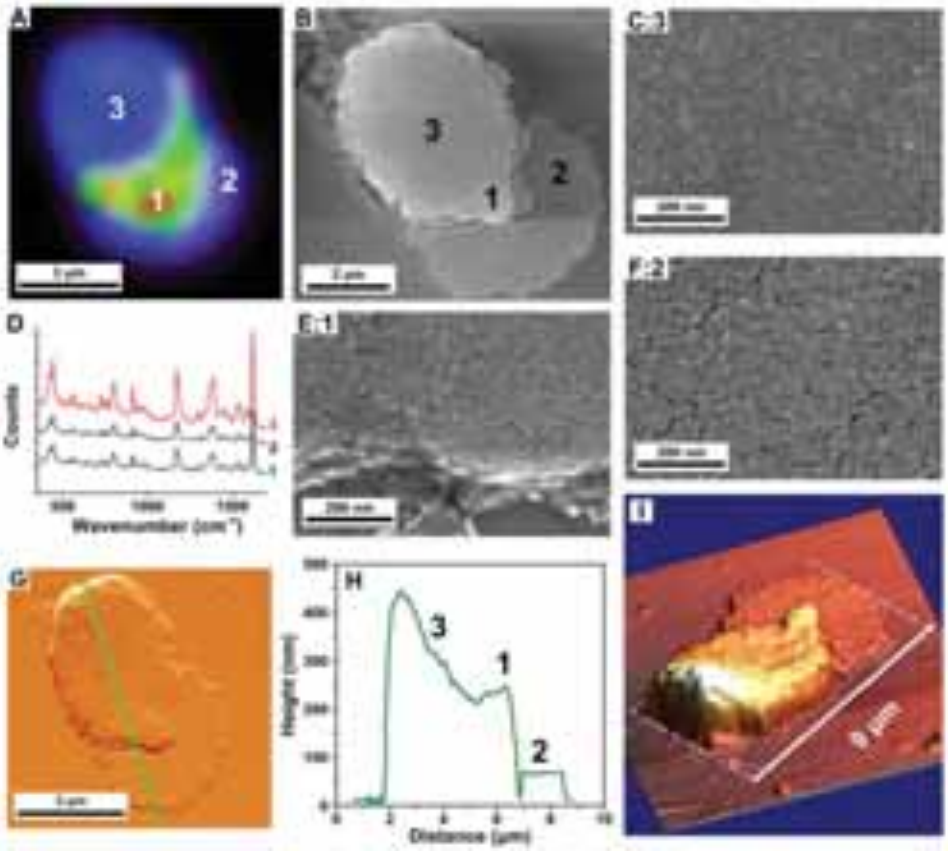

Figure IV.22. Characterization of gold nanorod supercrystal defects. All measurements were performed on the same supercystal. **A:** SERS image obtained by mapping SERS intensity of the crystal violet vibrational peak over 1618-1632 cm^{-1}. **B:** SEM images of the supercrystal at different magnifications, demonstrating organization at the surface in relevant areas **C, E-F:** SEM at higher magnification of area 1 (**E**), 2 (**F**) and 3 (**C**) as indicated in **B**. **D:** Average SERS spectra of CV in the regions denoted as 1, 2, 3 in **A**. Note that the signal intensity in region 2 (monolayer) is the same as in region 3 (multilayers). Region 1 shows surface defects and yields a higher signal. CV concentration was 10^{-6} M in ethanol, drop-casted on the substrate and dried under ambient conditions. The acquisition time was 500 ms, and the laser power was ≈0.15mW at an excitation wavelength of 633 nm. **G:** AFM image of the supercrystal. **H:** Height profile along the green line shown in **G**. **I:** Three dimensional AFM topography plot of the supercrystal.

Two important conclusions can be drawn from this analysis: first, SERRS mappings were crucial to assess the homogeneity of the field enhancement within gold nanorod supercrystals, as higher signals are recorded on local defects (i.e. single point measurements are not reliable); second, increasing the number of layers in a gold nanorod supercrystal does not necessarily represent a benefit for the SERRS signal. Indeed, additional SERS measurements on supercrystals comprising up to nine layers show that in all cases the

maximum SERRS intensity was uniform at near 700 counts, regardless of the total number of stacking layers (**Figures IV.22 - 23**). The analytical enhancement factor of these supercrystals was determined to be $1.23 \cdot 10^7$ and was calculated as the ratio between the Raman scattering intensity of CV in the presence and in the absence of the gold nanorod supercrystal, using the same experimental parameters.[127]

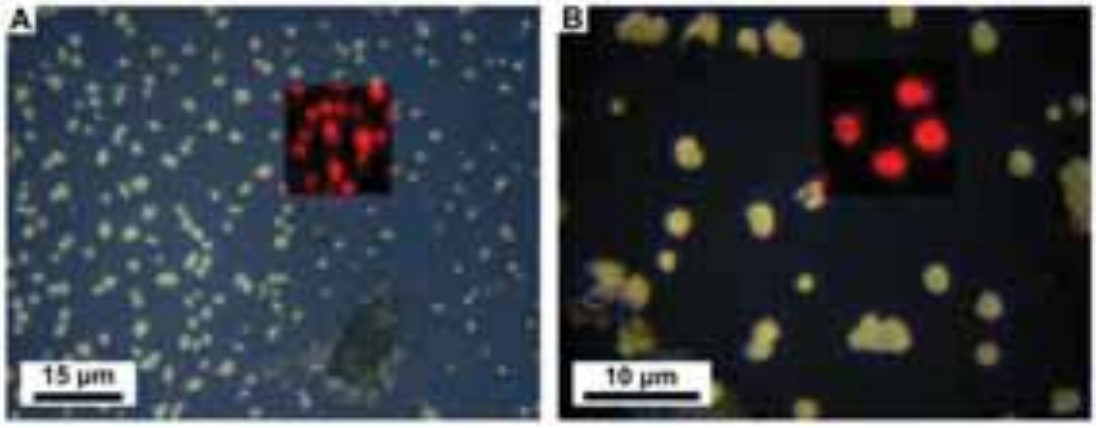

Figure IV.23. Large area Raman mappings on random supercrystals showing homogeneous signal intensity. **A-B:** optical microscopy images of two different samples where Raman mappings were measured. **Insets:** Superimposed SERS images obtained by mapping SERS intensity of the CV vibrational peak over 1618-1632 cm^{-1}. Concentration of CV before drop casting was 10^{-6} M, acquisition time 500 ms, and laser power ≈0.01 mW, at an excitation wavelength of 633 nm.

IV.2.3.3. Simulation of the Near-Field Properties of Supercrystals

To better understand the experimental results, we carried out detailed electromagnetic simulations based on MLFMA-MoM to determine the local electric field distribution and SERRS intensity for supercrystals comprising one, two, and three monolayers, but also trying to estimate the effect of additional layers. In the experiments, over one thousand gold nanorods contribute to the optical excitation in the focal volume of the laser beam. We thus aimed at simulating supercrystals composed of a large number of nanorods, so as to closely describe this complex system. Specifically, 3600 gold nanorods were used for a monolayer (≈3500 in a real system), 7200 for bilayers (≈7000 in a real system), 10800 for trilayers (≈10000 in a real system) and 14400 for tetralayers (≈14000 in a real system). It is important to stress that the number of unknowns in the calculation of the tetralayer case was above 47.6

million, which is far beyond the computational limits that have been reported so far in the literature.[122] Even though modeling of supercrystals with even larger dimensions was possible, it was considered impractical due to the high computational cost (ca. 5 hours per wavelength were required for the tetralayer case, on a workstation with four 8-core Intel Xeon E7-4820 processors at 2 GHz). Simulations were carried out considering illumination at normal incidence (parallel to the gold nanorod long axis) and linear polarization in the plane of the substrate. In the simulation, the incident light was focused onto the crystal surface with a numerical aperture of 0.85, in accordance with the experimental setup. For further similarity with the experimental system, we considered gold nanorods with octagonal cross section and dimensions of 58 nm in length and 17 nm in width, with a fixed distance between rods in the supercrystals of 2 nm.[13,118,119] Finally, we simulated supercrystals having a misorientation angle of 15° between two layers and an ABAB-type interlamellar packing, in an attempt to simulate the real experimental system. The SERS intensity was simply calculated as $|E\ (633\ nm)|^4$, and was not only determined on the surface of the nanostructures but also inside, which allowed us to evaluate the hotspot distribution and intensity, as a function of the number of layers (**Figure IV.24**). Interestingly, the results indicate that SERS enhancement was essentially the same at the surface of all supercrystals, around 10^4, and was higher at the gaps between nanorods, suggesting that the analyte would need to diffuse into the space between the nanorods if a more sensitive SERS detection were to be achieved. We therefore selected an analyte penetration depth of about 8 nm into the structures, in order to obtain comparable results between simulations and experiments, where we assumed that cleaning of the supercrystal surface by Ar^+ plasma treatment leads to improved penetration of the analyte in the gold nanorod structure. Additionally, the arrangement of the nanorods was observed to originate standing waves, which were distributed at different resonant depths according to the number of layers composing the supercrystals.[31] In this respect, more intense hotspots were distributed at various locations for different supercrystals: maximum hotspot intensity was higher at the bottom side of a monolayer, but higher on the top for a bilayer, at the middle layer for the trilayer and higher at the top layer for the tetralayer case (**Figure IV.24**).

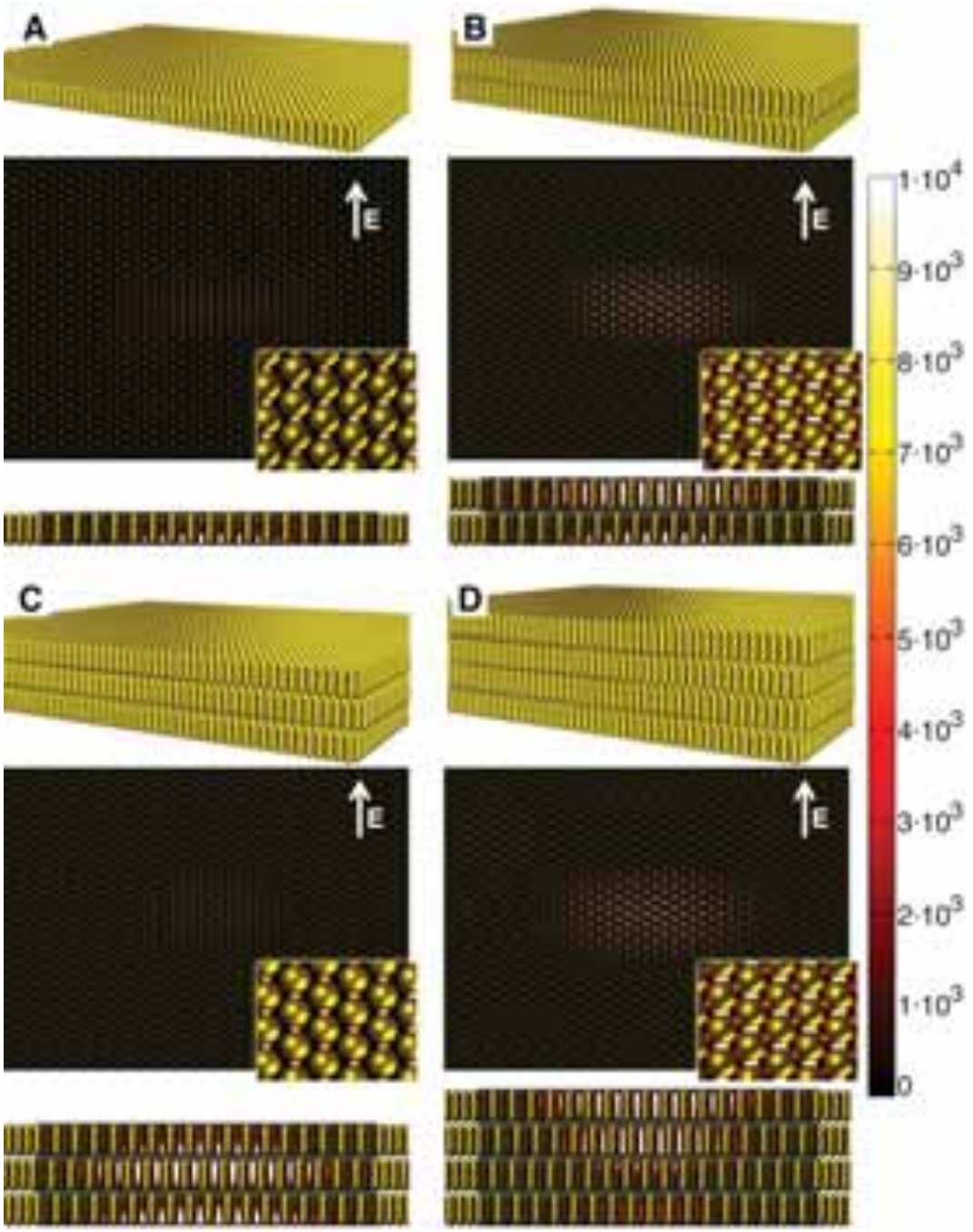

Figure IV.24: Simulation of hotspot distribution within supercrystals. A-D: SERS performance (calculated as $|E\ (633\ nm)|^4$) of gold nanorod supercrystals with different number of layers, simulated by MLMFA-MoM. In each case, the hotspot distribution is represented both as top view and cross section. **A:** monolayer; **B:** bilayer; **C:** trilayer; **D:** tetralayer. Arrows on top view images indicate in plane polarization direction.

In general, it could be stated that supercrystals comprising an odd number of layers display maximum enhancement at the inner structure, whereas supercrystals comprising an even number of layers have maximum enhancement at the very top, suggesting a symmetry effect on hotspot localization. The enhancement at the top layer was found to depend on the standing-wave pattern associated to the combination of the incident wave and the wave reflected at the bottom of the crystal. Therefore, this enhancement depends on the total depth of the structure (which in turn depends on the length of the nanorods, the interlamellae distance and the number of layers) and the wavelength of the laser that is being used. In our particular case, maximum enhancement occurring at the top layer was found for supercrystals with an odd number of layers but could also appear for an even number, if the above mentioned parameters were varied. The enhancement versus depth dependence follows a standing-wave pattern.

In the simulation we characterized standing wave patterns that in turn increased the total number of hotspots within the supercrystals as the number of layers was increased, thus we may expect an increase in the signal of multilayers compared to monolayers. However, this is not in agreement with the experiment, in which all supercrystals yielded similar SERRS intensity, regardless of the number of layers. Again, this is likely to be related to the limited penetration of the analyte (about 8 nm deep in the first layer), as the self-assembled monolayer comprises MUDOL at the gold nanorod surface, and the alkyl chains are likely to interdigitate so as to maintain the close packing, thereby precluding diffusion of the analyte within the structure. It is worth noting that the mismatch between the EF obtained in the experiment (near 10^7) and in the simulation (around 10^5) can be explained by the additional chemical enhancement and due to the resonance matching of CV at 633 nm in the experiment (SERRS vs. SERS).

As stated above, we find that the measured SERS signal of an analyte on a gold nanorod supercrystal arises from the upper layer only. We therefore calculated the SERS enhancement at the upper surface of the supercrystals, as a function of the excitation wavelength. As can be seen in **Figure IV.25**, when an excitation wavelength of 633 nm is used, the SERS signal is found to be almost identical for all supercrystals, in agreement with the experiment. Interestingly, in the spectral region considered, a maximum SERS signal at

580 nm was obtained for monolayers whereas for the trilayer the maximum shifted toward the IR region. For bilayers a maximum was observed at 710 nm, which is close to the maximum determined at 680 nm for tetralayer supercrystals.

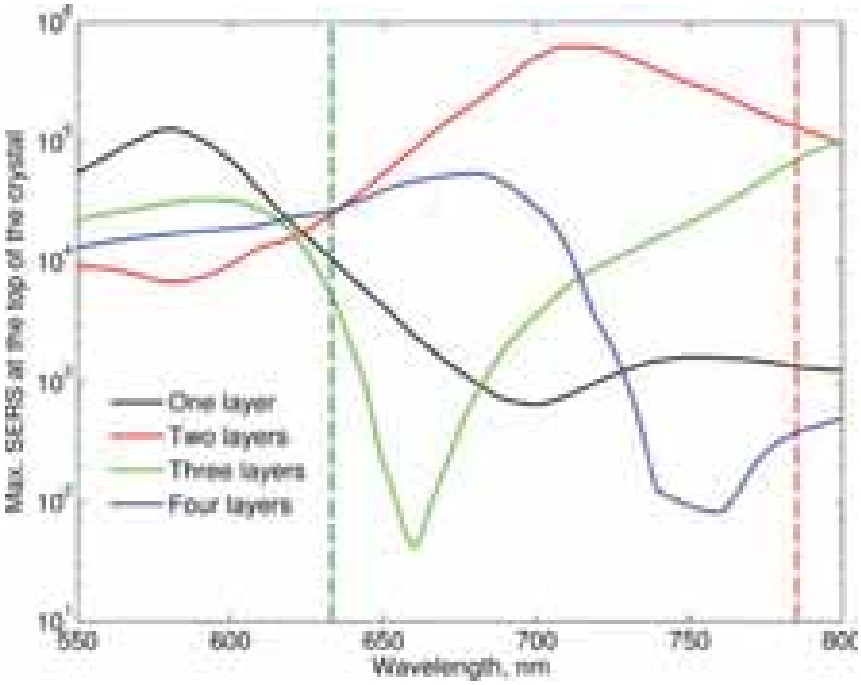

Figure IV.25: Calculated maximum SERS intensity at the upper surface of a supercrystal, as a function of the excitation wavelength. The dotted lines indicate the excitation wavelengths experimentally used in this work.

Therefore, the near field simulation confirms that the standing wave pattern strongly depends on the frequency of the incident light. Considering these simulations, we carried out an additional SERS investigation at 785 nm (**Figures IV.26**). A clear trend was observed showing that monolayers lead to two-fold smaller SERS signal than multilayers, confirming the results of the simulations (**Figure IV.25**).

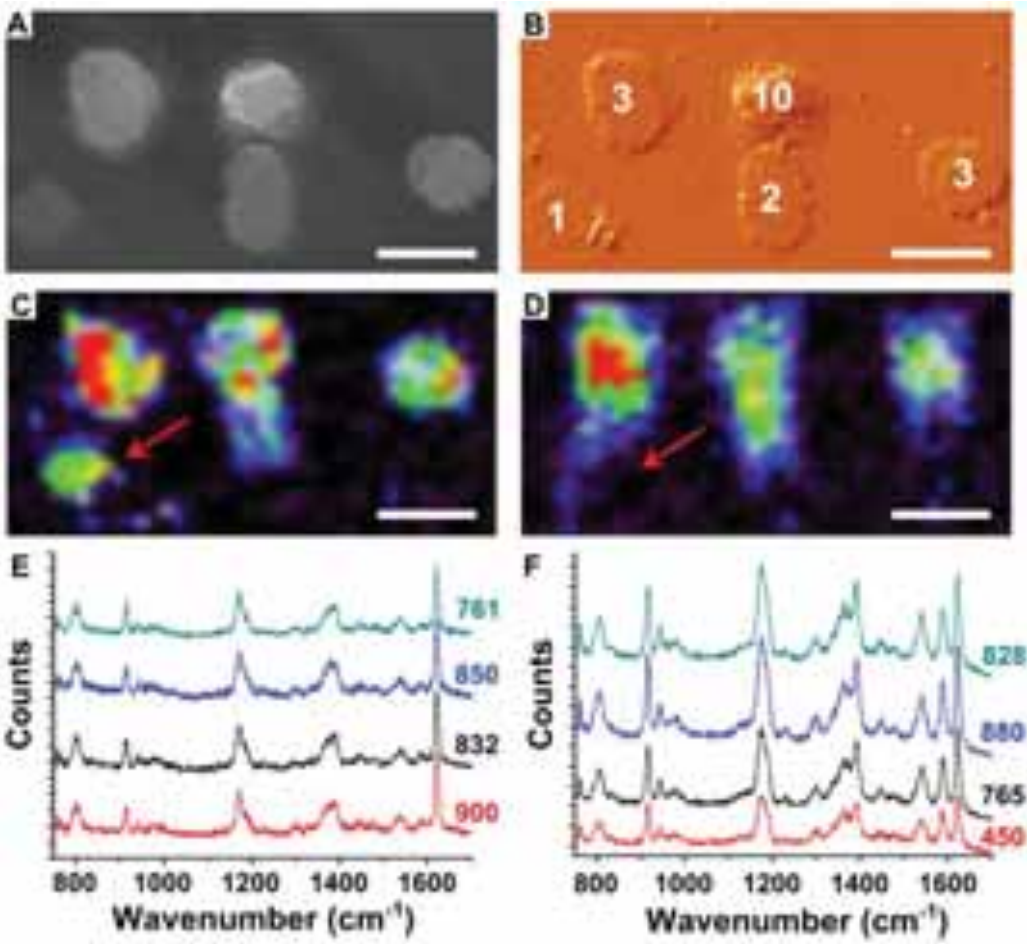

Figure S13. Comparison of CV SERS signal in nanorod multilayers. A: SEM image of gold nanorod supercrystals. **B:** AFM image of gold nanorod supercrystals; the numbers indicate the number of layers, derived from height profiles (not shown). **C-D:** SERS images of the same area acquired with excitation wavelengths of 633 nm (**C**) and 785 nm (**D**). The monolayer is not visible in D (red arrows). **E-F:** Comparison of SERS spectra of CV deposited on the surface of multilayers at 633 nm (**E**) and 785 nm (**F**). SERS data were acquired with a laser power of 0.01 mW at 633 nm and 1.16 mW at 785 nm; all other parameters were fixed: CV concentration before drop casting 10^{-6} M and acquisition time 500 ms. SERS maps were obtained using the intensity of CV vibrational peak over 1618-1632 cm^{-1}. All scale bar are 5 μm.

It is worth noting that the difference of signal between monolayers and bilayers is less than the predicted 100 fold. It is important to take into account that this near field plot only considers the enhancement factor at a horizontal plane, 8 nm deep in the upper layer, whereas a 3D integration would better describe the system. In our case, this was not attempted because of the high computational cost. Note that small differences between the experiment and the simulation parameters can lead to significant variations in the standing

wave pattern even if the model aims at describing as close as possible a gold nanorod supercrystal. Overall, the measured SERS signal was the same for all supercrystals at 633 nm excitation, in good agreement with the simulation, but variations of the signal at 785 nm excitation were found only between monolayers and multilayers.

IV.2.3.4. Conclusions

Robust plasmonic substrates displaying a high level of organization, with orientation of gold nanorods perpendicular to the substrate, were obtained by simple drop casting. The structural and optical properties of such gold nanorod supercrystals were investigated by various microscopy and spectroscopy techniques, with the objective to investigate the relation between the number of monolayers in gold nanorod supercrystals and their performance in Raman scattering enhancement. The results showed that the SERS signal on gold nanorod supercrystals is very homogeneous when using an excitation wavelength of 633nm, regardless of the number of layers, whereas variations can be observed at 785 nm. The experimental results were supported by accurate full-wave electromagnetic simulations using the M^3 solver. This is an *ad hoc* implementation of MLFMA yielding a dramatic reduction of the required memory footprint as plasmonic systems up to 47.6 million unknowns were simulated with a very small memory footprint of around ~2GB. This high performance computational study predicted the presence of a dense distribution of hotspots at different resonant depths depending on the number of gold nanorod layers. Overall, the results were interpreted by considering a short penetration depth of the analyte between the nanorod gaps, only at the upper layer of all gold nanorod supercrystals. Simulations were additionally used to predict further enhancements at different excitation wavelengths that could not be measured on our experimental setup but open possibilities to further studies. Improvements on supercrystal design allowing analyte diffusion are predicted to yield significantly higher enhancements that could pave the ways for next generation plasmonic devices, not only in sensor design but also in other fields such as catalysis or light harvesting systems.

IV.3. EXPERIMENTAL SECTION

IV.3.1. Materials

(1-mercaptoundec-11-yl)hexa(ethyleneglycol) (MUDOL, 90%), Crystal Violet (CV, dye content ≥ 90 %),), 5-bromosalicylic acid (technical grade, 90%), deuterium oxide (D_2O, 99.9 atom % D), Benzyldimethylhexadecylammonium chloride (BDAC), silver nitrate ($AgNO_3$, ≥99.0%), Hexadecyltrimethylammonium bromide (CTAB, ≥96%), L-ascorbic acid (≥99%), Hexadecyltrimethylammonium chloride (CTAC, 25 wt % in water), hydrogen tetrachloroaurate trihydrate ($HAuCl_4 \cdot H_2O$, ≥99.9%), sodium iodide (≥99.5%), trisodium citrate (≥98%) and sodium borohydride ($NaBH_4$, 99%) were purchased from Aldrich. All the chemicals were used as received. Milli-Q water (resistivity 18.2 MΩ·cm at 25 ºC) was used in all experiments. All glassware was washed with aqua regia, rinsed with water, sonicated three-fold for 3 min with Milli-Q water and dried before use.

IV.3.2. Synthesis of Gold Colloids

The synthesis of single crystal gold nanorods and their functionalization with MUDOL have been described in detail in section II.5.3 and III.4.3, respectively. The synthesis of gold nanotriangles was described in detail in section II.5.4. The synthesis of penta-twinned gold nanorods, and their elongation into silver-gold-silver penta-twinned bimetallic nanowires were described in detail in section II.5.5.

IV.3.3. EELS and CL Optical Characterization of Gold Nanotriangles (section IV.2.1)

The measurements were conducted by the group of Professor Mathieu Kociak (Laboratoire de Physique des Solides, Univiversité Paris-Sud, Orsay, France). The experiments are performed using a Vacuum Generator HB-501 STEM quipped with a cold field emission electron gun. Both CL and EELS measurements are carried out at an operation voltage of 100kV. The incident electron beam semi-angle for EELS is set to 7.5 mrad, resulting in typical currents of 10-20 pA for a probe size of 0.7 nm. The incident semi-angle for CL is set to 15 mrad, resulting in currents of more than 1 nA and a probe size of a few nanometers. The collection semi-angle is 9 mrad for EELS, while the solid detection angle is 1.2 π sterad for CL. Small homogeneous and larger nanoprisms are measured. The larger nanoprisms are

dropcasted on a standard TEM grid, while the small ones are dropcasted on graphene sheets (Ted Pella Single Layer Graphene). The thickness of the small and homogeneous nanoprisms is monitored by deliberately damaging the graphene sheet by extreme illumination conditions. This leads to the deterioration of the sheet and the subsequent tilt of nanoprism. The dispersion of the electron and optical spectrometers are carefully measured through different calibration procedures. The EELS calibration is performed by applying a 10V voltage difference on the drift tube and measuring the resulting spectral shift of the Zero Loss Peak (ZLP) of an averaged spectrum recorder in vacuum (vacuum ZLP). The CL calibration is performed by systematically recording an Hg lamp emission spectrum after the experiments. After acquisition, the EELS spectra are spectrally aligned and binned together. The resulting set of spectra is then deconvoluted by the vacuum ZLP through Richardson Lucy deconvolution.[128] The dark noise of the CCD camera together with a very small signal contribution coming from the substrate are removed from the CL spectra by averaging and subtracting a few spectra recorded from the substrate. After deconvoluted vacuum ZLP, is of the order of 150 meV. The spectral resolution for CL is of the order of 30 meV, as estimated from the FWHM of the emission lines of the Hg lamp. The EELS and CL local spectra shown on this article are averaged over a few pixels around the locations shown on the images. They are fitted to a single Gaussian function plus a sigmoid background to precisely include the calibration error as well as a possible fitting error. When the resonance energies and peak FWHM associated with the dipolar and higher order modes are discussed, the values also take into account an average over the resonances as measured at the three tips and sides of the nanoprism. In order to build maps such as the ones used in **Figure IV.3** and **Figure IV.4**, all the EELS spectra contained in the spatially resolved dataset are first normalized and subtracted from the ZLP.[26] Prior to fitting the noise of the CL spectra is reduced via principal component analysis.[129] Multi-peak fitting is performed on both EELS and CL datasets using a sum of Gaussian functions and a sigmoid background within each spectrum.[6] Maps of the amplitude of those peaks whose central energy is found within a given energy range are produced by assigning to each probe position the amplitude of the Gaussian function that is fitted within the corresponding spectrum in this energy range. For

all the maps shown in this paper, we make sure that only one fitted Gaussian function has its center in the selected, narrow energy range.

IV.3.4. Correlated Structural and Spectroscopic Characterization of Silver-Gold-Silver Bimetallic Nanowires (section IV.2.2)

Transmission electron microscopy (TEM) images were collected with a JEOL JEM1400PLUS instrument operating at 120 kV with carbon-coated 400 square mesh copper grids. All samples were centrifuged twice before blotting on the grid to reduce surfactant concentration. Optical extinction spectra were recorded using an Agilent Cary 5000 UV-Vis-NIR spectrophotometer in deuterated water. All the presented UV-Vis-NIR spectra were multiplied by the respective dilution factors to facilitate comparison of the data. HAADF-STEM images and electron tomography series were acquired by the group of Professor Sara Bals (EMAT, University of Antwerp, Belgium). Data were collected using an aberration corrected cubed FEI Titan 60—300 electron microscope operated at 200 kV. For the reconstruction of the series the Total Variation Minimization technique (TVM) was used. EELS plasmon maps, were acquired using a monochromated double aberration corrected cubed FEI Titan 50—80 electron microscope operated at 300 kV and yielding an energy resolution of 0.12 eV. For the analysis of the two EELS datasets, first a Richardson-Lucy deconvolution of the ZLP from the data was performed and then the ZLP was fitted and subtracted from the result, by using Hyperspy.[130] Since the points of the map passing over the rod still present a large background due to multiple phonon scattering, and are also noisier due to the lower counts, reducing the signal quality from those areas, a mask was used in the place of the NR.[131]

IV.3.5. Preparation of Gold Nanorod Supercrystals (section IV.2.3)

In a typical experiment, 10 μL of MUDOL coated gold nanorods colloid was drop casted on a glass substrate (Menzel-Gläzer, Thermo Scientific) and dried in a homemade system to slow down the evaporation rate up to twelve hours (see section III.2.1.1).

IV.3.6. Preparation of Gold Nanorod Supercrystal Substrates for SERS Spectroscopy Characterization (section IV.2.3)

Supercrystals were cleaned by Argon plasma (4W, 24 mbar Ar, 30 min) to remove organics that could interfere with Raman measurements. A solution of CV at 10^{-6} M in ethanol was drop casted on the substrate and dried under ambient conditions. Laser spot size was in the range of one micrometer in diameter.

IV.3.7. Correlated Structural and Spectroscopic Characterization of Gold Nanorod Supercrystals (section IV.2.3)

Gold nanorods were characterized by transmission electron microscopy (TEM, JEOL 2010, 120 keV). Argon plasma cleaning was performed in an Aja magnetron sputtering system (ATC 2200). SEM images were obtained in an ESEM Quanta250 FEG (FEI, The Netherlands). Raman scattering measurements were performed in a confocal scanning Raman microscope (micro-Renishaw InVia Reflex system equipped with Peltier-cooled charge-coupled device (CCD) detectors). The configuration involved a 1200 lines/mm diffraction grating, a 100× objective (NA=0.85) and excitation wavelengths of 633 nm. SERS images (4×4 μm) were recorded by mapping the spatial dependence of SERS intensity integrated at the main Raman peaks within the shift range 1570-1650 cm^{-1}, for each of the 15×15 points in the scan with P~0.01 mW and integration time 0.5 s. These scanning parameters were selected as a compromise to obtain a significant signal from CV without bleaching. AFM mapping was performed with a Bruker NanoScope V - MultiMode system in contact mode using a Bruker DNP-S10 cantilever (0.350 N/m). HAADF-STEM images and STEM-EELS maps were acquired in the laboratory of Professor Sara Bals (EMAT, University of Antwerp, Belgium), using a monochromated double aberration corrected cubed FEI-Titan 50-80 electron microscope, operated at 300kV and electron tomography series were acquired using an aberration corrected cubed FEI-Titan 60-300 electron microscope, operated at 300 kV. For the EELS data, a zero loss peak was acquired in vacuum with minimum noise in order to be fitted and subtracted from the EELS spectra acquired from the assemblies. The EELS data treatment was performed in EELSmodel.[132,133] For electron tomography, tilt series of HAADF-STEM images were acquired from -64° to +74° with a tilt

increment of 2°, by using a Fischione model 2020 single tilt tomography holder. The alignment of the series was performed by a combination of an automated and manual alignment by using the FEI Inspect3D software and IMOD, respectively.[134] The reconstruction was performed by using the Simultaneous Iterative Reconstruction Technique (SIRT) as implemented in the ASTRA toolbox using 150 iterations.[135,136] The reconstructed volume was visualized using the Amira 3D software.

IV.4. SIMULATIONS

IV.4.1. Gold Nanotriangles (section IV.2.1)

Boundary Element Method (BEM) numerical simulations were carried out using either BEM-3D[34] or the MNPBEM toolbox[137] with its EELS/CL extension,[138] with the CL spectra computed as described in reference [139]. Simulations including a substrate were performed by adding a 5 nm thin cylinder on which the nanoprism stands completely. To account for additional dissipation of the substrate, we arbitrarily multiply the imaginary part of the dielectric function of amorphous carbon by 2.[77] The amplitude maps of **Figure IV.5C** were obtained by calculating complete EELS and CL spectra at different probe positions and applying the same fitting procedure as for the experiment (see section IV.3.3).

IV.4.2. Silver-Gold-Silver Bimetallic Nanowires (section IV.2.2)

Optical extinction spectra, electric near-field intensity maps, and EELS intensities were calculated by solving the Maxwell equations in the presence of either an external light plane wave or an electron point charge moving with constant velocity (v=0.78c, corresponding to an acceleration voltage of 300 KV), respectively. The extinction calculations were averaged over NW orientations and light polarizations. For EELS, the electron was incident along a direction normal to the long wire axis. For simplicity, the wires were simulated as axially symmetric rods of the same volume as the actual penta-twinned nanowire, using the boundary-element method and exploiting the axial symmetry of the particles, as described elsewhere.[140] More precisely, the outer gold and silver NW interfaces are modeled as circular cylinders with hemi-spherical caps. The radius of the silver wire was considered to be 2 nm larger than that of the gold core. The latter had a length (diameter) of 210 nm (34 nm) in the

simulations of Fig. 1 and 180 nm (32 nm) in Figs. 2-4. Gold and silver were represented by their tabulated frequency-dependent complex dielectric functions.[76] The NWs were considered to be in vacuum (ε=1) for EELS and in deuterated water ($\varepsilon=1-0.30637\lambda^2/(\lambda^2+47.26686)+0.74659\lambda^2/(\lambda^2-0.00893)$, where λ is the free-space light wavelength in microns under optical illumination[141]) for optical extinction.

IV.4.3. Gold Nanorod Supercrystals (section IV.2.3)

A full-wave boundary-element-based method of moments (MoM) formulation for piecewise-homogeneous penetrable objects was used to solve Maxwell's equations.[123] Simulations were carried out by the groups of Professor Fernando Basteiro at the University of Vigo and Professor José Manuel Taboada at the University of Extremadura. As opposed to point-matching techniques, MoM enforces the boundary conditions in a variational sense over the whole boundary with the help of functionals. In this regard, Galerkin's testing procedure was adopted, meaning the testing functionals were the very same basis functions used to expand the unknown electric and magnetic surface equivalent currents, div-conforming Rao-Wilton-Glisson (RWG)[142] basis functions in our case. The discretization of the set of boundary equations derived from the Stratton-Chu surface integro-differential formulas results wan a non-sparse NxN matrix system of linear equations, being N=2M the number of unknowns and M the number of boundary mesh elements.

A major drawback inherent to MoM approaches is the rigorous evaluation of integrals including singular and hypersingular integrands stemming from the BEM kernel, the three-dimensional (3D) electrodynamic homogeneous Green's function, and its derivatives. The accurate evaluation of these terms, which in the developed code are handled via subtraction and analytical evaluation, is of foremost importance and will determine the accuracy of the method. This is in contrast to volumetric field-based formulations—finite-difference time-domain (FDTD) technique, finite-elements methods (FEM), e.g.—, usually free of such singularities. In return, nevertheless, MoM provides a key advantage in nanoplasmonics: as the field singularities and hotspots arising with LSPRs are analytically addressed, the method does not suffer from numerical dispersion or instability due to rapid field variations, as may be the case with volumetric solvers.

In addition, despite BEM reducing the problem's number of degrees of freedom if compared with the 3D parameterization involved in volumetric approaches, and hence rendering the problem more viable in terms of computational resources, a means to compress the rank-deficient MoM impedance matrix that expedites the $O(N^2)$ matrix-vector product (MVP) in the framework of an iterative solver is still paramount. Among the various algebraic or physics-based electrodynamic compression techniques found in the literature, the fast multipole method (FMM)[143] and its multilevel version (MLFMA)[144] are arguably the most successful, the latter achieving an impressive and error-controllable $O(N\log N)$ computational cost. The key to this high compression rate relies upon a decomposition of the Green's function in spherical harmonics and further plane-wave expansion. This allows for a factorization of the Green's function-based MoM cross-couplings through the Gegenbauer addition theorem, in virtue of which the non-nearest neighbor interactions can rather be grouped in communication "hubs", thus avoiding the N^2 all-to-all communication scheme present in uncompressed MoM. This grouping can be straightforwardly performed in a hierarchical multilevel fashion with an oct-tree decomposition of the geometry following a Cartesian grid. In doing so, the radiating/receiving centers of the groups lie on a regular 3D lattice and thus the translation operator among groups for a given direction in the plane-wave k-space can be seen as a circular 3D convolution. Consequently, it can be simultaneously sped up for all groups as a product in the transformed space through the use of a 3D fast Fourier transform (FFT). Such implementation has proved to solve large-scale plasmonic problems in an accurate and efficient way.[121,145]

One step forward in the full-wave analysis of electrically-large assemblies consisting of a reduced set of plasmonic nanoparticles highly repeated throughout the structure, consists of the hybridization of both MoM and MLFMA,[122] which exploits the repetition pattern inherent to this kind of nanostructures. Loosely put, the repeated self-coupling naturally-split problems are squarely solved throughout the factorization of their MoM impedance matrix blocks (dense, though small), enabling the Krylov-space iterative method—generalized minimal residual method (GMRES)—to focus solely on the cross-couplings through the surrounding medium, spectrally comptacted with MLFMA. This is done with the inclusion of a Jacobi diagonal block preconditioner which, through the lower-upper decomposition of

the repeated self-impedance submatrices and subsequent forward- backward substitutions, dramatically reduces the iteration count needed to reach a given residual error, strongly enhancing the convergence behavior of the electromagnetic solver.

When dealing with large densely-packed arrangements as the pieces of plasmonic metamaterial at hand, however, the geometrical features lead to such overly-populated meshes that the non-compressed interactions between nearest-neighbors in MLFMA yield the problem unfeasible, unless supercomputers are used. The origin of this limitation can be traced back to the plane-wave expansion of the Green's function, wherein the spherical Hankel function of the second kind present in the translation stage becomes unstable for small arguments, i. e., for low-frequency problems ruled by circuit-like evanescent wave physics rather than propagation physics. This is known as "sub-wavelength breakdown" and translates, in practice, into a geometry partition with a cellsize that should not go below $\sim\lambda/10$ at the finer level, being λ the wavelength in the background medium.

The present work exploits the repetition pattern found in metamaterials in order to compress these rank-deficient neighbor couplings in the finer level of the MLFMA decomposition, governed by quasi-electrostatic physics, through truncated singular value decompositions[146] that compensate their high computational demand, in relative terms with respect to the block size, with the fact that those coupling blocks are periodically repeated throughout the structure. If we consider the $2L$x$2L$ coupling block that defines the interaction between a pair of close strongly coupled nanorods, each discretized with L=1656 RWG's, its rank r for a prescribed threshold ε ($\varepsilon = 1e^{-3}$ has proved to be a judicious value) is found to be typically below $L/10$, and thereby the effective number of degrees of freedom can be fitted if the singular value decompositions factorization is truncated including only the first r singular values (σ), provided that $\sigma_{r+1} < \varepsilon\sigma_1$. If, in contrast to the more conventional Cartesian grid, the multilevel decomposition is defined in terms of growing sets of entire nanoparticles (nanorods in this case) that are periodically repeated, this compact representation for the coupling interactions among cells can be recycled. The memory footprint achieved with this approach for the four-layer case is in the order of only ~2 GB if $\varepsilon = 10^{-3}$ is chosen for truncation and ~20 GB without truncation. Otherwise, more than 300 TB would be needed

for conventional MLFMA with a Cartesian oct-tree starting at $\lambda/10$, rendering the analysis nonviable.

The authors would like to stress out that the developed methodology is a rigorous full-wave approach. Consequently, the scattering response does take into account all interactions, including edge effects, as infinite-structure considerations have been ruled out. The dispersive electric permittivity for Au was taken from ref. 76.

IV.5. REFERENCES

(1) Slaughter, L.; Chang, W.-S.; Link, S. *J. Phys. Chem. Lett.* **2011**, *2* (16), 2015–2023.

(2) Henry, A.-I.; Bingham, J. M.; Ringe, E.; Marks, L. D.; Schatz, G. C.; Van Duyne, R. P. *J. Phys. Chem. C* **2011**, *115* (19), 9291–9305.

(3) Raschke, G.; Sonnichsen, C.; Franzl, T.; Wilk, T.; von Plessen, G.; Feldmann, J.; Wilson, O.; Mulvaney, P. In *Quantum Electronics and Laser Science Conference, 2002. QELS'02. Technical Digest. Summaries of Papers Presented at the*; IEEE, 2002; p 33.

(4) Mock, J. J.; Barbic, M.; Smith, D. R.; Schultz, D. A.; Schultz, S. *J. Chem. Phys.* **2002**, *116* (15), 6755–6759.

(5) Peng, Y.; Xiong, B.; Peng, L.; Li, H.; He, Y.; Yeung, E. S. *Anal. Chem.* **2014**, *87* (1), 200–215.

(6) Mazzucco, S. Geuquet, . e , . St p han, O.; Van Roy, W.; Van Dorpe, P.; Henrard, L.; Kociak, M. *Nano Lett.* **2012**, *12* (3), 1288–1294.

(7) Ghosh Chaudhuri, R.; Paria, S. *Chem. Rev.* **2011**, *112* (4), 2373–2433.

(8) Kociak, M.; Stéphan, O. *Chem. Soc. Rev.* **2014**, *43* (11), 3865–3883.

(9) Williams, D. B.; Carter, C. B. *The transmission electron microscope*; Springer, 1996.

(10) Goris, B.; Polavarapu, L.; Bals, S.; Van Tendeloo, G.; Liz-Marzán, L. M. *Nano Lett.* **2014**, *14* (6), 3220–3226.

(11) DeSantis, C. J.; Skrabalak, S. E. *J. Am. Chem. Soc.* **2013**, *135* (1), 10–13.

(12) Bals, S.; Goris, B.; Liz-Marzán, L. M.; Van Tendeloo, G. *Angew. Chem. Int. Ed.* **2014**, *53* (40), 10600–10610.

(13) Goris, B.; Bals, S.; Van den Broek, W.; Carbó-Argibay, E.; Gómez-Graña, S.; Liz-Marzán, L. M.; Van Tendeloo, G. *Nat. Mater.* **2012**, *11* (11), 930–935.

(14) Peckys, D. B.; De Jonge, N. *Microsc. Microanal.* **2014**, *20* (01), 189–197.

(15) Kunstmann-Olsen, C. Belić, D. Brust, M. *Faraday Discuss.* **2015**.

(16) Scarabelli, L.; Sánchez-Iglesias, A.; Pérez-Juste, J.; Liz-Marzán, L. M. *J. Phys. Chem. Lett.* **2015**, *6* (21), 4270–4279.

(17) Hendel, T.; Wuithschick, M.; Kettemann, F.; Birnbaum, A.; Rademann, K.; Polte, J. *Anal. Chem.* **2014**, *86* (22), 11115–11124.

(18) Scarabelli, L.; Grzelczak, M.; Liz-Marzán, L. M. *Chem. Mater.* **2013**, *25* (21), 4232–4238.

(19) Baer, D. R.; Engelhard, M. H. *J. Electron Spectrosc. Relat. Phenom.* **2010**, *178-179*, 415–432.

(20) Baer, D.; Gaspar, D.; Nachimuthu, P.; Techane, S.; Castner, D. *Anal. Bioanal. Chem.* **2010**, *396* (3), 983–1002.

(21) Whelan, C. M.; Barnes, C. J.; Walker, C. G. H.; Brown, N. M. D. *Surf. Sci.* **1999**, *425* (2-3), 195–211.

(22) Yamamoto, N.; Araya, K.; de Abajo, F. G. *Phys. Rev. B* **2001**, *64* (20), 205419.

(23) De Abajo, F. G.; Aizpurua, J. *Phys. Rev. B* **1997**, *56* (24), 15873.

(24) Batson, P. E. *Phys. Rev. Lett.* **1982**, *49* (13), 936.

(25) de Abajo, F. G. *Phys. Rev. B* **1999**, *59* (4), 3095.

(26) Nelayah, J.; Kociak, M.; Stéphan, O.; Abajo, F. J. G. de; Tencé, M.; Henrard, L.; Taverna, D.; Pastoriza-Santos, I.; Liz-Marzán, L. M.; Colliex, C. *Nat. Phys.* **2007**, *3* (5), 348–353.

(27) Bosman, M.; Keast, V. J.; Watanabe, M.; Maaroof, A. I.; Cortie, M. B. *Nanotechnology* **2007**, *18* (16), 165505.

(28) Rivacoba, A.; Zabala, N.; Aizpurua, J. *Prog. Surf. Sci.* **2000**, *65* (1), 1–64.

(29) Bigelow, N. W.; Vaschillo, A.; Iberi, V.; Camden, J. P.; Masiello, D. J. *ACS Nano* **2012**, *6* (8), 7497–7504.

(30) Mirsaleh-Kohan, N.; Iberi, V.; Simmons Jr, P. D.; Bigelow, N. W.; Vaschillo, A.; Rowland, M. M.; Best, M. D.; Pennycook, S. J.; Masiello, D. J.; Guiton, B. S.; others. *J. Phys. Chem. Lett.* **2012**, *3* (16), 2303–2309.

(31) Vesseur, E. J. R.; de Waele, R.; Kuttge, M.; Polman, A. *Nano Lett.* **2007**, *7* (9), 2843–2846.

(32) Kuttge, M.; Vesseur, E. J. R.; Koenderink, A. F.; Lezec, H. J.; Atwater, H. A.; de Abajo, F. G.; Polman, A. *Phys. Rev. B* **2009**, *79* (11), 113405.
(33) Gómez-Medina, R.; Yamamoto, N.; Nakano, M.; Abajo, F. J. G. de. *New J. Phys.* **2008**, *10* (10), 105009.
(34) Myroshnychenko, V. ela yah, . Adamo, G. Geuquet, . Rodr guez- ern n dez, . as toriza-Santos, I. MacDonald, . . Henrard, L. Liz-Marz n , L. M.; Zheludev, N. I.; others. *Nano Lett.* **2012**, *12* (8), 4172–4180.
(35) Koh, A. L.; Bao, K.; Khan, I.; Smith, W. E.; Kothleitner, G.; Nordlander, P.; Maier, S. A.; McComb, D. W. *ACS Nano* **2009**, *3* (10), 3015–3022.
(36) Hohenester, U.; Ditlbacher, H.; Krenn, J. R. *Phys. Rev. Lett.* **2009**, *103* (10), 106801.
(37) Egerton, R. *Electron energy-loss spectroscopy in the electron microscope*; Springer Science & Business Media, 2011.
(38) García de Abajo, F. J. *Rev. Mod. Phys.* **2010**, *82* (1), 209–275.
(39) Yurtsever, A.; Zewail, A. H. *Nano Lett.* **2012**, *12* (6), 3334–3338.
(40) Yurtsever, A.; van der Veen, R. M.; Zewail, A. H. *Science* **2012**, *335* (6064), 59–64.
(41) Branda, F.; Silvestri, B.; Costantini, A.; Luciani, G. *J. Sol-Gel Sci. Technol.* **2015**, *73* (1), 54–61.
(42) Lai, Y. H.; Koo, S.; Oh, S. H.; Driskell, E. A.; Driskell, J. D. *Anal. Methods* **2015**.
(43) Pöselt, E.; Schmidtke, C.; Fischer, S.; Peldschus, K.; Salamon, J.; Kloust, H.; Tran, H.; Pietsch, A.; Heine, M.; Adam, G.; Schumacher, U.; Wagener, C.; Förster, S.; Weller, H. *ACS Nano* **2012**, *6* (4), 3346–3355.
(44) Hubert, F.; Testard, F.; Thill, A.; Kong, Q.; Tache, O.; Spalla, O. *Cryst. Growth Des.* **2012**, *12* (3), 1548–1555.
(45) Gómez-Graña, S.; Hubert, F.; Testard, F.; Guerrero-Martínez, A.; Grillo, I.; Liz-Marzán, L. M.; Spalla, O. *Langmuir* **2012**, *28* (2), 1453–1459.
(46) Wang, L.-Y.; Smith, K. W.; Dominguez-Medina, S.; Moody, N.; Olson, J. M.; Zhang, H.; Chang, W.-S.; Kotov, N. A.; Link, S. *ACS Photonics* **2015**.
(47) Olson, J.; Dominguez-Medina, S.; Hoggard, A.; Wang, L.-Y.; Chang, W.-S.; Link, S. *Chem Soc Rev* **2015**, *44* (1), 40–57.
(48) Chang, W.-S.; Slaughter, L. S.; Khanal, B. P.; Manna, P.; Zubarev, E. R.; Link, S. *Nano Lett.* **2009**, *9* (3), 1152–1157.
(49) Sherry, L. J.; Chang, S.-H.; Schatz, G. C.; Van Duyne, R. P.; Wiley, B. J.; Xia, Y. *Nano Lett.* **2005**, *5* (10), 2034–2038.
(50) Sherry, L. J.; Jin, R.; Mirkin, C. A.; Schatz, G. C.; Van Duyne, R. P. *Nano Lett.* **2006**, *6* (9), 2060–2065.
(51) Weeber, J.-C.; Dereux, A.; Girard, C.; Krenn, J. R.; Goudonnet, J.-P. *Phys. Rev. B* **1999**, *60* (12), 9061.
(52) Douillard, L.; Charra, F.; Korczak, Z.; Bachelot, R.; Kostcheev, S.; Lerondel, G.; Adam, P.-M.; Royer, P. *Nano Lett.* **2008**, *8* (3), 935–940.
(53) Rossouw, D.; Couillard, M.; Vickery, J.; Kumacheva, E.; Botton, G. A. *Nano Lett.* **2011**, *11* (4), 1499–1504.
(54) Joulain, K.; Carminati, R.; Mulet, J.-P.; Greffet, J.-J. *Phys. Rev. B* **2003**, *68* (24), 245405.
(55) Stockman, M. I.; Faleev, S. V.; Bergman, D. J. *Phys. Rev. Lett.* **2001**, *87* (16), 167401.
(56) Dereux, A.; Girard, C.; Weeber, J.-C. *J. Chem. Phys.* **2000**, *112* (18), 7775–7789.
(57) Boudarham, G.; Kociak, M. *Phys. Rev. B* **2012**, *85* (24), 245447.
(58) De Wilde, Y.; Formanek, F.; Carminati, R.; Gralak, B.; Lemoine, P.-A.; Joulain, K.; Mulet, J.-P.; Chen, Y.; Greffet, J.-J. *Nature* **2006**, *444* (7120), 740–743.
(59) Ouyang, F.; Isaacson, M. *Philos. Mag. B* **1989**, *60* (4), 481–492.
(60) de Abajo, F. G.; Kociak, M. *Phys. Rev. Lett.* **2008**, *100* (10), 106804.
(61) Hörl, A.; Trügler, A.; Hohenester, U. *Phys. Rev. Lett.* **2013**, *111* (7), 076801.
(62) Schmidt, F. P.; Ditlbacher, H.; Hofer, F.; Krenn, J. R.; Hohenester, U. *Nano Lett.* **2014**, *14* (8), 4810–4815.
(63) Vesseur, E. J. R.; García de Abajo, F. J.; Polman, A. *Nano Lett.* **2009**, *9* (9), 3147–3150.
(64) Losquin, A.; Camelio, S.; Rossouw, D.; Besbes, M.; Pailloux, F.; Babonneau, D.; Botton, G. A.; Greffet, J.-J.; Stéphan, O.; Kociak, M. *Phys. Rev. B* **2013**, *88* (11), 115427.

(65) ela yah, . ociak, M. St p han, O. Geuquet, . Henrard, L. Garc a de Aba o, . . as toriza-Santos, I. Liz-Marz n , L. M.; Colliex, C. *Nano Lett.* **2010**, *10* (3), 902–907.
(66) Bigelow, N. W.; Vaschillo, A.; Camden, J. P.; Masiello, D. J. *ACS Nano* **2013**, *7* (5), 4511–4519.
(67) Collins, S. M.; Midgley, P. A. *Phys. Rev. B* **2013**, *87* (23), 235432.
(68) Collins, S. M.; Nicoletti, O.; Rossouw, D.; Ostasevicius, T.; Midgley, P. A. *Phys. Rev. B* **2014**, *90* (15), 155419.
(69) Sánchez-Iglesias, A.; Pastoriza-Santos, I.; Pérez-Juste, J.; Rodríguez-González, B.; García de Abajo, F. J.; Liz-Marzán, L. M. *Adv. Mater.* **2006**, *18* (19), 2529–2534.
(70) Scarabelli, L.; Coronado-Puchau, M.; Giner-Casares, J. J.; Langer, J.; Liz-Marzán, L. M. *ACS Nano* **2014**, *8* (6), 5833–5842.
(71) Gu, L.; Sigle, W.; Koch, C. T.; Ögüt, B.; van Aken, P. A.; Talebi, N.; Vogelgesang, R.; Mu, J.; Wen, X.; Mao, J. *Phys. Rev. B* **2011**, *83* (19), 195433.
(72) Das, P.; Chini, T. K.; Pond, J. *J. Phys. Chem. C* **2012**, *116* (29), 15610–15619.
(73) Hao, E.; Schatz, G. C. *J. Chem. Phys.* **2004**, *120* (1), 357–366.
(74) Zagonel, L. F.; Mazzucco, S.; Tencé, M.; March, K.; Bernard, R.; Laslier, B.; Jacopin, G.; Tchernycheva, M.; Rigutti, L.; Julien, F. H.; others. *Nano Lett.* **2010**, *11* (2), 568–573.
(75) de Abajo, F. G.; Howie, A. *Phys. Rev. B* **2002**, *65* (11), 115418.
(76) Johnson, P. B.; Christy, R. W. *Phys. Rev. B* **1972**, *6* (12), 4370–4379.
(77) Hagemann, H.-J.; Gudat, W.; Kunz, C. *J. Opt. Soc. Am.* **1975**, *65* (6), 742.
(78) Bosman, M.; Anstis, G. R.; Keast, V. J.; Clarke, J. D.; Cortie, M. B. *Acs Nano* **2011**, *6* (1), 319–326.
(79) Mazzucco, S.; Stéphan, O.; Colliex, C.; Pastoriza-Santos, I.; Liz-Marzan, L. M.; Garcia de Abajo, J.; Kociak, M. *Eur. Phys. J. Appl. Phys.* **2011**, *54* (03), 33512.
(80) Bosman, M.; Ye, E.; Tan, S. F.; Nijhuis, C. A.; Yang, J. K.; Marty, R.; Mlayah, A.; Arbouet, A.; Girard, C.; Han, M.-Y. *Sci. Rep.* **2013**, *3*.
(81) Bohren, C. F.; Huffman, D. R. *Absorption and scattering of light by small particles*; John Wiley & Sons, 2008.
(82) Zuloaga, J.; Nordlander, P. *Nano Lett.* **2011**, *11* (3), 1280–1283.
(83) Alonso-González, P.; Albella, P.; Neubrech, F.; Huck, C.; Chen, J.; Golmar, F.; Casanova, F.; Hueso, L. E.; Pucci, A.; Aizpurua, J.; others. *Phys. Rev. Lett.* **2013**, *110* (20), 203902.
(84) Kats, M. A.; Yu, N.; Genevet, P.; Gaburro, Z.; Capasso, F. *Opt. Express* **2011**, *19* (22), 21748–21753.
(85) Etchegoin, P. G.; Le Ru, E. C.; Meyer, M. *J. Chem. Phys.* **2006**, *125* (16), 164705.
(86) Husnik, M.; von Cube, F.; Irsen, S.; Linden, S.; Niegemann, J.; Busch, K.; Wegener, M. *Nanophotonics* **2013**, *2* (4), 241–245.
(87) Chu, M.-W.; Myroshnychenko, V.; Chen, C. H.; Deng, J.-P.; Mou, C.-Y.; García de Abajo, F. J. *Nano Lett.* **2009**, *9* (1), 399–404.
(88) Dorfmüller, J.; Vogelgesang, R.; Khunsin, W.; Rockstuhl, C.; Etrich, C.; Kern, K. *Nano Lett.* **2010**, *10* (9), 3596–3603.
(89) Valev, V. K.; Silhanek, A. V.; De Clercq, B.; Gillijns, W.; Jeyaram, Y.; Zheng, X.; Volskiy, V.; Aktsipetrov, O. A.; Vandenbosch, G. A. E.; Ameloot, M.; Moshchalkov, V. V.; Verbiest, T. *Small* **2011**, *7* (18), 2573–2576.
(90) Baffou, G.; Quidant, R. *Laser Photonics Rev.* **2013**, *7* (2), 171–187.
(91) Liu, M.; Lee, T.-W.; Gray, S.; Guyot-Sionnest, P.; Pelton, M. *Phys. Rev. Lett.* **2009**, *102* (10).
(92) Wang, X.; Zhang, Z.; Hartland, G. V. *J. Phys. Chem. B* **2005**, *109* (43), 20324–20330.
(93) Ahn, S.-H.; Kim, D.-S.; Seo, D.; Choi, W.; Yi, G.-R.; Song, H.; Park, Q.-H.; Kim, Z. H. *Phys. Chem. Chem. Phys.* **2013**, *15* (12), 4190–4194.
(94) Denkova, D.; Verellen, N.; Silhanek, A. V.; Valev, V. K.; Dorpe, P. V.; Moshchalkov, V. V. *ACS Nano* **2013**, *7* (4), 3168–3176.
(95) Dorfmüller, J.; Vogelgesang, R.; Weitz, R. T.; Rockstuhl, C.; Etrich, C.; Pertsch, T.; Lederer, F.; Kern, K. *Nano Lett.* **2009**, *9* (6), 2372–2377.

(96) Olmon, R. L.; Krenz, P. M.; Jones, A. C.; Boreman, G. D.; Raschke, M. B. *Opt. Express* **2008**, *16* (25), 20295.
(97) Okamoto, H.; Imura, K. *J. Phys. Chem. Lett.* **2013**, *4* (13), 2230–2241.
(98) Nicoletti, O.; Wubs, M.; Mortensen, N. A.; Sigle, W.; van Aken, P. A.; Midgley, P. A. *Opt. Express* **2011**, *19* (16), 15371.
(99) Guiton, B. S.; Iberi, V.; Li, S.; Leonard, D. N.; Parish, C. M.; Kotula, P. G.; Varela, M.; Schatz, G. C.; Pennycook, S. J.; Camden, J. P. *Nano Lett.* **2011**, *11* (8), 3482–3488.
(100) Rodríguez-González, B.; Attouchi, F.; Cardinal, M. F.; Myroshnychenko, V.; Stéphan, O.; García de Abajo, F. J.; Liz-Marzán, L. M.; Kociak, M. *Langmuir* **2012**, *28* (24), 9063–9070.
(101) Goris, B.; Van den Broek, W.; Batenburg, K. J.; Heidari Mezerji, H.; Bals, S. *Ultramicroscopy* **2012**, *113*, 120–130.
(102) Giannini, V.; Fernández-Domínguez, A. I.; Heck, S. C.; Maier, S. A. *Chem. Rev.* **2011**, *111* (6), 3888–3912.
(103) Stewart, M. E.; Anderton, C. R.; Thompson, L. B.; Maria, J.; Gray, S. K.; Rogers, J. A.; Nuzzo, R. G. *Chem. Rev.* **2008**, *108* (2), 494–521.
(104) Brongersma, M. L.; Halas, N. J.; Nordlander, P. *Nat. Nanotechnol.* **2015**, *10* (1), 25–34.
(105) Aroca, R. F. *Phys. Chem. Chem. Phys.* **2013**, *15* (15), 5355–5363.
(106) Tokel, O.; Inci, F.; Demirci, U. *Chem. Rev.* **2014**, *114* (11), 5728–5752.
(107) Alvarez-Puebla, R. A.; Liz-Marzán, L. M. *Angew. Chem. Int. Ed.* **2012**, *51* (45), 11214–11223.
(108) Schlücker, S. *Angew. Chem. Int. Ed.* **2014**, *53* (19), 4756–4795.
(109) Jain, P. K.; El-Sayed, M. A. *Chem. Phys. Lett.* **2010**, *487* (4), 153–164.
(110) Halas, N. J.; Lal, S.; Chang, W.-S.; Link, S.; Nordlander, P. *Chem. Rev.* **2011**, *111* (6), 3913–3961.
(111) Beermann, J.; Novikov, S. M.; Albrektsen, O.; Nielsen, M. G.; Bozhevolnyi, S. I. *JOSA B* **2009**, *26* (12), 2370–2376.
(112) Evlyukhin, A. B.; Kuznetsov, A. I.; Novikov, S. M.; Beermann, J.; Reinhardt, C.; Kiyan, R.; Bozhevolnyi, S. I.; Chichkov, B. N. *Appl. Phys. B* **2012**, *106* (4), 841–848.
(113) Zhang, S.-Y.; Regulacio, M. D.; Han, M.-Y. *Chem. Soc. Rev.* **2014**, *43* (7), 2301–2323.
(114) Alvarez-Puebla, R. A.; Agarwal, A.; Manna, P.; Khanal, B. P.; Aldeanueva-Potel, P.; Carbó-Argibay, E.; Pazos-Pérez, N.; Vigderman, L.; Zubarev, E. R.; Kotov, N. A.; others. *Proc. Natl. Acad. Sci.* **2011**, *108* (20), 8157–8161.
(115) Thorkelsson, K.; Bai, P.; Xu, T. *Nano Today* **2015**, *10* (1), 48–66.
(116) Peng, B.; Li, G.; Li, D.; Dodson, S.; Zhang, Q.; Zhang, J.; Lee, Y. H.; Demir, H. V.; Yi Ling, X.; Xiong, Q. *ACS Nano* **2013**, *7* (7), 5993–6000.
(117) Gómez-Graña, S.; Pérez-Juste, J.; Alvarez-Puebla, R. A.; Guerrero-Martínez, A.; Liz-Marzán, L. M. *Adv. Opt. Mater.* **2013**, *1* (7), 477–481.
(118) Hamon, C.; Novikov, S.; Scarabelli, L.; Basabe-Desmonts, L.; Liz-Marzán, L. M. *ACS Nano* **2014**, *8* (10), 10694–10703.
(119) Hamon, C.; Postic, M.; Mazari, E.; Bizien, T.; Dupuis, C.; Even-Hernandez, P.; Jimenez, A.; Courbin, L.; Gosse, C.; Artzner, F.; Marchi-Artzner, V. *ACS Nano* **2012**, *6* (5), 4137–4146.
(120) Xie, Y.; Guo, S.; Ji, Y.; Guo, C.; Liu, X.; Chen, Z.; Wu, X.; Liu, Q. *Langmuir* **2011**, *27* (18), 11394–11400.
(121) Sol s, D. M. Taboada, . M. Obelleiro, . Liz-Marz n , L. M. Garc a de Aba o, F. J. *ACS Nano* **2014**, *8* (8), 7559–7570.
(122) Solis, D.; Araujo, M.; Landesa, L.; Garcia, S.; Taboada, J.; Obelleiro, F. *Photonics Journal* **2015**, *7* (3), 4800709.
(123) Solis, D.; Taboada, J.; Obelleiro, F. *Transaction on Antennas and Propagation, IEEE* **2015**, *63* (15), 2141 - 2152
(124) Ye, X.; Jin, L.; Caglayan, H.; Chen, J.; Xing, G.; Zheng, C.; Doan-Nguyen, V.; Kang, Y.; Engheta, N.; Kagan, C. R.; Murray, C. B. *ACS Nano* **2012**, *6* (3), 2804–2817.
(125) Singh, A.; Dickinson, C.; Ryan, K. M. *ACS Nano* **2012**, *6* (4), 3339–3345.
(126) Apte, A.; Bhaskar, P.; Das, R.; Chaturvedi, S.; Poddar, P.; Kulkarni, S. *Nano Res.* **2014**, *8* (3), 907–919.

(127) Le Ru, E. C.; Blackie, E.; Meyer, M.; Etchegoin, P. G. *J. Phys. Chem. C* **2007**, *111* (37), 13794–13803.
(128) Gloter, A.; Douiri, A.; Tence, M.; Colliex, C. *Ultramicroscopy* **2003**, *96* (3), 385–400.
(129) Edwards, P. R.; Sleith, D.; Wark, A. W.; Martin, R. W. *J. Phys. Chem. C* **2011**, *115* (29), 14031–14035.
(130) de la Peña, F.; Berger, M.-H.; Hochepied, J.-F.; Dynys, F.; Stephan, O.; Walls, M. *Ultramicroscopy* **2011**, *111* (2), 169–176.
(131) Rossouw, D.; Botton, G. A. *Opt. Express* **2012**, *20* (7), 6968.
(132) Verbeeck, J.; Van Aert, S. *Ultramicroscopy* **2004**, *101* (2), 207–224.
(133) Verbeeck, J.; Van Aert, S. Available at www.eelsmodel.uantwerpen.be (accessed Nov 17, 2015).
(134) Kremer, J. R.; Mastronarde, D. N.; McIntosh, J. R. *J. Struct. Biol.* **1996**, *116* (1), 71–76.
(135) van Aarle, W.; Palenstijn, W. J.; De Beenhouwer, J.; Altantzis, T.; Bals, S.; Batenburg, K. J.; Sijbers, J. *Ultramicroscopy* **2015**.
(136) Palenstijn, W. J.; Batenburg, K. J.; Sijbers, J. *J. Struct. Biol.* **2011**, *176* (2), 250–253.
(137) Hohenester, U.; Trügler, A. *Comput. Phys. Commun.* **2012**, *183* (2), 370–381.
(138) Hohenester, U. *Comput. Phys. Commun.* **2014**, *185* (3), 1177–1187.
(139) Martin, J.; Kociak, M.; Mahfoud, Z.; Proust, J.; Gérard, D.; Plain, J. *Nano Lett.* **2014**, *14* (10), 5517–5523.
(140) García de Abajo, F. J.; Howie, A. *Phys. Rev. B* **2002**, *65* (11), 115418.
(141) Kedenburg, S.; Vieweg, M.; Gissibl, T.; Giessen, H. *Opt. Mater. Express* **2012**, *2* (11), 1588.
(142) Rao, S. M.; Wilton, D. R.; Glisson, A. W. *Antennas Propag. IEEE Trans. On* **1982**, *30* (3), 409–418.
(143) Coifman, R.; Rokhlin, V.; Wandzura, S. In *Antennas and Propagation Society International Symposium, 1993. AP-S. Digest*; IEEE, 1993; pp 48–51.
(144) Song, J.; Lu, C.-C.; Chew, W. C. *Antennas Propag. IEEE Trans. On* **1997**, *45* (10), 1488–1493.
(145) Taboada, J. M.; Araujo, M. G.; Basteiro, F. O.; Rodríguez, J. L.; Landesa, L. *Proc. IEEE* **2013**, *101* (2), 350–363.
(146) Golub, G. H.; Van Loan, C. F. *Matrix computations*; JHU Press, **2012**; Vol. 3.

CHAPTER

CONCLUSIONS

Overall the work described in this thesis dealt with various aspects regarding synthetic control of nanoparticle size, shape and composition, as well as with their use as building blocks for the design of self-assembled nanostructures with promising applications as biosensors based on surface enhanced Raman scattering. Even though specific conclusions have been extracted in each section, the presented material can be summarized by drawing the following conclusions:

1) SINGLE CRYSTAL GOLD NANORODS
   a) A new synthetic protocol was devised for the synthesis of single crystal gold nanorods: the aspect ratio and the dimensions of the obtained nanoparticles were tuned by exploiting the reduction properties of 5-Bromo Salicylic acid.
   b) Taking advantage of the narrow size distribution and the high shape-yield of the so-produced colloids, gold nanorods supercrystals were prepared by means of a templated self-assembly approach, with a certain degree of control over supercrystal height and shape. The produced nanostructures display a high degree of internal order, with the building blocks preferentially aligned in perpendicular direction to the substrate.
   c) In order to elucidate the plasmonic properties of such nanostructures we performed extensive correlated structural and optical analysis on different supercrystals. This allowed us to demonstrate that the previously postulated relationship between the number of nanorod layers and the corresponding enhancing properties are not justified. We hypothesize that the high density of hot-spots generated via such self-assembly can only be exploited if the analytes can diffuse within the supercrystals. Additional experiments are currently being performed in this direction in our group, where the nanorod layers are intercalated by thin mesoporous silica layers, which additionally confer a higher stability to the nanostructures and allow the diffusion of small analytes.

2) GOLD NANOTRIANGLES

a) We developed the first synthetic protocol for the production of highly homogeneous gold nanotriangles with a shape-yield comparable to that of single crystal gold nanorods (after purification), as well as the possibility of tuning the plasmon band across the visible through variation of the triangle edge length.

b) Single gold nanotriangles were analyzed through electron energy loss spectroscopy and cathodoluminescence in a correlated study. Thanks to their small size (below 60 nm in edge length) their plasmonic properties can be interpreted within the quasi-static approximation. This allowed us to demonstrate that while electron energy loss spectroscopy is able to probe both bright and dark plasmonic modes, cathodoluminescence only reveals the radiative ones. We additionally demonstrated a close relationship between electron energy loss spectroscopy and extinction on one hand and between cathodoluminescence and scattering on the other hand.

3) SILVER-GOLD-SILVER BIMETALLIC NANOWIRES

a) We introduced the concept of *controlled living nanowire growth*, which allowed us to achieve a high degree of control over the reduction of silver on the tips of penta-twinned gold nanorods. In particular, a zero-order kinetics was imposed on silver reduction using a microfluidic system, which allowed us to avoid side reactions and to enforce a linear relationship between the amount of added precursor and the final length of the bimetallic nanowires

b) We analyzed the plasmonic properties of single nanoantennas using electron energy loss spectroscopy. Interpretation of the results by means of extensive simulations allowed us to investigate the influence of the gold core on the plasmonic properties of the bimetallic nanostructures.

CHAPTER

VI

APPENDIX

VI.1 THEORETICAL DERIVATION OF THE QUASISTATIC MODAL DECOMPOSITIONS

In the following we adopt an analytical approach derived from the non-retarded BEM formalism in the quasistatic limit,[1–5] essentially consisting in using a rigorous eigenmode expansion of the surface charge induced by a given excitation that is valid for any homogeneous arbitrarily shaped object. For the sake of simplicity, we restrict the model to objects in vacuum. However, the effect of dissipation, which we want to address, is partly taken into account through the imaginary part of the dielectric function of the object itself. We consider an object of permittivity (ω) surrounded by vacuum, and make use of the notation introduced in **Figure VI.1**.

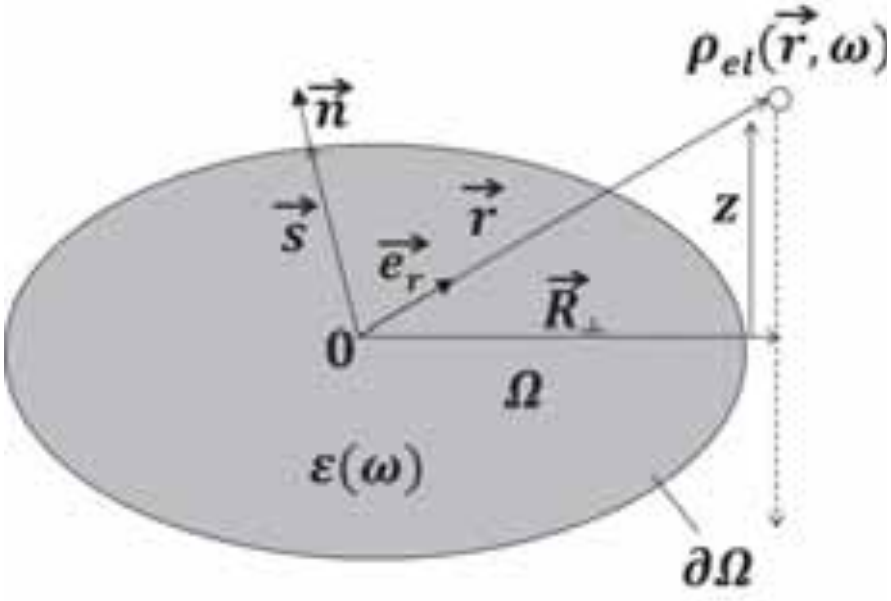

Figure VI.1: Schematic representation of a generic 3d system containing an object Ω of dielectric function $\epsilon(\omega)$ surrounded by vacuum. Here, O denotes the origin of the space coordinates, $\vec{r}$ is an arbitrary coordinate vector, $\vec{s}$ is a vector pointing to the surface $\partial\Omega$, and $\vec{n}$ is a normal unit vector located at the surface position $\vec{s}$ and pointing outside the object. An electron travelling at a distance $\vec{R}^{\perp}$ from the origin along the z direction is modeled through an electric charge density $\rho_{el}(\vec{r},\omega)$.

In the quasistatic limit, the interaction between an external charge and the object can be studied by solving the Poisson equation.

$$\vec{\nabla} \cdot \left[\tilde{\epsilon}(\vec{r},\omega)\vec{\nabla}\phi(\vec{r},\omega)\right] = -4\pi\rho_{ext}(\vec{r},\omega) \quad \textbf{[VI.1]}$$

where $\phi(\vec{r},\omega)$ is the electric potential expressed in time-Fourier space,

$$\tilde{\epsilon}(\vec{r},\omega) = \begin{cases} \epsilon(\omega) & \vec{r} \in \\ 1 & \vec{r} \notin \\ \frac{1}{2}[1+\epsilon(\omega) & \vec{r} \in \partial \end{cases} \quad \textbf{[VI.2]}$$

is a space and frequency dependent dielectric function, and $\rho_{ext}(\vec{r},\omega)$ is the external charge (see **Figure VI.1**). In what follows, we adopt a BEM which consists in expressing the electric potential in terms of surface-charge distributions located at the boundaries of the object. This allows us to interpret the interaction between a given excitation and the object through the excitation of surface eigenmodes.[2]

VI.1.1. Optical Properties

The optical properties can be calculated by considering setting the external charge to zero while introducing an external potential source.[6,7] The solution of the Poisson equation is then

$$\phi(\vec{r},\omega) = \phi^{ext}(\vec{r},\omega) + \phi^{sca}(\vec{r},\omega) \quad \textbf{[VI.3]}$$

Where $\vec{E}^{ext}(\omega) = -\vec{\nabla}^{ext}\phi(\vec{r},\omega)$ is the external field and $\phi^{sca}(\vec{r},\omega)$ is the scattered electric potential. We express the latter as a function of the induced surface charge distribution $\sigma(\vec{s},\omega)$ as

$$\phi^{sca}(\vec{r},\omega) = \oint_{\partial} d\vec{s}\,\frac{\sigma(\vec{s},\omega)}{|\vec{r}-\vec{s}|} \quad \textbf{[VI.4]}$$

Expanding $\sigma(\vec{s},\omega)$ wirhin the orthonormal basis of surface eigenmodes $\sigma_i(\vec{s})$ of eigenvalues λ_i,[2] we can write the scattered electric potential as

$$\phi^{sca}(\vec{r},\omega) = -\frac{1}{2\pi}\sum_i \frac{1}{\lambda_1+1} f_i(\omega)\langle \vec{n}\cdot\vec{E}^{ext}(\omega), \phi^i(\vec{r})\rangle \phi^i(\vec{r}) \quad \textbf{[VI.5]}$$

where $\vec{n}$ denotes the unit vector located at position $\vec{s}$ on the boundary of the object, normal to the boundary, and pointing outwards. In the above equation, we define

$$f_i(\omega) = \frac{\lambda_i+1}{\lambda_i-\lambda(\omega)} \quad \textbf{[VI.6]}$$

where

$$\lambda(\omega) = \frac{1+\epsilon(\omega)}{1-\epsilon(\omega)} \quad \textbf{[VI.7]}$$

and

$$\langle \vec{n}\cdot\vec{E}^{ext}(\omega), \phi^i(\vec{r})\rangle = \oint_\partial d\vec{s}\vec{n}\cdot\vec{E}^{ext}(\omega), \phi^i(\vec{s})^* \quad \textbf{[VI.8]}$$

where

$$\phi_i(\vec{r}) = \oint_\partial \frac{\sigma_i(\vec{s})}{|\vec{r}-\vec{s}|} d\vec{s} \quad \textbf{[VI.9]}$$

is the eigenpotential of mode *i*. Expanding each eigenpotential in the dipolar approximation within equation **[VI.5]**, one can express the far-field scattered electric potential as

$$\phi_{FF}^{sca}(\vec{r},\omega) = -\frac{1}{|\vec{r}|^2}\vec{p}(\omega)\cdot\vec{e}_r + o\left(\frac{1}{|\vec{r}|^2}\right) \quad \textbf{[VI.10]}$$

where $\vec{e}_r$ is a unit vector along the direction of $\vec{r}$,

$$\vec{p}(\vec{r}) = -\frac{1}{2\pi}\sum_{i=d} \frac{1}{\lambda_i+1} f_i(\omega)\langle \vec{n}\cdot\vec{E}^{ext}(\omega), \phi^i(\vec{r})\rangle \vec{p}_i \quad \textbf{[VI.11]}$$

and

$$\vec{p}_i = \oint_{\partial} \sigma_i(\vec{s})\vec{s}d\vec{s} \quad \textbf{[VI.12]}$$

is the dipole moment of mode i. Notice that the sum runs only over dipolar modes, for which $\vec{p}_i \neq \vec{0}$. As seen from the far field, the illuminated particle is thus equivalent to a dipole of moment $\vec{p}(\omega)$. The extinction and absorption cross-sections are thus given by[8]

$$C_{abs}(\omega) = -\frac{4\pi}{|E^{ext}(\omega)|} k\mathrm{Im}\{\vec{p}(\omega) \cdot \vec{E}^{ext}(\omega)\} \quad \textbf{[VI.13]}$$

$$C_{sca}(\omega) = \frac{8\pi}{3} k^4 |\vec{p}(\omega)|^2 \quad \textbf{[VI.14]}$$

where $k = \frac{\omega}{c}$ is the free space wave vector. Introducing here the expression for $\vec{p}(\omega)$given by quation **[VI.11]**, the extinction and scattering cross-section reduce to:

$$C_{abs}(\omega) = \frac{2}{c}\frac{1}{|E^{ext}(\omega)|}\omega \sum_{i=d} \frac{1}{\lambda_i + 1} \mathrm{Im}\{f_i(\omega)\}\langle \vec{n} \cdot \vec{E}^{ext}(\omega), \phi^i(\vec{r})\rangle \, \vec{p}_i \cdot \vec{E}^{ext}(\omega) \quad \textbf{[VI.15]}$$

$$C_{sca}(\omega) \approx \frac{2}{3\pi c^4}\omega^4 \sum_{i=d} \frac{1}{(\lambda_i + 1)^2} |f_i(\omega)|^2 \left|\langle \vec{n} \cdot \vec{E}^{ext}(\omega), \phi^i(\vec{r})\rangle \, \vec{p}_i\right|^2 \quad \textbf{[VI.16]}$$

In the expression for the scattering cross-section, we have neglected the crossed terms involving the interaction between different modes in $|\vec{p}(\omega)|^2$ because in most situations the spectral response $f_i(\omega)$ are well separated.

VI.1.2. Fast-Electron-Based Spectroscopies

In a classical dynamic approach, the energy lost by a fast electron interacting with a dielectric object is described by the work performed against the electron by a scattered electric field. Considering the electron as a point-like charge moving with constant velocity $\vec{v}$ along a straight-line trajectory $\vec{r} = \vec{r}_e(t) = (\vec{R}^{\perp}, z)$, the electron energy-loss (EEL) probability is given by:[9]

$$_{EELS}\left(\vec{R}^{\perp}, \omega\right) = \frac{e}{\pi\hbar\omega} \int dt\, \Re\left\{e^{-i\omega t}\vec{v} \cdot \vec{E}_{el}^{sca}(\vec{r}_e(t), \omega)\right\} \textbf{[VI.17]}$$

where $-e$ is the charge of the electron and $\vec{v}$ is its velocity. $\vec{E}_{el}^{sca}(\vec{r}, \omega)$ is the electron-induced electric field expressed in time-Fourier space. Likewise, the cathodoluminescence (CL) probability is related to the electromagnetic energy radiated into the far field, and can be calculated from:[9]

$$_{CL}\left(\vec{R}^{\perp}, \omega\right) = \frac{1}{4\pi^2\hbar k} \int_{4\pi} \left|\vec{f}_{el}(\vec{e}_r, \omega)\right| d\ \ \vec{e}_r \textbf{[VI.18]}$$

where

$$\vec{E}_{FF}^{sca}(\vec{r}, \omega) = \lim_{r\to}\ \vec{E}_{el}^{sca}(\vec{r}, \omega) = \frac{e^{ikr}}{r}\vec{f}_{el}(\vec{e}_r, \omega) \textbf{[VI.19]}$$

Is the far-field electron induced electric field. Following the notation introduced in the previous section and adopting the quasistatic approximation, the electron-induced electric field is obtained by inserting into the Poisson equation a source term $\rho_{el}(\vec{r}, \omega)$ given by

$$\rho_{el}(\vec{r}, \omega) = -\frac{e}{v}\delta\left(\vec{R} - \vec{R}^{\perp}\right)e^{i\omega z/v} \textbf{[VI.20]}$$

(i.e., a time-Fourier transformed electron charge distribution). The solution of the Poisson equation thus reads[2]

$$\phi(\vec{r}, \omega) = \phi_{el}^{ext}(\vec{r}, \omega) + \phi_{el}^{sca}(\vec{r}, \omega) \textbf{[VI.21]}$$

where

$$\phi_{el}^{ext}(\vec{r},\omega) = \int d\vec{r}\ \frac{\rho_{el}(\vec{r}\,',\omega)}{\epsilon(\vec{r}\,',\omega)|\vec{r}-\vec{r}\,'|} \quad \textbf{[VI.22]}$$

is a source screened electric potential,

$$\phi_{el}^{sca}(\vec{r},\omega) = \oint_{\partial} d\vec{s}\ \frac{\sigma_{el}(\vec{s},\omega)}{|\vec{r}-\vec{s}|} \quad \textbf{[VI.23]}$$

is the electron-induced electric potential, and $\sigma_{el}(\vec{s},\omega)$ is the electron-induced surface charge. Expressing the electron-induced electric potential as:

$$\phi_{el}^{sca}(\vec{r},\omega) = \int d\vec{r}\ \ G(\vec{r},\vec{r}\,',\omega)\rho_{el}(\vec{r}\,',\omega) \quad \textbf{[VI.24]}$$

where $G(\vec{r},\vec{r}\,',\omega)$ is the scalar Green function satisfying, if $\vec{r}$ does not belong to the object, the modal decomposition:[4]

$$G(\vec{r},\vec{r}\,',\omega) = -\sum_i f_i(\omega)\phi_i(\vec{r})\phi_i^*(\vec{r}\,') \quad \textbf{[VI.25]}$$

One finds, when considering an electron trajectory that does not penetrate the object

$$\phi_{el}^{sca}(\vec{r},\omega) = \frac{e}{v}\sum_i f_i(\omega)\tilde{\phi}_i^*(\vec{R}^{\perp},\tfrac{\omega}{v})\,\phi_i(\vec{r}) \quad \textbf{[VI.26]}$$

where $\tilde{\phi}_i^*(\vec{R}^{\perp},\frac{\omega}{v})$ is the Fourier transform of $\phi_i(\vec{r})$ along z. Writing the induced electric field as $\vec{E}_{el}^{sca}(\vec{r},\omega) = -\vec{\nabla}\phi_{el}^{sca}(\vec{r},\omega)$, the EEL probability thus reads[4]

$$_{EELS}\left(\vec{R}^{\perp},\omega\right) = \frac{e^2}{\pi\hbar v^2}\sum_i \mathrm{Im}\left\{f_i(\omega)\right\}\left|\tilde{\phi}_i(\vec{R}^{\perp},\tfrac{\omega}{v})\right|^2 \quad \textbf{[VI.27]}$$

Expanding again each eigenpotential in the dipolar approximation within equation **[VI.26]**, one can express the far-field scattered electric potential as

$$\phi_{el,FF}^{sca}(\vec{r},\omega) = \frac{1}{|\vec{r}|^2}\vec{p}\left(\vec{R}^{\perp},\omega\right)\cdot\vec{e}_r + o\left(\frac{1}{|\vec{r}|^2}\right) \textbf{[VI.28]}$$

where

$$\vec{p}\left(\vec{R}^{\perp},\omega\right) = \frac{e}{v}\sum_{i=d} f_i(\omega)\tilde{\phi}_i^*(\vec{R}^{\perp},\tfrac{\omega}{v})\vec{p}_i \textbf{[VI.29]}$$

is the electron-induced dipole moment. Although we calculate this dipole in the electrostatic limit, we can still use it to express the scattering amplitude as:[10]

$$\vec{f}_{el}(\vec{e}_r,\omega) = -k^2\vec{e}_r\times\vec{p}\left(\vec{R}^{\perp},\omega\right)\times\vec{e}_r \textbf{[VI.30]}$$

The CL probability thus results from the electron-induced dipole moment as

$$_{\mathrm{CL}}\left(\vec{R}^{\perp},\omega\right) = \frac{1}{4\pi^2\hbar}k^3\int_{4\pi}\left|\vec{p}\left(\vec{R}^{\perp},\omega\right)\right|^2 d\ \ _{\vec{\mathrm{e}}\mathrm{r}} \textbf{[VI.31]}$$

Where $\vec{p}_{\perp}\left(\vec{R},\omega\right) = \vec{p}\left(\vec{R},\omega\right) - \vec{e}_r\cdot\vec{p}\left(\vec{R},\omega\right)\cdot\vec{e}_r$ is the transverse component of the electron-induced dipole moment. Inserting equation **[VI.29]** into equation **[VI.31]** and neglecting the crossed terms $f_i(\omega)f_j(\omega)^*$ with $i\neq j$, the CL probability finally reduces to

$$_{CL}\left(\vec{R}^{\perp},\omega\right) \approx \frac{1}{4\pi^2v^2\hbar c^3}\omega^3\sum_{i=d}|f_i(\omega)|^2\left|\int_{4\pi}\vec{p}_{i\perp}\,d\ \ _{\vec{\mathrm{e}}\mathrm{r}}\right|^2\left|\tilde{\phi}_i(\vec{R}^{\perp},\tfrac{\omega}{v})\right|^2 \textbf{[VI.32]}$$

where $\vec{p}_{i\perp} = \vec{p}_i - \vec{e}_r\cdot\vec{p}_i\,\vec{e}_r$ is the transverse component of the dipole moment of mode *i*.

VI.1.3. Interpretation: Drude Model

We here draw some interpretations of the above modal decomposition when considering a general ideal case. For a given mode, the rosanance energies as measured by the techniques depend on the dielectric properties of the medium through $f_i(\omega)$.

We examine what happens for model SP modes by considering an ideal metal object surrounded by vacuum. In order to do this, we take $\epsilon(\omega)$ as a Drude dielectric function:

$$\epsilon(\omega) = 1 - \frac{\omega_p^2}{\omega^2 + i\ \omega} \textbf{ [VI.33]}$$

where ω_p is the bulk plasmon frequency and is a phenomenological damping rate. We than find:

$$f_i(\omega) = \frac{\tilde{\omega}_i^2}{\tilde{\omega}_i^2 - \omega^2 - i\ \omega} \textbf{ [VI.34]}$$

where:

$$\tilde{\omega}_i = \sqrt{1+\lambda_i}\frac{\omega_p}{\sqrt{2}} \textbf{ [VI.35]}$$

Verifies $\lambda(\tilde{\omega}_i) = \lambda_i$ in the particular case $= 0$. The imaginary part and square modulus of $f_i(\omega)$ thus read:

$$\mathrm{Im}\{f_i(\omega)\} = \frac{\tilde{\omega}_i^2 \omega}{^2\omega^2 + (\omega^2 - \tilde{\omega}_i^2)^2} \textbf{ [VI.36]}$$

$$|f_i(\omega)|^2 = \frac{\tilde{\omega}_i^4}{^2\omega^2 + (\omega^2 - \tilde{\omega}_i^2)^2} \textbf{ [VI.37]}$$

Making the damping rate tend to zero, we note that:

$$\log_{\ \to 0} \mathrm{Im}\{f_i(\omega)\} = \delta(\omega - \tilde{\omega}_i) \textbf{ [VI.38]}$$

$$\log_{\ \to 0} |f_i(\omega)|^2 = \delta(\omega - \tilde{\omega}_i) \textbf{ [VI.39]}$$

With no dissipation, a dipolar mode is thus resonant at its eigenenergy irrespective of the technique. However, in a general case of non-zero dissipation, $\mathrm{Im}\{f_i(\omega)\} \propto \omega|f_i(\omega)|^2$, which implies that the maximum of $\mathrm{Im}\{f_i(\omega)\}$is blueshifted with respect to the maximum of $|f_i(\omega)|^2$. However, taking into account the right energy dependent prefactors of the modal decompositions, we note that a spectrally isolated dipole mode actually contributes to $_{EELS}(\vec{R}^{\perp},\omega) \sim \frac{1}{\omega^2}\ _{CL}(\vec{R}^{\perp},\omega)$ and $C_{ext}(\omega) \sim \frac{1}{\omega^2} C_{sca}(\omega)$. Therefore, the CL (scattering) resonance of such mode is predicted to be blueshifted relative to its EELS (extinction) resonance. We note a similar conclusion has already been drawn for extinction and scattering, using a classical harmonic oscillator model, in Ref.[11]. Finally, this model shows that the magnitude of the shift between $\mathrm{Im}\{f_i(\omega)\}$ and $|f_i(\omega)|^2$, andm by extension, between EELS and CL and extinction and scattering, directly depends on the amount of dissipation. This is exemplified by the resonance energies plotted as a function of the damping rate shown in **Figure VI.2**. In this particular example, we consider a single mode with $\widetilde{\omega}_i = 2.0$ eV and neglect the frequency dependence of the Fourier transform of the eigenpotential in EELS and CL expressions.

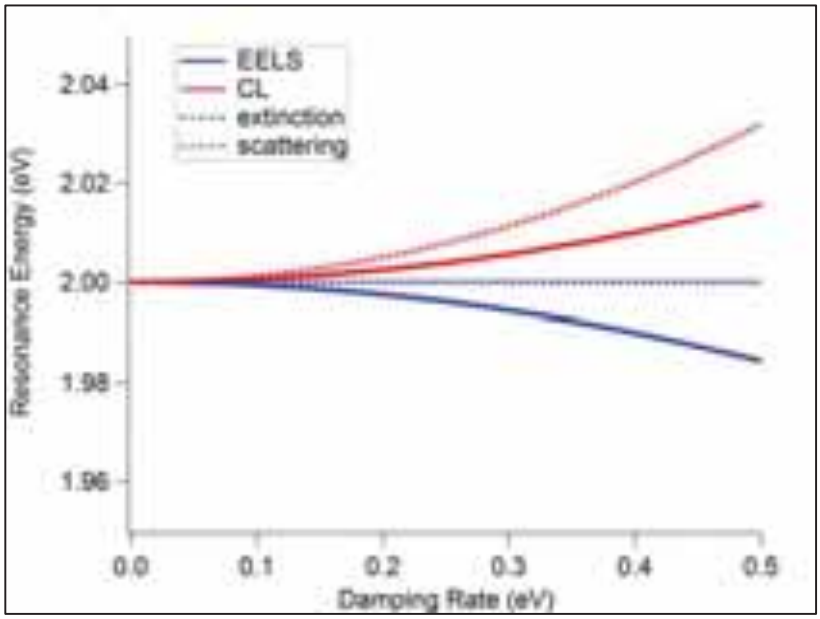

Figure VI.2: EELS, CL, extinction and scattering resonance energies as a function of damping rate. We take $\widetilde{\omega}_i = 2.0$ eV.

VI.2. REFERENCES

(1) Ouyang, F.; Isaacson, M. *Philos. Mag. B* **1989**, *60* (4), 481–492.
(2) De Abajo, F. G.; Aizpurua, J. *Phys. Rev. B* **1997**, *56* (24), 15873.
(3) Hohenester, U.; Ditlbacher, H.; Krenn, J. R. *Phys. Rev. Lett.* **2009**, *103* (10), 106801.
(4) Boudarham, G.; Kociak, M. *Phys. Rev. B* **2012**, *85* (24), 245447.
(5) Hörl, A.; Trügler, A.; Hohenester, U. *Phys. Rev. Lett.* **2013**, *111* (7), 076801.
(6) Stockman, M. I.; Faleev, S. V.; Bergman, D. J. *Phys. Rev. Lett.* **2001**, *87* (16), 167401.
(7) Shalaev, V. M.; Sarychev, A. K. *Phys. Rev. B* **1998**, *57* (20), 13265–13288.
(8) Bohren, C. F.; Huffman, D. R. *Absorption and scattering of light by small particles*; John Wiley & Sons, 2008.
(9) De Abajo, F. G. *Rev. Mod. Phys.* **2010**, *82* (1), 209.
(10) John David Jackson. *Classical Electrodynamics*; **1999**.
(11) Kats, M. A.; Yu, N.; Genevet, P.; Gaburro, Z.; Capasso, F. *Opt. Express* **2011**, *19* (22), 21748–21753.

CHAPTER

VII

RESUMEN

Síntesis y auto-ensamblaje racional de nanopartículas plasmónicas anisótropas.

VII.1. OBJETIVOS

Este trabajo de tesis se ha llevado a cabo dentro del proyecto ERC Advanced Grant *Plasmaquo* (nº 267867), centrado en el desarrollo de nuevos materiales plasmónicos nanoestructurados basados en ensamblajes cristalinos de nanopartículas anisótropas, para ser utilizados como potenciadores ópticos en espectroscopía Raman para la detección de moléculas de señalización entre bacterias (Quorum Sensing). El enfoque principal ha sido el desarrollo de nuevas rutas sintéticas y el auto-ensamblaje de nanoparticulas de oro y plata, con la intencion de controlar sus propiedades plasmónicas. En particular, la capacidad de ensamblar nanopartículas en nanoestructuras ordenadas se basa en una estrecha dispersión de tamaños en los bloques constituyentes ("building blocks"). Por lo tanto, la primera parte del trabajo experimental se dedica a la optimización de los diversos procedimientos de síntesis. Dado que el objetivo final es la aplicación de estas nanoestructuras en espectroscopía Raman mejorada en superficie (SERS), nuestros esfuerzos sintéticos se centraron en nanopartículas de oro y plata: mientras que la plata presenta mejores propiedades plasmónicas, el oro es químicamente más inerte y resistente a la oxidación, y ofrece una gama más amplia de posibilidades sintéticas. El auto-ensamblaje de los componentes básicos de síntesis se ha optimizado para controlar la formación de nanoestructuras con diferentes tamaños y formas en grandes áreas (en el orden de centímetros cuadrados). Asimismo, se ha dado importancia al bajo coste y la reproducibilidad en la fabricación de los dispositivos. La parte experimental se llevó a cabo principalmente en el Laboratorio de Bionanoplasmónica de CIC biomaGUNE en Donostia-San Sebastián (España), complementado por dos periodos de estancia de investigación en la Universidad de Hamburgo (Alemania) y en la Universidad de Rice, en Houston (Estados Unidos de América). Es importante destacar que parte de los resultados incluidos en esta tesis han surgido de colaboraciones con grupos externos, principalmente en relación a la interpretación teórica de los resultados y los estudios por tomografía electrónica avanzada, así como el análisis plasmónico por técnicas de microscopía electrónica. Gracias a la experiencia complementaria de nuestro laboratorio y de nuestros colaboradores, hemos sido capaces de desarrollar protocolos sintéticos mejorados para la síntesis química de

diferentes tipos de nanopartículas plasmónicas, así como para poner en práctica su autoensamblaje dirigido en nanoestructuras plasmónicas para el diseño de biosensores.

En el Capítulo II, se comienza presentando un panorama general del estado de la técnica para la síntesis de nanopartículas anisótropas de metales nobles, seguido por la presentación de los protocolos sintéticos optimizados. Se investigó el efecto de la adición de ácido 5-bromosalicílico en la síntesis de nanorods oro monocristalinos, explotando sus propiedades reductoras como un nuevo método para ajustar la relación de aspecto de los nanorods (sección II.2.7). Se propone además un nuevo enfoque para el sobrecrecimiento controlado de nanopartículas de oro, basado en su redispersión en una disolución de precursor de oro pre-reducido. En la sección II.3 se describe la optimización de la síntesis de nanotriángulos de oro a través del control del grado de maclado en las semillas de oro. Por último, en la sección II.4 mostramos la deposición selectiva de plata sobre las puntas de nanorods de oro pentamaclados, introduciendo el concepto de crecimiento controlado lineal de nanocables. Mediante una velocidad de deposición de plata constante, se encontró que la longitud de los cables aumenta linealmente con el tiempo, lo cual nos permite suprimir reacciones colaterales y producir nanocables longitudes de hasta varias micras de una manera altamente controlada y sin pérdida de calidad.

En el capítulo III se aborda el autoensamblaje de nanopartículas. Se empaquetaron nanorods de oro monocristalinos en supercristales con altura variable (hasta varias micras). Hemos explotado las propiedades superficiales de los nanorods mediante recubrimiento con un tiol neutro, así como el secado confinado en un molde de PDMS. Bajo condiciones experimentales adecuadas, los nanorods se organizan en fases esmécticas extendidas, con la mayoría de los nanorods dispuestos con sus ejes largos perpendiculares al sustrato (sección II.1). Estos supercristales presentan una alta concentración de puntos calientes (“hot spots”), haciendo de estos sustratos candidatos de interés para aplicaciones en espectroscopía Raman mejorada en superficie (SERS).

Por último, en el capítulo IV centramos nuestra atención en la caracterización de nanoestructuras plasmónicas. Se realizó el análisis de partículas individuales para

nanotriángulos (sección IV.2.1) y nanocables bimetálicos de plata-oro-plata (sección IV.2.2). Se realizó una comparación experimental usando espectroscopia por pérdida de energía de electrones y catodoluminiscencia sobre las mismas partículas, lo cual ha permitido su correlación con los conceptos de campo lejano clásico de extinción y secciones eficaces de dispersión. En el caso de los nanocables bimetálicos de plata-oro-plata, la espectroscopia por pérdida de energía de electrones nos permitió investigar la influencia de los núcleos de oro sobre las propiedades ópticas de los nanoantenas plasmónicas. En la sección IV.2.3, se analizan las propiedades de campo cercano de los supercristales formados por nanorods de oro, centrando nuestra atención en la relación entre el número de capas y la distribución de los puntos calientes. Se demuestra que aumentando el número de capas de nanorods no se garantiza un aumento en la magnitud del campo eléctrico en la capa superior de los supercristales.

En su conjunto, esta tesis presenta un avance significativo, tanto en la síntesis como en el auto-ensamblaje de diferentes nanopartículas plasmónicas anisótropas. Los resultados presentados podrían tener importantes aplicaciones en campos diversos, como la nanomedicina, los biosensores o la catálisis.

VII.2. INTRODUCCIÓN

La nanotecnología puede representar el mayor salto tecnológico en la historia humana, proporcionando soluciones innovadoras a los muchos desafíos que amenazan nuestro futuro: promete ordenadores más rápidos, más seguridad, una vida más larga y saludable y una tierra más limpia. La nanotecnología "tiene que ver con sistemas cuyas estructuras y componentes ofrecen propiedades, fenómenos y procesos físicos, químicos y biológicos, nuevos y mejorados debido a su tamaño nanométrico" (US National Nanotechnology Initiative).[1] Entre todas las propiedades dependientes del tamaño, la aparición de plasmones en la nanoescala es probablemente uno de los efectos más importantes. La plasmónica se ha convertido en una de las ramas más activas de la nanotecnología, con la promesa de realizar contribuciones significativas en muchos campos diferentes, como la energía, la medicina, los biosensores, la electrónica, etc.[2–13] Estos plasmones dependen de la naturaleza del metal, del

tamaño de partícula, de su geometría, de las moléculas que se encuentren en su superficie y de las propiedades dieléctricas del medio. Además, los plasmones se pueden acoplar entre sí cuando dos partículas se sitúan a una distancia suficientemente cerca, incrementando la intensidad del campo eléctrico generada en la zona intermedia entre las partículas (formación de "hot-spots"). Esto es de gran interés de cara a la espectroscopía de dispersión Raman aumentada (SERS), como técnica de detección de moléculas ultrasensible. Estas características han sido la base para un enorme desarrollo en el campo de la Química Coloidal para la obtención de nanopartículas con composición, tamaño y geometría determinados, y también por su auto-ensamblaje en nanoestructuras ordenadas. La anisotropía no sólo ofrece una herramienta versátil para afinar la respuesta óptica de las nanopartículas de oro y plata, a través de variaciones en sus LSPRs, sino también importantes cambios en la conductividad electrónica a través de efectos de confinamiento, y sobre la actividad catalítica a través de la disponibilidad de caras de alto índice cristalino que pueden facilitar la adsorción y reacciones que no son posibles en otras superficies.[14–24] Las nanopartículas de metales nobles existen en una amplia variedad de formas, que van desde sólidos platónicos a nanoestructuras ramificadas o irregulares. [16,19,24–30] La **Figura VII.1** muestra las principales tipos de formas en nanopartículas anisotrópicas.

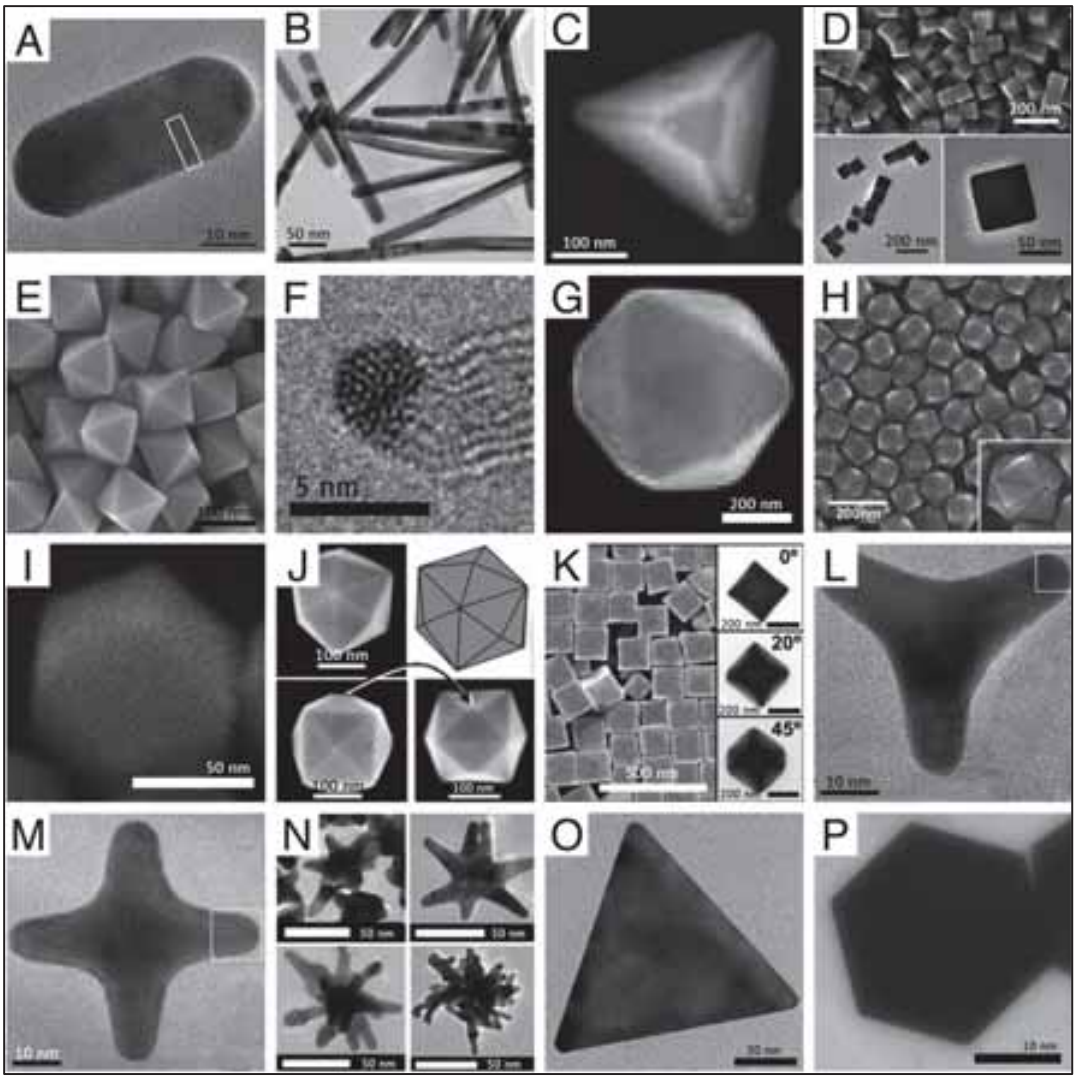

Figura VII.1: Las principales formas de nanopartículas de metales nobles observadas mediante microscopía electrónica de transmisión (TEM) y de barrido (SEM): A: nanorod de oro monocristalino, **B:** nanorod de oro pentamaclado, **C:** tetraedro de oro, **D:** cubo de paladio, **E:** octaedros de oro, **F:** decaedro de oro, **G:** icosaedro de oro, **H:** trisoctaedros de oro, **I:** dodecaedro rómbico de oro, **J:** tetrahexaedro de platino, **K:** hexaedro cóncavo de oro, **L:** trípodo de oro, **M:** tetrápodo de oro, **N:** nanoestrella de oro, **O:** triángulo o prisma de oro, and **P:** placa hexagonal de oro. Adaptado de **A:** Ref. 31, **C & G:** Ref. 26, **D:** Ref. 27, **E:** Ref. 32, **F:** Ref. 33, **H:** Ref. 34, **I:** Ref. 35, **J:** Ref. 36, **K:** Ref. 37, **L & M:** Ref. 38, **N:** Ref. 39, **O:** Ref. 40, and **P:** Ref. 41**.**

Un punto de inflexión histórico en el desarrollo de la síntesis eficiente de nanopartículas anisotropicas ha sido la introducción del concepto de crecimiento mediado por semillas. El crecimiento mediado por semillas es una síntesis muy versátil. Este método implica la síntesis de pequeñas semillas de nanopartículas metálicas (con forma esférica) en combinación con una disolución de crecimiento que contiene una sal de oro y surfactantes, provocando crecimiento anisótropo.[42–44] De esta manera, la nucleación y el crecimiento de los cristales anisótropos están separados temporal y físicamente, lo cual permite un control muy preciso sobre la forma de nanopartículas.[14,19,42–47] La morfología del producto final depende de distintos factores, incluyendo el tamaño y la forma de la semilla, la concentración de los distintos componentes de la solución de crecimiento y la relación entre la sal metálica y el reductor en la disolución de crecimiento.[14,16,20,24,28,42] La síntesis de nanopartículas de alta calidad es crucial para su auto-ensamblaje en nanoestructuras complejas. El interés en este campo ha crecido porque el auto-ensamblaje es reconocido como una de las estrategias más generales para la generación de nanoestructuras ordenadas,[48–51] con posibles aplicaciones en microelectrónica,[52] fotónica,[53,54] u óptica de campo cercano,[55] entre otros. La última década ha sido testigo de una intensa actividad en el campo, que ha llevado al desarrollo de numerosas estrategias diferentes para la producción de estructuras ordenadas utilizando “building blocks” en la escala nanométrica y micrométrica. Para definir auto-ensamblaje debemos tener en cuenta algunas características esenciales:

1) La estructura obtenida debe presentar un cierto grado de orden.
2) El conjunto se logra mediante el equilibrio entre las interacciones de atracción y repulsión, dividido en corta[56,57] y larga distancia.[58–60]
3) La existencia de un diseño. Los “building blocks” se eligen para obtener una estructura particular, explotando las propiedades que están codificadas en los propios building-blocks.[57,61–69]

De esta forma, el auto-ensamblaje de nanopartículas de metales nobles puede ser visto como "ingeniería de plasmones y hot-spots", con aplicaciones prometedoras para la detección

óptica de una amplia variedad de analitos (metales pesados,[70,71] oligonucleótidos,[72] aminoácidos,[73,74] proteínas,[75] agentes patógenos,[76] o toxinas[77]), SERS,[78–85] metamateriales,[86–88] y fotovoltaica.[89] Los impresionantes avances en la síntesis y el auto-ensamblaje de una amplia gama de nanoobjetos con nuevas propiedades ópticas han exigido el desarrollo de nuevas técnicas de caracterización que permitan el análisis de sistemas nanométricos con mayor detalle.[90–94] La comprensión de las propiedades plasmónicas de nanoestructuras de metales nobles requiere el estudio de sus propiedades ópticas y su correlación con el tamaño de partícula, forma, composición y química superficial.[90,91,95] La posibilidad de relacionar las propiedades estructurales y ópticas a nivel de un nanoobjeto aislado es pues crucial para la comprensión y el desarrollo de los fenómenos ópticos en la escala nanométrica.

VII.3. NANORODS DE ORO

Los nanorods de oro han sido el primer ejemplo de nanoestructura plasmónica anisótropa sintetizada por química "húmeda".[8] Desde principios de los años 2000, los nanorods de oro han recibido una atención creciente a causa de sus propiedades ópticas y plasmónicas ajustables, que los hacen candidatos ideales para una amplia gama de aplicaciones, tales como la fotovoltaica,[96] espectroscopias mejoradas en superficies, [7,97] detección[6,7,60] y terapia[2,98]. El mecanismo de formación de los nanorods de oro sigue suscitando gran interés, ya que un modelo general nos permitiría identificar el diseño de una ruta sintética para cada nanoestructura.[16,24,99,100] En la sección II.2.7 se propone un sistema con dos agentes reductores que comprende una combinación de ácido salicílico y ascórbico. Mientras que el ácido salicílico pre-reduce Au(III) a Au(I) en la disolución de crecimiento, el ácido ascórbico participa en la reducción autocatalítica de Au(I) a Au(0), que se produce de forma selectiva sobre la superficie metálica. Hemos demostrado que este sistema de dos agentes reductores ofrece nuevas posibilidades hacia la adaptación de la morfología y las propiedades ópticas de nanorods de oro (**Figura VII.2**).

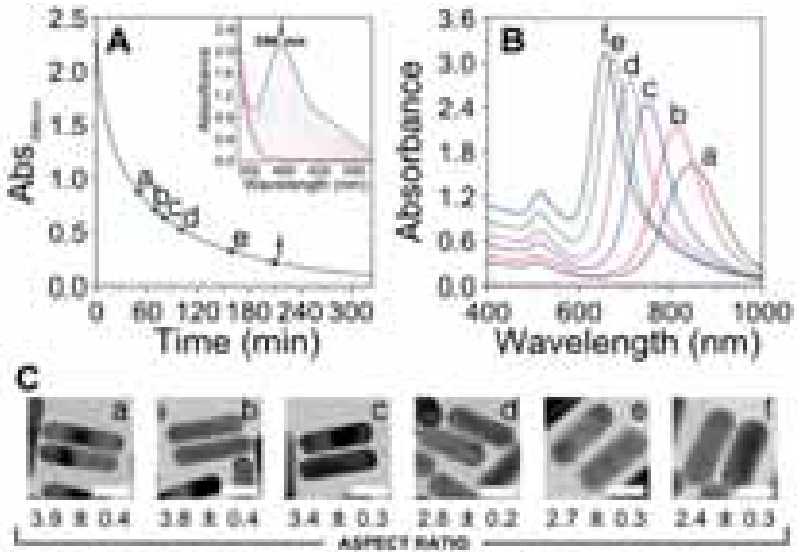

Figura VII.2. El grado de pre-reducción por acido salicílico afecta tanto a la relación de aspecto como a la cantidad de oro reducida. A: Estudio cinético del paso de pre-reducción (recuadro: espectros UV-vis completos). **B:** Espectros UV-vis-NIR de los diversos coloides de nanorods obtenidos cambiando el tiempo de pre-reducción. Abs_{396nm}: 0.88 (a); 0.71 (b); 0.64 (c); 0.53 (d); 0.33 (e); 0.22 (f) **C:** Imágenes de TEM representativas de nanorods obtenidos con diferentes tiempos de pre-reducción (las etiquetas corresponden a los de los espectros en **B**). Barras de escala: 20 nm

Nuestras observaciones indican que el ácido salicílico influye en la reacción de crecimiento tanto cinéticamente como termodinámicamente, inhibiendo el crecimiento isótropo y contribuyendo al desplazamiento hacia el azul observado en la síntesis de nanorods monocristalinos de oro. Cuando no se ha completado la reducción durante la síntesis, se puede inducir la reducción completa del precursor de oro a través de la adición de ácido ascórbico, sin renunciar a la posibilidad de ajustar la relación de aspecto de los nanorods. Aparte de los nuevos conocimientos mecanicistas de estos resultados, las propiedades reductoras del ácido salicílico pueden ser explotadas para estabilizar nanorods de oro en disoluciones de Au(I). Hemos demostrado que el sobrecrecimiento puede llevarse a cabo en presencia de iones Ag^+, estabilizando de este modo la anisotropía, es decir, evitando una transición de rod a octaedro, como se obtiene, por ejemplo, en el sobre-crecimiento en ausencia de plata (**Figura VII.3**). Esto sugiere la posibilidad de adaptar las dimensiones y propiedades ópticas de nanorods de oro mediante la selección de las condiciones apropiadas para el sobrecrecimiento.

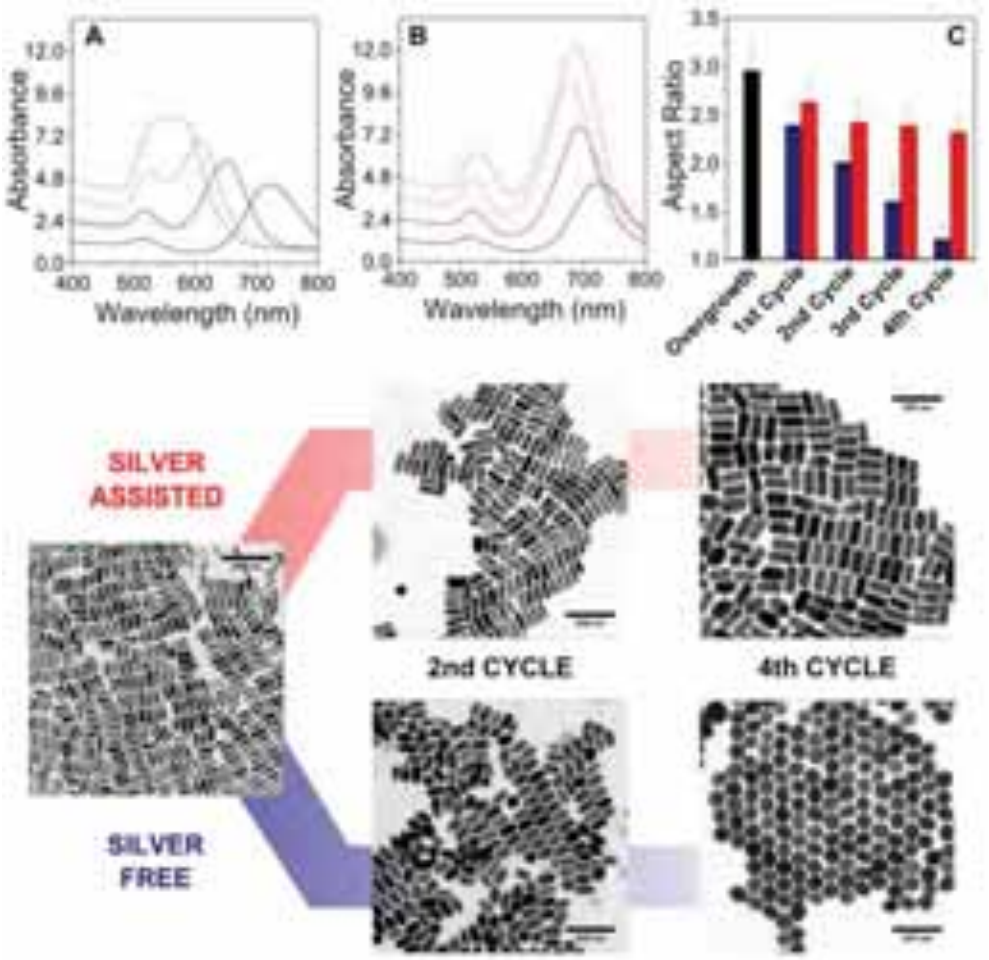

Figura VII.3. Panel superior: Espectro UV-vis-NIR después de cada paso de sobrecrecimiento. **A:** caso sin plata; **B:** caso con plata. Los espectros de color negro corresponden al punto de partida común para las reacciones de sobrecrecimiento. **C:** Evolución de la relación de aspecto para cada ciclo de sobrecrecimiento para los dos casos: sin (azul) y con (rojo) plata. **Panel inferior:** Imágenes de TEM que muestran la evolución de la forma de la muestra inicial (imagen central-izquierda) después de dos y cuatro ciclos sin (línea azul) y con (línea roja) plata. Barras de escala: 200 nm.

Combinando el auto-ensamblaje de nanopartículas de oro y la capacidad de diseño de superficies por medio de técnicas de litografía blanda, hemos desarrollado un método sencillo que nos ha permitido crear supercristales de nanorods de oro sobre sustratos arbitrarios en un solo paso. Para hacer frente a los problemas de reproducibilidad que muestran los métodos existentes en literatura, se utilizó un molde hecho del elastómero PDMS con cavidades de tamaño micrométrico. Estas cavidades ayudan a regular la evaporación del coloide de nanopartículas de oro directamente sobre un sustrato de interés.

Este nos permite tener un alto grado de control sobre la morfología de los supercristales y al mismo tiempo modificar la topografía del sustrato en aéreas de centímetros cuadrados (**Figura VII.4A**). Los nanorods de oro sintetizados han sido funcionalizados con MUDOL, un ligando anfífilo terminado en grupo tiol y soluble en agua, conocido por inducir fases esmécticas tras la evaporación del disolvente.[58,101] Para la formación de los ensamblajes, se depositó una gota de suspensión de nanorods de oro entre el molde y un sustrato plano (vidrio, silicio o rejillas de TEM revestidas de carbono), dejándolo secar durante varias horas bajo condiciones de temperatura y humedad típicas de laboratorio. Posteriormente, la plantilla de PDMS se retiró cuidadosamente, obteniendo líneas de supercristales bien definidos con dimensiones que replican los de las cavidades del molde. En comparación con el método de "drop casting" se puede observar claramente una notable mejoría en la homogeneidad y en la distribución ordenada de los supercristales. Para investigar la organización de los "building blocks" dentro de los supercristales, se llevó a cabo un análisis detallado de la estructura interna por ablación parcial de los supercristales usando litografía de iones focalizados (FIB, de sus siglas en inglés) en combinación con microscopía electrónica de barrido de alta resolución (HR-SEM, de sus siglas en inglés) para obtener imágenes de la sección transversal de los supercristales (**Figura VII.4D**). Este método, denominado "Slice & View" permite la representación en 3D de la estructura de la muestra. La mayoría de los nanorods de oro se han encontrado de pie, con sus ejes largos perpendiculares al sustrato, y se observó un alto grado de orden de largo alcance inter e intra-lamelar (**Figura VII.4E**).

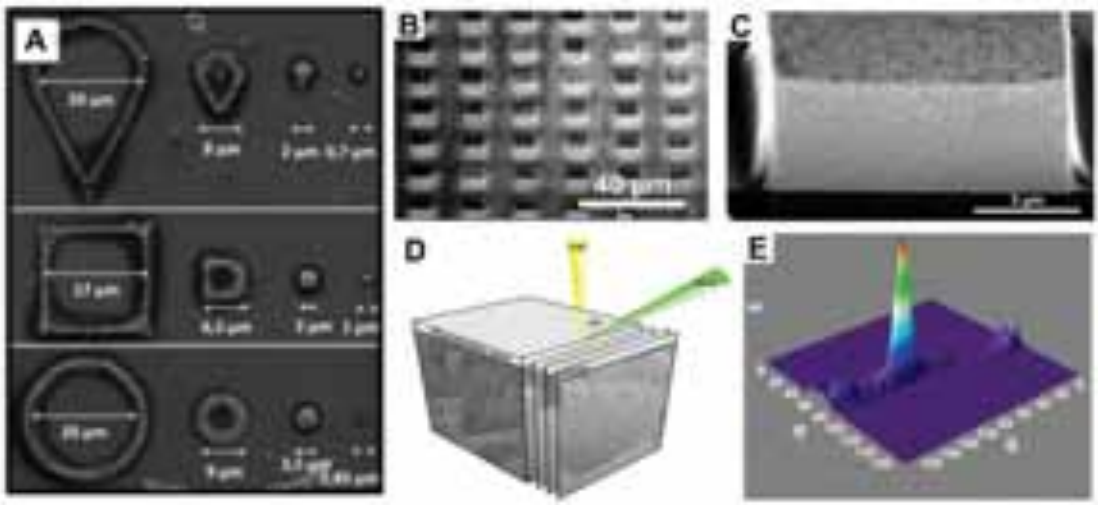

Figura VII.4. Supercristales de nanorods de oro formados por ensamblaje usando un molde de PDMS. A: Imágenes de SEM que muestran la topografía del sustrato a escala nanométrica. B-C: Caracterización por SEM a diferentes magnificaciones de supercristales de nanorods de oro obtenidos a partir de cavidades de 12 micras y [Au^0] inicial de 375 mM. Se pueden observar claramente grandes dominios de nanorods de oro orientados en la misma dirección. D: Representación esquemática de la técnica Slice&View, utilizada para la reconstrucción en 3D de la organización espacial de los nanorods de oro dentro de los supercristales. E: Mapa de dispersión de la orientación, que revela la distribución de la orientación de los nanorods.

Además, los sustratos estructurados se utilizaron como plataforma de detección, con una respuesta SERS homogénea e intensa para todos los diferentes tamaños y formas de los supercristales. Por otra parte, la alta estabilidad química de los nanorods de oro nos permitió almacenar los sustratos durante meses, lo cual es importante de cara a la fabricación de dispositivos para aplicaciones en biomedicina. En general, la reproducibilidad, la lectura óptica rápida, la alta sensibilidad, junto con la simplicidad de fabricación, hacen estos ensamblajes altamente atractivos para el diseño de las plataformas de detección de alto rendimiento. Con el fin de optimizar la preparación de los supercristales para su aplicación en SERS, es necesario caracterizar adecuadamente sus propiedades plasmónicas. La correlación precisa de la estructura y propiedades ópticas se hace más complicada cuando se trata de grandes ensamblajes en lugar de nanopartículas individuales, debido a la gran cantidad de interacciones entre los "building blocks". Por ejemplo, aunque se había sugerido una relación entre la altura de los supercristales (es decir, el número de capas apiladas de nanorods de oro) y el factor de mejora (EF, de sus siglas en inglés) de estas arquitecturas, es

necesario un estudio sistemático que incluya simulaciones detalladas.[114,116,117] Hemos realizado un estudio detallado de la respuesta SERS de supercristales con diferente número de capas de nanorods de oro. Nuestro análisis correlaciona SEM/STEM y AFM, así como espectroscopia de dispersión Raman, caracterizando la organización y las propiedades ópticas de los supercristales. Los resultados experimentales se complementaron por una implementación especial del método numérico de onda completa ("full-wave numerical method") de reciente introducción en el contexto de la nanoplasmónica.[121] Este método nos permitió simular supercristales compuestos por decenas de miles de nanorods de oro, prediciendo con precisión la respuesta de dispersión de un sistema plasmónico complejo con cajas de simulación realistas en cuanto a dimensión. La estructura y la organización local de los nanorods dentro de los supercristales se investigaron en detalle, tal como se resume en la **Figura VII.5**. El orden hexagonal de los nanorods dentro de la capa se observó por SEM (**Figura VII.5A**), AFM, HAADF-STEM y tomografía electrónica (**Figura VII.5B - F**). La caracterización tridimensional de los supercristales por tomografía electrónica confirmó el desplazamiento de las capas de nanorods de oro, de tipo A-B-A, dato que se ha utilizado para las simulaciones de cara a la interpretación de sus propiedades ópticas. Además, se observaron patrones de interferencia tipo Moiré en imágenes de multicapas debidos a un pequeño grado de desplazamiento rotacional entre capas vecinas,[102,103] lo cual demuestra la simetría cuasi-cristalina de los ensamblajes en multicapas de nanorods de oro. Se encontró que los patrones de interferencia Moiré son diferentes en distintos supercristales (**Figura VII.5D – E**), lo que significa que el ángulo de desplazamiento entre dos capas no siempre es el mismo. Esto sugiere un mecanismo de formación de las superestructuras por ensamblaje de capas ordenadas de nanorods en solución, seguido de un proceso de deposición en el que cada monocapa se coloca encima de la anterior.[102]

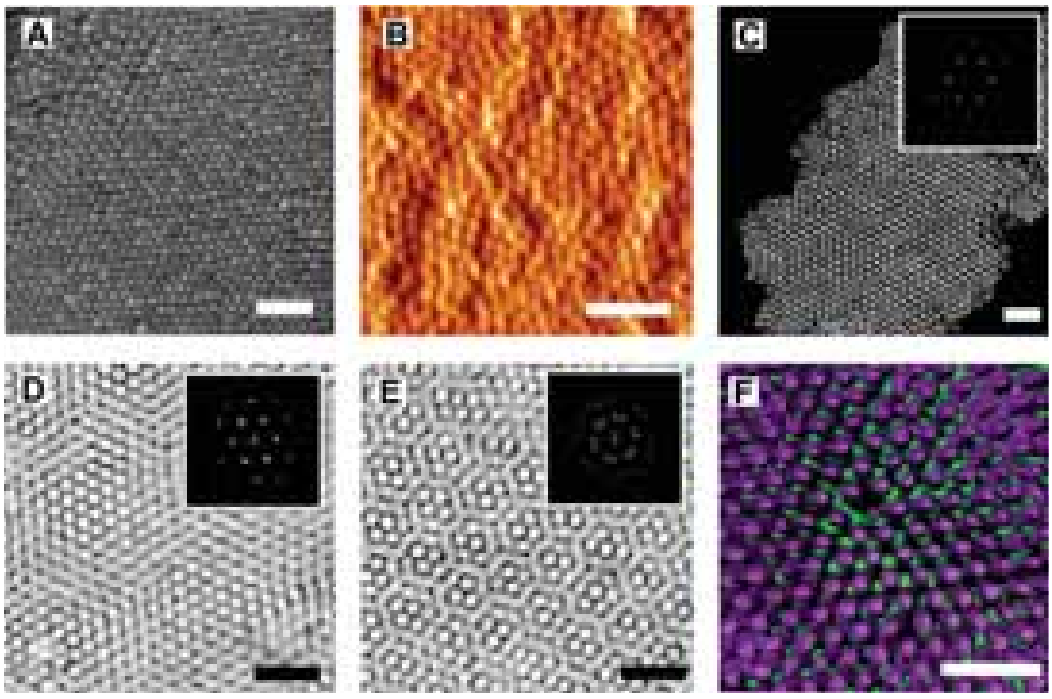

Figura VII.5. Caracterización de supercristales de nanorods de oro. A: Imagen SEM de la superficie superior de un supercristal. **B:** Imagen AFM de la superficie superior de un supercristal. **C-E:** Imágenes HAADF-STEM de diferentes supercristales, depositados encima de una película de SiN, incluyendo una monocapa (**C**) y dos bicapas diferentes (**D - E**). Se muestran los patrones de FFT de las imágenes. **F:** Reconstrucción por tomografía electrónica de una bicapa de nanorods de oro que muestra la capa superior de color morado y la capa inferior de color verde. Todas las barras de escala son de 100 nm.

Las propiedades ópticas de los supercristales se investigaron también a través de su rendimiento en SERS, tal como se muestra en la **Figura VII.6**. El colorante orgánico Violeta Cristal (de sus siglas en inglés, CV) fue seleccionado como un modelo de analito debido a su química y características físicas bien conocidas. Es importante mencionar que las medidas de SERS se realizaron antes de la caracterización estructural, ya que tanto el haz de electrones en SEM como la punta de AFM podrían depositar cargas, contaminar o dañar la superficie de los supercristales. Los resultados demuestran que un aumento en el número de capas de un supercristal de nanorods de oro no representa necesariamente un beneficio para la señal de SERS. De hecho, medidas de SERS adicionales en supercristales que comprenden hasta nueve capas de nanorods muestran que en todos los casos la intensidad máxima SERRS es uniforme, independientemente del número total de capas (**Figura VII.6C**).

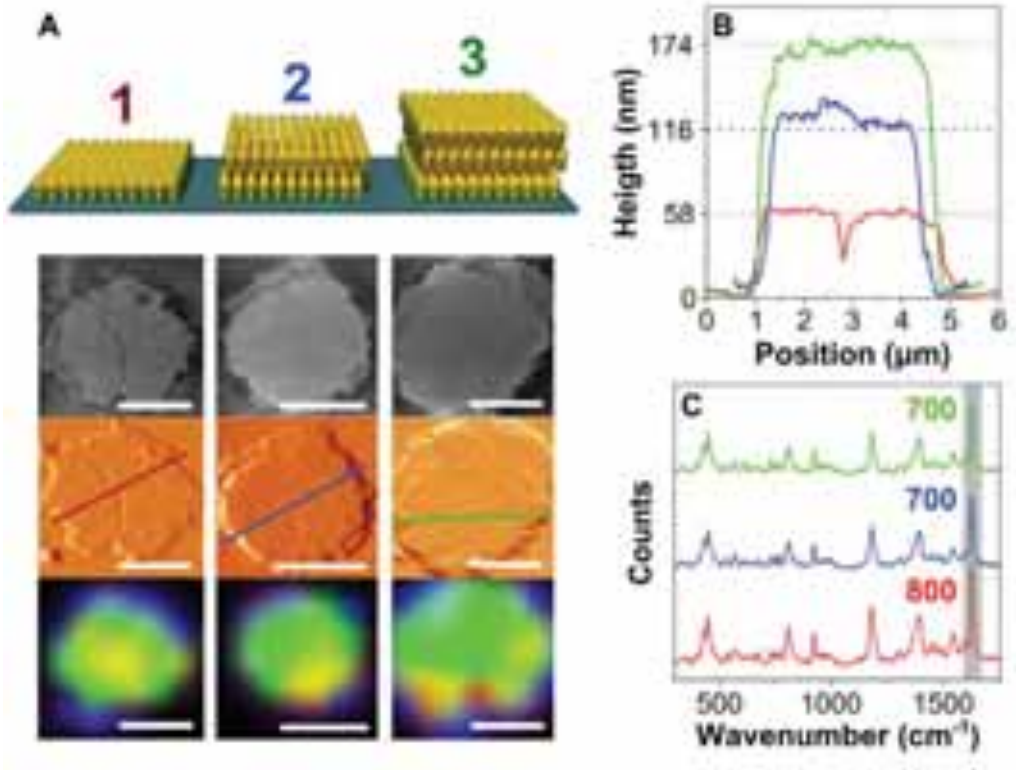

Figura VII.6. Caracterización óptica de supercristales de nanorods de oro con 1, 2 y 3 capas. A: Esquemas que representan supercristales compuestos de 1, 2 y 3 capas, junto con (de arriba a abajo): SEM, AFM e imágenes SERRS. Las imágenes SERRS se obtuvieron mediante la asignación de la intensidad SERRS del pico de vibración de CV sobre 1618-1632 cm^{-1}. En todas las imágenes las barras de escala son 2 micras. **B:** Perfiles de altura de una monocapa (rojo), una bicapa (azul) y una tricapa (verde), a lo largo de las líneas que se muestran en la imagen de AFM en **A**; las líneas de puntos indican los valores esperados para mono, bi y tricapas. **C:** Espectros SERRS de CV medidos en una monocapa (rojo), bicapa (azul) y tricapa (verde). El área gris indica el rango espectral integrado para la generación de las imágenes de SERRS en **A**.

En general, los resultados fueron interpretados considerando una profundidad corta de penetración del analito entre los nanorods, y solamente en la capa superior de todos los supercristales. Creemos que una posible mejora en el diseño de estos supercristales que permitiese la difusión del analito en todo el supercristal podría producir señales de SERS significativamente más intensas, allanando así el camino para la fabricación de dispositivos plasmónicos de próxima generación, no sólo en el diseño de sensores, sino también en otros campos, como los sistemas de catálisis o de colección de luz.

VII.4. NANOTRIÁNGULOS DE ORO

El rendimiento de los métodos habituales de síntesis de nanotriángulos de oro suele ser inferior a 30 - 40% y las partículas a menudo muestran una amplia distribución de tamaños. Por otra parte, estas nanopartículas presentan baja estabilidad frente a la oxidación, por lo que suelen cambiar de forma a las pocas horas después de su preparación.[104] Todos estos factores han obstaculizado seriamente la aplicación de nanotriángulos para el desarrollo de dispositivos plasmónicos. En el caso de nanotriángulos de oro, el crecimiento anisótropo se activa por la presencia de iones yoduro en una disolución de crecimiento que no contiene plata, a partir de semillas recubiertas por CTAC. En la sección II.3, proponemos un nuevo protocolo sintético que produce nanotriángulos con un mayor rendimiento (> 50%) y con dispersión en tamaños de hasta el 4%. Aunque el presente método de síntesis permite mejorar significativamente el rendimiento y la distribución de tamaños, todavía se obtiene una cantidad importante de subproductos, dificultando el uso directo de estos nanotriángulos para aplicaciones que requieren alta calidad de partículas y bandas plasmónicas estrechas. Por lo tanto, hemos introducido una etapa de purificación, tratando de eliminar dichos subproductos. La purificación por las llamadas "depletion forces" presenta numerosas ventajas, ya que permite aumentar el volumen de producción fácilmente, es selectiva en forma y tamaño, relativamente rápida y altamente eficiente. Estos aspectos nos permitieron purificar nanotriángulos de oro de una manera simple y rápida, alcanzando un rendimiento final en la forma del 95% (**Figura VII.7C**). Además, pequeñas variaciones del protocolo sintético nos permiten cambiar el tamaño de los nanotriángulos entre 50 y 150 nm (**Figura VII.7B**), lo cual se traduce en valores de LSPR desde 630 hasta 740 nm (**Figura VII.7A**).

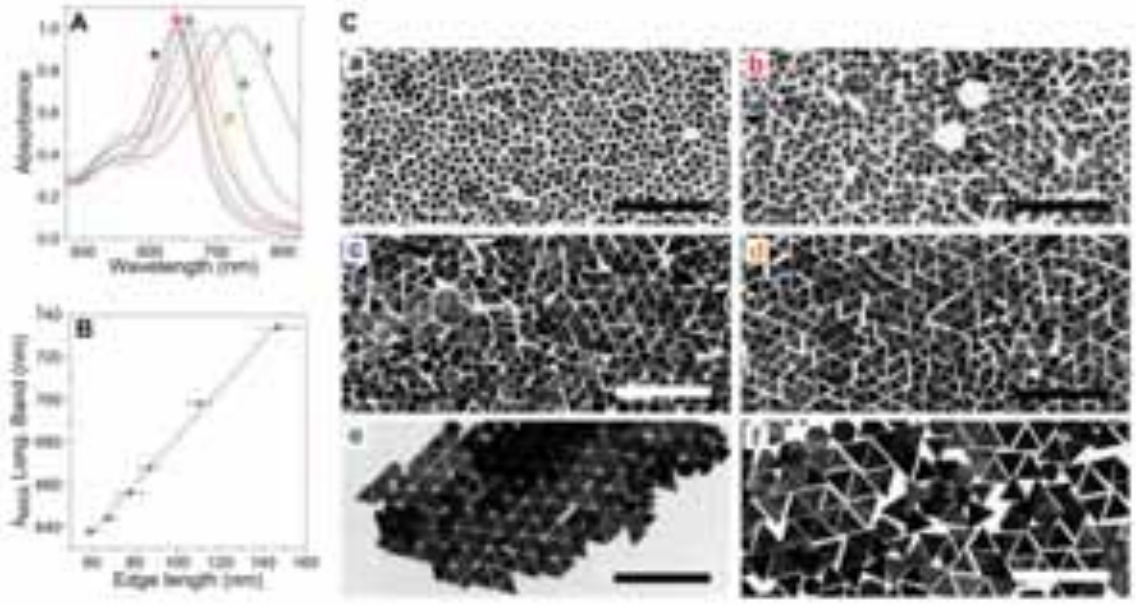

Figura VII.7. Ajuste del tamaño de nanotriángulos de oro A: Espectros correspondientes a las muestras purificadas, obtenidas con diferentes cantidades de semilla: (a): 1,2 mL, (b): 800 µL, (c): 600 µL, (d): 400 µL, (e) 200 µL y (f): 100 µL. Todos los espectros se normalizaron en el máximo de su LSPR. **B:** Correlación lineal entre la longitud del lado de los nanotriángulos de oro y el máximo de su LSPR, con coeficiente de Pearson R^2> 0.994. **C:** Imágenes TEM de nanotriángulos de oro purificados, de diferentes tamaños. Las etiquetas corresponden a las utilizadas en **A.** Barras de escala: 500 nm.

La posibilidad de sintetizar nanotriángulos tan pequeños nos ofrece la posibilidad de estudiar sus propiedades plasmónicas por catodoluminiscencia (CL) y EELS, interpretando los resultados bajo la aproximación cuasiestática. Se realizaron medidas de los mismos triángulos con las dos técnicas, lo cual nos ha permitido comparar de forma inequívoca ambas señales (**Figura VII.8A**). Este procedimiento difiere significativamente de los publicados anteriormente, donde medidas de CL y EELS estaban realizadas en nanopartículas relacionadas pero distintas,[105] ya que incluso pequeños cambios en las dimensiones o el medio ambiente pueden cambiar significativamente las energías de los modos plasmonicos,[95] y por lo tanto poner en peligro cualquier comparación cuantitativa entre CL y EELS. Los resultados nos permitieron clasificar directamente los modos plasmónicos en radiativos y no radiativos. Hemos demostrado que con EELS es posible medir ambos tipos de modos plasmónicos, mientras CL sólo permite medir los modos radiativos (**Figura VII.8B**). Además, un modo radiativo, dependiendo del tamaño y el

sustrato, puede ser observable a diferentes energías de resonancia en EELS y CL, concepto que ha sido demostrando teóricamente desde hace varios años.[106–108] Estos resultados están de acuerdo con simulaciones electromagnéticas por BEM (**Figura VII.8B**), que también indican que tales diferencias espectrales se deben a la disipación de la luz y son similares a los observados entre la extinción óptica y la dispersión de luz. Estas conclusiones se pueden extrapolar a partículas más grandes, por lo que el presente trabajo arroja luz sobre la recuperación experimental de información espectral y espacial de plasmones.

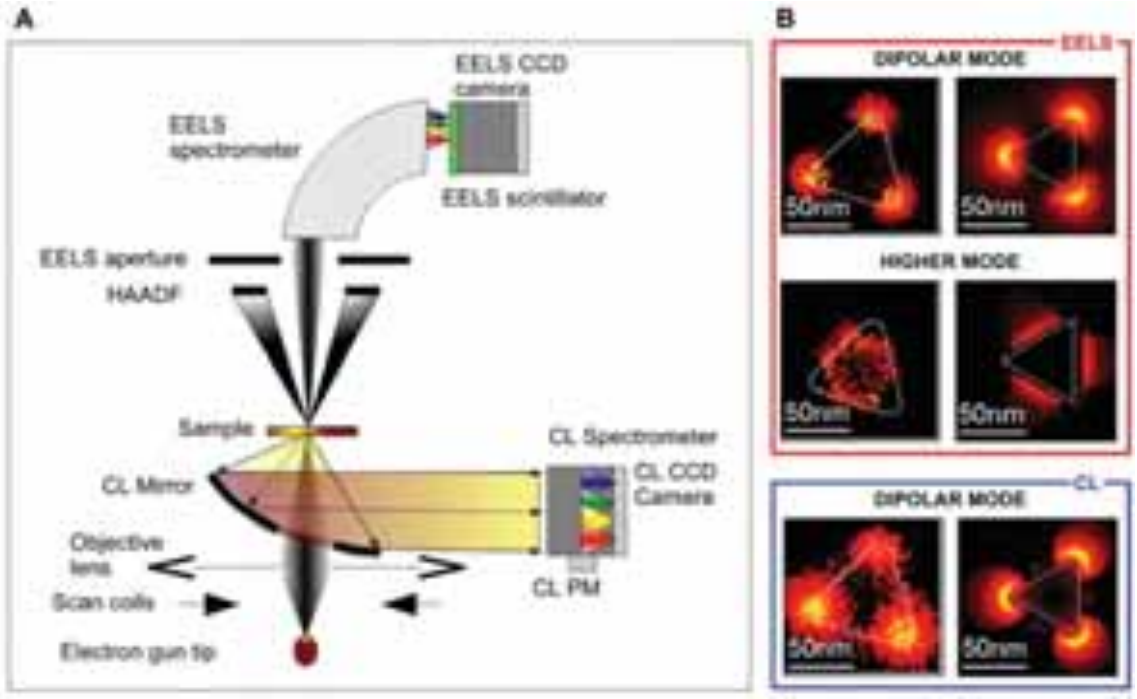

Figura VII.8. A: Esquema de un STEM equipado con sistemas de detección de CL y EELS. **B:** Mapas de amplitud correspondientes a medidas experimentales (izquierda) y simuladas por BEM (derecha) del modo dipolar (EELS y CL) y de los modos de orden superior (EELS). EELS y CL fueron normalizados a sus máximos independientemente. Las líneas blancas superpuestas en los mapas indican la forma del prisma obtenida de la imagen HAADF.

VII.5. NANOCABLES BIMETÁLICOS DE PLATA-ORO-PLATA

En la sección II.4 se presenta la optimización del recubrimiento con plata de nanorods de oro pentamaclados para la síntesis de nanoantenas plasmónicas de alta calidad con actividad plasmónica en el infrarrojo cercano y medio. Mantener una distribución estrecha de tamaños se hace más difícil cuando se aumenta la anisotropía, por lo que hemos desarrollado el concepto de "controlled living nanowire growth" análogo a la "controlled living polymerization reaciton" (CLPR).[109] Controlando la adición de precursores de plata por medio de un dispositivo que utiliza una bomba de jeringa, hemos conseguido un crecimiento lineal de plata sobre los núcleos de oro. Este procedimiento nos permitió evitar la nucleación de nanopartículas de plata durante el crecimiento de los nanocables y mejorar así de forma significativa la uniformidad en tamaño del producto, y predecir con precisión las dimensiones finales del sistema bimetálico. Como resultado, se obtuvieron coloides de nanocables de plata-oro-plata que presentan hasta nueve picos plasmónicos bien definidos, distribuidos sobre todo el intervalo de longitudes de onda visible-NIR, con un control estricto sobre la longitud total de los nanocables, hasta varias micras, correspondiente a relaciones de aspecto por encima de 100 (**Figura VII.9A - E**). Al comparar los factores de calidad ("Q-factors") experimentales con los obtenidos a partir de los espectros simulados por BEM, los espectros calculados dan valores sólo un 25% mayores en comparación con los experimentales (**Figura VII.9F - G**). Esto pone de relieve claramente la baja distribución de tamaño de las muestras obtenidas.

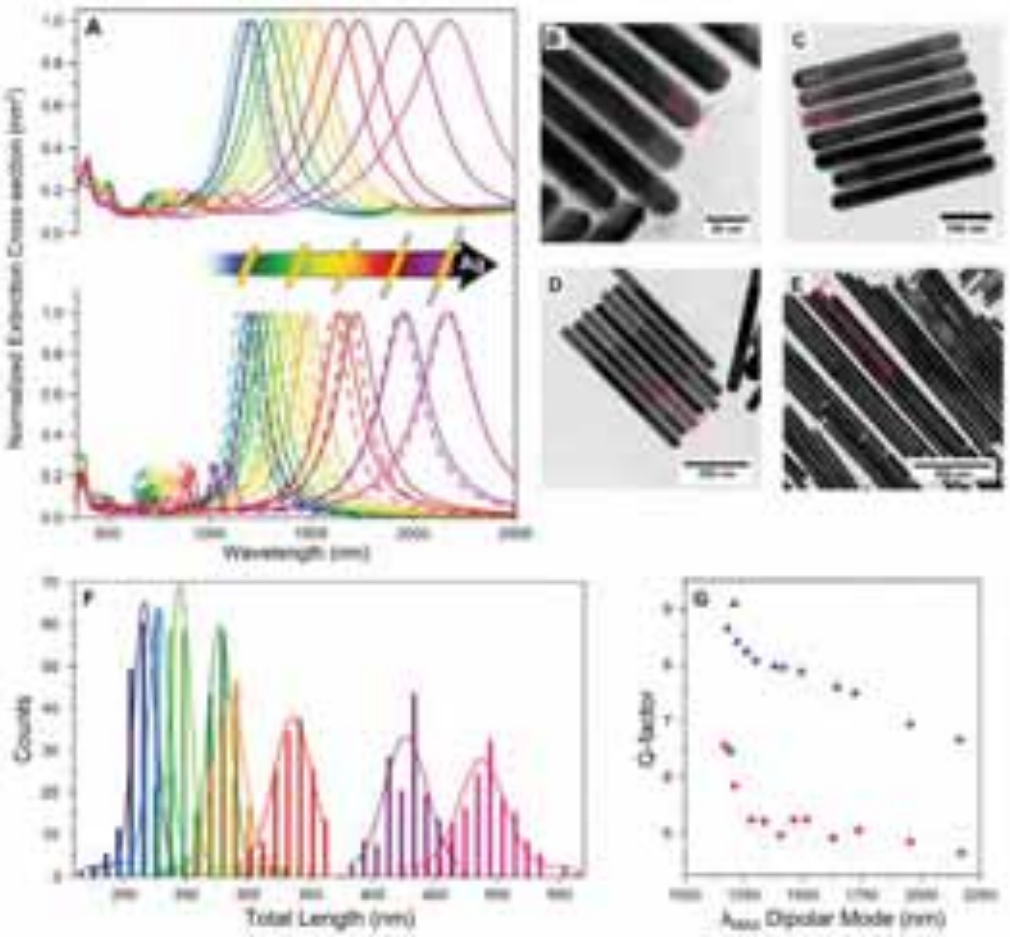

Figura VII.9. A: Panel superior: Espectros Vis-NIR registrados durante el crecimiento de plata; el nanorod de oro se muestra como una curva de puntos negros; **Panel Inferior:** Espectros de extinción calculados por BEM con (curvas continuas) y sin (curvas de trazos) núcleo de oro. Las dimensiones de los nanocables corresponden a las experimentales (el mismo código de color). **B-E:** Imágenes de TEM de cuatro muestras con valores diferentes de *AgEn*: = 0.72, 1.2, 2.4, 11.52, correspondientes a un crecimiento de plata por cada punta de 33 ± 6 nm, 61 ± 9 nm, 130 ± 20 nm y 660 ± 90 nm, y resonancias de plasmón dipolares longitudinales respectivamente en 1405 nm, 1630 nm y 2170 nm. El plasmón dipolar para **E** está más allá de nuestro rango espectral de medida. **F:** Histogramas de distribución de la longitud total de las 8 muestras mostradas en **A** (mismo código de color). **G:** Evolución del factor de calidad de la banda plasmónica dipolar experimental (diamantes de color rosa) en función de su energía. Esta tendencia es confirmada por cálculos de BEM (triángulos azules). El círculo negro es el factor de calidad de los núcleos de oro iniciales.

Para explotar eficientemente el confinamiento electromagnético de campo cercano y poner en práctica la aplicación de antenas ópticas, es útil tener una comprensión detallada de la relación entre la estructura de las nanoantenas y las distribuciones espaciales/espectrales de los diferentes modos plasmonicos.[107,110] Hemos realizado un estudio estructural y óptico correlacionado de diferentes muestras de nanocables bimetálicos para entender la influencia del núcleo de oro en las propiedades ópticas (**Figura VII.10**). Se analizaron los espectros de extinción óptica de nanocables en disoluciones de agua pesada **(Figura VII.9B)** y se ha hecho un análisis detallado por TEM (**Figura VII.10A, C**) y EELS (**Figuras VII.10D**). Ambos métodos experimentales fueron complementados por cálculos de BEM, en presencia y en ausencia del núcleo de oro.

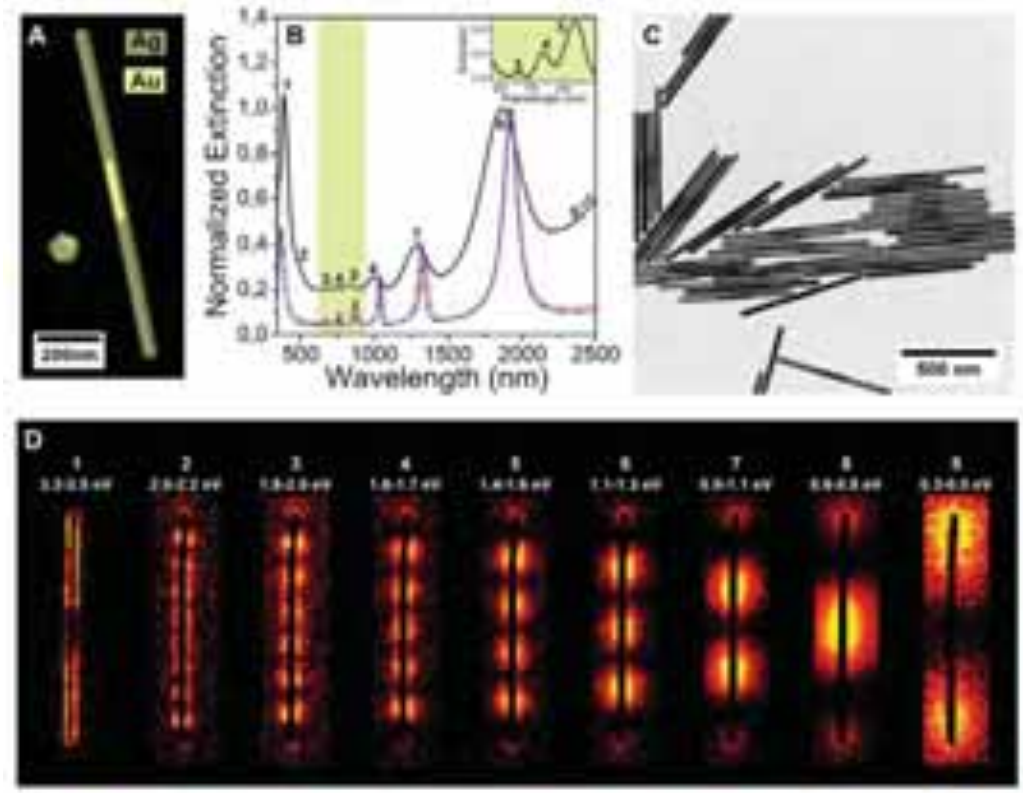

Figura VII.8 A: Reconstrucción por tomografía electrónica de un nanocable, con vista frontal (izquierda) y lateral (derecha): los colores verde y amarillo corresponden a la plata y el oro, respectivamente. **B:** Espectro vis-NIR de una disolución coloidal de nanocables largos (Ag_{en} = 5,3, línea negra) en comparación con los espectros simulados en presencia (rojo) y ausencia (azul) del núcleo de oro. Recuadro: zoom del área marcada en verde para discernir los modos 5, 6 y 7. **C:** Imagen TEM representativa que muestra la estrecha distribución de tamaños de los nanocables bimetálicos preparados. **D:** Distribución espacial de los modos plasmónicos medida por EELS; los números se refieren a los mismos modos que en **B**.

La caracterización EELS nos ha permitido identificar todas las bandas plasmónicas encontradas en el análisis UV-vis-NIR (**Figura VII.10B, D**). Hemos sido capaces de demostrar que el núcleo de oro no interfiere con la propagación de plasmones superficiales en nanocables largos, mientras que su influencia se limita a los modos de energía más altos. Este procedimiento abre nuevas posibilidades para la explotación de las resonancias plasmónicas en las regiones del IR cercano y medio.

VII.6. CONCLUSIONES GENERALES

El trabajo descrito en esta tesis aborda diversos aspectos relacionados con el control sintético del tamaño, forma y composición de nanopartículas, así como su uso para el diseño de nanoestructuras auto-ensambladas con aplicaciones en biosensores basados en dispersión Raman aumentada en superficie. Aunque se han extraído conclusiones específicas en cada sección, se pueden destacar las siguientes conclusiones generales:

1) NANORODS DE ORO MONOCRISTALINOS
   a) Se ha diseñado un nuevo protocolo sintético para la preparación de nanorods de oro monocristalinos: se pueden ajustar la relación de aspecto y las dimensiones de las nanopartículas explotando las propiedades reductoras del ácido 5-bromosalicílico.
   b) Aprovechando la estrecha distribución de tamaños y el alto rendimiento en geometría de los coloides obtenidos, se prepararon supercristales de nanorods de oro monocristalinos por medio del uso de moldes, con cierto control sobre la altura y la forma de los supercristales. Las nanoestructuras producidas presentan un alto grado de orden interno, con las nanopartículas alineadas preferentemente en dirección perpendicular al sustrato.
   c) A fin de elucidar las propiedades plasmónicas de dichas nanoestructuras hemos realizado una extensa correlación estructural y óptica sobre varios supercristales. Esto nos ha permitido demostrar que la suposición de que el número de capas se correlaciona con las propiedades de aumento de campo, no está justificada. Se propone que la alta densidad de hot-spots en estas estructuras sólo se puede aprovechar si los analitos pueden difundir al interior de los supercristales.

2) NANOTRIANGULOS DE ORO

   a) Hemos desarrollado el primer protocolo sintético que permite preparar nanotriángulos de oro con un rendimiento en la geometría comparable al de los nanorods, lo cual requiere una etapa de purificación.

   b) Se ha analizado el comportamiento plasmónico de nanotriángulos individuales mediante EELS y catodoluminiscencia. Gracias a su pequeño tamaño (menor de 60 nm en lado) sus propiedades plasmónicas se pueden interpretar usando la aproximación cuasiestática. Esto nos ha permitido demostrar que EELS puede ver modos plasmónicos brillantes y oscuros, mientras que la catodoluminiscencia solo revela los modos radiativos. Hemos demostrado también una relación directa entre EELS y extinción por una parte y entre catodoluminiscencia y scattering por otra.

3) NANOCALBES DE PLATA-ORO-PLATA

   a) Hemos introducido el concepto de ·controlled living nanowire growth", el cual nos ha permitido obtener un alto grado de control sobre la reducción de plata en las puntas de nanorods de oro pentamaclados. En particular, se ha forzado una cinética de orden cero usando un sistema microfluídico, evitando así reacciones colaterales y forzando una relación lineal entre la cantidad de precursor añadida y la longitud final de los nanocables bimetálicos.

   b) Se han analizado también las propiedades plasmónicas de nanoantenas individuales por EELS. La interpretación de los resultados mediante métodos numéricos ha permitido investigar la influencia del núcleo de oro sobre las propiedades plasmónicas de estas nanoestructuras bimetálicas.

VII.7. REFERENCIAS

(1) Washington, D.C.: National Science and Technology Council, Committee on Technology, Subcommittee on Nanoscale Science, Engineering and Technology 2000.
(2) de Aberasturi, D. J.; Serrano-Montes, A. B.; Liz-Marzán, L. M. *Adv. Opt. Mater.* **2015**, *3* (5), 602–617.
(3) Hamon, C.; Liz-Marzán, L. M. *Chem. - Eur. J.* **2015**, *21* (28), 9956–9963.
(4) Chen, H.; Shao, L.; Li, Q.; Wang, J. *Chem. Soc. Rev.* **2013**, *42* (7), 2679–2724.
(5) Pérez-Juste, J.; Pastoriza-Santos, I.; Liz-Marzán, L. M.; Mulvaney, P. *Coord. Chem. Rev.* **2005**, *249* (17–18), 1870–1901.
(6) Vigderman, L.; Khanal, B. P.; Zubarev, E. R. *Adv. Mater.* **2012**, *24* (36), 4811–4841.
(7) Langer, J.; Novikov, S. M.; Liz-Marzán, L. M. *Nanotechnology* **2015**, *26* (32), 322001.
(8) Huang, X.; Neretina, S.; El-Sayed, M. A. *Adv. Mater.* **2009**, *21* (48), 4880–4910.
(9) Guerrero-Martínez, A.; Barbosa, S.; Pastoriza-Santos, I.; Liz-Marzán, L. M. *Curr. Opin. Colloid Interface Sci.* **2011**, *16* (2), 118–127.
(10) Huang, X.; El-Sayed, I. H.; El-Sayed, M. A. *Methods Mol. Biol. Clifton NJ* **2010**, *624*, 343–357.
(11) Li, N.; Zhao, P.; Astruc, D. *Angew. Chem. Int. Ed.* **2014**, *53* (7), 1756–1789.
(12) Lohse, S. E.; Murphy, C. J. *J. Am. Chem. Soc.* **2012**, *134* (38), 15607–15620.
(13) Thorkelsson, K.; Bai, P.; Xu, T. *Nano Today* **2015**, *10* (1), 48–66.
(14) Dreaden, E. C.; Alkilany, A. M.; Huang, X.; Murphy, C. J.; El-Sayed, M. A. *Chem. Soc. Rev.* **2012**, *41* (7), 2740–2779.
(15) Eustis, S.; El-Sayed, M. A. *Chem. Soc. Rev.* **2006**, *35* (3), 209–217.
(16) Grzelczak, M.; Pérez-Juste, J.; Mulvaney, P.; Liz-Marzán, L. M. *Chem. Soc. Rev.* **2008**, *37* (9), 1783–1791.
(17) Kennedy, L. C.; Bickford, L. R.; Lewinski, N. A.; Coughlin, A. J.; Hu, Y.; Day, E. S.; West, J. L.; Drezek, R. A. *Small* **2011**, *7* (2), 169–183.
(18) Kumar, S.; Nann, T. *Small* **2006**, *2* (3), 316–329.
(19) Lim, B.; Xia, Y. *Angew. Chem. Int. Ed.* **2011**, *50* (1), 76–85.
(20) Lohse, S. E.; Murphy, C. J. *Chem. Mater.* **2013**, *25* (8), 1250–1261.
(21) Tao, A. R.; Habas, S.; Yang, P. *Small* **2008**, *4* (3), 310–325.
(22) Sardar, R.; Funston, A. M.; Mulvaney, P.; Murray, R. W. *Langmuir* **2009**, *25* (24), 13840–13851.
(23) Zhang, H.; Jin, M.; Xiong, Y.; Lim, B.; Xia, Y. *Acc. Chem. Res.* **2013**, *46* (8), 1783–1794.
(24) Langille, M. R.; Personick, M. L.; Zhang, J.; Mirkin, C. A. *J. Am. Chem. Soc.* **2012**, *134* (35), 14542–14554.
(25) Huang, M. H.; Chiu, C.-Y. *J. Mater. Chem. A* **2013**, *1* (28), 8081.
(26) Kim, F.; Connor, S.; Song, H.; Kuykendall, T.; Yang, P. *Angew. Chem. Int. Ed.* **2004**, *43* (28), 3673–3677.
(27) Niu, W.; Zhang, L.; Xu, G. *ACS Nano* **2010**, *4* (4), 1987–1996.
(28) Sau, T. K.; Rogach, A. L. *Adv. Mater.* **2010**, *22* (16), 1781–1804.
(29) Wiley, B.; Sun, Y.; Mayers, B.; Xia, Y. *Chem. - Eur. J.* **2005**, *11* (2), 454–463.
(30) Quan, Z.; Wang, Y.; Fang, J. *Acc. Chem. Res.* **2013**, *46* (2), 191–202.
(31) Park, K.; Drummy, L. F.; Wadams, R. C.; Koerner, H.; Nepal, D.; Fabris, L.; Vaia, R. A. *Chem. Mater.* **2013**, *25* (4), 555–563.
(32) Li, C.; Shuford, K. L.; Chen, M.; Lee, E. J.; Cho, S. O. *ACS Nano* **2008**, *2* (9), 1760–1769.
(33) Montejano-Carrizales, J. M.; Rodríguez-López, J. L.; Pal, U.; Miki-Yoshida, M.; José-Yacamán, M. *Small* **2006**, *2* (3), 351–355.
(34) Yu, Y.; Zhang, Q.; Lu, X.; Lee, J. Y. *J. Phys. Chem. C* **2010**, *114* (25), 11119–11126.
(35) Wu, H.-L.; Kuo, C.-H.; Huang, M. H. *Langmuir* **2010**, *26* (14), 12307–12313.
(36) Tian, N.; Zhou, Z.-Y.; Sun, S.-G.; Ding, Y.; Wang, Z. L. *Science* **2007**, *316* (5825), 732–735.
(37) Zhang, J.; Langille, M. R.; Personick, M. L.; Zhang, K.; Li, S.; Mirkin, C. A. *J. Am. Chem. Soc.* **2010**, *132* (40), 14012–14014.
(38) Chen, S.; Wang, Z. L.; Ballato, J.; Foulger, S. H.; Carroll, D. L. *J. Am. Chem. Soc.* **2003**, *125* (52), 16186–16187.

(39) Yuan, H.; Khoury, C. G.; Hwang, H.; Wilson, C. M.; Grant, G. A.; Vo-Dinh, T. *Nanotechnology* **2012**, *23* (7), 075102.
(40) DuChene, J. S.; Niu, W.; Abendroth, J. M.; Sun, Q.; Zhao, W.; Huo, F.; Wei, W. D. *Chem. Mater.* **2013**, *25* (8), 1392–1399.
(41) Lin, G.; Lu, W.; Cui, W.; Jiang, L. *Cryst. Growth Des.* **2010**, *10* (3), 1118–1123.
(42) Sau, T. K.; Murphy, C. J. *J. Am. Chem. Soc.* **2004**, *126* (28), 8648–8649.
(43) Jana, N. R.; Gearheart, L.; Murphy, C. J. *Adv. Mater.* **2001**, *13* (18), 1389–1393.
(44) Nikoobakht, B.; El-Sayed, M. A. *Chem. Mater.* **2003**, *15* (10), 1957–1962.
(45) Xia, Y.; Xiong, Y.; Lim, B.; Skrabalak, S. E. *Angew. Chem. Int. Ed.* **2009**, *48* (1), 60–103.
(46) Liz-Marzán, L. M. *Chem. Commun.* **2012**, *49* (1), 16–18.
(47) Xiong, Y.; Xia, Y. *Adv. Mater.* **2007**, *19* (20), 3385–3391.
(48) Whitesides, G. M.; Boncheva, M. *Proc. Natl. Acad. Sci.* **2002**, *99* (8), 4769–4774.
(49) Whitesides, G. M.; Grzybowski, B. *Science* **2002**, *295* (5564), 2418–2421.
(50) Klimov, V. I. *Science* **2000**, *290* (5490), 314–317.
(51) Sun, S. *Science* **2000**, *287* (5460), 1989–1992.
(52) Sirringhaus, H.; Kawase, T.; Friend, R. H.; Shimoda, T.; Inbasekaran, M.; Wu, W.; Woo, E. P. *Science* **2000**, *290* (5499), 2123–2126.
(53) Jenekhe, S. A. *Science* **1999**, *283* (5400), 372–375.
(54) Xia, Y.; Gates, B.; Yin, Y.; Lu, Y. *Adv. Mater.* **2000**, *12* (10), 693–713.
(55) Wu, M.-H.; Whitesides, G. M. *Appl. Phys. Lett.* **2001**, *78* (16), 2273.
(56) Sánchez-Iglesias, A.; Grzelczak, M.; Altantzis, T.; Goris, B.; Perez-Juste, J.; Bals, S.; Van Tendeloo, G.; Donaldson Jr, S. H.; Chmelka, B. F.; Israelachvili, J. N.; others. *ACS Nano* **2012**, *6* (12), 11059–11065.
(57) Ni, W.; Mosquera, R. A.; Pérez-Juste, J.; Liz-Marzán, L. M. *J. Phys. Chem. Lett.* **2010**, *1* (8), 1181–1185.
(58) Hamon, C.; Postic, M.; Mazari, E.; Bizien, T.; Dupuis, C.; Even-Hernandez, P.; Jimenez, A.; Courbin, L.; Gosse, C.; Artzner, F.; Marchi-Artzner, V. *ACS Nano* **2012**, *6* (5), 4137–4146.
(59) Ni, S.; Leemann, J.; Wolf, H.; Isa, L. *Faraday Discuss* **2015**, *181*, 225–242.
(60) Hamon, C.; Liz-Marzán, L. M. *Chem. - Eur. J.* **2015**, *21* (28), 9956–9963.
(61) Yabu, H.; Shimomura, M. *Adv. Funct. Mater.* **2005**, *15* (4), 575–581.
(62) Kim, H. S.; Lee, C. H.; Sudeep, P. K.; Emrick, T.; Crosby, A. J. *Adv. Mater.* **2010**, *22* (41), 4600–4604.
(63) Harris, D. J.; Hu, H.; Conrad, J. C.; Lewis, J. A. *Phys. Rev. Lett.* **2007**, *98* (14), 148301.
(64) Byun, M.; Hong, S. W.; Qiu, F.; Zou, Q.; Lin, Z. *Macromolecules* **2008**, *41* (23), 9312–9317.
(65) Lin, Z. *J. Polym. Sci. Part B Polym. Phys.* **2010**, *48* (24), 2552–2557.
(66) Wang, D.; Nap, R. J.; Lagzi, I.; Kowalczyk, B.; Han, S.; Grzybowski, B. A.; Szleifer, I. *J. Am. Chem. Soc.* **2011**, *133* (7), 2192–2197.
(67) Walker, D. A.; Leitsch, E. K.; Nap, R. J.; Szleifer, I.; Grzybowski, B. A. *Nat. Nanotechnol.* **2013**, *8* (9), 676–681.
(68) Gang, O.; Zhang, Y. *ACS Nano* **2011**, *5* (11), 8459–8465.
(69) r zelcza er mant urst iz- a rz n , L. M. *ACS Nano* **2010**, *4* (7), 3591–3605.
(70) Yu, C.-J.; Tseng, W.-L. *Langmuir* **2008**, *24* (21), 12717–12722.
(71) D'Agostino A Taglietti A Bassi B Donà A Pallavicini P *J. Nanoparticle Res.* **2014**, *16* (10), 1–11.
(72) Elghanian, R.; Storhoff, J. J.; Mucic, R. C.; Letsinger, R. L.; Mirkin, C. A. *Science* **1997**, *277* (5329), 1078–1081.
(73) Wang, J.; Zhang, P.; Li, C. M.; Li, Y. F.; Huang, C. Z. *Biosens. Bioelectron.* **2012**, *34* (1), 197–201.
(74) Sudeep, P. K.; Joseph, S. T. S.; Thomas, K. G. *J. Am. Chem. Soc.* **2005**, *127* (18), 6516–6517.
(75) Lee, J.; Hernandez, P.; Lee, J.; Govorov, A. O.; Kotov, N. A. *Nat. Mater.* **2007**, *6* (4), 291–295.
(76) Parab, H. J.; Jung, C.; Lee, J.-H.; Park, H. G. *Biosens. Bioelectron.* **2010**, *26* (2), 667–673.
(77) Wang, L.; Zhu, Y.; Xu, L.; Chen, W.; Kuang, H.; Liu, L.; Agarwal, A.; Xu, C.; Kotov, N. A. *Angew. Chem. Int. Ed.* **2010**, *49* (32), 5472–5475.
(78) Nie, S.; Emory, S. R. *science* **1997**, *275* (5303), 1102–1106.

(79) Hou, J.; Zhang, H.; Yang, Q.; Li, M.; Song, Y.; Jiang, L. *Angew. Chem.* **2014**, *126* (23), 5901–5905.
(80) Peng, B.; Li, G.; Li, D.; Dodson, S.; Zhang, Q.; Zhang, J.; Lee, Y. H.; Demir, H. V.; Yi Ling, X.; Xiong, Q. *ACS Nano* **2013**, *7* (7), 5993–6000.
(81) Fraire, J. C.; Pérez, L. A.; Coronado, E. A. *ACS Nano* **2012**, *6* (4), 3441–3452.
(82) Wei, W.; Chen, K.; Ge, G. *Adv. Mater.* **2013**, *25* (28), 3863–3868.
(83) Fan, M.; Andrade, G. F.; Brolo, A. G. *Anal. Chim. Acta* **2011**, *693* (1), 7–25.
(84) Lee, Y. H.; Lee, C. K.; Tan, B.; Rui Tan, J. M.; Phang, I. Y.; Ling, X. Y. *Nanoscale* **2013**, *5* (14), 6404.
(85) Alvarez-Puebla, R. A.; Agarwal, A.; Manna, P.; Khanal, B. P.; Aldeanueva-Potel, P.; Carbó-Argibay, E.; Pazos-Pérez, N.; Vigderman, L.; Zubarev, E. R.; Kotov, N. A.; others. *Proc. Natl. Acad. Sci.* **2011**, *108* (20), 8157–8161.
(86) Kabashin, A. V.; Evans, P.; Pastkovsky, S.; Hendren, W.; Wurtz, G. A.; Atkinson, R.; Pollard, R.; Podolskiy, V. A.; Zayats, A. V. *Nat. Mater.* **2009**, *8* (11), 867–871.
(87) Garwe, F.; Huebner, U.; Clausnitzer, T.; Kley, E.-B.; Bauerschaefer, U. 2005; Vol. 5955, p 59550T – 59550T – 8.
(88) Young, K. L.; Ross, M. B.; Blaber, M. G.; Rycenga, M.; Jones, M. R.; Zhang, C.; Senesi, A. J.; Lee, B.; Schatz, G. C.; Mirkin, C. A. *Adv. Mater.* **2014**, *26* (4), 653–659.
(89) Mubeen, S.; Lee, J.; Singh, N.; Krämer, S.; Stucky, G. D.; Moskovits, M. *Nat. Nanotechnol.* **2013**, *8* (4), 247–251.
(90) Slaughter, L.; Chang, W.-S.; Link, S. *J. Phys. Chem. Lett.* **2011**, *2* (16), 2015–2023.
(91) Henry, A.-I.; Bingham, J. M.; Ringe, E.; Marks, L. D.; Schatz, G. C.; Van Duyne, R. P. *J. Phys. Chem. C* **2011**, *115* (19), 9291–9305.
(92) Raschke, G.; Sonnichsen, C.; Franzl, T.; Wilk, T.; von Plessen, G.; Feldmann, J.; Wilson, O.; Mulvaney, P. In *Quantum Electronics and Laser Science Conference, 2002. QELS'02. Technical Digest. Summaries of Papers Presented at the*; IEEE, 2002; p 33.
(93) Mock, J. J.; Barbic, M.; Smith, D. R.; Schultz, D. A.; Schultz, S. *J. Chem. Phys.* **2002**, *116* (15), 6755–6759.
(94) Peng, Y.; Xiong, B.; Peng, L.; Li, H.; He, Y.; Yeung, E. S. *Anal. Chem.* **2014**, *87* (1), 200–215.
(95) a zzucco eu uet e tép han, O.; Van Roy, W.; Van Dorpe, P.; Henrard, L.; Kociak, M. *Nano Lett.* **2012**, *12* (3), 1288–1294.
(96) Atwater, H. A.; Polman, A. *Nat. Mater.* **2010**, *9* (10), 205–213.
(97) Lal, S.; Grady, N. K.; Kundu, J.; Levin, C. S.; Lassiter, J. B.; Halas, N. J. *Chem. Soc. Rev.* **2008**, *37* (5), 898–911.
(98) Webb, J. A.; Bardhan, R. *Nanoscale* **2014**, *6* (5), 2502–2530.
(99) Lohse, S. E.; Burrows, N. D.; Scarabelli, L.; Liz-Marzán, L. M.; Murphy, C. J. *Chem. Mater.* **2013**, 34–43.
(100) Niu, W.; Zhang, L.; Xu, G. *Nanoscale* **2013**, *5* (8), 3172–3181.
(101) Xie, Y.; Guo, S.; Ji, Y.; Guo, C.; Liu, X.; Chen, Z.; Wu, X.; Liu, Q. *Langmuir* **2011**, *27* (18), 11394–11400.
(102) Singh, A.; Dickinson, C.; Ryan, K. M. *ACS Nano* **2012**, *6* (4), 3339–3345.
(103) Apte, A.; Bhaskar, P.; Das, R.; Chaturvedi, S.; Poddar, P.; Kulkarni, S. *Nano Res.* **2014**, *8* (3), 907–919.
(104) Banholzer, M. J.; Harris, N.; Millstone, J. E.; Schatz, G. C.; Mirkin, C. A. *J. Phys. Chem. C* **2010**, *114* (16), 7521–7526.
(105) yroshnychen o ela yah Adamo eu uet odr guez- ern n dez Pastoriza- an tos a cDonald en rard iz- a rz n , L. M.; Zheludev, N. I.; others. *Nano Lett.* **2012**, *12* (8), 4172–4180.
(106) de Abajo, F. G. *Phys. Rev. B* **1999**, *59* (4), 3095.
(107) Kociak, M.; Stéphan, O. *Chem. Soc. Rev.* **2014**, *43* (11), 3865–3883.
(108) García de Abajo, F. J. *Rev. Mod. Phys.* **2010**, *82* (1), 209–275.
(109) In *IUPAC Compendium of Chemical Terminology* ič ir t ošata B en ins A c au ght A Eds.; IUPAC: Research Triagle Park, NC, 2009.
(110) Koh, A. L.; Bao, K.; Khan, I.; Smith, W. E.; Kothleitner, G.; Nordlander, P.; Maier, S. A.; McComb, D. W. *ACS Nano* **2009**, *3* (10), 3015–3022.

PUBLICATIONS LIST

1. S.E. Lohse, N. D. Burrows, L. Scarabelli, L. M. Liz-Marzán, C.J. Murphy, *Anisotropic Metal Nanocrystal Growth: the Role of the Halides*, **Chem. Mater.**, 2013, 26, 34 – 43

2. L. Scarabelli, M. Grzelczak, L.M. Liz-Marzán, *Tuning Gold Nanorod Synthesis through Prereduction with Salicylic Acid*, **Chem. Mater.**, 2013, 25, 4232 – 4238

3. L. Scarabelli, M. Coronado-Puchau, J.J. Giner-Casares, J. Langer, L.M. Liz-Marzán, *Monodisperse Gold Nanotriangles: Size Control, Large-Scale Self-Assembly and Performance in Surface Enhanced Raman Scattering*, **ACS Nano**, 2014, 8, 5833 – 5842

4. C. Hamon, S. Novikov, L. Scarabelli, L. Basabe-Desmonts, L.M. Liz-Marzán, *Hierarchical Self-Assembly of Gold Nanoparticles Into Patterned Plasmonic Nanostructures*, **ACS Nano**, 2014, 8, 10694 – 10703

5. Losquin, L.F. Zagonel, V. Myroshnychenko, B. Rodríguez-González, M. , L. Scarabelli, J. Förstner, L.M. - , F.J. , O. , M. Kociak, *Unveiling Nanometer Scale Extinction and Scattering Phenomena Through Combined Electron Energy Loss Spectroscopy and Cathodoluminescence*, **Nano Letters**, 2015, 15, 1229 – 1237

6. M. Mayer, L. Scarabelli, K. March, T. Altantzis, M. Tebbe, M. Kociak, S. Bals, , A. Fery, L.M. Liz-Marzán, *Controlled Living Nanowire Growth: Precise Control over the Morphylogy and Optical Properties AgAuAg Bimetallic Nanowires*, **Nano Letters**, 2015, 15, 5427 – 5437

7. Hamon, S.M. Novikov, L. Scarabelli, D.M. Solís, T. Altantzis, S. Bals, J.M. Taboada, F.Obelleiro, L.M. Liz-Marzán, *Collective Plasmonic Properties in Few-Layer Gold Nanorod Supercrystals*, **ACS Photonics**, 2015, *2*, 1482 – 1488.

8. A.B. Serrano-Montes, D.J. de Aberasturi, J. Langer, J.J. Giner-Casares, L. Scarabelli - , *A General Method for Solvent Exchange of Plasmonic Nanoparticles and Self-Assembly into SERS-Active Monolayers*, **Langmuir**, 2015, 31, 9205 – 9213

9. L.Scarabelli, A. Sánchez-Iglesias, J. Pérez-Juste, L.M. Liz-Marzán, *A "Tips and Tricks" Practical Guide to the Synthesis of Gold Nanorods,* **J. Phys. Chem. Lett.**, 2015, 6, 4270 – 4279

10. B.B. Rajeeva, D.S. Hernandez, M. Wang, E. Perillo, L. Lin, L. Scarabelli, B. Pingali, L.M. Liz-Marzán, A.K. Dunn, J.B. Shear, Y. Zheng, *Regioselective Localization and Tracking of Biomolecules on Single Gold Nanoparticles*, **Advanced Science**, 2015, 2, 1500232

11. M. Wang, B.B. Rajeev, L. Scarabelli, L.M. Liz-Marzán, L. Jensen, Y. Zheng, *Photoswitchable Rabi Splitting in Fluorescence of Metal-Molecule Nanohybrids*, **submitted**

12. E. Modin, C. Hamon, M.N. Sanz-Ortiz , E. Hill, L. Scarabelli, A. Chuvilin, L.M. Liz-Marzán, *Hierarchical Organization and Molecular Diffusion in Gold Nanorod/Silica Supercrystal Nanocomposites*, **manuscript in preparation**

13. C. Hamon, M. Henriksen-Lacey, A. La Porta, J. Langer, L. Scarabelli, A.B. Serrano-Montes, G. González-Rubio, L. Basabe-Desmonts and L.M. Liz-Marzán, *Tunable Nanoparticle and Cell Assembly Using Combined Self-Powered Microfluidics and Micro-Contact Printing*, **manuscript in preparation**

14. L. Scarabelli, D.J. de Aberasturi, J.P. Merkl, C. Schmidtke, A. Feld, H. Welle and L.M. Liz-Marzán, *Encapsulation of Noble Metal Nanoparticles through Seed Emulsion Polymerization: Biocompatible SERS active Nanotags,* **manuscript in preparation**

ACKNOWLEDGMENT

First of all, I would like to say an enormous general thank you to all of you. These have been by far the best three years of my life, and they wouldn't have been the same without you guys! Science is passion, and passions are meaningless without someone to share them with; thanks for being amazing!!

Moreover, I would like to thank Plasmaquo (ERC Advanced Grant 267867) for the funding.

Thanks Luis, for accepting a long-hair-weird-looking Italian guy like me as a PhD student! Thanks for always believing in my skills, respecting my opinion and pushing me to work at the top of my possibilities, never accepting less than my very best.

Thanks to the *Marzanos*, past and present members! I'll remember all of you, all the good days spent together, always setting up a smile, cheering up those facing a bad day. Thank you Juanjo! Thanks for all your help, with your experience and professionalism. I'll make treasure of all your advices. Thanks Marta-Saaaaan, for sharing my obsession for details and for trying to fix my Spanish (that I won't forget... I promise!!). Thanks Su, for being Su! You are a wonderful person! When I'll be a grown-up scientist I hope to be like you! Thanks Ata! Finally I'll stop asking you so many favors… so, if I say that you are my favorite technician it won't sound so suspicious anymore. Thanks Malte, my personal climbing teacher! Your positive attitude and your smiles always made my day a little better! Thanks Judith and Dorleta! For all the night spent together, either working or having fun! Thanks for cheering me up so many times. Thanks Cirillo Prosciutto (alias Giacomo Hamon)! You are probably the best F.F. that I'll ever meet! We'll share other good hamburgers, as always matched with your (very) bad jokes…. Thanks Ana and Andrea, for sharing with me the torture of writing down three years of work. We started this adventure together, and I'm very happy to finish it the same way. It would have been so much harder doing it alone.

Thank you Staaaaaav!! My favorite Cypriot! All the evenings spent together, with good food, good conversation and a nice movie gave me the energy for doing my best every day! I wish you all the best in your life, and I hope to see you again very soon!

A big thanks to all my old friends! Even though I chose to leave, I know that you are always there for me, ready to make me feel at home. I owe you the little part of mental sanity that I have left... and probably all the one I lost too! Thanks Engy! You know I love talking chemistry with you; your brilliant mind always reminds me why I love my work so much. I'm sure you will accomplish great things in your career and I still "secretly" hope to work with you one day.

A special thanks to my parents: you always believed in me, even before I start believing in myself; and thank you Martina, for being always present when I needed you. You all taught me to think with my own head, and I will never thank you enough for this.

Thanks to you... "my happy person". Sometimes lab-life can be really hard, but you were always there, at my side even when far away; I've always found in you an inextinguishable source of strength, able to cheer me up and keep my dreams alive. To learn how to take my decisions without you will be my hardest challenge.